

Metabolic investigation of the microalga *Emiliana huxleyi* in laboratory and mesocosm experiments with focus on viral infection

Dissertation

zur Erlangung des akademischen Grades

doctor rerum naturalium (Dr. rer. nat.)

vorgelegt dem Rat der Chemisch-Geowissenschaftlichen Fakultät der

Friedrich-Schiller-Universität Jena

von

Mag. rer. nat. (Biologie) Michaela A. Mauß

geboren am 23.10.1982 in Melk a. d. Donau, Österreich

Gutachter

1.

2.

3.

Tag der öffentlichen Verteidigung:

**In one drop of water are found all the secrets of all
the oceans.**

Kahlil Gibran

Acknowledgments

Approximately four years ago I started my thesis coming as a “naive” marine biologist that knew nothing about metabolomics into a chemistry laboratory. That I did not quit right away, when fully realizing what my project was supposed to be, was beside my intention never to give up also due to the help and understanding of many people. Here is the right place to attribute my thanks to them.

First, I want to appreciate my supervisor Prof. Dr. Georg Pohnert, who accepted me in his group and enabled me to work in marine science. His constant advice, support and input on my project gave me a better understanding of chemical ecology and enabled me to prepare this thesis. His help did not end, when during the last month of writing I took refuge in Israel.

Further, I thank Prof. Dr. Maria Mittag for her helpful comments as my second supervisor.

Special thanks go to my cooperation partner Dr. Assaf Vardi at the Weizmann Institute of Science in Rehovot, Israel. He taught me much about viruses and made me aware again of my roots in marine biology. By inviting me to join their experiment, he provided the center of my research for more than two years and towards the end of my thesis he offered me a place for manuscript and thesis writing in his group.

I appreciate Dr. Dominique Marie and Dr. Ian Probert from the Station Biologique de Roscoff, France, for introducing me to flow cytometry and methods of viral infection of *Emiliania huxleyi* cultures. I am grateful to Prof. Dr. Ulrich S. Schubert for access to a flow cytometer.

Thanks to all the members of the Pohnert group. I cannot put into words how much I owe to my companion in the laboratory and friend Andrea Bauer. We share many precious memories (both laboratory-related and private) and she sometimes even tolerated my choice of music. Through her I got a better clue about chemistry as she was always the first one to address with my “stupid chemical questions of a biologist” and I hope I could also help her with biology. Thanks also to my second laboratory mate, Anett Kaulfuß, for her patience with my frequent outbursts, her thoughtful comments and the fun we shared in our “vegetarians’ laboratory”. Thanks to Dr. Katharina Grosser and Caroline Kurth for their companionship, their advices and the good times. Katha, I know I still owe you the Skype-wine meeting and Caro thanks for all the tea-time breaks, lunches, and talkative times we spent together as well as for proofreading this thesis. I appreciate Dr. Charles Vidoudez for making me acquainted with metabolomics, his open ear for my repeated questions after he had left the laboratory, and for his helpful comments on this thesis. I feel grateful for the help of Tino Jaschinski, Jan Grüneberg, and Dr. Martin Rempt, who were in charge of the GCT and assisted me through all the tricks the “Diva” played on me until we finally decided I might

better take over charge of this instrument myself. I am thankful for helpful inputs especially in statistics from Dr. Thomas Wichard and some funny distractions, when he came to our laboratory for talking. Thanks to Dr. Carsten Paul for enduring me for three weeks in Sweden and good comments on my experimental design. I thank Dr. Astrid Spielmeyer for her methodological comments and discussions on my project. Thanks also to Hannes Richter for providing his help whenever it was needed, to Madlen Kühn for all the organizational work she had because of my “foreign origin”, to Phillipp Richter for constant troubleshooting of my computer and to Björn Gebser for helping me with dimethylsulfoniopropionate measurements. I am grateful to Stefanie Wolfram for frequent discussions and to Constanze Kuhlisch for her social qualities, her great help to improve this thesis, and holding high the flag of marine biology after I took my leave. I appreciate the help of Johannes Wißen in developing suitable culture conditions for *E. huxleyi*. Thanks to Friederike Irmer, Raphael A. Seidel, Johannes Frenkel, Julia Erdmann, Michael Deicke, Dominique Jacquemoud, Katharina Eick, and Taghreed Alsufyani for discussions and the time we shared.

I am grateful to Dr. Shilo Rosenwasser for our fruitful work together on the viral infection experiment at the Weizmann Institute. I appreciate Dr. Daniella Schatz for her support and comments and Uri Sheyn for accepting me in the office. Thanks to Dr. Carmit Ziv and to all the other people from the Vardi laboratory for the good times we shared in Israel.

I would like to thank all the people, who participated in the mesocosm experiments in Sweden and especially Norway, helped me with sampling and provided data. Thanks to Dr. Maria Segovia and her Spanish group for organizing the mesocosm experiment in Norway followed by a workshop in Malaga.

I want to acknowledge my funding sources: ILRS for the funding of my project, ASSEMBLE for supporting a stay at the Station Biologique de Roscoff, MesoAqua for grants to participate in two mesocosm projects, the Minerva Stiftung of the Max Plank Gesellschaft for a short-term research fellowship, the VolkswagenStiftung for funding my flights to and from Israel, and all the people from the Weizmann Institute that enabled my two stays there.

Without the support and encouragement of my family and especially my parents this research would not have been possible. For their constant trust and support, although they did not always think it a good idea that I become a marine scientist, I feel every grateful.

Many thanks go to my boy-friend Marco for his support and for filling all the lonely evenings and nights during the intensive writing phase in Israel with his companionship and talk.

I am grateful to Wolfgang Angeringer for encouraging me to leave Austria and accept a project in Germany as well as to my friends Regina Parzer, Astrid Hösl, and Theresa Stadler, who always provided me a heartily welcome back home.

Table of content

1	Introduction.....	1
1.1	The ecological role of phytoplankton	1
1.2	Coccolithophores.....	2
1.2.1	Coccolithophores - important players in global carbon cycling	2
1.2.2	Coccolithophores under future ocean conditions.....	4
1.2.3	<i>Emiliania huxleyi</i> and its complex haplo-diploid life cycle	6
1.3	Marine viruses.....	8
1.3.1	Marine viruses – important agents in the marine environment.....	8
1.3.2	Effects of viral activity on phytoplankton and biogeochemical cycling.....	10
1.3.3	<i>Emiliania huxleyi</i> virus (EhV)	13
1.4	Metabolomics	15
1.4.1	Introduction to metabolomics	15
1.4.2	Metabolomics of microalgae.....	17
1.5	Thesis objectives	19
2	<i>Metabolic differences between diploid and haploid <i>Emiliania huxleyi</i> cells and of cells in different growth phases revealed by comparative metabolomics.....</i>	21
2.1	Experimental design	21
2.2	Results	23
2.2.1	Culture development	23
2.2.2	General correlation patterns based on metabolic profiles	27
2.2.3	Life phases of <i>Emiliania huxleyi</i>	30
2.2.4	Interphase comparison of haploid cells	33
2.3	Discussion	38
3	<i>Metabolic variation induced by CO₂ and iron manipulation during a mesocosm experiment.....</i>	47
3.1	Experimental design	47
3.2	Results	50
3.2.1	Phytoplankton growth	50
3.2.2	Bacterial and viral abundance	54
3.2.3	Experimental additions and nutrient levels	56
3.2.4	Separation patterns based on metabolic profiles	58
3.2.5	Metabolic profiling of specific treatments at different time intervals.....	66
3.2.6	General affiliation of metabolic classes to specific treatments	67
3.2.7	Combination of low CO ₂ /DFB-, low CO ₂ /DFB+, and high CO ₂	69
3.2.8	Low and high CO ₂	78
3.2.9	Dynamic changes in metabolic profiles in the control (low CO ₂ /DFB-) over time	80
3.3	Discussion	88

4	<i>Rewiring of host metabolism by large viruses infecting the cosmopolitan bloom-forming alga <i>Emiliana huxleyi</i></i>	99
4.1	Experimental design	99
4.2	Results	102
4.2.1	Infection dynamics of <i>Emiliana huxleyi</i> and its specific viruses	102
4.2.2	Dynamic modulation of metabolism with proceeding viral infection	104
4.2.3	Correlation of metabolome and transcriptome profiles	110
4.2.4	The effect of viral infection on amino acids and small amines	110
4.2.5	Effects of viral infection on glycolysis	111
4.2.6	The role of fatty acid biosynthesis in viral infection	114
4.2.7	Induction of the pentose phosphate pathway during late viral infection	115
4.2.8	The role of terpene and sterol biosynthesis in viral progeny assembly	118
4.2.9	Effect of viral challenge of virus-resistant <i>E. huxleyi</i> host strains on terpene and sterol biosynthesis	122
4.3	Discussion	123
5	Conclusion	133
6	Experimental procedures	137
6.1	Solvents	137
6.2	Cultivation	137
6.2.1	Phytoplankton cultures and viruses	137
6.2.2	Preparation of viral lysate and storage conditions	138
6.2.3	Medium	139
6.3	Large volume cultures (20 L)	139
6.3.1	Design of 20 L culture vessels	139
6.3.2	Culture vessel preparation	140
6.3.3	Sampling process	142
6.3.4	Remarks	142
6.4	Metabolomics – general method	143
6.4.1	Metabolite extraction and derivatization	143
6.4.2	GC-MS analysis	144
6.4.3	Measurement of standards	145
6.4.4	Data processing	145
6.4.5	Statistical analysis	146
6.4.6	Metabolite identification	147
6.4.7	Data availability	148
6.5	<i>Emiliana huxleyi</i> life and growth phases (method of Chapter 2)	148
6.5.1	Experimental setup and culture preparation	148
6.5.2	Monitoring of growth parameters and photosynthetic activity	149
6.5.3	Sampling of intracellular metabolites	150
6.5.4	Analysis of intracellular metabolites	151
6.5.5	Statistical analysis	151
6.6	Mesocosm (method of Chapter 3)	152
6.6.1	Set-up of the mesocosms	152
6.6.2	Filling of mesocosms	154

6.6.3	Preparation of sampling equipment	154
6.6.4	Sampling of mesocosms	155
6.6.5	Sampling for bacterial and viral abundance measurements	155
6.6.6	Bacterial and viral enumeration	156
6.6.7	Sampling of intracellular metabolites	157
6.6.8	Analysis of intracellular metabolites	157
6.6.9	Identification of intracellular metabolites	158
6.6.10	Statistical analysis	158
6.6.11	Remarks	159
6.7	Viral infection (method of Chapter 4)	160
6.7.1	Experimental set-up and infection	160
6.7.2	Sampling of infected and non-infected <i>E. huxleyi</i> cultures	160
6.7.3	Analysis of intracellular metabolites	161
6.7.4	Inhibition of fatty acid biosynthesis	161
6.7.5	Inhibition of terpene biosynthesis	162
6.7.6	Enumeration of life and dead <i>E. huxleyi</i> cells	163
6.7.7	Intra- and extracellular viral abundance	163
6.7.8	Analysis of free metabolites in viral capsids	164
6.7.9	Virus-resistant <i>E. huxleyi</i> strains	165
References		167
Appendices		179
Curriculum Vitae		207
Selbständigkeitserklärung		208

List of figures

Figure 1.1: Coccolithophore distribution.	2
Figure 1.2: The role of coccolithophores in biochemical cycles.	3
Figure 1.3: Microscopy images of <i>Emiliana huxleyi</i>	6
Figure 1.4: Scheme of the haplo-diploid life cycle of <i>Emiliana huxleyi</i>	7
Figure 1.5: Viral replication strategies.	9
Figure 1.6: The “viral shunt”.	10
Figure 1.7: Effect of marine viruses on phytoplankton.	12
Figure 1.8: Image of <i>Emiliana huxleyi</i> virus (EhV) particles.	13
Figure 2.1: Scheme of the experimental design.	22
Figure 2.2: Growth parameters of <i>Emiliana huxleyi</i> cultures.	24
Figure 2.3: Flow cytometry measurement images of <i>Emiliana huxleyi</i> cells in the life phase experiment.	25
Figure 2.4: Flow cytometry measurement images of <i>Emiliana huxleyi</i> cells in the growth phase experiment. ...	26
Figure 2.5: Multivariate separation of intracellular <i>Emiliana huxleyi</i> metabolites by canonical analysis of principal coordinates (CAP).	29
Figure 2.6: Vector plots of metabolites significantly correlated with life phases.	30
Figure 2.7: Vector plots of metabolites significantly correlated with growth phases.	34
Figure 3.1: Experimental design of the mesocosm experiment.	49
Figure 3.2: Phytoplankton growth during the mesocosm experiment.	52
Figure 3.3: Flow cam images of larger phytoplankton groups and ciliates.	53
Figure 3.4: Bacterial and viral abundance.	55
Figure 3.5: Observation of experimental additions and nutrient levels.	57
Figure 3.6: Multivariate separation of mesocosms by canonical analysis of principal coordinates (CAP).	60
Figure 3.7: Multivariate separation of different treatments in mesocosms by canonical analysis of principal coordinates (CAP) displayed at different time intervals.	62
Figure 3.8: Multivariate separation of specific treatments by canonical analysis of principal coordinates (CAP) at different time intervals.	66
Figure 3.9: Vector plots of metabolites significantly correlated with the combination of low CO ₂ /DFB-, low CO ₂ /DFB+, and high CO ₂	70
Figure 3.10: Vector plots of metabolites significantly correlated with low or high CO ₂	79
Figure 3.11: Vector plots of metabolites significantly correlated with different time intervals in the control.	82
Figure 4.1: Scheme of the experimental design with metabolomic and transcriptomic workflow.	101
Figure 4.2: Infection dynamics and ultrastructural analysis of <i>E. huxleyi</i> and its specific viruses.	103
Figure 4.3: Viral-induced remodeling of host metabolism during infection.	109
Figure 4.4: Viral-induced rewiring of host glycolysis facilitating fatty acid biosynthesis.	112
Figure 4.5: Induction of the pentose phosphate pathway and nucleotide biosynthesis during viral infection. ..	116
Figure 4.6: Terpene and sterol biosynthesis via the mevalonate pathway is required for viral replication.	120
Figure 4.7: Viral challenging of resistant host strains.	123
Figure 4.8: Rewiring of host metabolism during lytic viral infection.	125
Figure 6.1: Scheme of the 20 L culture vessel.	141
Figure 6.2: Structure of the fungal siderophore desferrioxamine B (DFB).	153

List of tables

<i>Table 2.1: Statistical diagnostic values of differences between growth phases.</i>	<i>28</i>
<i>Table 2.2: Heat map of metabolites correlated with life phases.....</i>	<i>31</i>
<i>Table 2.3: Relative sterol content.....</i>	<i>32</i>
<i>Table 2.4: Heat map of metabolites correlated with growth phases.....</i>	<i>36</i>
<i>Table 3.1: Numbers of detected signals.</i>	<i>59</i>
<i>Table 3.2: Statistical diagnostic values of canonical analysis of principal coordinates (CAP).</i>	<i>61</i>
<i>Table 3.3: Numbers of detected metabolites important for separation of the different parameters, in different metabolic classes.</i>	<i>68</i>
<i>Table 3.4: Heat map of normalized intensities of identified metabolites correlated with the treatment combination low CO₂/DFB-, low CO₂/DFB+, and high CO₂ or the single parameter CO₂.....</i>	<i>73</i>
<i>Table 3.5: Heat map of normalized intensities of identified metabolites correlated with metabolic profiles of the control over time.</i>	<i>84</i>
<i>Table 4.1: Average number of detected metabolites.</i>	<i>104</i>
<i>Table 4.2: Fold changes of identified metabolites detected during viral infection.</i>	<i>105</i>
<i>Table 4.3: Statistical support values of canonical analysis of principle coordinates (CAP).</i>	<i>108</i>
<i>Table 4.4: List of identified metabolites in EhV201 virions.....</i>	<i>119</i>
<i>Table 6.1: MS spectra libraries used for metabolite identification.</i>	<i>147</i>
<i>Table 6.2: Irradiance through the bags of the mesocosm enclosures and lids.....</i>	<i>153</i>

Zusammenfassung/Abstract

Zusammenfassung

Emiliania huxleyi ist eine weltweit verbreitete Coccolithophoride (Kalkalge), die großflächige Algenblüten bildet. Da sie eine hohe Photosyntheserate besitzt und ein Exoskelett aus kleinen Kalzitplättchen produziert, nimmt sie eine zentrale Rolle im marinen Kohlenstoffkreislauf ein. Virusinfektionen führen regelmäßig zum Zusammenbruch ihrer alljährlichen Frühjahrsblüten. Daher versuchte ich anhand einer Stoffwechselanalyse ein besseres Bild ihrer ökologischen Rolle bezüglich der Lebens- und Wachstumszyklen zu erhalten und Mechanismen zur Regulation der Virusinfektion aufzuklären.

Zwei Lebenszyklusphasen von *E. huxleyi* existieren: eine diploide, Algenblüten-bildende, die in zahlreichen Studien untersucht wird und eine haploide, noch wenig untersuchte. Basierend auf einer vergleichenden Analyse variiert die Zusammensetzung von Metaboliten (Stoffwechselprodukten) zwischen den Lebenszyklusphasen. Beispielsweise zeigten fünf spezifische Metabolite eine Korrelation zu diploiden Zellen. Aber auch die unterschiedlichen Wachstumsphasen der Zellen variieren hinsichtlich ihrer Metabolitzusammensetzung, was sich auf ihre ökologische Rolle auswirken kann. Ich konnte spezifische Metabolitgruppen während ganz bestimmter Zellwachstumsphasen (der exponentiellen Phase, der stationären Phase oder der Absterbephase) beobachten. Der Zuckeralkohol Mannitol etwa trat während exponentiellem Wachstum haploider Zellen in höherer Konzentration auf als in den anderen Wachstumsphasen. Im Gegensatz dazu waren Fettsäuren mit der stationären Phase und Sterole mit der Absterbephase korreliert. Zusätzlich konnte ich die Komplexität der Metabolitzusammensetzung während einer Mesokosmosstudie überprüfen, da es teilweise möglich war, spezifische metabolische Änderung einer bestimmten Planktongruppe zuzuordnen. Außerdem schlugen sich Änderungen des Kohlendioxidgehaltes und der Eisenverfügbarkeit im Wasser in der Metabolitzusammensetzung der Planktonpopulation nieder. In Mesokosmen mit erhöhtem bioverfügbarem Eisengehalt etwa traten die höchsten Konzentrationen von zahlreichen Sacchariden, Fettsäuren, vier Substraten des Citratzyklus, den meisten detektierten Aminosäuren und einigen Sterolen auf.

Bisher wissen wir nicht, welche (bio)chemischen Prozesse unabdingbar für die Reproduktion von Viren sind und in der Folge zwangsläufig zur Lyse der Wirtszelle führen. Deshalb versuchte ich durch die Untersuchung von Metabolitprofilen gesunder *E. huxleyi* Zellen, sowie von mit einem lytischen oder nicht-lytischen Virus infizierter Zellen, Unterschiede in der Metabolitzusammensetzung zu finden. Die so erhaltenen Daten wiesen auf eine grundlegende Neuordnung des Wirtsmetabolismus während des Infektionsverlaufes hin. Dies äußerte sich in unterschiedlichen Metabolitzusammensetzungen von gesunden, lytisch und nicht-lytisch infizierten Zellen. In Übereinstimmung mit parallel erstellten Transkriptom-Daten wiesen die Metabolitprofile auf eine verstärkte Glykolyse zu Beginn der lytischen Infektion hin, mittels derer Energie in eine erhöhte Fettsäureproduktion transferiert wurde. Spezifische Hemmung der Fettsäurebiosynthese führte zu einer konzentrationsabhängigen Reduktion an freigesetzten Viren. Dies lieferte einen weiteren Hinweis auf den Zusammenhang zwischen erfolgreicher Virusproduktion und erhöhter Fettsäuresynthese. Der Mevalonatweg zur Terpen- und Sterolbiosynthese nimmt eine weitere zentrale Rolle während der lytischen Infektion ein, da eine spezifische Hemmung dieses Biosyntheseweges zu einer starken Reduktion der Virenfreisetzung führte. Außerdem konnte ich das dominierende Sterol der Wirtsalge, Epibrassicasterol, in den Virionmembranen nachweisen. Es liegt daher nahe, dass von der Wirtsalge produzierte Sterole für die Produktion der Virionmembran nötig sind. Somit beschreibt die vorliegende Arbeit einen Mechanismus der gezielten Manipulation des Wirtsmetabolismus durch das Virus. Zusätzlich schlage ich potentielle Abwehrmechanismen des Wirts vor, indem dieser im späteren lytischen Infektionsverlauf spezifisch für die Virenproduktion nötige Biosynthesewege hinunter reguliert.

Zusammengenommen belegen diese Ergebnisse die Komplexität des Metabolismus von *E. huxleyi* und heben die grundlegende Bedeutung der Lipidsynthese in der Physiologie und biologischen Interaktion dieser Alge hervor. Dies zeigt sich sowohl während des regulären Zellzyklus als auch während lytischer viraler Infektion.

Abstract

The cosmopolitan coccolithophore *Emiliana huxleyi* can form massive blooms. With a high photosynthetic capacity and the formation of a calcite exoskeleton it constitutes a key player of global carbon cycling. Specific viruses frequently terminate annual *E. huxleyi* spring blooms making the alga an attractive target for investigations in the context of its ecological role as well as mechanisms of viral infection, which I addressed by metabolic analysis.

While the diploid, bloom-forming life phase of *E. huxleyi* is intensively studied, the less abundant haploid life phase is often overlooked. Comparative metabolic profiling revealed a unique metabolic composition for each life phase. Further, the growth stage of cells influences the metabolic composition and thus has an ecological impact. I observed changes in intensities of specific metabolic classes during growth (exponential, stationary, and declining phase). Five metabolites showed a significant correlation with the diploid life phase. Concerning the correlations of metabolites with growth phases in haploid cells a complex pattern was observed for saccharides as for example mannitol showed its highest concentration in the exponential phase, whereas fatty acids were correlated with the stationary and sterols with the declining phase. A mesocosm study confirmed the complexity of phytoplankton metabolism. Changes in metabolic profiles could partly be tracked back to the plankton group contributing the metabolite. Furthermore, carbon dioxide and iron manipulation affected metabolic profiles. Most saccharides, fatty acids, four detected tricarboxylic acid cycle substrates, most amino acids, and many sterols showed a significant correlation to the well growing iron-manipulation treatment.

Since (bio)chemical host-virus interactions leading to viral reproduction and finally host cell lysis are hitherto poorly understood, I aimed to determine changes in metabolic patterns during infection of *E. huxleyi* with either a lytic or non-lytic virus. Metabolome data pointed out a profound rewiring of host metabolism over the course of infection resulting in distinct metabolic profiles for cells infected by either virus in comparison to non-infected cells. In accordance with transcriptome data collected during the same experiment, metabolic profiles indicated changes in energy shuffling facilitating fatty acid production via induced glycolysis after the onset of lytic infection. The dependence of successful viral replication on this shift towards fatty acids is reflected in a dose-dependent reduction in viral release during specific inhibition of

the fatty acid biosynthesis. Further, the mevalonate branch of terpene and sterol biosynthesis occupies a pivotal role during lytic viral infection. Specific inhibition of this biosynthesis route strongly reduced viral release and the presence of epibrassicasterol, the dominant host sterol, was detected in virion membranes. Hence, sterols produced by the host are probably essential for the production of virion membranes. Therefore, I describe a mechanism by which the virus remodeled specific host metabolic biosynthesis pathways for production of viral progeny and propose potential host defense mechanisms such as the reduction of specific biosynthesis pathways essential for viral replication with proceeding lytic infection.

Taken together these results indicate the metabolic variability of *E. huxleyi* and the tremendous role of the lipid metabolic machinery both during regular cell cycling and lytic viral infection.

Abbreviations

1N	haploid
2N	diploid
A	amine
AA	amino acid
ACD	aragonite compensation depth
acetyl-CoA	acetyl coenzyme A
Alc	alcohol
AMDIS	Automated Mass Spectral Deconvolution and Identification System
ANOVA	analysis of variance
AU	arbitrary unit
BAH	Biological Institute Helgoland
C	chloroplast
C75	4-methylene-2-octyl-5-oxotetrahydrofuran-3-carboxylic acid
CA	carboxylic acid
CaCO ₃	calcium carbonate
CAP	canonical analysis of principal coordinates
CCD	calcite compensation depth
Chl <i>a</i>	chlorophyll <i>a</i>
CO ₂	carbon dioxide
CODA	Component Detection Algorithm
compl.	complex
C _{org}	organic carbon
CS	complex saccharide
D	day
DBE	double bond equivalent
ddW	double distilled water
Decl.	declining
deriv.	derivative
DFB	desferrioxamine B
DHA	docosaheptaenoic acid
DMS	dimethyl sulfide
DMSO	dimethyl sulfoxide
DMSP	dimethylsulfoniopropionate
DNA	deoxyribonucleic acid
DOM	dissolved organic matter
DRE	dynamic range extension
ds	double-stranded
DXR	deoxy-D-xylulose-5-phosphate reductoisomerase
EDTA	ethylenediaminetetraacetic acid
EhV	<i>Emiliana huxleyi</i> virus
ELISA	enzyme linked immunosorbent assay
ESI	electron spray ionization
EST	expressed sequence tags
Exp.	exponential
F ₀	initial fluorescence

FA	fatty acid
FAD	flavin adenine dinucleotide
FIA	flow injection analysis
FAS	fatty acid synthase
Fe	iron
F _m	maximum fluorescence
GC	gas chromatograph/gas chromatography
h	hour
HC	hydrocarbon
HCMV	human cytomegalovirus
HCO ₃ ⁻	hydrogen carbonate
HCV	Hepatitis C virus
HMGR	3-hydroxy-3-methylglutaryl-CoA reductase
HNLC	high nitrogen low chlorophyll
hpi	hours post infection
HPLC	high-performance liquid chromatography
HSV-1	Herpes Simplex virus-1
iso.	isomer
KSHV	Kaposi's Sarcoma-associated herpesvirus
LC	liquid chromatography
LDPE	low density polyethylene
M	mesocosm
MCP	major capsid protein
MCQ	Mass Chromatographic Quality
ME	methyl ester
MEP	methylerythritol phosphate
met.	metabolite
MET-IDEA	Metabolomics Ion-based Data Extraction Algorithm
MOI	multiplicity of infection
MS	mass spectrometer/mass spectrometry
MSTFA	N-methyl-N-(trimethylsilyl)trifluoroacetamide
MVA	mevalonate
N	nucleus
n.c.	not calculable
n.d.	not detected
N:P	nitrogen to phosphorus ratio
NADPH	nicotinamide adenine dinucleotide phosphate (reduced form)
NCLDV	nucleocytoplasmic large DNA viruses
NCMA	Provasoli-Guillard National Center for Marine Algae and Microbiota
NIST	National Institute of Standards and Technology
NMR	nuclear magnetic resonance
No.	number
NSW	natural sea water
O	others
P	phosphate
PAR	photosynthetically active radiation
PC	polycarbonate

PCD	programmed cell death
pCO ₂	partial pressure of gaseous carbon dioxide
PDH	pyruvate hydrolase
PE	polyethylene
PES	polyethersulfone
p. i.	post infection
POM	particulate organic matter
PP	pyrophosphate
PPL	polypropylene
PPP	pentose phosphate pathway
PSII	photosystem II
PVDF	polyvinylidene difluoride
qPCR	quantitative polymerase chain reaction
RFU	relative fluorescence units
RNA	ribonucleic acid
ROS	reactive oxygen species
RPM	reads per million
RT	retention time
S	saccharide
SA	sugar acid
SAC	sugar alcohol
sac.	saccharide
SD	standard deviation
SEM	scanning electron microscopy
Si	silica
ss	single-stranded
ST	sterol
Stat.	stationary
T	terpene
TCA	tricarboxylic acid cycle
TEM	transmission electron microscopy
TMS	trimethylsilyl
Tris	tris(hydroxymethyl)aminomethane
UDP	uridine diphosphate
unsat.	unsaturated
UV	ultraviolet
VLP	virus-like particle
vs.	versus
WDXRF	wavelength dispersive X-ray fluorescence spectroscopy
WGCNA	weighted correlation network analysis
Δ^2	square correlation
λ	eigenvalue

Abbreviations of enzyme names

Glycolysis

PGM	glucose-1-phosphate phosphodismutase
HXK	hexokinase
PGI	phosphoglucoisomerase
PFK	6-phosphofructokinase
FBPA	fructose-bisphosphate aldolase
TPI	triose phosphate isomerase
GAPDH	glyceraldehyde phosphate dehydrogenase
PGK	phosphoglycerate kinase
PGAM	phosphoglycerate mutase
ENO	enolase
PK	pyruvate kinase

Tricarboxylic acid (TCA) cycle

PDH	pyruvate dehydrogenase complex
-----	--------------------------------

Amino acid biosynthesis

ALT	alanine transferase
GOGAT	glutamate synthase
GS	glutamine synthase
AST	aspartate transaminase
PHGDH	3-phosphoglycerate dehydrogenase
PSPH	phosphoserine phosphatase
CYSO	cysteine synthase/O-phosphoserine sulfhydrylase/cystathionine beta-synthase

Fatty acid biosynthesis

ACC	acetyl-CoA carboxylase
FABF	β -ketoacyl-[acyl-carrier-protein] synthase I
FABG	β -ketoacyl-[acyl-carrier-protein] synthase II
FABH	β -ketoacyl-[acyl-carrier-protein] synthase III

Pentose phosphate pathway

GOD	glucose 1-dehydrogenase
GNL	gluconolactonase
GLC	gluconokinase
G6PD	glucose-6-phosphate dehydrogenase
6PGL	6-phosphogluconolactonase
6PGD	6-phosphogluconic dehydrogenase
RPE	ribulose-phosphate 3-epimerase
RPI	ribose-5-phosphate isomerase
RBKS	ribokinase
TKT	transketolase
TAL	transaldolase

Nucleotide biosynthesis

PRPS	ribose-5-phosphate to 5-phosphoribosyl α -1-pyrophosphate (PRPP) synthetase
RNR	ribonucleotide reductase
PFAS	phosphoribosylformylglycinamide synthase
PAICS	phosphoribosylaminoimidazole carboxylase

Nucleotide biosynthesis substrates

UMP	uridine monophosphate
dCTP	deoxycytidine triphosphate
CTP	cytidine triphosphate
UTP	uridine triphosphate
UDP	uridine diphosphate
dUDP	deoxyuridine diphosphate
dUTP	deoxyuridine triphosphate
dUMP	deoxyuridine monophosphate
dTMP	deoxythymidine monophosphate
dTTP	deoxythymidine triphosphate
IMP	inosine monophosphate
AMP	adenosine monophosphate
ATP	adenosine triphosphate
dATP	deoxyadenosine triphosphate
GMP	guanosine monophosphate
GTP	guanosine triphosphate
dGTP	deoxyguanosine triphosphate

Terpenoid biosynthesis: mevalonate pathway

ACAT	acetyl-CoA C-acetyltransferase
HMGS	3-hydroxy-3-methylglutaryl-CoA synthase
HMGR	3-hydroxy-3-methylglutaryl-CoA reductase
MVK	mevalonate kinase
PMVK	phosphomevalonate kinase
MVD	diphosphomevalonate decarboxylase

Terpenoid biosynthesis: methylerythritol phosphate pathway

DXPS	1-deoxy-D-xylulose-5-phosphate synthase
DXR	1-deoxy-D-xylulose-5-phosphate reductoisomerase
MCT	2-C-methyl-D-erythritol 4-phosphate cytidylyltransferase
CMK	4-(cytidine 5'-diphospho)-2-C-methyl-D-erythritol kinase
MCS	2-C-methyl-D-erythritol 2,4-cyclodiphosphate synthase
HDS	(E)-4-hydroxy-3-methylbut-2-enyl-diphosphate synthase
HDR	4-hydroxy-3-methylbut-2-enyl-diphosphate reductase

Shared pathways

IPPI	isopentenyl-diphosphate delta-isomerase
ISPS	isoprene synthase
GPS	geranyl-diphosphate synthase
FPS	2,6-farnesyl diphosphate synthase
GGPS	geranylgeranyl diphosphate synthase
GGPR	geranylgeranyl diphosphate reductase

1 Introduction

1.1 The ecological role of phytoplankton

Plankton (Greek *planktos*: wandering) comprises organisms in aquatic environments that due to their limited mobility are not able to cover distances by own power, but are forced to drift along with the water currents. This group includes all different kinds of organisms from large jelly fish to hardly visible unicellular ones. The autotrophic, photosynthetic fraction is called “phytoplankton” and consists of microscopic unicellular organisms that play an important role in marine ecosystems.

As photosynthetic organisms, phytoplankton are a source of oxygen to the atmosphere and in parallel provide a major sink for carbon dioxide. Marine phytoplankton is the key player of primary production in the oceans. Although their biomass represents less than 1% of the photosynthetic biomass on earth, marine phytoplankton are responsible for nearly half of the global photosynthesis and carbon fixation (Field et al., 1998). Their total contribution to photosynthetic carbon fixation is estimated to lead to a formation of ~45 gigatons of organic carbon (C_{org}) per year with an average turnover time of phytoplankton carbon in the order of a week or less (Falkowski et al., 1998). This enables marine phytoplankton to constitute the basis of the marine food web (Link, 2002). Phytoplankton derived organic matter is shuffled through different consumer levels of the food web resulting in recycling in the upper oceanic layers or is finally sequestered into the deeper ocean, a process contributing to the “biologic carbon pump” (Ducklow et al., 2001).

Occasionally, during favorable environmental conditions phytoplankton are able to grow exponentially, locally reaching high abundances, which are referred to as algal blooms. The fate of phytoplankton in the oceans is affected by several parameters. Abiotic factors such as light, nutrient availability and temperature constitute a spatial and temporal limitation for marine primary production (Field et al., 1998). Further, biotic factors such as grazers and viruses have a structuring effect on marine phytoplankton, especially during bloom events (Brussaard et al., 1995).

An aspect in phytoplankton worth mentioning is their diversity as several taxonomic classes contribute to this functional type. Important representatives belong to the division Haptophyta, unicellular chlorophyll *a* + *c* containing algae that are

distinguished from other groups by the possession of a haptonema (Greek *hapsis*: touch) (de Vargas et al., 2007). This group consists of the classes Pavlovophyceae (1 order) and Prymnesiophyceae (6 orders) (Jordan et al., 2004) with calcifying representatives of the latter being referred to as “coccolithophores” (Figure 1.1).

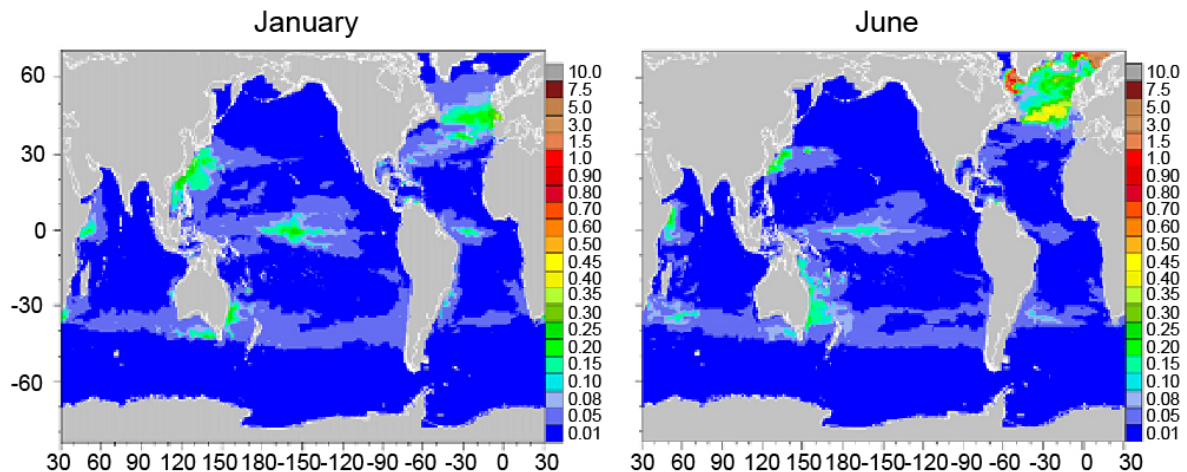


Figure 1.1: Coccolithophore distribution. Estimated areal distribution of coccolithophores in January and June (in chlorophyll units, mg m⁻³). Adapted from Gregg and Casey (2007).

1.2 Coccolithophores

1.2.1 *Coccolithophores - important players in global carbon cycling*

Coccolithophores are unicellular marine algae that play a significant role in the world's oceans. As the name indicates, this group includes all haptophytes that are able to produce calcified scales (coccoliths) at least during part of their life cycle (Billard and Inouye, 2004). They are considered to be the most productive calcifying organisms on earth (Rost and Riebesell, 2004) with an estimated contribution to total phytoplankton biomass of 11% (Gregg and Casey, 2007). By secretion of their tiny composite exoskeleton, this group accounts for approximately half of all recent oceanic calcium carbonate (CaCO₃) precipitation (Milliman, 1993). The function of coccoliths was much debated on, but putatively involves protection against predation, a biochemical advantage by direct utilization of hydrogen carbonate (HCO₃⁻) for photosynthesis, and a mechanism to regulate flotation or light (Young, 1987). Attention was further drawn to coccolithophores as during the formation of large blooms that consist of representatives of this group, satellite imagery allows the

observation of light reflected by loose coccoliths drifting in the water (Holligan et al., 1983; Balch et al., 1991).

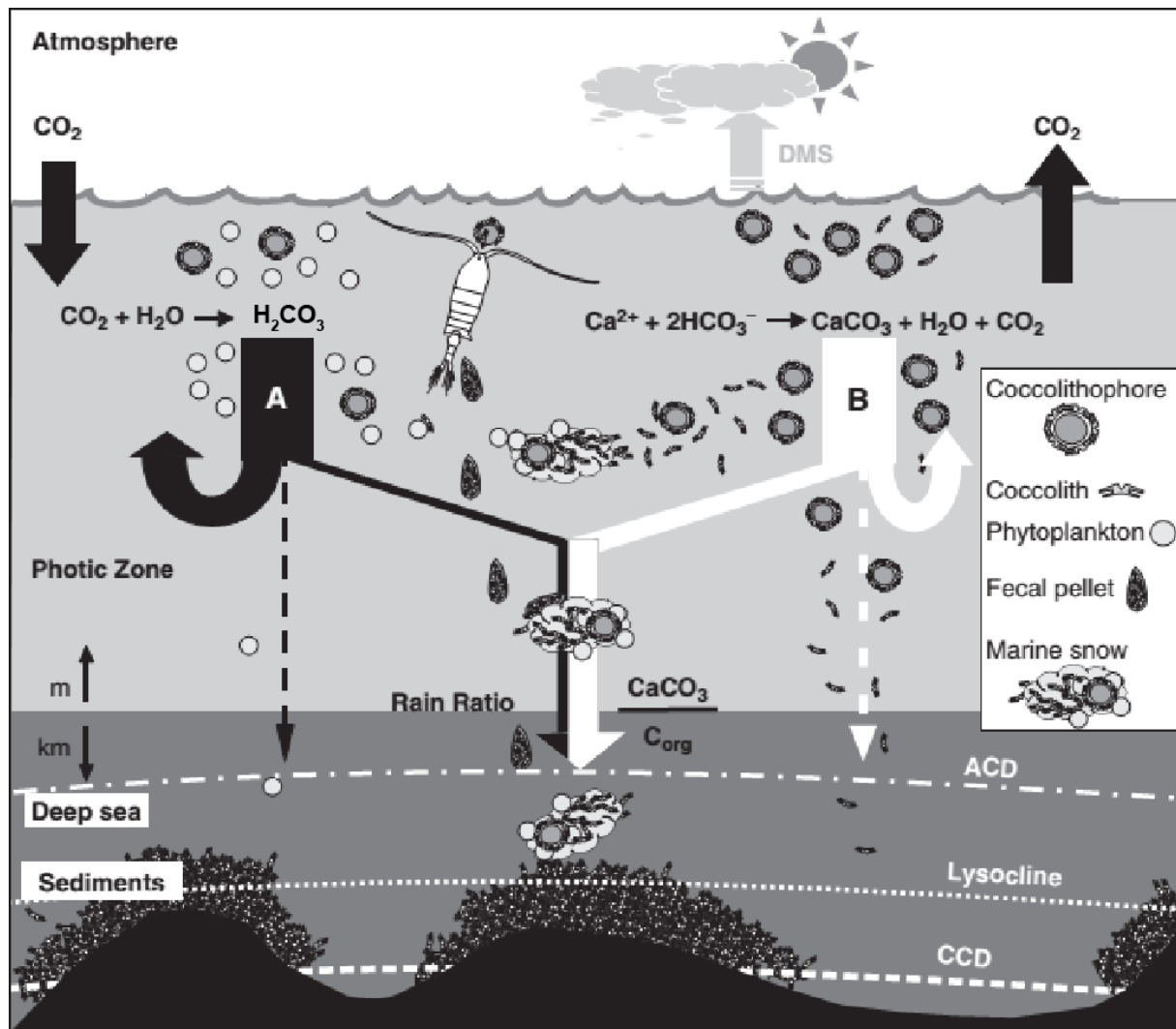


Figure 1.2: The role of coccolithophores in biochemical cycles. Through the production of calcite plates (coccoliths) coccolithophores are key players in global carbon cycling. They actively participate in gas exchange (carbon dioxide, CO_2 and dimethyl sulfide, DMS) between seawater and atmosphere, and contribute to the export of organic carbon (C_{org}) and calcium carbonate (CaCO_3) to deeper oceanic layers and deep-sea sediments. As calcifying, photoautotroph organisms they contribute to two main cycles: The ballasting effect of their coccoliths on aggregates results in the sinking of marine snow, thereby driving the “oceanic carbon pump” (A), a process removing CO_2 from the atmosphere. In parallel, through the calcification reaction they are the main actors of the “carbonate counter-pump” (B), which in contrast is a short-term source of atmospheric CO_2 . Thus, coccolithophore biomineralization tightly couples the organic and carbonate pump. For the last 220 million years fossil archives accumulated at the seafloor, because certain types of coccoliths are particularly resistant to dissolution in the three main carbonate dissolution horizons: the aragonite compensation depth, ACD, the lysocline, and the calcite compensation depth, CCD. The lysocline corresponds to the depth in the water column with a critical undersaturation with respect to CaCO_3 , where further complete dissolution of foraminifera takes place. *Adapted from de Vargas et al. (2007), inspired by Rost and Riebesell (2004).*

Since this group is able to produce calcite plates, its role in carbon fixation is critical. Coccoliths initiate the accumulation of marine snow thereby ballasting organic matter which consequently sinks to deep oceanic layers. Therefore, coccolithophores constitute suitable drivers of the open ocean “biological carbon pump” (de Vargas et al., 2007; Honjo et al., 2008) (Figure 1.2A). Contrastingly, a study monitoring an intensive bloom event reported an increase in dissolved gaseous CO₂ relative to total inorganic CO₂ in areas where the calcite concentration is high. Within this intense coccolithophore bloom alkalinity was affected by calcification strong enough to result in a local reduction of the air-sea CO₂ gradient (Robertson et al., 1994). As CaCO₃ formation reduces alkalinity it affects the equilibrium between different forms of dissolved inorganic carbon, thereby driving a “carbonate counter pump” (Rost and Riebesell, 2004) (Figure 1.2B). Thus, coccolithophores are thought to contribute both to the biologic carbon pump and to the carbonate counter pump (Rost and Riebesell, 2004). Further, coccolithophore blooms contribute to the global sulfur cycle by production and release of dimethylsulfoniopropionate (DMSP). This substance is extracellularly transferred into dimethyl sulfide (DMS), a bioactive gas found to play a role in cloud formation and therefore in global climate regulation (Simo, 2001; Malin and Steinke, 2004) (Figure 1.2).

1.2.2 Coccolithophores under future ocean conditions

CO₂ release to the atmosphere from burning of fossil fuels will partly be absorbed in the oceans and result in ocean acidification. Until the end of this century this ongoing process will probably lead to a pH reduction of 0.4 units (Caldeira and Wicket, 2003). Such predicted changes in ocean pH are greater than any experienced during the past 300 million years (Caldeira and Wicket, 2003) and will thus have a tremendous impact on marine organisms.

In coccolithophores such as *Emiliania huxleyi* and *Gephyrocapsa oceanica* increased CO₂ concentration leads to reduced calcite production accompanied by an increased proportion of malformed coccoliths and incomplete coccospheres (Riebesell et al., 2000b). This was also reflected in a reduced ratio of calcite precipitation to organic matter production (Riebesell et al., 2000b). Further, net specific growth rate of *E. huxleyi*, rate of calcification per cell, elemental stoichiometry

of uptake and production processes were found to be sensitive to changes in partial pressure of gaseous CO₂ (pCO₂) (Engel et al., 2005). Productivity and distribution of coccolithophores are affected both directly through acidification of surface seawater and indirectly through increasing upper-ocean thermal stratification (Rost and Riebesell, 2004). The case of *Coccolithus braarudii* demonstrates that responses to acidification might differ among species as effects on calcification and photosynthesis were observed at a higher threshold than in other coccolithophore species (Krug et al., 2011). In contrast, one study stated an increase of calcification and net primary production in *E. huxleyi* under high pCO₂ and further reported a 40% increase in coccolith mass deposited in the deep oceans over the last 220 years (Iglesias-Rodriguez et al., 2008). As these results are in stark contrast to all other studies on the effects of elevated CO₂ levels on coccolithophores, other authors suspect that shortcomings in the methodology compromised the data interpretation (Riebesell et al., 2008).

In general, it is accepted that increasing oceanic CO₂ concentrations will have a strong impact on coccolithophores resulting in an estimated areal decrease of blooms by up to 50% by the middle of this century in the North Atlantic (Iglesias-Rodriguez et al., 2002). Thus, potential feedbacks to increasing atmospheric CO₂ arising from changes in photosynthesis, calcification or a shift in the dominance of coccolithophores may be crucial when trying to forecast future climate change (Rost and Riebesell, 2004).

Additionally, ocean acidification will probably lead to a decrease in iron availability as was demonstrated by Shi et al. (2010). Acidification of media containing different iron compounds decreased the iron uptake rate in diatoms and coccolithophores. Thus, ocean acidification is likely to increase the iron stress of phytoplankton populations in some areas of the ocean. Regions where phytoplankton production is regularly limited by iron are for example the so called high nitrogen, low chlorophyll (HNCL) regions. They show an excess of surface nitrate and phosphate but low productivity and comprise large areas in the Southern oceans (Martin and Fitzwater, 1988). Such iron limitation can reduce active CO₂ and HCO₃⁻ uptake resulting in diminished growth rates and a reduction of the efficiency of mechanisms sustaining inorganic carbon fixation in *E. huxleyi* (Schulz et al., 2007).

1.2.3 *Emiliania huxleyi* and its complex haplo-diploid life cycle



Figure 1.3: Microscopy images of *Emiliania huxleyi*. (A) Scanning electron microscopy (SEM) image of a diploid, calcified cell as observed in the mesocosm (see 3.2.1), light micrographs of (B) diploid, calcified cells, and of (C) haploid cells with flagella visible above.

Emiliania huxleyi (Lohmann) Hay & Mohler, 1967 (Figure 1.3) is the most abundant species among coccolithophores and probably the most important calcifier in the world's oceans (Westbroek et al., 1989). It was estimated that its coccoliths account for approximately one third of the total marine CaCO_3 production (Iglesias-Rodriguez et al., 2008). The existence of several ecotypes potentially enables the wide distribution of this species in nature (Paasche, 2002).

Further, this cosmopolitan species is responsible for intensive blooms covering several hundreds to thousands of square kilometers which are even detectable from space (e.g. Holligan et al., 1983; Brown and Yoder, 1994). Among the largest documented *E. huxleyi* blooms was an intensive event south of Iceland (North Atlantic) in 1991 covering 250,000 km² (Holligan et al., 1993). Such large-scale episodic events are potentially favored by a high genomic variability allowing this alga to cope with a wide variety of environmental conditions (Read et al., 2013). Blooms especially occur in eutrophic regions often in a succession following diatom spring blooms at temperate latitudes (Tyrell and Merico, 2004). This is probably due to a nutritional advantage of *E. huxleyi* over diatoms as soon as silicate levels drop low but nitrate, phosphate, and other nutrients are still abundant (Tyrell and Merico, 2004).

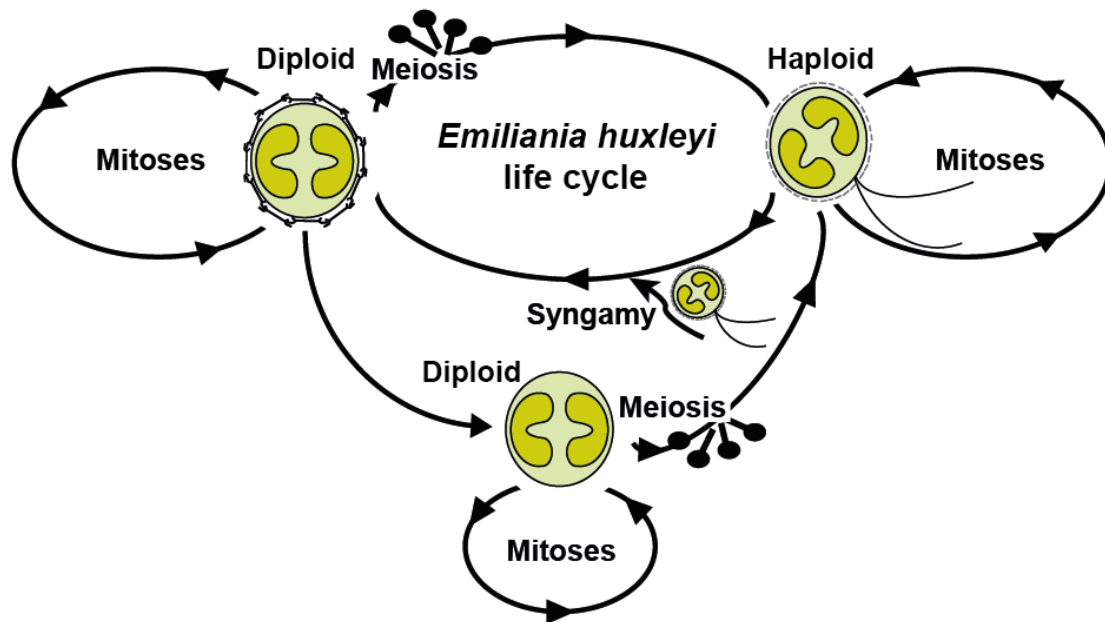


Figure 1.4: Scheme of the haplo-diploid life cycle of *Emiliana huxleyi*. A detailed description of the life cycle is given in the text below. *Illustration based on Klaveness (1972), Green et al. (1996), and Houdan et al. (2004).*

An interesting trait of this alga is its complex haplo-diploid life cycle (Figure 1.4) displaying two basic levels of ploidy (Green et al., 1996; Houdan et al., 2004). *E. huxleyi* exists in a heterococcolith bearing, diploid stage alternating with a motile, flagellated cell form that is haploid and bearing organic scales (Houdan et al., 2004). Additionally, reports describe a diploid, non-motile, naked stage, which alternates with the diploid calcified cell (Klaveness, 1972; Green et al., 1996). These naked cells are regarded as culture mutants and are not considered as part of the regular life cycle (Paasche, 2002). Each of these cell types is able to reproduce vegetatively and to maintain stable populations (Green et al., 1996). Although haploid cells occasionally occur in diploid cultures, observation of sexual behavior in this species is missing (Houdan et al., 2004).

The diploid, bloom-forming life phase mostly found in nature is intensively studied. In contrast, the role of the haploid phase is still poorly explored. Green et al. (1996) state a potential function of the haploid form in acting as gametes. Indication for the occurrence of meiosis and the sexual life cycle in nature was recently found during a mesocosm experiment (Frada et al., 2012). Haploid *E. huxleyi* cells increased in abundance after the demise of the natural bloom by viruses (Frada et al., 2012). In general, among algae a haplo-diploid life cycle is regarded to be

favorable in a seasonally changing environment or in a habitat comprising two, to some extent different niches (Stebbins and Hill, 1980). So Rokitta et al. (2011) interpreted differences detected at the transcriptome level of *E. huxleyi* life phases as a specialization to varying ecological niches. Their analyses indicated differences in genome expression, proteome maintenance and metabolic processing in the life phases with the latter being up-regulated at transcriptional level in haploid relative to diploid cells. Further, only diploid cells are susceptible to viral infection whereas haploid ones are resistant indicating also differences in physiological traits regarding the phenotype (Frada et al., 2008). Consequently, large *E. huxleyi* blooms mainly consisting of diploid cells (e.g. Holligan et al., 1993) are regularly terminated by a specific double-stranded DNA (dsDNA) virus (Bratbak et al., 1993; Wilson et al., 2002).

1.3 Marine viruses

1.3.1 *Marine viruses – important agents in the marine environment*

Viruses (Latin *virus*: poison) are per definition a microscopic entity of genetic material (either single-stranded (ss) or double-stranded (ds) DNA or RNA) surrounded by a protein coat with some additionally being covered by lipids (Fuhrman, 1999). As they have no own intrinsic metabolism, viruses rely on their host's metabolic machinery to provide the necessary building blocks for viral replication (Fuhrman, 1999). Since the detection of *Mimivirus*, a giant virus that possesses its own virophage (a virus infecting another virus) named “Sputnik” (La Scola et al., 2008), it is under much debate whether viruses should be regarded as “life forms” or as “biological entity” (Raoult and Forterre, 2008; Moreira and López-García, 2009; and related correspondence).

The number of viruses in the oceans is overwhelming as they constitute the most abundant entities. Typically, 10^6 to 10^9 virus-like particles (VLPs) mL^{-1} are found in aquatic systems (Bergh et al., 1989). Using the volume of the oceans ($\sim 1.3 \cdot 10^{21}$ L) and an average viral abundance of $3 \cdot 10^9 \text{ L}^{-1}$, total viral numbers were estimated to amount to 10^{30} viruses in the oceans (Suttle, 2005b) with approximately 10^{23} viral infections occurring every second (Suttle, 2007). Nevertheless, it can be assumed that the majority of viruses are not yet discovered, as the virosphere, the proportion

of the Earth where viruses occur or that is affected by them, includes every surface of the planet down to the depths of the oceans (Suttle, 2005a).

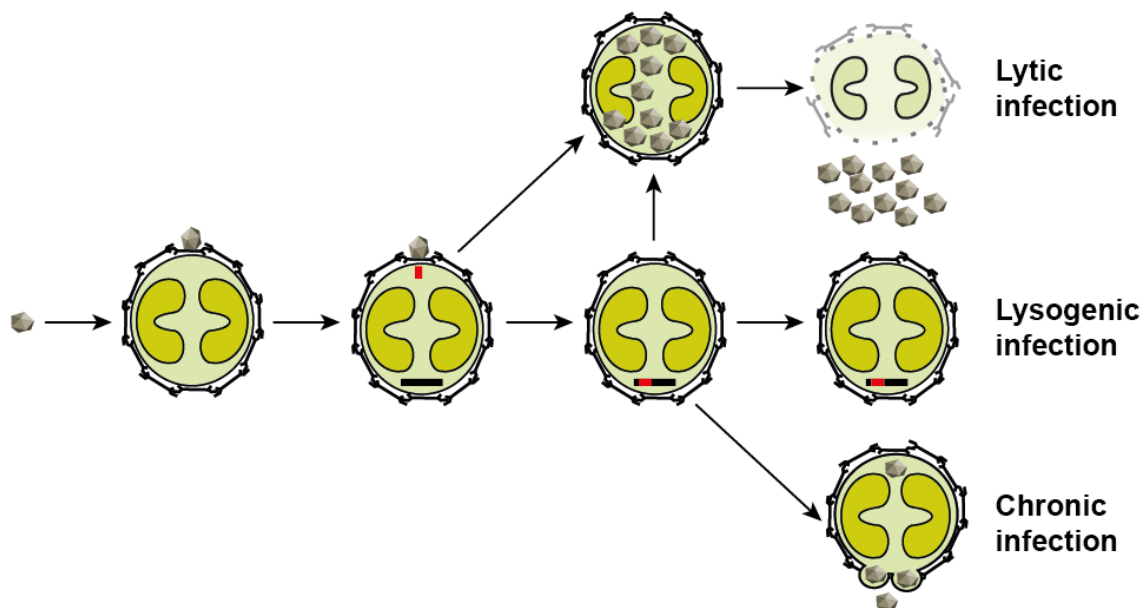


Figure 1.5: Viral replication strategies. Top: lytic infection leading to host cell death upon viral release. Mid: lysogenic infection with viral nucleic acid (red) integrated into the host genome (black). An external factor might trigger switching towards lytic infection (indicated by an arrow). Bottom: chronic infection resulting in release of only few viruses at a time without much harm to the host. Arrows indicate the proceeding of the infection. The host cell is illustrated as a coccolithophore, which is representative for a marine autotrophic unicellular organism. *Illustration based on Fuhrman (1999), Madigan et al. (2000), and Brussaard (2004a).*

As viruses lack an intrinsic metabolism, they function as parasites relying on a host cell for synthesis of nucleic acids and capsid proteins needed for the assembly of progeny (Fuhrman, 1999; Brussaard, 2004a). After takeover of the host's metabolic machinery viral progeny are formed *de-novo* within the host cell (Brussaard, 2004a). Three basic replication strategies of marine viruses exist (Figure 1.5), all starting with a virus binding to a cell and injecting its nucleic acids. In lytic infection, the host is directed to produce viral progeny that is released via host cell lysis (Fuhrman, 1999; Brussaard, 2004a). Lysogeny (in bacteriophages also called "latency" or "temperance") results in integration of the nucleic acid of the viral genome into the host genome, where it stays dormant (or "temperate") and is replicated with its host's genome. An induction event, for example stress to the host, can trigger a switch from lysogenic to lytic infection (Fuhrman, 1999; Brussaard, 2004a). In contrast, in chronic infection viral progeny is consistently released from

cells in a non-lethal fashion via budding or extrusion over several generations (Fuhrman, 1999).

1.3.2 Effects of viral activity on phytoplankton and biogeochemical cycling

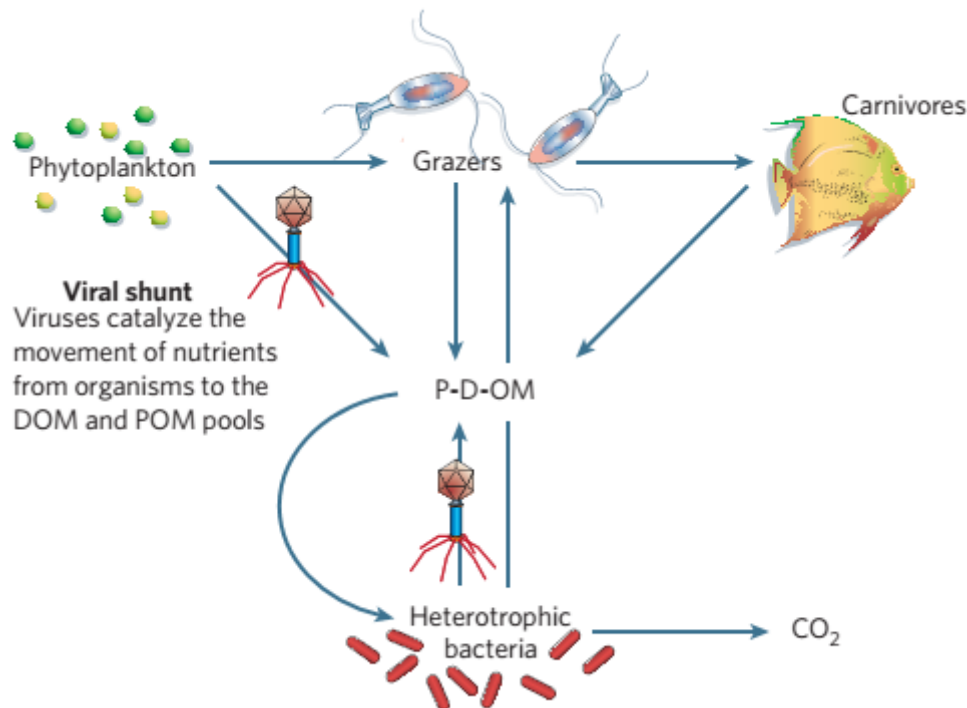


Figure 1.6: The “viral shunt”. As main primary producer phytoplankton provides energy in the marine environment, which is consumed by grazers (e.g. copepods) that are themselves preyed upon by carnivores. Each trophic level further releases a significant amount of organic matter either in the form of living organisms (particulate organic matter, POM) or in the form of exudates, and dead released material (dissolved organic matter, DOM). The resulting pool supports the growth of heterotrophic microorganisms (both bacteria and archaea). Viral infection resulting in cell lysis increases the DOM pool thereby shutting down the flow of carbon and nutrients from phytoplankton and bacteria to higher trophic levels. As a consequence carbon respiration increases, whereas its transfer to higher trophic levels in the marine food web decreases. *Adapted from Suttle (2005b).*

Especially by killing the host cell, viral activity influences global biogeochemical cycles (Wommack and Colwell, 2000; Suttle, 2005b). Carbon and nitrogen are used for primary production by phytoplankton and are consequently cycled through the oceanic food web (Wommack and Colwell, 2000). Losses of primary production are recycled by aquatic bacterial populations as they regenerate nutrients which can effectively increase the proportion of primary production available for higher trophic levels in the marine food web. This process is called the “microbial

loop” (Azam et al., 1983). Viral lysis releases cell debris from the phytoplankton or bacterial host (living organisms) into the dissolved organic matter (DOM) pool (Fuhrman, 1999). As a net effect this “viral shunt” increases community respiration and diverts the carbon flux away from higher trophic levels (Wommack and Colwell, 2000; Suttle, 2005b). It is regarded to function in stimulating nutrient and energy cycling to favor bacterial production (Fuhrman, 1999). An estimated maximum of 25% of photosynthetically fixed carbon cycles through the viral shunt (Wilhelm and Suttle, 1999). Further, viral activity affects the biological carbon pump as viral lysis promotes carbon sinking rates into the deep ocean, where it is sequestered (Fuhrman, 1999) (Figure 1.6).

Besides affecting biogeochemical cycling, viruses can play a crucial role in regulating phytoplankton populations and dynamics (Brussaard, 2004a). Although viruses can possibly infect hosts from different species or even genera, the subset of hosts a virus typically infects is narrower than for example the range of grazers such as protists or zooplankton (Weitz and Wilhelm, 2012). This is especially true in phytoplankton as here, due to a species-specific host selection, viral infection can affect the population of a specific algal species, thereby enhancing coexistence of competing phytoplankton. After removal or reduction of high abundant taxa, lower abundant ones might follow or overtake them, which results in natural bloom succession with viruses acting as diversity regulator (Brussaard, 2004a). By removal of the most abundant taxa viruses even contribute to bloom termination as was shown in several studies on *E. huxleyi* (e.g. Bratbak et al., 1993; Wilson et al., 2002).

Viruses can further influence their phytoplankton host in several direct ways at the population level or the level of the individual (Figure 1.7). As already mentioned the most obvious and prominent effect is phytoplankton mortality. Viruses might also act as evolutionary enhancer, because they can serve as gene reservoir and by horizontal gene transfer can change the ecological niche of their host (Sullivan et al., 2005). Further, several viruses carry so called “auxiliary metabolic genes” presenting critical, rate-limiting steps of host metabolism (Breitbart, 2012). A prominent example constitute genes encoding for the photosystem II (PSII) detected in cyanophages (Lindell et al., 2005) and assumed to provide energy support during viral infection when host photosynthesis genes are suppressed.

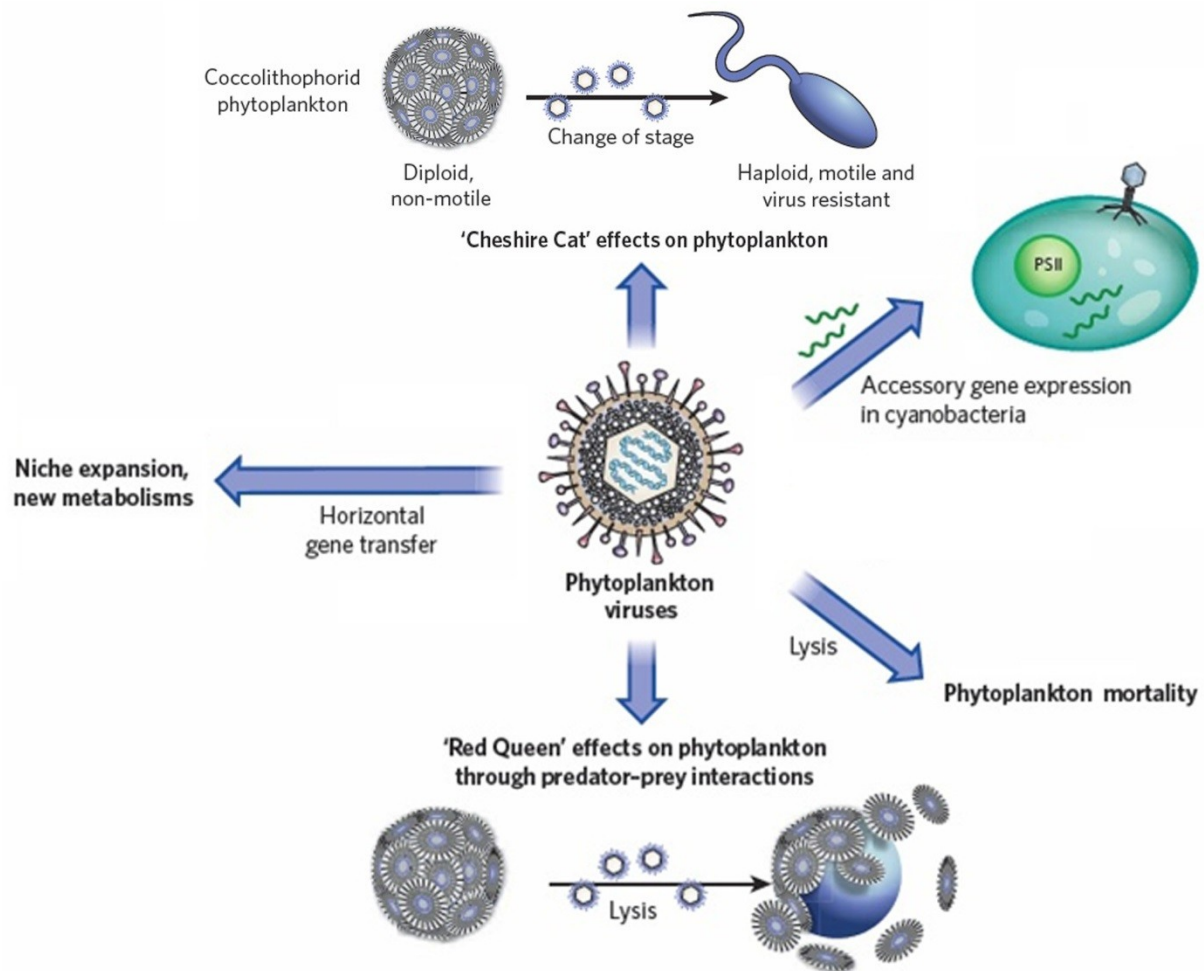


Figure 1.7: Effect of marine viruses on phytoplankton. Marine phytoplankton viruses including eukaryotic viruses and cyanophages can affect their host in various ways, the prevalent being phytoplankton mortality via host cell lysis. Upon infection a virus might also transfer genetic material either deriving from a previous host (horizontal gene transfer) or a part of its own genome (accessory gene expression in cyanobacteria), which can enable niche expansion. Further, two interaction scenarios have been proposed: the “Red Queen” effect, and the “Cheshire Cat” hypothesis. In the former virus and host maintain a relation similar to a predator-prey interaction and are evolving in parallel in a kind of “arms race” developing different resistance mechanisms until finally the virus lyses its host cell (illustrated as a coccolithophore). The “Cheshire Cat” hypothesis proposes a life phase transition for coccolithophores in which the diploid susceptible life phase escapes from viral infection undergoing meiosis and turning to a motile, haploid stage, which is resistant to viral infection. Abbreviation: PSII, photosystem II. Adapted from Rohwer and Thurber (2009).

Further, two evolutionary models exist, describing rather contrary concepts based on or supported by observations in coccolithophores (Figure 1.7). The so called “Red Queen hypothesis” describes an evolutionary “arms race” between host and virus in which each has to “run” (meaning evolve) just to stay in place (Rohwer and Thurber, 2009). In *Emiliania huxleyi* virus (EhV) the existence of viral genes involved in ceramide production seem to support this hypothesis (Bidle et al., 2007).

Ceramide is a sphingolipid that induces programmed cell death (PCD) in plants (Liang et al., 2003). The presence of genes involved in its synthesis in viruses was interpreted as the subversion of an originally host-derived pathway into a viral mechanism. Thereby, the former apoptotic host pathway, which was supposed to prevent viral spreading by organized host cell death, became a regulation mechanism of the virus to initiate host cell death after effective viral assembly inside the host cell (Bidle et al., 2007). In *E. huxleyi* an alternative escape strategy named the “Cheshire Cat” effect was described. As only diploid cells of this alga are susceptible to viral infection an increase in resistant haploid cells in infected cultures has been interpreted as phase shift constituting an escape from viral infection (Frada et al., 2008).

1.3.3 *Emiliana huxleyi* virus (EhV)

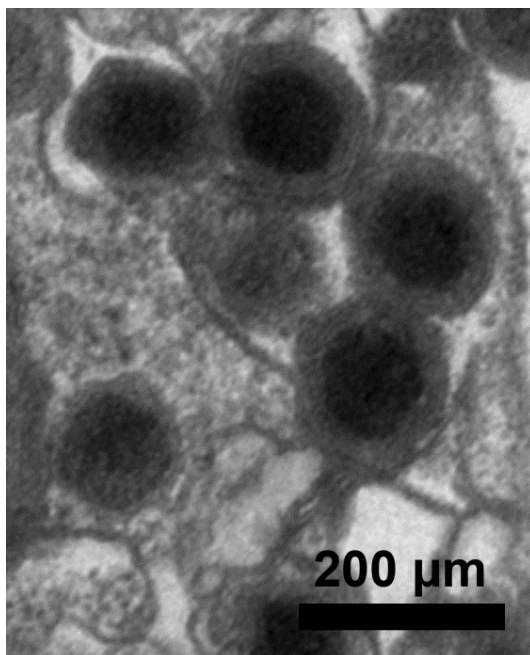


Figure 1.8: Image of *Emiliana huxleyi* virus (EhV) particles. Electron transmission (TEM) micrograph depicting the presence of EhV particles inside an infected *E. huxleyi* cell. (Image courtesy of D. Schatz.)

Emiliana huxleyi virus (EhV) (Figure 1.8) was taxonomically assigned as a *Coccolithovirus* (Schroeder et al., 2002) within the monophyletic *Phycodnaviridae*. The latter constitute a diverse and rapidly expanding family of large, dsDNA viruses infecting algae (Wilson et al., 2009). Their evolutionary root is suggested to lie within the nucleocytoplasmic large DNA viruses (NCLDV) (Wilson et al., 2009). As other members of the *Phycodnaviridae* EhV is icosahedral in shape, possesses a capsid diameter of 160-180 nm, and a burst size of 400-1000 VLPs (Brussaard, 2004a).

The genome size of EhV is approximately 400 kbp and it contains more than 450 predicted coding sequences (Nissimov et al., 2012). Several representatives of

EhV have been recently sequenced among them the type strain EhV86 isolated from the English Channel in 1999 (Wilson et al., 2005), EhV163 deriving from a Norwegian fjord in 2000, and EhV201 isolated from the English Channel in 2001 (Allen et al., 2007). Genome analysis of EhV revealed a cluster of putative sphingolipid biosynthetic genes (Wilson et al., 2005) and such sphingolipids, especially glycosphingolipids, are common constituents of lipid membranes (Fulton et al., 2014). Electron micrographs indicate the existence of an internal lipid membrane (Schroeder et al., 2002) and an external membrane potentially deriving from a release mechanism via budding observed in EhV86 (Mackinder et al., 2009).

Blooms of its host, the coccolithophore *E. huxleyi*, are an attractive field to study host-virus dynamics. EhV is the main reason for bloom demise of this alga (e.g. Bratbak et al., 1993; Jacquet et al., 2002; Schroeder et al., 2002; Wilson et al., 2002). According to Bratbak et al. (1993) viral lysis contributed 25-100% of net mortality of *E. huxleyi* during mesocosm experiments conducted at the Norwegian coast.

Metabolic mechanisms preceding cell lysis of *E. huxleyi* by EhV are not fully understood, although several recent studies collected data on specific metabolic classes or gene expression during viral infection. Using high-performance liquid chromatography with electron spray ionization mass spectrometry (HPLC/ESI-MS) Vardi et al. (2009) identified virus specific glycosphingolipids in infected *E. huxleyi* cells whereas in healthy cells only host specific lipids were present. Adding purified glycosphingolipids the authors could even induce biochemical hallmarks of PCD in uninfected cells (Vardi et al., 2009). EhV infection further led to distinct differences in amount and composition of fatty acids between healthy and infected *E. huxleyi* cells as in latter fatty acid composition shifted from polyunsaturated to monounsaturated and saturated fatty acids (Evans et al., 2009). Further, EhV infection affects photosynthesis both at transcriptional (Kegel et al., 2010) and pigment synthesis level, where it led to a decrease in carotenes but an increase in diatoxanthin relative to chlorophyll *a* (Llewellyn et al., 2007). Both a laboratory-based approach using expressed sequence tags (EST) and a mesocosm study indicated the importance of lipid metabolism during viral infection (Kegel et al., 2010; Pagarete et al., 2011).

However, how EhV manipulates host metabolism and specifically lipid synthesis was hitherto hardly understood. At the beginning of this study it was so far unknown which mechanisms lead to viral reproduction and finally result in host cell

lysis and at which point the host cell might still be able to prevent this process. A better understanding of viral induced metabolic changes in this algal host-virus model is the topic of part of this thesis and will help to shade light on the more general metabolic mechanisms of viral infection.

1.4 Metabolomics

1.4.1 *Introduction to metabolomics*

The “metabolome” per definition constitutes the full set of metabolites present either within a single cell, tissue, or organism in a particular physiological or developmental state. This term was first mentioned in connection with metabolic control analysis (Oliver et al., 1998). In this approach relative concentration changes at metabolic level were interpreted as the outcome of gene deletion or over-expression. Therefore, their measurement was suggested as a suitable tool to elucidate functions of novel genes discovered by genomic approaches in yeast (Oliver et al., 1998). This is considered as the beginning of the more modern “metabolomics” technology, an approach that by targeting an organism’s metabolome links its genotype to the phenotype (Fiehn, 2002).

Modern “omics” technologies, a term combining genomics, transcriptomics, proteomics, and metabolomics, support the exploration of functional processes and allow to gain new insights into complex metabolic processes (Fiehn et al., 2000; Jamers et al., 2009) as are for example involved in microbial interactions in the marine environment. Since substrates and products transformed during cellular metabolism can be monitored, metabolomics provides the possibility to directly measure biochemical activity (Patti et al., 2012). Due to the high complexity of the metabolome its analysis by a single analytical approach is technically impossible (Lisec et al., 2006; Jamers et al., 2009). Therefore, several approaches either being targeted or non-targeted are commonly applied. Among the targeted approaches metabolite target analysis is mostly used for screening purposes as it is restricted to only a few compounds related to a specific metabolic reaction (Jamers et al., 2009). The approach of metabolic profiling monitors a specified (“targeted”) number of metabolites at the level of pathways of specific interest (Schauer and Fernie, 2006). In contrast, the non-targeted approach of metabolic fingerprinting is applied for the

classification of samples according to their origin or biological context (Jamers et al., 2009). Therefore, it is of a more global scope as it intends to simultaneously target as many metabolites as possible (Patti et al., 2012).

Analytical methods commonly applied for metabolic analyses include either nuclear magnetic resonance (NMR) or mass spectrometry (MS) technologies (Patti et al., 2012). Among the latter especially a coupling with gas chromatography (GC) based methods constitute a comprehensive tool for metabolite target analysis as well as metabolite profiling, because they are more sensitive than NMR and more robust than liquid chromatography (LC) based separation technologies (Lisec et al., 2006). Further, modern instruments allow the analysis of large sets of samples that contain a broad spectrum of compounds. Additionally, improved algorithmic tools for data analysis that include identification by comparison to spectral libraries enable the elucidation of biologically relevant information (Fiehn, 2008). Therefore, GC-MS-based metabolite profiling offers a relatively high throughput methodology of good balance between sensitivity and reliability covering the central pathways of primary metabolism (Lisec et al., 2006; Fiehn, 2008).

Despite recent major developments several challenges for the application of metabolomics remain. Metabolite extraction is critical for a qualitative analysis and in marine samples for example salts or pigments are reported interfering factors (Goulitquer et al., 2012). Pigments, which constitute an important part of algae such as coccolithophores (Llewellyn et al., 2007), were observed to influence the complete derivatization of amino acids, consequently reducing detection levels of this compound class (Colombini et al., 1999). Hence, discrimination during extraction is important. Further, rapid quenching of metabolic processes prior to extraction is regarded as critical (Lisec et al., 2006). This aspect is problematic in aqueous samples as typically quenching is achieved by addition of -70°C cold 70% methanol (Lee and Fiehn, 2008). This might be possible in microalgae samples with high cell abundance, but for algae with lower growth rates and abundances as *E. huxleyi* (Paasche, 2002) quenching is more complicated. Thus, for data comparability between laboratory and mesocosm samples and for avoidance of large amounts of methanol waste, samples in this study were not quenched, but sampled and extracted within a limited and defined time frame.

Data analysis constitutes another challenge, because the annotation of unknown peaks and data interpretation concerning their biological importance is still difficult (Fiehn, 2008). Although several bioinformatics tools support steps of data annotation (Goulitquer et al., 2012), identification is commonly limited to about half of the detected metabolites (Fiehn et al., 2000). Closing such gaps in annotation requires the extension and easy accessibility of existing spectral databases (Fiehn, 2008). The complexity of metabolic data prevents manual interpretation by eye, but necessitates multivariate data analysis (Jansen et al., 2009). This can be used for visualization of the large number of compounds obtained by metabolomics analysis and can be combined with statistical analysis to determine the relationship between levels of different metabolites (Jansen et al., 2009). The latter presents a key aspect for metabolic data interpretation, because it enables comparability of metabolite contents even between several samples and determines metabolites that are significant for the discrimination between different conditions (Goulitquer et al., 2012). Further, a comparative approach offers the possibility to focus specifically on metabolites that experience the strongest concentration changes under the analyzed conditions, because from the variety of all detected metabolites it determines those showing a correlation to a treatment of interest. Thereby, it reveals highly relevant metabolites, which otherwise might have been overlooked in the mass of unchanged or only slightly affected compounds. Such a comparative analysis was for example successfully performed by Vidoudez and Pohnert (2012) and was also applied to most of the metabolic data sets presented in this study.

1.4.2 *Metabolomics of microalgae*

In recent years, metabolomics has developed as a powerful tool to explore the physiology and chemical ecology of algae. At the beginning marine metabolic studies emphasized on the identification and quantification of secondary metabolites of specific economic value. Most of these studies were limited to laboratory-based approaches (Jamers et al., 2009 and references within). Although they might not reflect all natural conditions, laboratory experiments constitute a useful tool to assess an organism's complex metabolic potential and response under controlled conditions, before it is possible to understand the complexity of interactions in the natural environment (Vidoudez and Pohnert, 2012).

Thus, over the last few years the number of studies targeting the metabolism of marine algae is constantly increasing. That algal strains can be differentiated based on their metabolic fingerprint was proven by a study on the cryptic diatom *Chaetoceros socialis* which exhibited approximately 400 compounds in a LC-MS based approach (Huseby et al., 2012). Although fingerprinting analysis as used for this study constitutes a reliable tool to access qualitative and quantitative differences in metabolic markers, it does not allow identification. So the metabolites responsible for this separation remained unclear (Huseby et al., 2012). The same applies for a recent metabolic fingerprinting approach that revealed growth phase dependent differences in waterborne exudates deriving from the diatoms *Skeletonema marinoi* and *Thalassiosira pseudonana* (Barofsky et al., 2009). Such growth phase dependent patterns were also reflected intracellular in *S. marinoi*, because growth phases could be distinguished based on metabolic profiles of whole cells (Vidoudez and Pohnert, 2012). Carbohydrates for example exhibited complex patterns as different representatives of these metabolites were correlated with different growth phases and amino acids were found to be significant for separating the exponential from stationary and declining phase (Vidoudez and Pohnert, 2012). Further, Lee and Fiehn (2008) showed the influence of harvesting time and the number of cell cycles undergone by the freshwater chlorophyte *Chlamydomonas reinhardtii*. Their results emphasized the importance of considering differences in growth phases of microalgae for sampling as they can influence the outcome of metabolic profiling.

These examples represent some recent metabolic studies mainly focusing on diatoms. Other phytoplankton groups are by far less studied. For coccolithophores one recently published metabolite profiling protocol targeting the limited number of 26 metabolites in *E. huxleyi* is available (Obata et al., 2013), whereas other approaches focused on a specific biosynthesis pathway such as lipid biosynthesis (e.g. Chuecas and Riley, 1969; Maxwell et al., 1980; Viso and Marty, 1993; Fernández et al., 1994). A more complete metabolic analysis of a coccolithophore or the observation of metabolic changes during complex interactions such as viral infection was hitherto missing and is the subject of this thesis.

1.5 Thesis objectives

This thesis focuses on the coccolithophore *Emiliana huxleyi* (Lohmann) Hay & Mohler, 1967. With the recent developments in the field of metabolomics and a comprehensive method for comparative metabolic profiling available in our laboratory (Vidoudez and Pohnert, 2012), time was ripe to investigate this ecologically important alga under the following aspects.

As the multitude of life and growth phase stages can be assumed to be reflected in the metabolome of *E. huxleyi*, **Chapter 2** presents a comparative metabolic profiling of these stages in laboratory cultures of the alga.

After elucidation of *E. huxleyi*-specific metabolic patterns in the laboratory I intended to confirm the results under more natural conditions in the framework of a mesocosm experiment. In parallel, the metabolic performance of the alga under future ocean conditions, which are expected to constitute a major challenge to this calcifying organism, were monitored. The focus here lay on the detection of changes correlated with the influence of ocean acidification due to an increased amount of dissolved gaseous carbon dioxide in the sea water or on aspects interrelated with a changing iron bioavailability. The findings of this study are described in **Chapter 3**.

Although the crucial role of marine viruses in the demise of *E. huxleyi* blooms has been long recognized, metabolic processes ultimately resulting in host cell lysis are, with the exception of the involvement of viral sphingolipids, hitherto mostly unexplored. To gain a better understanding of how the virus rewires host metabolism, I participated in a combined metabolomic and transcriptomic analysis targeting viral infection by a lytic and a non-lytic virus. Metabolic rewiring of several biosynthesis pathways as detected in this study is presented in **Chapter 4** emphasizing on the metabolome. Results are discussed in context with the transcriptome data.

2 Metabolic differences between diploid and haploid *Emiliania huxleyi* cells and of cells in different growth phases revealed by comparative metabolomics¹

2.1 Experimental design

This study addresses the metabolic differences in diploid and haploid *Emiliania huxleyi* (strains RCC1216 and RCC1217, see 6.5.1) to gain an insight into the variability of these life stages on the metabolome level. In addition, I explore the general variability by including a comprehensive metabolic profiling during different growth phases of the poorly explored haploid cells. A recent study on diatoms showed that growth phases have a significant influence on metabolism and gave insights into physiological adaptations to variable environmental conditions (Vidoudez and Pohnert, 2012). Such considerations are crucial, if ecological and physiological conclusions are concerned. Several analyses targeting specific metabolic pathways in *E. huxleyi* especially aiming at lipid biosynthesis have been undertaken (e.g. Chuecas and Riley, 1969; Maxwell et al., 1980; Viso and Marty, 1993; Fernández et al., 1994), but mostly exponentially growing diploid cells were used. Exceptions are two studies distinguishing lipid composition in exponential and stationary phase (Bell and Pond, 1996; Pond and Harris, 1996). A recent metabolic profiling approach on diploid *E. huxleyi* cells targeted a limited number of substances in particular amino acids and sugars (Obata et al., 2013), but took neither life nor growth phase variations into account. Therefore, to achieve the challenging task of observing these ecologically important aspects, I adapted an existing metabolomic approach developed for diatoms based on gas chromatography coupled to mass spectrometry (GC-MS) (Vidoudez and Pohnert, 2012).

As I aimed to address two main features of the alga *E. huxleyi*, namely life and growth phases, I conducted two separate experiments. For the life phase experiment diploid and haploid cells were grown in 1.5 L cultures and sampled twice to obtain a

¹ Parts of this chapter are based on the manuscript: Mausz M.A., and G. Pohnert. Phenotypic diversity of diploid and haploid *Emiliania huxleyi* cells and of cells in different growth phases revealed by comparative metabolomics. This manuscript was accepted for publication by the Journal of Plant Physiology.

profile of intracellular metabolites during the early and late exponential phase. I used seven diploid and ten haploid biological replicates, as for each sampling the total culture was taken and three replicates of diploid cells did not grow (Figure 2.1A).

In the accompanying experiment targeting growth phases, haploid *E. huxleyi* metabolome samples were taken twice in each of the growth phases (exponential, stationary, and declining phase) (Figure 2.1B) from 20 L cultures. Data were statistically tested for differences in the metabolic profiles of the individual samplings and treated accordingly to be able to analyze growth specific patterns. In addition to metabolic analysis, metadata were sampled on a daily basis to monitor the general performance of the alga. These included *E. huxleyi* cell abundance, chlorophyll *a* (Chl *a*), and photosystem II (PSII) efficiency. As the growth phase experiment was conducted for a longer time period and bacteria were not excluded to avoid artificial stress related to their exclusion (Vidoudez and Pohnert, 2012), their abundance during the course of the experiment was also determined.

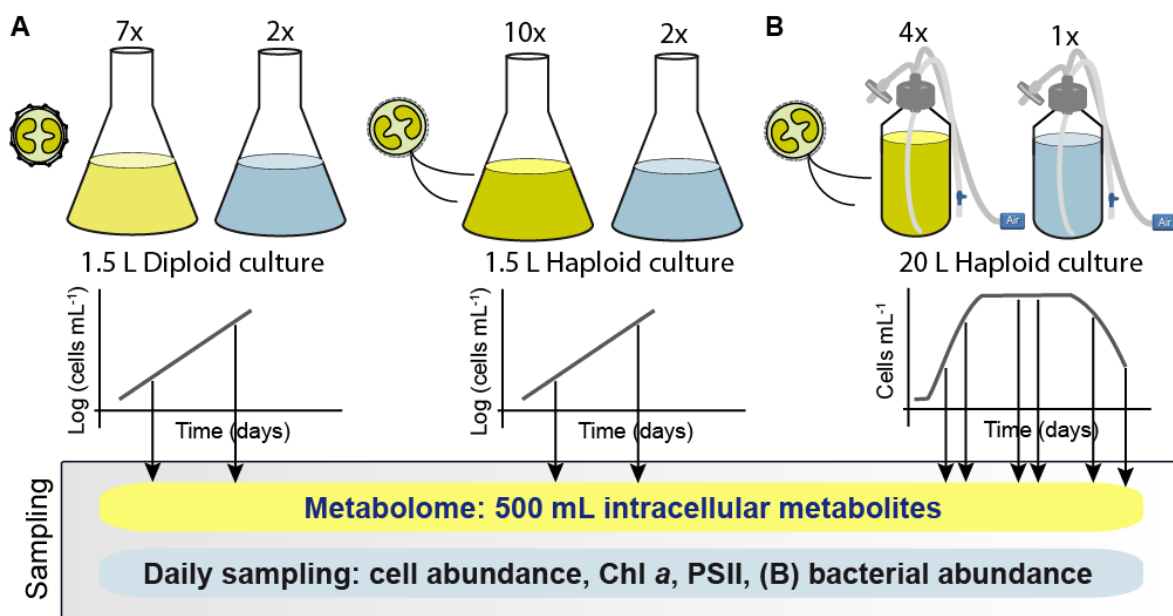


Figure 2.1: Scheme of the experimental design. General scheme presenting the set-up of the (A) life phase and (B) growth phase experiment. A blue filling represents a medium control. Arrows indicate sampling for intracellular metabolites. Daily sampling included *E. huxleyi* cell abundance, chlorophyll *a* (Chl *a*), photosystem II (PSII) efficiency, and additionally bacterial abundance only in the growth phase experiment.

2.2 **Results**

2.2.1 ***Culture development***

The pre-cultures were performing differently in terms of cell growth resulting in different cell abundances and consequently, I inoculated diploid cultures at lower cell numbers than haploid cultures. Further, an absolute minimum cell number ($3 \cdot 10^5$ cells mL⁻¹ and $8 \cdot 10^5$ cells mL⁻¹, see 6.5.3) was used as criterion for metabolite sampling. During the experiment average growth rates for both life phases of *E. huxleyi* (diploid, 2N: 0.87, and haploid, 1N: 0.83) were not significantly different ($P = 0.905$, Mann-Whitney rank sum test, see 6.5.5). In both life phases cell abundance increased significantly during the course of the experiment (2N: $P = 0.003$, 1N: $P < 0.001$, paired t-test, see 6.5.5) (Figure 2.2A). Chl *a* fluorescence reflected this pattern (Figure 2.2B). PSII efficiency was relatively stable during the experiment with a slightly higher average value in haploid cells (2N: 0.5, 1N: 0.6) (Figure 2.2C).

For the growth phase experiment cell counts showed that the samplings were performed in different growth stages (Figure 2.2D). During the exponential phase cell abundance increased significantly ($P = 0.014$, paired t-test, see 6.5.5) at an average growth rate of 0.61. In contrast, I observed no significant differences in cell numbers for the samplings in the stationary phase ($P = 0.382$, paired t-test, see 6.5.5), whereas in the declining phase cell abundances decreased significantly ($P = 0.009$, paired t-test, see 6.5.5). Chl *a* fluorescence showed a similar trend, but maximum levels were reached later than maximum cell abundances (Figure 2.2E). PSII efficiency was higher during exponential phase (average 0.52) and decreased slightly during the transition from exponential to stationary phase (Figure 2.2F). This parameter was relatively stable during stationary (0.47) and declining phase (0.44). Thus, PSII efficiency decreased in average by 0.08 from the exponential to the declining phase. Exceptions to this pattern were the inoculation day (day 0), and day 15, where all cultures showed a reduction in PSII efficiency (both 0.36). In general, the four replicate cultures thus exhibited the same overall behavior and grew synchronized.

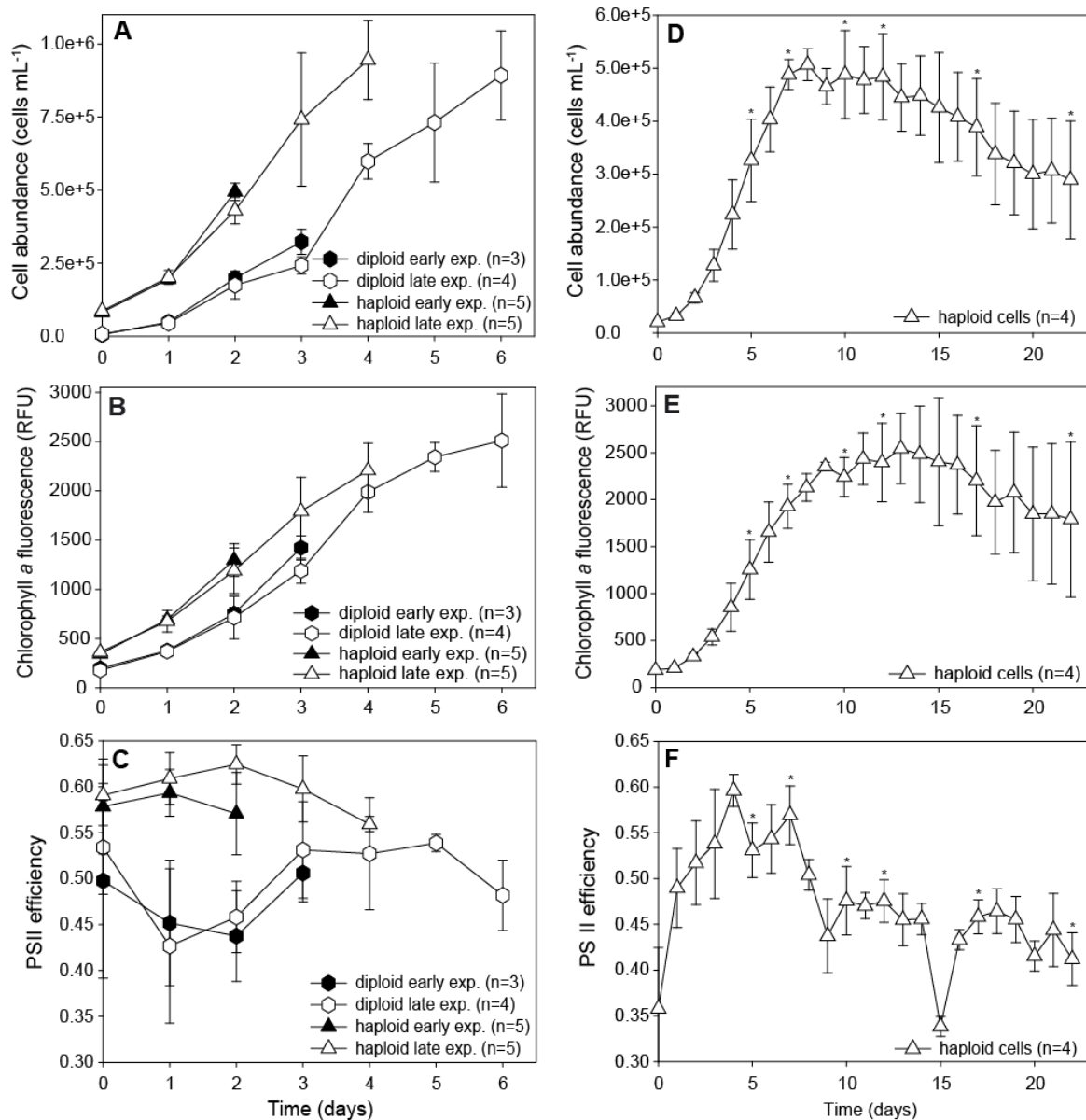


Figure 2.2: Growth parameters of *Emiliana huxleyi* cultures. (A) Cell counts, (B) chlorophyll *a* fluorescence, and (C) photosystem II (PSII) efficiency of diploid and haploid cultures that were sampled for metabolomics analyses at different time points during exponential growth. Early exponential (exp.) refers to biological replicates sampled completely on day 2 (haploid, 1N) or day 3 (diploid, 2N), and late exp. indicates replicates completely taken on day 4 (1N) or day 6 (2N). Independent of early or late sampling all biological replicates derived from the same pre-culture. For comparison (D) cell counts, (E) chlorophyll *a* fluorescence, and (F) PSII efficiency of haploid cells sampled in different growth phases for metabolomics analyses are given. “*” indicates the sampling points. The number of replicates (*n*) is indicated in the figure legends. Abbreviation: RFU, relative fluorescence units.

I did not specifically determine the cell volume of diploid and haploid cultures in the life phase or the growth phase experiment. Nevertheless, based on flow cytometry images calcified diploid cells possessing several layers of coccoliths surrounding the cell surface were larger in cell size than haploid cells. Non-calcified

diploid cells, which increased in abundance at the second sampling, were comparable in cell size to haploid cells (Figure 2.3). In the growth phase experiment flow cytometry images indicated that cell size was stable during the course of growth (Figure 2.4). Using flow cytometry counts I further observed bacterial co-growth, which peaked early after inoculation but later stayed relatively constant. At the first sampling point in exponential phase (day 5) bacterial abundance was $1.47 \pm 0.27 \cdot 10^7$ cells mL⁻¹ which slightly increased to $1.95 \pm 0.31 \cdot 10^7$ cells mL⁻¹ in stationary phase (day 10), and to $2.32 \pm 0.24 \cdot 10^7$ cells mL⁻¹ in mid declining phase (day 17).

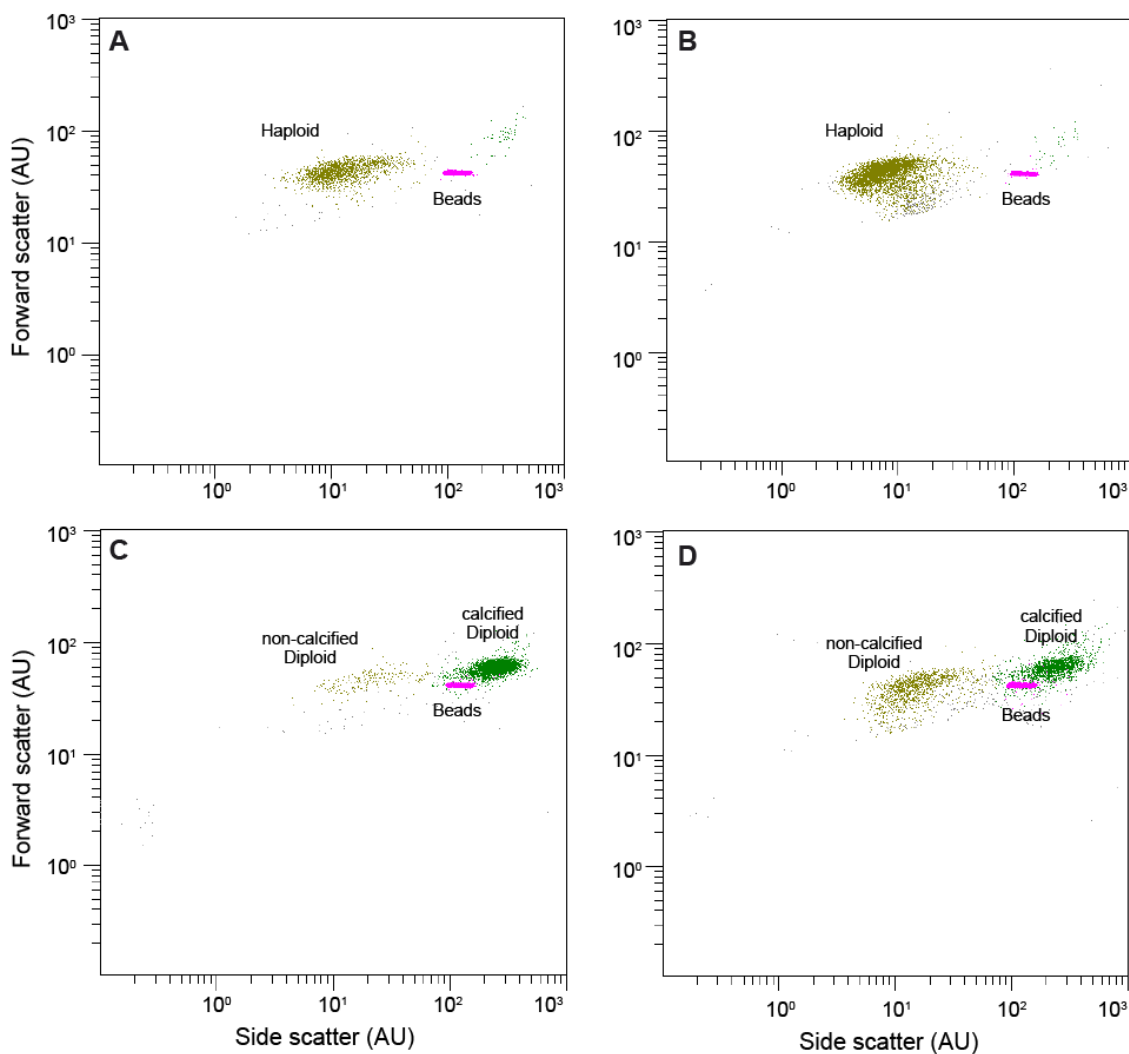


Figure 2.3: Flow cytometry measurement images of *Emiliana huxleyi* cells in the life phase experiment. Images show the positioning of cells on days when metabolite samples were taken. Population of haploid cells (A) at day 2, and (B) at day 4. Populations of calcified and non-calcified diploid cells (C) at day 3, and (D) at day 6. A light green population indicates haploid cells or non-calcified diploid cells and a dark green population calcified diploid cells. Magenta dots represent beads (\varnothing 3.6 μ m) used for data calibration. Abbreviation: AU, arbitrary unit.

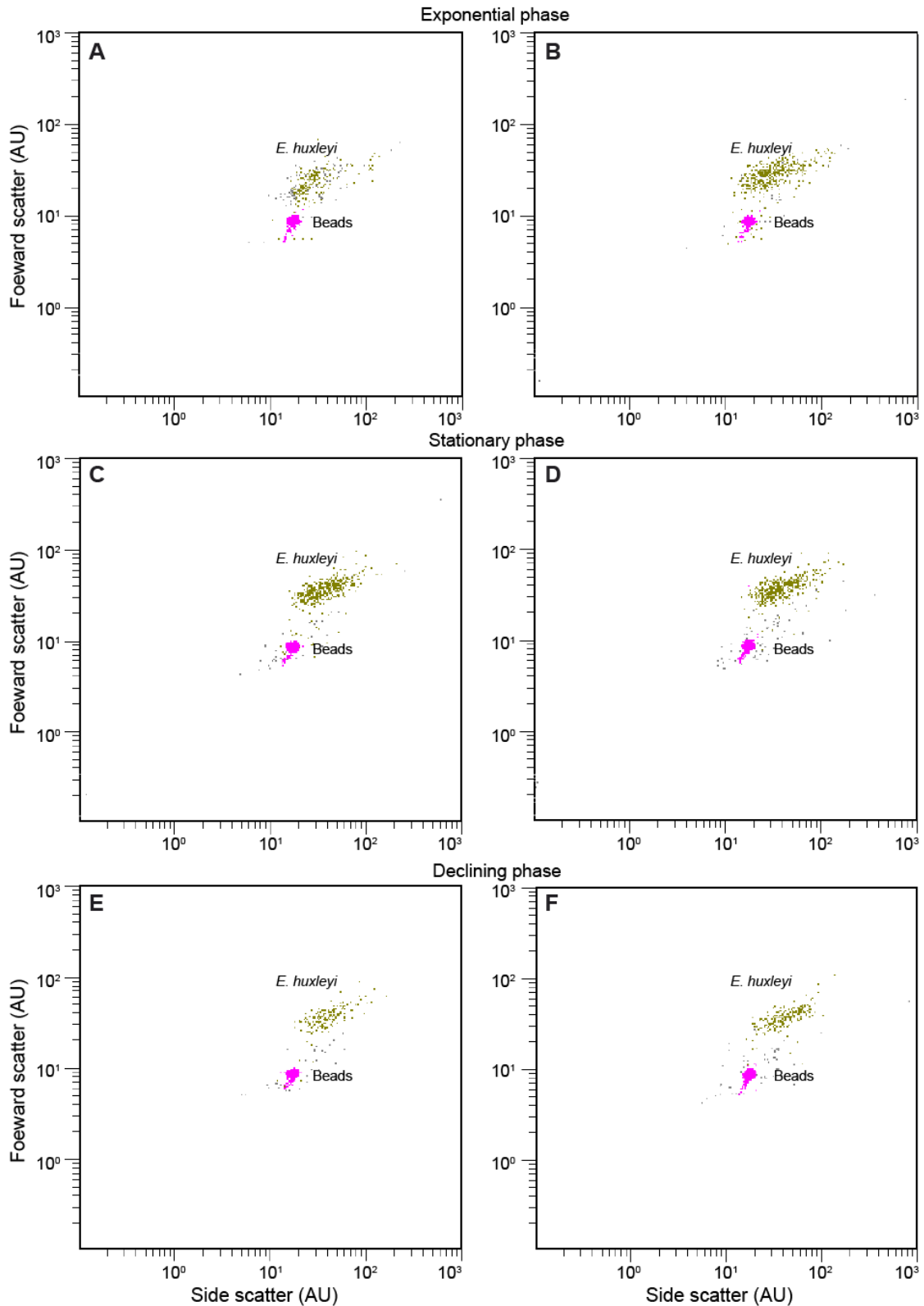


Figure 2.4: Flow cytometry measurement images of *Emiliana huxleyi* cells in the growth phase experiment. Images show the positioning of cells on days when metabolite samples were taken. Population of haploid cells in the exponential phase (A) at day 5, and (B) at day 7, in the stationary phase (C) at day 10, and (D) at day 12, and in the declining phase (E) at day 17, and (F) at day 22. A light green population indicates haploid cells and magenta dots represent beads (Ø 1.0 µm) used for data calibration. Abbreviation: AU, arbitrary unit.

2.2.2 General correlation patterns based on metabolic profiles

After all chromatograms were analyzed for assignable metabolite signals (see 6.4.4 to 6.4.6), I found comparable numbers for detectable intracellular metabolites in the life phase and growth phase experiments. In the former, the actual number of peaks (corresponding to detected metabolites) was slightly higher in the haploid (423 ± 47 , $n = 10$) than the diploid phase (404 ± 42 , $n = 7$). In the growth phase experiment the number of peaks slightly increased with time (381 ± 32 , 414 ± 12 , 418 ± 17 , $n = 8$ in exponential, stationary and declining phase, respectively). After peaks deriving from standards or putative contaminations were excluded (see 6.4.4), the number of signals retained for the constrained statistical analysis was 317 signals for life phases and 322 for growth phases (see 6.4.5).

Since diploid and haploid life phase were generated from two independent cultures, I could not assume that the total intensity of metabolites per cell is constant among the samples. Thus, it was not possible to apply normalization by peak sum, which, in contrast, was used for data obtained in the growth phase experiment. Hence, cell numbers were used to normalize metabolic data in the life phase experiment prior to a canonical analysis of principal coordinates (CAP). This analysis clearly separated diploid from haploid cells (eigenvalue 0.9827) and proved that the single obtained axis was related to differences between the life phases (correlation Δ^2 0.9657) (Figure 2.5A). This finding was further supported by cross validation with a misclassification error of 0% and a differentiation of the groups in the multivariate space was supported by permutation test ($P = 0.0001$).

For haploid cells I assumed the above mentioned constant metabolic intensity to be fulfilled, because they derived from the same biological replicate. Thus, to the contrary to the previous analysis I used sum normalized areas of each metabolite, which represent a relative concentration of the compound of interest for statistical analysis in the growth phase experiment. The two consecutive samplings of each growth phase were found to be significantly different (discriminant analysis using the CAP program) (Table 2.1). Thus, each sampling was used as group and the underlying metabolic differences between the six samplings in the growth phases resulted in four separating axes (Figure 2.5B). These were supported by the CAP diagnostic values (eigenvalues 0.97586, 0.95697, 0.84539, and 0.77443). Further, a high correlation of the axes related to differences between the different samplings

within the growth phases was confirmed for at least the first two axes (correlation Δ^2 0.95231, 0.91579, 0.71468, and 0.59974). Here, the misclassification error was 8.33%, representing two out of 24 samples being misclassified, and the permutation test was significant ($P = 0.0001$). These data indicate a significant separation of all six samplings based on metabolic profiles and the obtained axes well represent those differences.

Table 2.1: Statistical diagnostic values of differences between growth phases. List of statistical support values testing the two samplings in each growth phase for differences by canonical analysis of principal coordinates (CAP). Data present eigenvalues (λ) and squared correlation (Δ^2) for the 1st CAP axis, misclassification error, and the P value of the permutation test. A high eigenvalue (> 0.9), a low misclassification error, and a significant permutation test ($P < 0.05$) indicate a significant separation by the corresponding axis.

Sampling	Constrained canonical axis		Statistics	
	1 st axis		Cross validation	Permutation test
	λ	Δ^2	Misclassification error	Trace statistic
Exp. 1 vs. Exp. 2	0.9031	0.81559	0%	0.0279
Stat. 1 vs. Stat. 2	0.97028	0.94144	0%	0.0279
Decl. 1 vs. Decl. 2	0.88134	0.77676	12.50%	0.0152

Abbreviations: Decl., declining, Exp., exponential, Stat., stationary, vs., versus. Numbers 1 and 2 refer to the first and second sampling in the particular growth phases.

Graphically, the second sampling in the stationary phase and the two samplings in the declining phase were not well resolved (Figure 2.5B). Thus, the differences between growth phases were not well defined, when all six samplings were used. To get a better impression of differences between the growth phases in haploid cultures related to metabolic patterns, I separated between the first and second sampling. Therefore, I used either the first or second sample in each growth phase as group and analyzed them for differences by CAP. In the first sampling, differences in metabolic profiles between the growth phases lead to their significant separation (Figure 2.5C) by the corresponding axes (eigenvalues 0.98542, and 0.95321). Furthermore, the correlation of the axes to differences between growth phases was supported (correlation Δ^2 0.97105, and 0.9086). The first obtained axis thus seems to separate the exponential from the other two phases, whereas the second axis differentiates between the stationary and the declining phase. All samples were assigned correctly by the cross validation test (misclassification error 0%) and the permutation test also indicated a significant difference between growth

phases ($P = 0.0002$). In the second sampling, metabolic differences between growth phases resulted in a well defined separation by the axes, although the second canonical axis contributed less (Figure 2.5D) (eigenvalues 0.95535, and 0.82094, correlation Δ^2 0.9127, and 0.87394). None of the samples was misclassified (misclassification error 0%) and significant differences between metabolite patterns were supported by the permutation test ($P = 0.0005$).

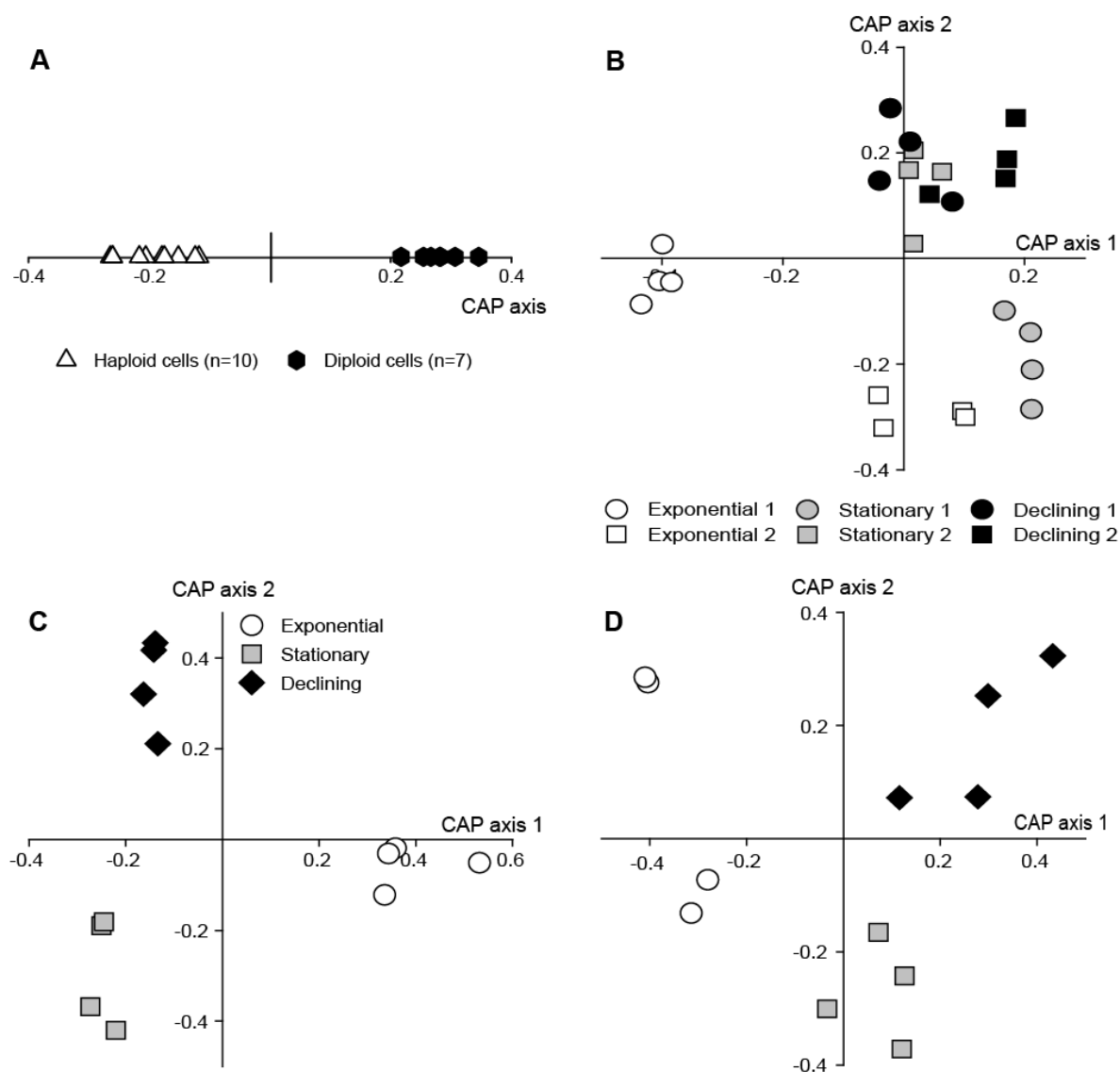


Figure 2.5: Multivariate separation of intracellular *Emiliana huxleyi* metabolites by canonical analysis of principal coordinates (CAP). (A) Separation of samples generated in the exponential phase of diploid ($n=7$) and haploid ($n=10$) cells. (B) Separation of haploid cells in exponential, stationary and declining growth phase from two consecutive samplings in each growth phase ($n=4$). Separation of haploid cells in exponential, stationary and declining phase from (C) the first sampling, and (D) the second sampling ($n=4$).

Based on the observed separation patterns of the two consecutive samplings (Figure 2.5C, D), I chose the first sampling to analyze the correlations of metabolic patterns to growth phases. This decision was emphasized by the better CAP support values obtained for this sampling as well as the better graphical separation.

2.2.3 Life phases of *Emiliana huxleyi*

Generally, 39 metabolites showed either a significant correlation to the diploid or haploid life phase (Figure 2.6, and Appendix Table 1). Among these approximately one third could be identified (Table 2.2) and another third assigned to a metabolic class, whereas 12 separating peaks remained unknown (Figure 2.6A). Saccharides (9 compounds e.g. xylose, or fructose, plus two complex saccharides among them maltose) and related substances (the sugar acid threonic acid, mannitol, and another unidentified sugar alcohol) constituted the most abundant group among the significantly correlated metabolites (Figure 2.6B). Only few substances of other compound classes were significantly correlated with either of the life phases (e.g. 3 carboxylic acids, one amino acid, and 3 sterols) (Figure 2.6C, D).

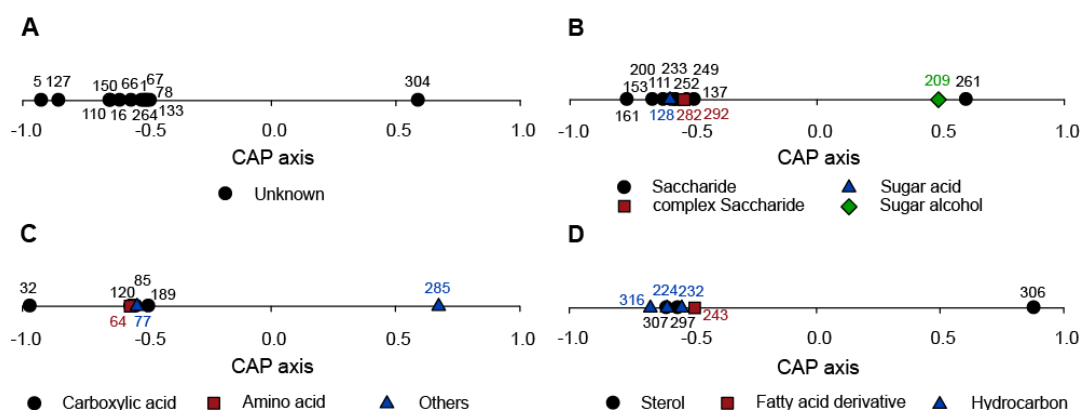


Figure 2.6: Vector plots of metabolites significantly correlated with life phases. Vector plots of metabolites significant for the separation between diploid and haploid life phase according to canonical analysis of principal coordinates (CAP) arranged in categories. For clarity only the tip of the vector is presented. (A) Unidentified metabolites assigned as unknown, (B) saccharides and other carbohydrates, (C) amino acids, carboxylic acids and metabolites that could not be assigned into one of the general groups (others), and (D) lipids and hydrocarbons. Metabolites with positive x-axis values correlate with diploid, those with negative values with haploid cells (compare Figure 2.3A). Numbers correspond to metabolites in Table 2.2 and Appendix Table 1.

The relation of a metabolite with a specific phase was determined by visualizing the correlation coefficients of this metabolite on the CAP axes in form of vectors (see 6.4.5). These vectors then point in the direction of a specific growth phase (compare Figures 2.6, and 2.7).

Interestingly, only five of the significantly correlated metabolites showed a higher concentration in the diploid life phase: the sugar alcohol mannitol (metabolite 209), the putative metabolite adenosine (met. 285), the sterol epibrassicasterol (met. 306), an unidentified saccharide (met. 261) and an unknown compound (met. 304) (Figure 2.6, and Appendix Table 1). All other substances including all the remaining saccharides were found in higher concentrations in the haploid life phase as well as the amino acid isoleucine (met. 64), and carboxylic acids such as 3-hydroxypropanoic acid or citric acid (met. 32, and 189) (Figure 2.6C). Further, we observed higher concentrations of lumichrome (met. 77) in 1N cells.

Table 2.2: Heat map of metabolites correlated with life phases. Heat map of relative intensities of identified intracellular metabolites significantly correlated with the CAP axis separating diploid and haploid life phase of exponentially growing *E. huxleyi* cultures.

No.	Model- ion	RT	Metabolite	Class	Diploid life phase	Haploid life phase
32	177.1	6.25	3-Hydroxypropanoic acid	Carboxylic acid		
64	158.1	7.68	Isoleucine*	Amino acid		
77	184	8.08	Lumichrome	Other		
128	292.1	9.96	Threonic acid	Sugar acid		
153	103.1	10.72	Xylose*	Saccharide		
189	273.1	11.96	Citric acid*	Carboxylic acid		
200	307.2	12.30	Fructose*	Saccharide		
209	205.1	12.72	Mannitol [†] *	Sugar alcohol		
243	179.1	13.99	Octadecenoic acid deriv.	Fatty acid deriv.		
285	236.1	16.89	Adenosine [†] ??	Other		
292	204.1	17.40	Maltose*	compl. Saccharide		
297	253.2	18.21	Cycloergostatriene ?	Sterol		
306	129.1	20.21	Epibrassicasterol [†]	Sterol		
307	363.3	20.56	Ergosterol*	Sterol		

Gray coloring reflects the intensities of the metabolites with light gray for low and dark gray for high intensities. Metabolites tagged with “[†]” are highly correlated with the diploid life phase. If marked by “*”, identification was confirmed by a standard. Metabolites tagged with a “?” had a reverse match of 700 - 800 or, if marked by “??”, of 600 - 700. Abbreviation: compl., complex, deriv., derivative, No., number, RT, retention time.

Especially among sterols the difference between the life phases was evident. Ergosterol (met. 307) was approximately 13-fold increased and a putative cycloergostatriene (met. 297) was only detected in haploid cells (Table 2.3). In contrast, as mentioned above only for epibrassicasterol this pattern was opposite (Figure 2.6D). Free fatty acids did not play a role in separating diploid and haploid life phase. Indeed, besides an octadecenoic acid related metabolite showing higher concentrations in the 1N cells, no fatty acid or derivative was correlated with either life phase.

Table 2.3: Relative sterol content. Data of all detected sterols from all samplings are presented as percentage relative to the dominant sterol epibrassicasterol at its highest concentration (life phase experiment: in diploid cells, growth phase experiment: during the declining phase). “-” indicates that a sterol was not detected in the corresponding data set.

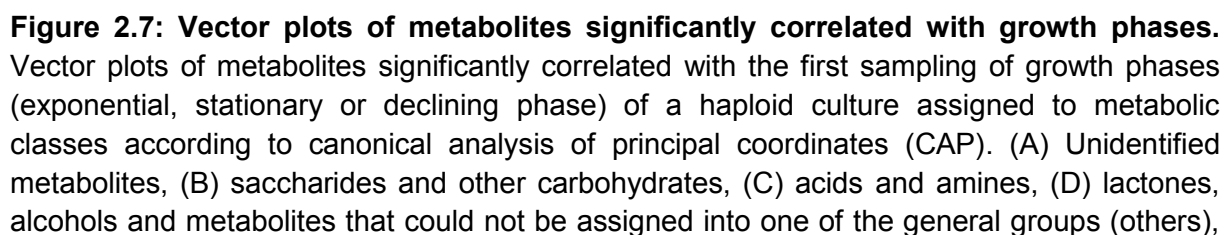
No.	RT	Metabolite	Life phases		Growth phases		
			Diploid (%)	Haploid (%)	Exp. (%)	Stat. (%)	Decl. (%)
294	17.98	Sterol ?	-	-	1.25 ± 0.81	4.33 ± 1.18	9.94 ± 3.36
296	18.21	Cycloergostatriene ?	-	0.67 ± 0.63	4.72 ± 2.26	22.13 ± 13.50	59.53 ± 27.83
301	18.69	Ergostatriene	1.79 ± 1.70	1.63 ± 1.61	6.61 ± 2.91	19.21 ± 4.20	54.91 ± 23.70
302	18.81	Sterol ??	2.13 ± 1.93	2.12 ± 1.82	6.16 ± 2.35	11.97 ± 2.26	23.62 ± 6.75
304	19.06	Sterol ?	-	-	0.11 ± 0.05	2.20 ± 1.67	8.95 ± 4.29
310	20.22	Epibrassicasterol	100.00 ± 30.20	8.02 ± 2.24	59.83 ± 28.64	87.20 ± 14.80	100.00 ± 24.67
312	20.56	Ergosterol*	0.37 ± 0.56	5.06 ± 3.71	14.12 ± 7.36	31.78 ± 17.72	43.90 ± 16.38

If marked by “*”, identification was confirmed by a standard. Metabolites tagged with a “?” had a reverse match of 700 - 800 or, if marked by “??”, of 600 - 700. Abbreviations: Decl., declining, Exp., exponential, No., number, RT, retention time, Stat., stationary.

2.2.4 Interphase comparison of haploid cells

To investigate the correlation of specific metabolites to growth phases I used the first sampling in each growth phase as described above. The resulting data sets representing the three growth phases showed more pronounced differences than the samples from the life phase experiment. A higher number of metabolites accounted for the separation (158 signals as opposed to 39 from the previous experiment) (Figure 2.7, and Appendix Table 2). In total 38.0% of these metabolites could be identified (60 peaks) (Table 2.4) and another 21.5% assigned to a metabolite class (34 signals). Of the significantly correlated compounds 40.5% could not be identified (64 peaks) (Figure 2.7A). The most abundant substance class consisted of saccharides (31 compounds plus 4 complex saccharides) and related substances (1 sugar acid, 6 sugar alcohols). Free fatty acids (15 peaks) and their derivatives (3 signals) represented another large group. Further, we detected for example 5 carboxylic acids, 2 amines, 2 lactones, 4 terpenes, and 4 sterols.

Saccharides and related compounds, the substance class with the most detected discriminating metabolites, were observed in all three growth phases, but dominated in the stationary and the declining phase (Figure 2.7B). Many saccharides, e.g. galactose, galactosylglycerol, and digalactosylglycerol (met. 198, 263, and 305), two hexoses (met. 233, and 246), two complex saccharides (beta-D-methylgalactopyranoside, met. 314, and a disaccharide, met. 315), and the sugar acid threonic acid (met. 128) were significantly correlated with the stationary phase. Several other saccharides such as xylose, ribose, and glucose (met. 149, 154, and 203), a hexose and a putative pentapyranose (met. 206, and 155) as well as two disaccharides (met. 278, and 280) were important for the separation of the declining phase (Figure 2.7B). Sugar alcohols showed highest concentrations during the later growth phases with putative galactinol (met. 299) and two unidentified ones (met. 163, and 259) being slightly more abundant in the stationary phase. An inositol isomer (met. 223), and another unidentified sugar alcohol (met. 202) were positively correlated with the declining phase. The exception in this pattern constituted mannitol (met. 205) which showed a strong induction in the exponential compared to the other phases (Figure 2.7B). Vectors pointing towards the exponential phase were also observed in 1,6-anhydroglucose, a hexose, and a putative pentafuranose (met. 152, 208, and 185) as well as some unidentified (mono)saccharides (Figure 2.7B).



(E) fatty acids, their derivatives and hydrocarbons, and (F) sterols and terpenes. The insert indicates the correlation to the individual phases. Metabolites with positive x-axis and negative y-axis values correlate with the exponential phase, those with negative x- and y-axis values to stationary, and metabolites with negative x-axis and positive y-axis values to declining phase (compare Figure 2.3C). Numbers correspond to metabolites in Table 2.4 and Appendix Table 2. Abbreviations: compl., complex, Decl., declining, Exp., exponential, sac., saccharide, Stat., stationary.

Only two amino acids were significantly correlated with any of the growth phases (Figure 2.7C). Among these putative beta-alanine (met. 101) showed highest concentrations in the exponential phase, whereas putative hydroxy-proline (met. 121) was correlated with the stationary phase. An unidentified amine with the sum formula C_3H_8NCl (met. 3) was assigned to the same growth phase, whereas another amine had a vector pointing between declining and exponential phase (met. 51) (Figure 2.7C). The carboxylic acids 3-hydroxypropanoic acid, pyrrole-2-carboxylic acid, and an unidentified one (met. 29, 81, and 91) accumulated in the exponential phase, whereas 2-hydroxypropanoic acid (met. 11) was correlated with the stationary and another unidentified one (met. 120) with the declining phase (Figure 2.7C).

Both detected alcohols, putative 2,3-butanediol monoacetate and an unidentified long-chain alcohol (met. 25, and 272), showed highest concentrations in the stationary phase (Figure 2.7D). The same correlation pattern was also observed for the threonic acid-1,4-lactone (met. 87) (Figure 2.7D). In contrast, the putative galactono-1,4-lactone (met. 175) separated the exponential phase. In the exponential phase I detected higher concentrations of several substances that were not assigned to a specific metabolite class like two hydroxypyridines, 2,3-dihydroxypropanal, and a pyrazine/hydroquinone derivative (met. 8, 31, 44, and 22). Further, both lumichrome, and glycerol (met. 76, and 27) possessed vectors pointing between exponential and declining phase. As was the case for many saccharides, the putative nucleoside adenosine (met. 284) was significantly correlated with the declining phase (Figure 2.7D).

For lipids and related substances we observed a high specificity of the subgroups for one explicit growth phase (Figure 2.7E, F). Interestingly, fatty acids showed a high correlation with stationary phase and also exhibited high concentrations in the declining phase. Exceptions constituted nonanoic acid (met. 85), and the fatty acid derivative 3,4,5-trihydroxypentanoic acid (met. 162),

which possessed vectors pointing between exponential and declining phase. Hexanoic acid, hexadecanoic acid methylester (met. 15, and 207), and the fatty acid derivative hydroxyisovaleric acid (met. 46) showed highest concentrations in the declining phase (Figure 2.7E). Furthermore, two out of three hydrocarbons (met. 265, and 321) were correlated with the stationary, whereas the remaining one was correlated with the exponential phase (Figure 2.7E). The acyclic terpenes neophytadiene, and two isomers of 1,3-phytadiene (met. 191, 197, and 200) also possessed vectors pointing towards the exponential phase. In contrast, I observed a higher accumulation of the phenolic terpene alpha-tocopherol (met. 309) as well as of the three sterols ergostatriene, putative cycloergostatriene and an unidentified sterol (met. 301, 296, and 304) in the declining phase. Epibrassicasterol, the dominant sterol among those detected in *E. huxleyi* (Table 2.3), possessed a vector pointing between stationary and declining phase (Figure 2.7F).

Table 2.4: Heat map of metabolites correlated with growth phases. Heat map of relative intensities of identified intracellular metabolites significantly correlated with the first two CAP axes separating the growth phases in haploid *E. huxleyi* cultures. Metabolites are arranged in classes according to their highest concentration in exponential (Exp.), stationary (Stat.), and declining (Decl.) phase.

No.	Model-Ion	RT	Metabolite	Class	Exp.	Stat.	Decl.
101	174,1	8,92	beta-Alanine ?	Amino acid			
29	177,1	6,26	3-Hydroxypropanoic acid	Carboxylic acid			
81	240,1	8,25	Pyrrole-2-carboxylic acid	Carboxylic acid			
91	255,1	8,58	Carboxylic acid ?	Carboxylic acid			
85	117	8,35	Nonanoic acid	Fatty acid			
162	129	11,12	3,4,5-Trihydroxypentanoic acid ?	Fatty acid deriv.			
175	129,1	11,59	D(-)-Galactono-1,4-lactone ?	Lactone			
8	152	5,19	Pyridine, 2-hydroxy-	Other			
22	167,1	5,89	Pyrazine or Hydroquinone deriv.	Other			
27	103,1	6,12	Glycerol	Other			
31	152,1	6,31	Pyridine, 3-hydroxy-	Other			
44	103,1	6,84	2,3-Dihydroxypropanal	Other			
76	184	8,08	Lumichrome	Other			
181	295,1	11,83	1,3-Benzenedicarboxylic acid, ester deriv.	Other			
238	122,1	13,86	Oleanitrile	Other			
100	201,1	8,90	Monosaccharide ?	Saccharide			
139	258,1	10,32	Monosaccharide	Saccharide			
152	217,1	10,82	1,6-Anhydroglucose ?	Saccharide			
183	217,1	11,87	Monosaccharide ??	Saccharide			
185	217,1	11,94	Monosaccharide (Pentafuranose) ?	Saccharide			
208	204,1	12,85	Hexose	Saccharide			
211	205,1	12,97	Saccharide deriv.	Saccharide			
249	204,1	14,27	Saccharide ?	Saccharide			

Table 2.4 continued

No.	Model-Ion	RT	Metabolite	Class	Exp.	Stat.	Decl.
205	205,1	12,71	Mannitol*	Sugar alcohol			
222	121,1	13,33	unsaturated Hydrocarbon	Hydrocarbon			
191	123,1	12,19	Neophytadiene ⁺	Terpene			
197	123,1	12,36	(Z)-1,3-Phytadiene	Terpene			
200	123,1	12,49	(E)-1,3-Phytadiene	Terpene			
25	117	6,03	2,3-Butanediol, monoacetate ?	Alcohol			
272	108,1	15,80	long-chained Alcohol	Alcohol			
3	165	5,00	C ₃ H ₈ NCl	Amine			
121	237,1	9,75	Hydroxy-proline ?	Amino acid			
11	117,1	5,40	2-Hydroxypropanoic acid	Carboxylic acid			
167	143,1	11,38	Tetradecanoic acid ME	Fatty acid			
188	256,2	12,11	Pentadecanoic acid ME	Fatty acid			
193	117	12,24	Tetradecanoic acid *	Fatty acid			
204	117	12,67	Fatty acid	Fatty acid			
209	117	12,91	Pentadecanoic acid*	Fatty acid			
228	117	13,56	Hexadecanoic acid*	Fatty acid			
241	108,1	13,96	Octadecatrienoic acid ME	Fatty acid			
256	117	14,63	9-Octadecenoic acid	Fatty acid			
257	117	14,67	Octadecenoic acid	Fatty acid			
258	117	14,78	Octadecanoic acid*	Fatty acid			
270	285,3	15,63	Octadecanoic acid deriv. ??	Fatty acid			
274	105,1	16,02	Docosahexaenoic acid	Fatty acid			
114	103,1	9,37	2,4-Bishydroxybutanoic acid ?	Fatty acid deriv.			
87	247,1	8,46	Threonic acid-1,4-lactone, <i>trans</i> -	Lactone			
95	239,1	8,70	Dihydroxybenzene ?	Other			
99	205,1	8,85	Monosaccharide	Saccharide			
112	234,1	9,30	Monosaccharide	Saccharide			
134	205,1	10,20	Monosaccharide	Saccharide			
198	362,2	12,42	Galactose*	Saccharide			
233	204,1	13,70	Hexose	Saccharide			
246	204,1	14,11	Hexose	Saccharide			
260	204,1	14,94	Saccharide ?	Saccharide			
263	204,1	15,08	Galactosylglycerol	Saccharide			
264	370,2	15,18	Saccharide ?	Saccharide			
269	204,1	15,41	Saccharide	Saccharide			
276	204,1	16,36	Saccharide	Saccharide			
292	204,1	17,86	Saccharide ?	Saccharide			
305	204,1	19,44	Digalactosylglycerol	Saccharide			
128	292,1	9,96	Threonic acid	Sugar acid			
163	133,1	11,20	Sugar alcohol ?	Sugar alcohol			
259	358,2	14,93	Sugar alcohol ?	Sugar alcohol			
299	204,1	18,52	Galactinol ?	Sugar alcohol			
314	204,1	21,31	beta-D-Methylgalactopyranoside ?	compl. Sac.			
315	204,1	21,73	Disaccharide ?	compl. Sac.			
265	180,1	15,22	unsaturated Hydrocarbon	Hydrocarbon			
321	292,3	25,69	unsaturated Hydrocarbon	Hydrocarbon			
310	251,2	20,22	Epibrassicasterol	Sterol			
51	174,1	7,09	unidentified Amine	Amine			
120	248,1	9,71	Carboxylic acid ?	Carboxylic acid			
15	173,1	5,56	Hexanoic acid	Fatty acid			

Table 2.4 continued

No.	Model- ion	RT	Metabolite	Class	Exp.	Stat.	Decl.
207	143,1	12,80	Hexadecanoic acid ME	Fatty acid			
46	247,1	6,90	3-Hydroxyisovaleric acid	Fatty acid deriv.			
284	236,1	16,89	Adenosine ??	Other			
149	103,1	10,72	Xylose*	Saccharide			
154	103,1	10,89	Ribose*	Saccharide			
155	217,1	10,91	Pentapyranose ?	Saccharide			
156	205,1	10,93	Monosaccharide ?	Saccharide			
158	204,1	10,99	Monosaccharide ?	Saccharide			
203	319,2	12,61	Glucose*	Saccharide			
206	204,1	12,76	Hexose	Saccharide			
217	217,1	13,21	Saccharide deriv.	Saccharide			
226	217,1	13,47	Monosaccharide	Saccharide			
251	319,2	14,37	Saccharide ?	Saccharide			
202	217,1	12,55	Sugar alcohol	Sugar alcohol			
223	217	13,37	Inositol isomer	Sugar alcohol			
278	204,1	16,48	Disaccharide	compl. Sac.			
280	361,2	16,63	Disaccharide	compl. Sac.			
296	253,2	18,21	Cycloergostatriene ?	Sterol			
301	380,4	18,69	Ergostatriene	Sterol			
304	378,3	19,06	Sterol ?	Sterol			
309	237,1	19,75	alpha-Tocopherol *	Terpene			

Gray coloring reflects the intensities of the metabolites with light gray for low and dark gray for high intensities. If marked by “*”, identification was confirmed by a standard or, if indicated by “+”, by an authentic natural sample (see 6.4.3). Metabolites tagged with a “?” had a reverse match of 700 - 800 or, if marked by “??”, of 600 - 700. Abbreviations: compl., complex, deriv., derivative, ME, methyl ester, No., number, RT, retention time, Sac., saccharide.

2.3 Discussion

The here described method for GC-MS based comparative metabolic profiling proved suitable to investigate differences between life and growth phases of the coccolithophore alga *E. huxleyi*. It could be readily adapted from a protocol developed for the diatom *Skeletonema marinoi* (Vidoudez and Pohnert, 2012). Only one GC-MS based protocol for targeted metabolite profiling focusing on 26 metabolites from five different compound classes in *E. huxleyi* was reported previously (Obata et al., 2013). Furthermore, this study only analyzed diploid cells. The here presented approach covered 322 metabolites, both identifiable and unknown ones, deriving from at least twelve different metabolic classes as defined in Table 2.4. The CAP data analysis approach that was previously successfully applied on metabolomic data sets of micro- (Vidoudez and Pohnert, 2012; Paul et al., 2013) and macroalgae (Nylund et al., 2011) proved to be fully applicable for metabolic

profiling of *E. huxleyi*. Since only minor adaptations to the general protocol were required in comparison to the analysis of pelagic diatoms, I conclude that the methods applied here will also be suitable for the investigation of other coccolithophores and most likely other phytoplankton classes.

To validate a metabolic study, metadata describing the biological performance of the investigated organism are essential (Fiehn et al., 2007). Therefore, I carefully monitored the most important parameters for the investigated *E. huxleyi* cultures. Average growth rates of diploid and haploid cells were comparable to previously reported ones in the same strains (von Dassow et al., 2009), although other reports observed lower growth rates in diploid cells (Rokitta et al., 2011). In haploid cultures used for the growth phase experiment the average growth rate was lower than in haploid cultures used for the life phase experiment but still within the variability of reported values (Paasche, 2002). As mentioned by Kruskopf and Flynn (2006) Chl *a* fluorescence is inappropriate to estimate biomass. In several representative phytoplankton species these authors observed that a decline in chlorophyll:carbon ratio during nutrient limitation was offset in part by increased chlorophyll fluorescence (Kruskopf and Flynn, 2006). Thus, I alternatively used cell abundance counts to monitor the development of the cultures. The reduction in PSII efficiency between exponential and stationary phase of haploid cells might be related to reduced nutrient supply (Lippemeier et al., 2001), although other authors (Kruskopf and Flynn, 2006) have a more critical view on this relation and suggest not to draw conclusions from PSII efficiency values on nutritional states. The lower PSII efficiency rate right after inoculation (day 0) probably resulted from stress during the transfer followed by an increase to a stable level indicative for rapid recovery and acclimation of the cultures. Independent of the real reason for changes in PSII efficiency, this parameter was similar for cells in the life phase experiment, which further supports the similarity of the biological replicates. The different levels of PSII efficiency observed during the growth phase experiment further reflect differences between phases.

Bacteria proliferating during the early phase of the experiment might have influenced the behavior of our haploid cultures, but their presence was accepted for several reasons. Due to their large pore size (~1.2 µm) the filters used for our extraction method did not efficiently retain bacterial cells and so their direct contribution to the detected intracellular metabolic profiles is probably negligible. Nevertheless, I cannot exclude an indirect effect on the metabolome by the excretion

of bacterial exudates. But as they were found in comparable numbers in all replicates of the growth phase experiment and the haploid cultures used in this study originally derived from the diploid ones (Houdan et al., 2005; von Dassow et al., 2009), I assume that the influence of bacteria did not change the outcome of the comparative metabolic profiling as also stated by Paul et al. (2013). Further, as pointed out by Vidoudez and Pohnert (2012) phytoplankton always co-exist with a bacterial flora and thus their exclusion in form of axenic cultures would cause stress on the algae and prevent to draw conclusions on their natural performance. This is especially relevant, if an alga was shown to interact with bacteria as was the case for *E. huxleyi*, where a potential symbiotic bacterium favors cell growth during the exponential phase (Seyedsayamdost et al., 2011).

Although I detected a large number of metabolites, only a part of them were discriminating between life or growth phases of *E. huxleyi* cells in the comparative approach. Only those metabolites with a separating effect will be further discussed. However, this should not imply that I did not observe more and other metabolites in the total metabolome as for example was the case for amino acids.

In the haploid life phase of *E. huxleyi* most metabolites that caused the separation in CAP were up-regulated. This larger number of signals detected in higher concentrations in haploid cells allowed a significant correlation to this life phase. Since the diploid phase of *E. huxleyi* is bloom forming (e.g. Holligan et al., 1983; Brown and Yoder, 1994) and, thus, dominant in the oceans, this might be contra intuitive on first glance. One reason for their dominance might be explained by diploid cells not exhibiting photoinhibition at high irradiance whereas haploid ones do, although the life phases show no differences in pigment content (Houdan et al., 2005). This would suggest a higher photosynthesis rate, higher growth and, hence, a more active metabolism which is in contrary to metabolomic data. But despite the finding that diploid cells possess a 20% higher transcriptome richness (von Dassow et al., 2009), transcriptomic expression levels indicated an up-regulation in primary metabolism specific for haploid *E. huxleyi* cells in terms of processes such as carbon metabolism, tricarboxylic acid cycle and general energy metabolism (Rokitta et al., 2011) consistent with results presented here. Such differences might result in niche separation of life phases. The streamlined metabolism of haploid cells might contribute to a suggested competitive advantage in post-bloom waters (Rokitta et al., 2011), whereas diploid cells might have advantages exploiting a diversity of rich

environments (von Dassow et al., 2009). But since the environmental role of haploid cells is not yet clarified, this has to be considered as a rather speculative scenario. Nevertheless, with the variability at the transcript level in mind a differentiation between *E. huxleyi* life phases in the metabolome seems verified. This is for example illustrated as haploid cells showed an increased expression of genes related to carbon and primary metabolism (Rokitta et al., 2011) which was reflected by the concentration increase of many primary metabolites I observed in haploid cells. I can further exclude that the detected differences in metabolite abundance are due to a higher biovolume of haploid cells. Flow cytometry data confirmed comparable cell sizes for haploid and non-calcified diploid cells. Therefore, as the coccoliths did not contribute to the extracted metabolites and since by using normalization by cell numbers I applied the same amount of cells in both life phases, the total biovolume of diploid and haploid cells was roughly identical.

Besides life phase aspects, the growth stage of the organism under observation influences the outcome of metabolic profiling. Our comparative analysis of metabolic profiles during exponential, stationary and declining phase of haploid *E. huxleyi* cells demonstrated that composition and concentration of metabolites are highly dependent on this parameter. Depending on the growth phase, metabolic profiles showed a high specificity for certain metabolites or even a whole metabolic class. This effect and its importance for the outcome of physiological and ecological experiments was previously demonstrated in bacteria (e.g. Koek et al., 2006) and other microalgae (Paul et al., 2009; Barofsky et al., 2010; Vidoudez and Pohnert, 2012). Variation of *E. huxleyi* lipid profiles during growth was previously observed by Pond and Harris (1996), supporting the data presented here.

The observed relations of saccharides and related metabolites stand representative for the complexness of carbohydrate production and functioning in *E. huxleyi*. In diploid cells the significant correlation to mannitol can be explained by its importance as major storage carbohydrate (Obata et al., 2013). Together with the high concentration of an unidentified saccharide in diploid cells this might be a hint for differences in early steps of carbon formation between life phases. Concerning the relationship of saccharides to *E. huxleyi* growth phases the following hypothetic scenario might explain the detected variations: In exponential phase due to high photosynthesis rates and carbon assimilation, monosaccharides are built up and accumulate in the cells as carbon and energy storage products (Raven and Beardall,

2003). This process includes mannitol which, as in the diploid life phase, also seems to perform an important function in carbon storage in exponential growing haploid cells. Later, when during stationary phase resources become limited, this storage pool is consumed and as a consequence mannitol levels decrease. Since other saccharides are still present in high abundance, active photosynthesis to some extent still seems to favor their accumulation. The higher concentration of threonic acid during this phase and to some extent also in the declining phase might result from its nature as breakdown product of ascorbic acid (Helsper and Loewus, 1982), a cofactor in de-epoxidation steps of the xanthophyll cycle further functioning in removal of free radicals and their precursors (Raven and Beardall, 2003). As stress increases in later growth phases this radical scavenging process might be expected to be initiated during stationary phase. The same catabolic reaction might explain elevated concentrations of the threonic acid-1,4-lactone in the stationary and also in the declining phase, although it should be mentioned that I did not detect ascorbic acid itself. Galactosylglycerol and digalactosylglycerol, two other carbohydrates accumulating in stationary phase, might derive from lipid mobilization as they constitute de-acetylated forms of galactolipids, which occur in photosynthetic tissue of algae and higher plants (van Hummel, 1975). Their appearance could be a further indication for increased shortages in energy and the resulting exploitation of alternative sources. During declining phase, breakdown of structural polysaccharides could result in the accumulation of mono- and disaccharides and increasing glucose levels might derive from reduction of the storage compound beta-D-glucan, which was reported to accumulate during stationary phase in *E. huxleyi* (Varum et al., 1986). In parallel, sugar alcohols functioning as scavengers for free radicals (Raven and Beardall, 2003) might be produced in highly stressed cells. Accumulation of an inositol isomer could be due to degradation of lipids such as phosphatidylinositol as was speculated by Vidoudez and Pohnert (2012). Further, an isoenzymatic inositol dehydrogenase in haptophytes (detected in *Isochrysis galbana*) might indicate the function of this metabolite within a shuttle mechanism for reducing power between mitochondrion and cytosol (Gross and Meyer, 2003).

Amino acids play no major role in separating life phases of *E. huxleyi* or its growth phases. This finding is in opposite to other growth related studies in marine algae which showed an increase in the cellular amino acid concentration during growth (e.g. Kluender et al., 2009; Vidoudez and Pohnert, 2012). Out of all amino

acids detected merely isoleucine correlates with haploid cells in the life phase experiment. Further, in examining correlations with either growth phases I only found two amino acids to be significant. By their targeted metabolic approach Obata et al. (2013) detected twelve amino acids in *E. huxleyi* during late logarithmic phase, which was also sampled in this study. In our comparative approach only few of the amino acids correlated with growth phases, which, as mentioned above, does not imply that they are not present in *E. huxleyi* as I detected a few more among non-discriminating metabolites. The applied method is able to detect this compound class as shown here and in other studies (Vidoudez and Pohnert, 2012; Paul et al., 2013). Why the two discriminating amino acids beta-alanine and hydroxy-proline, which both derive from the tricarboxylic acid cycle, correlated with different growth phases is not completely clear. Free amino acid content was suggested to be cumulatively used to indicate the nitrogen status of phytoplankton cells, since their production is assumed to be high as long as nitrogen is not limiting (Admiraal et al., 1986; Haberstroh and Ahmed, 1986). Stress related studies using untargeted metabolomics showed an up-regulation of amino acids, which is explained by a breakdown of proteins (e.g. Bölling and Fiehn, 2005). In contrast, the observed lack of an up-regulation of free amino acids in *E. huxleyi* might reflect a general rapid metabolic processing and/or integration into proteins preventing the accumulation of free amino acids.

Polar low molecular weight carboxylic acids showed no general pattern and have to be considered separately. 3-Hydroxypropanoic acid was significantly related to both haploid life phase and exponential growth phase. An unidentified carboxylic acid correlated with haploid cells showed highest concentrations in the declining phase. The other two carboxylic acids correlated with haploid cells (citric acid and an unidentified one) showed no specific pattern when growth phases were analyzed. It should be mentioned that citric acid occurred in higher concentrations in the earlier samplings of haploid cells, which might be explained by changes in the tricarboxylic acid cycle activity with continuing growth. Further, three out of five carboxylic acids important for growth phase separation displayed highest concentrations in exponential phase; the remaining two in one of the other phases. Therefore, the transcriptomic based evidence of close connection between amino acid and carboxylic acid metabolism in haploid *E. huxleyi* cells shown by Rokitta et al. (2011) can only be partly supported on the metabolic level.

Although free fatty acids play an important role in differentiating between the stationary and the other phases, they play no role in life phase separation, since diploid and haploid metabolite profiles showed no differences concerning these compounds. This is in accordance with a previous study on fatty acid composition in flagellated and coccolith cells of *E. huxleyi* reporting a similar lipid composition for life phases but highest levels of neutral lipids including fatty acids in late stationary phase (Bell and Pond, 1996). It has to be considered that the method employed here allows only monitoring free fatty acids and simple esters and, thus, does not reflect the general lipid content. Pond and Harris (1996) documented a decrease in total fatty acid per cell between logarithmic and stationary phase, a fact not confirmed on the level of free fatty acids investigated in our study. I mainly observed free saturated fatty acids which usually do not contribute much to the total fatty acid pool, where high levels of unsaturated fatty acids dominate (Chuecas and Riley, 1969; Viso and Marty, 1993; Bell and Pond, 1996; Pond and Harris, 1996). This still allows the conclusion that the level of free saturated fatty acids does not follow similar trends as total lipids or total fatty acid content.

In *E. huxleyi* cells, sterols are apparently highly regulated, because they showed pronounced patterns associated with life and growth phases. The fact that I detected seven sterols of which four were significantly correlated with growth phases in haploid cells confirms a general high variability of this metabolite class in marine microalgae (Volkman, 2003 and references within). (24S)-24-Methylcholesta-5,22E-dien-3 β -ol, also called epibrassicasterol, is the major sterol found in diploid *E. huxleyi* cells (Maxwell et al., 1980). In our spectrum library database only the non-silylated substance (22E)-ergosta-5,22-dien-3 β -ol (synonymous to brassicasterol, the α -epimer of epibrassicasterol) was available. Nevertheless, I identified the peak giving the best hit to this sterol as epibrassicasterol based on its molecular ion (m/z 470), characteristic fragments (m/z 255 and 380), and the fact that, in accord with a previous report (Maxwell et al., 1980), it constituted the dominant sterol in the diploid life phase of this experiment. Lower amounts of epibrassicasterol and the presence of two sterols with slightly different mass spectra and retention times (putative cycloergostatriene and ergosterol) in haploid cells might hint for differences in cell membrane properties (Hartmann, 1998) between life phases. With respect to growth phases, all detected sterols except epibrassicasterol were correlated with the declining phase. Epibrassicasterol was highly abundant during both stationary and

declining phase. One among the sterols showed no trimethylsilylated hydroxyl group and possessed a molecular ion at m/z 380 indicating a C_{28} backbone structure. The intensive fragment at m/z 255 is characteristic for $\Delta^{5,22}$ sterols (Souchet and Laplante, 2007). Therefore, this sterol can be assumed to possess a C_{28} $\Delta^{5,22}$ structure in accordance with an ergostatriene. The fact that all these sterols accumulated in the declining phase probably indicates their important structural and regulating role in biological membranes previous to cell death (Hartmann, 1998). Further, this observation would fit well to high concentrations of alpha-tocopherol, which synergistically with beta-carotene acts as effective radical-trapping antioxidant in membranes (Palozza and Krinsky, 1992) and contributes to stress tolerance in plants (Munne-Bosch, 2005). Such processes would be highly relevant for heavily stressed cells under the adverse conditions during the declining phase. In contrast, the correlation of neophytadiene and the two isomers of 1,3-phytadiene to the exponential phase might be explained by their putative origin as alteration products of phytol (Grossi et al., 1996). As the latter is needed for photosynthesis, it seems reasonable to expect compounds potentially deriving from it at highest concentrations during exponential cell growth. This is further supported by the detection of these terpenes during exponential growth in the freshwater algae *Botryococcus braunii*, and *Volvox aureus* (Zhang and Sachs, 2007).

Besides members of these important metabolite classes several individual compounds showed specific correlation patterns with either a life phase or one of the growth phases. Important among these was the putative adenosine (good spectral match of the main fragments and the retention time to two library entries), which was one of the few metabolites highly correlated with the diploid life phase and further present in highest concentrations during the declining phase. Adenosine has been previously identified in metabolite profiles of the diatom *Cocconeis scutellum* (Nappo et al., 2009). Its presence in diploid cells might be correlated with its role in energy balance (Stringer et al., 2011) and hint for differences in energy shuffling between diploid and haploid cells. On the other hand, adenosine has been reported to increase under stress or distress and to possess a cytoprotective function, which might explain its dominance in the declining phase (Fredholm, 2007).

Lumichrome (7,8-dimethylalloxazine) was also significantly correlated with the exponential growth phase. This metabolite is the main degradation product of riboflavin (transformation yield in sea water: 96%), which is extremely sensitive to

sunlight (Dunlap and Susic, 1986). Rapid transformation of riboflavin into lumichrome under light conditions would fit to its accumulation in exponentially growing *E. huxleyi* cells, because it constitutes the growth phase with the highest photosynthetic activity. The previous detection of lumichrome as an excretion product of the diatom *Phaeodactylum tricornutum* supports a potential importance for microalgae (Seritti et al., 1994). This compound also acts as a quorum sensing agonist that binds to LasR (Rajamani et al., 2008), but whether it is indeed excreted to interfere with bacterial signaling or not needs to be further explored.

In conclusion I can state that comparative metabolic profiling is suitable to analyze complex metabolic patterns in the coccolithophore *E. huxleyi*. By the application of CAP I could detect specific metabolites highly correlating with either the diploid or haploid life phase. Further, I discerned separate groups of intracellular metabolites varying between exponential, stationary or declining phase. Only five metabolites (putative adenosine, epibrassicasterol, mannitol, an unknown saccharide, and an unknown compound) displayed higher concentrations in diploid cells, whereas all other discriminating compounds exhibited higher abundances in haploid cells. The potential storage compound mannitol correlated with both the diploid life phase and the highly productive exponential growth phase. Furthermore, epibrassicasterol, the most abundant sterol, was important for separating the diploid life phase. In general, sterol metabolism seems to be of particular importance as it was both highly related to life and growth phase specific patterns. In opposition to several other studies, I did not observe a discriminating effect of amino acids. In contrast, free fatty acids were nearly exclusively correlated with the stationary phase. My results indicate that not only species composition but also differences in metabolic levels might be relevant for the diversity observed in plankton. This is supported by the fact that several of the detected discriminating metabolites are known to play key roles in physiology and in ecological interactions of the producer. Since I found different metabolic patterns in haploid cells, these results are important to be considered for further studies. Here I thus lay a basis for future work addressing the so far only purely understood role of haploid *E. huxleyi* cells in the natural system.

3 Metabolic variation induced by CO₂ and iron manipulation during a mesocosm experiment

This chapter presents results from a mesocosm experiment conducted at the Norwegian National Mesocosm Centre, Espegrend, Norway, between the 5th (day 0) and 27th (day 22) of June 2012, an international project combining expertise on different topics from various countries. The initial experimental design was developed by Maria Segovia, University of Malaga, Spain, Maria Maldonado, University of British Columbia, Canada, and Francisco Lazaro, University of Zaragoza, Spain.

Parts of this chapter are intended to be used in a manuscript about metabolic changes during carbon dioxide and iron manipulation in a mesocosm for later publication. Further, we anticipate a publication of the general experimental design together with growth patterns of plankton groups, physical and chemical parameters co-authored by all participants of the mesocosm experiment.

3.1 Experimental design

Although laboratory experiments on phytoplankton cultures constitute a convenient tool to assess changes in metabolism during different growth phases or treatments, drawing conclusions of ecological relevance is problematic. In natural communities metabolic signaling of other phytoplankton species or predators will influence the alga under investigation and therefore change patterns observed in the laboratory. To test the conclusions drawn from *Emiliania huxleyi* cultures for their relevance in natural phytoplankton communities, I chose to participate in a mesocosm experiment. Outdoor mesocosms as those used in this study present a large enclosure containing the natural plankton community submitted to natural light and temperature conditions. They are a convenient tool to test hypotheses under semi-natural conditions without conducting extensive field sampling. In contrast to the latter, it allows manipulation through the execution of specific treatments of interest or introduction of specific species. Further, an addition of nutrients can lead to the induction of a desired bloom.

For the experiment twelve mesocosm enclosures containing 11 m³ of the natural plankton community and covered by lids were deposited floating in Raunefjorden, Norway, alongside a raft (for details on the mesocosm enclosures and the experiment see 6.6). By nutrient addition (N:P at 30:1) favorable conditions to initiate a coccolithophore bloom were established (Engel et al., 2004). Six of the mesocosm enclosures were exposed to either present day carbon dioxide (CO₂) (low CO₂: 390 ppm) or increased CO₂ levels (high CO₂: 1000 ppm), respectively, the latter simulating the atmospheric CO₂ concentration as predicted for the year 2100 (IPCC, 2007). Further, addition of the chelating agent desferrioxamine B (DFB) to six of the enclosures affected the amount of bioavailable iron (Fe). This second treatment was conducted at a later time point (day 6) to allow sufficient phytoplankton development prior to a changed iron bioavailability. In total, we conducted triplicates of four different treatments: low CO₂/DFB- (control), low CO₂/DFB+, high CO₂/DFB+, and high CO₂/DFB- (Figure 3.1A). To reduce the effort of the CO₂ treatment, enclosures of the same treatment were aligned (Figure 3.1B) instead of using a randomized set-up. Since abiotic conditions such as light or temperature in general were identical between the enclosures, this set-up was preferable and the potential effect of clustering due to changing conditions observed by others (Martínez-Martínez et al., 2006) regarded as negligible. In addition to the mesocosm experiment, fjord water was sampled to estimate the divergence of the experimental mesocosms to the non-manipulated situation in the fjord.

CO₂ and Fe manipulation conducted in the mesocosms were aimed to investigate the performance of the calcifying *E. huxleyi* under potentially acidified future ocean conditions. I joined the experiment to assess metabolic profiles during a semi-natural *E. huxleyi* bloom and to monitor changes in the metabolome induced by acidic conditions or an alteration of bioavailable Fe. Therefore, I sampled intracellular metabolites and quantified bacterial and viral abundance as metadata, to observe potential additional effectors of metabolic changes. Metabolic profiles obtained from the control (low CO₂/DFB-), which can be assumed to nearest reflect the natural *E. huxleyi* bloom situation, can further be compared to laboratory results allowing better assessment of the ecological relevance of the previous findings with isolated cultures (see chapter 2).

In addition to *E. huxleyi* abundance, cell numbers of other phytoplankton groups that occurred in the phytoplankton community of the mesocosms as well as

bacterial and viral abundances were monitored. These data are presented together with several parameters such as pH, dissolved and particulate Fe or nutrient concentrations, as they were necessary to understand the development and performance of the phytoplankton community during the mesocosm experiment. As these data were provided by other members of the international team, their origin is indicated in the figure legends.

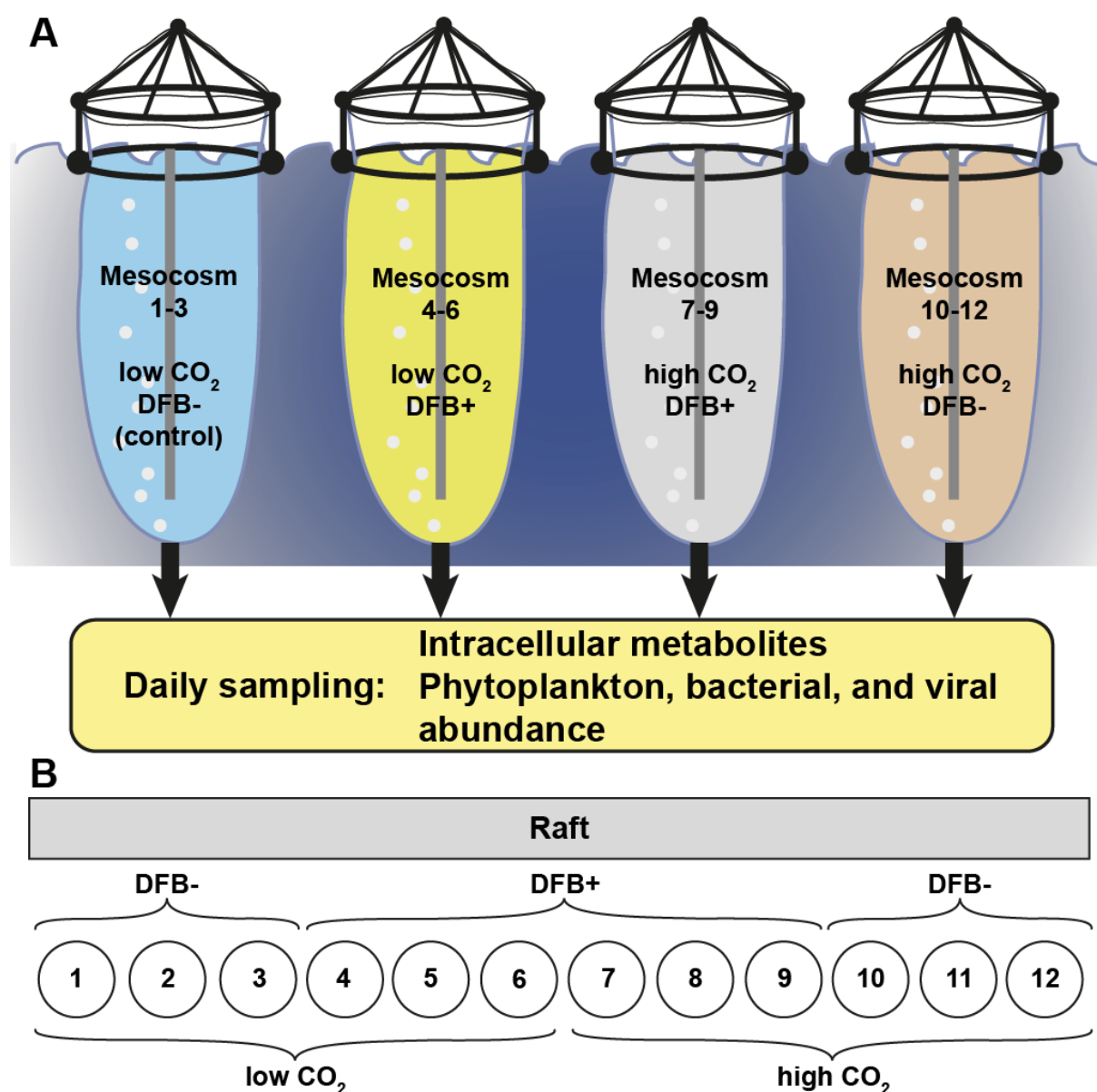


Figure 3.1: Experimental design of the mesocosm experiment. (A) Set-up of the 12 mesocosm enclosures indicating treatments and parameters sampled daily and necessary for metabolome analysis. Low CO₂ refers to ambient CO₂ levels (390 ppm), high CO₂ to a CO₂ level as predicted for the year 2100 (1000 ppm). (B) Distribution of mesocosm enclosures alongside the raft with corresponding treatments. Abbreviation: DFB, desferrioxamine B. Symbols: “+”, addition, “-”, no addition.

3.2 **Results**

3.2.1 ***Phytoplankton growth***

As anticipated we observed an *E. huxleyi* bloom, which contrasted the fjord water, in all mesocosms due to the nutrient addition. Further, CO₂ and iron manipulation affected phytoplankton growth. One among the mesocosms, enclosure 3, showed a different growth behavior than the other mesocosms in the same treatment (enclosures 1 and 2), and thus had to be excluded from all data analyses. The reason for continuing exponential growth exhibited by the organisms in mesocosm 3 was an unintended iron induction by the light and temperature sensor (see 6.6.11) located in this enclosure. Therefore, although not statistically correct, the mean plus/minus standard deviation (\pm SD) of two biological replicates is shown for the treatment low CO₂/DFB- (control).

Chlorophyll *a* (Chl *a*) generally decreased in all mesocosm enclosures from the first measurement point (day 3, $\sim 4.7 \mu\text{g L}^{-1}$) onwards until day 11 ($\sim 1.0 \mu\text{g L}^{-1}$) (Figure 3.2A). In the fjord water Chl *a* concentrations stayed at a similar level after the onset of the experiment with a slight increase from day 9 to 10, but afterwards decreased until the end of the experiment. In contrast, in the enclosures treatment dependent differences occurred after day 11. The control (low CO₂/DFB-) exhibited slightly induced Chl *a* concentrations after day 11 and increased until the end of the experiment (day 22). In the second low CO₂ treatment with addition of the Fe chelating agent (low CO₂/DFB+) Chl *a* strongly increased and peaked approximately at day 15. This treatment showed a significant difference from the control and both treatments with elevated CO₂ levels (high CO₂/DFB+ and high CO₂/DFB-) on day 15 ($P < 0.001$, and $P = 0.016$, respectively, two way analysis of variance, ANOVA, using Holm-Sidak method for pairwise multiple comparison procedure, see 6.6.10 for details on statistical analysis). The same treatment was significantly different from all other treatments on day 22 ($P = 0.035$, two way ANOVA). In contrast, treatments exposed to elevated CO₂ levels only showed a stronger increase in Chl *a* after day 15 (Figure 3.2A). Chl *a* concentration of these treatments was significantly different to the control on day 15 ($P < 0.001$, two way ANOVA with pairwise multiple comparison) (Figure 3.2A).

Cell abundance data demonstrated that we successfully induced an *E. huxleyi* bloom, which was most pronounced in one treatment (Figure 3.2B). In the fjord water *E. huxleyi* cell abundance remained low during most of the experiment only slightly increasing from day 14 onwards (Figure 3.2B). In contrast, after a lag phase of a few days, *E. huxleyi* in the treatment low CO₂/DFB+ grew exponentially until day 20 thereby exceeding 60,000 cells mL⁻¹. It showed significant differences in *E. huxleyi* cell abundance to all other treatments from day 11 onwards ($P = 0.012$ on day 11, $P = 0.003$ on day 12, and $P < 0.001$ from day 14 onwards, one way ANOVA with pairwise multiple comparison). In the control (low CO₂/DFB-) mesocosms *E. huxleyi* cell abundance peaked on day 10, decreased afterwards until day 14 and exhibited a second maximum at the end of the experiment, which nearly reached 20,000 cells mL⁻¹. Both high CO₂-treatments showed a similar pattern peaking at day 11 and growing from day 17 onwards until the end of the experiment (Figure 3.2B). *E. huxleyi* cell abundance of the control and treatments with elevated CO₂ were significantly different from each other on days 17 and 18 ($P = 0.009$ and $P = 0.028$, respectively, one way ANOVA using a general linear model without interactions).

Besides *E. huxleyi*, which constituted the dominant phytoplankton taxon, we quantified cell abundance for cyanobacteria of the genus *Synechococcus* (0.6-2 µm), picoeukaryotes (0.1-2 µm), and small (2-7 µm) and big nanoeukaryotes (6-20 µm) (Figure 3.2C-F). In the mesocosm enclosures cell abundances strongly differed between the different phytoplankton groups. In the fjord water *Synechococcus* spp. grew exponentially from day 3 onwards reaching a final abundance of nearly 50,000 cells mL⁻¹ on day 20 (Figure 3.2C). In contrast, this group showed nearly arrested growth in all treatments until day 9 and decreased between day 9 and 12 (Figure 3.2C). Afterwards in both low CO₂ treatments *Synechococcus* spp. grew linearly reaching different final abundances. In treatments exposed to high CO₂ *Synechococcus* spp. showed linear growth after day 18 reaching a final abundance of approximately 1000 cells mL⁻¹. Picoeukaryotes were low in abundance at the beginning in the fjord water and showed an abundance peak on day 21 (Figure 3.2D). This phytoplankton group displayed no pronounced difference in cell abundance between treatments, except that cells in treatments with elevated CO₂ reached a slightly higher abundance at the maximum on day 6 (Figure 3.2D). Afterwards, the number of picoeukaryotes decreased until day 11 and stayed low for the rest of the experiment.

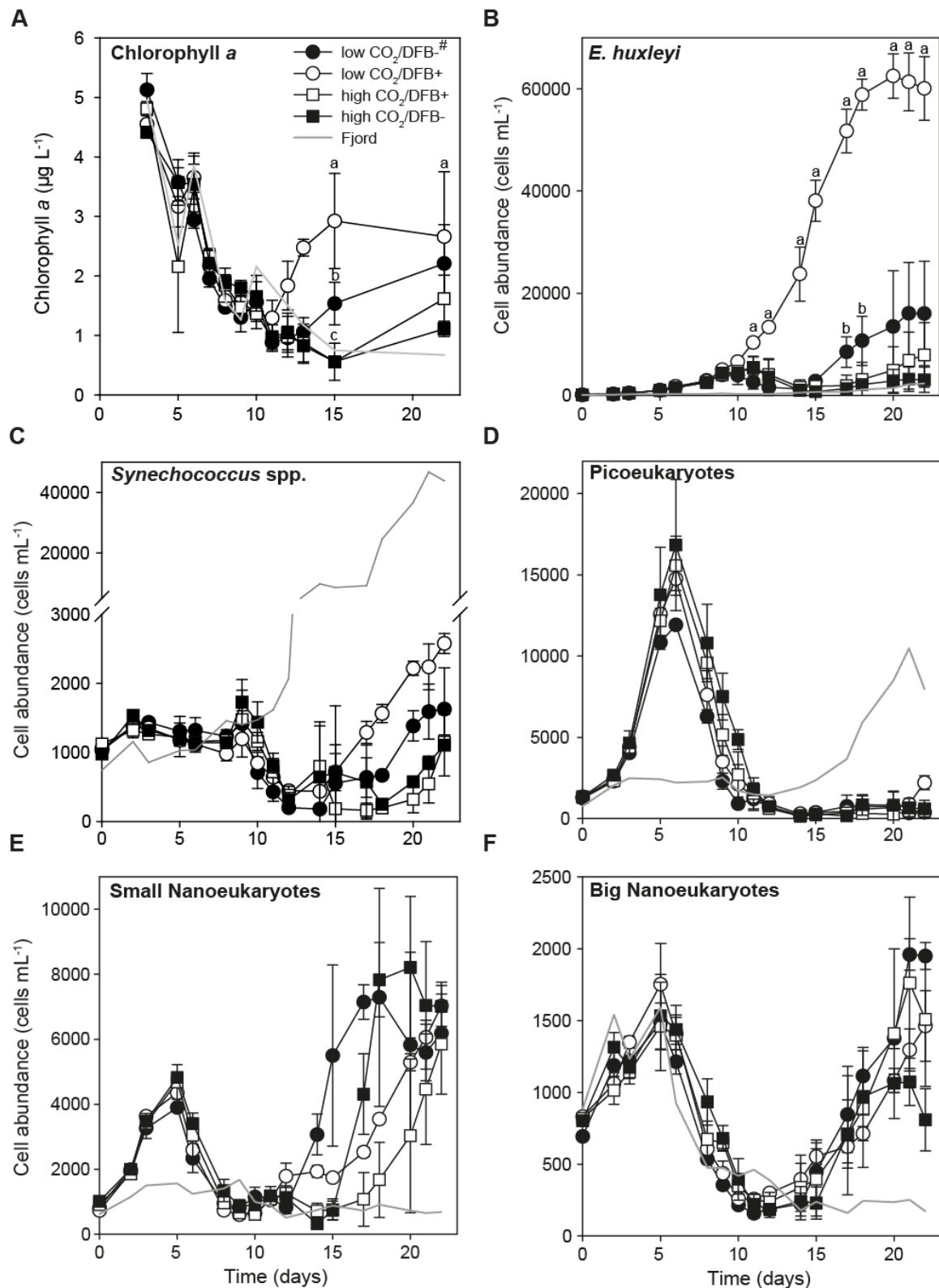


Figure 3.2: Phytoplankton growth during the mesocosm experiment. (A) Chlorophyll *a* concentration assessed by fluorescence spectroscopy and cell abundances of (B) *E. huxleyi*, (C) *Synechococcus* spp., (D) picoeukaryotes, (E) small, and (F) big nanoeukaryotes in all mesocosms and the fjord water measured by flow cytometry (mean \pm SD, $n=3$; $\#n=2$). Some abundance values possess a low range of the standard deviation. Small letters indicate significant differences between treatments for Chl *a* concentration and *E. huxleyi* cell abundance (compare text). Note differences in the y-axis scaling. Data provided by S. Berger (Chl *a*), and A. Larson (flow cytometry). Abbreviation: DFB, desferrioxamine B.

Whereas in the fjord water small nanoeukaryotes only occurred in low abundance during the whole observation period, big nanoeukaryotes peaked on day 5, but after a decrease remained at low abundance during the second half of the experiment (Figure 3.2E, F). Small and big nanoeukaryotes in all treatments reflected the growth pattern observed in the fjord showing no differences between treatments until day 12 and both groups peaked on day 5 followed by an abundance decrease (Figure 3.2E, F). Afterwards, small nanoeukaryotes in treatments without DFB addition recovered quicker than those with the chelating agent added, reaching a maximum abundance of approximately 8,000 cells mL⁻¹ around day 18 (Figure 3.2E). Big nanoplankton grew exponentially in all treatments from day 14 onwards reaching their highest abundance in the control on day 21 (Figure 3.2F).

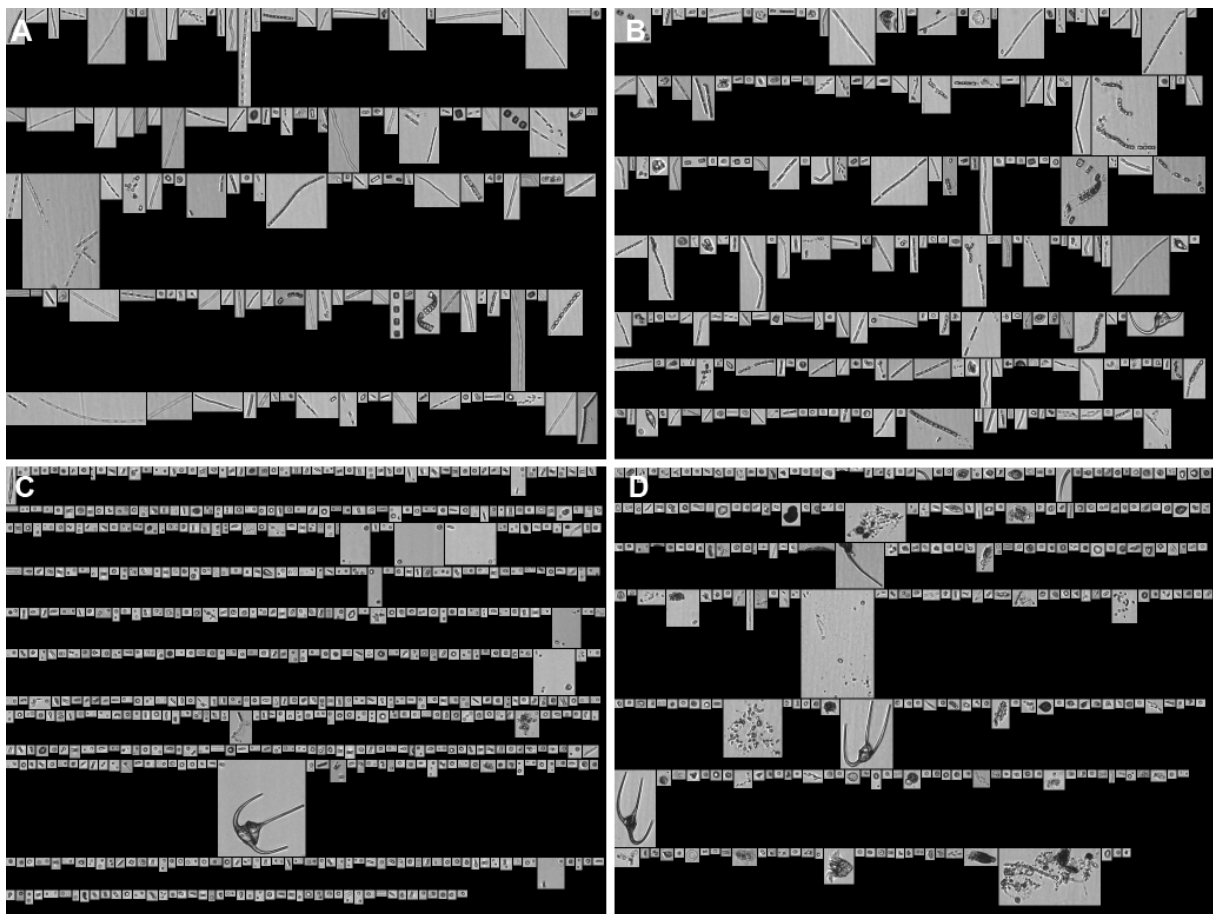


Figure 3.3: Flow cam images of larger phytoplankton groups and ciliates. Flow cam images of control mesocosm 1 assessed on (A) day 1, (B) day3, (C) day 9, and (C) day 21. Images and preliminary data provided by S. Berger.

The abundance of larger phytoplankton groups such as diatoms was measured by flow cam, but only preliminary data for the control on day 3 are available so far. On day 3 diatoms reached 861 colonies mL⁻¹ with *Skeletonema* sp.

as the most abundant taxon accounting for 798 colonies mL^{-1} in the control. (The word colony here refers to a group of cells, probably presenting a chain of diatoms.) Flow cam images further documented the occurrence and decline of diatom chains. Chain forming diatoms were observed in the mesocosm enclosures right after the onset of the experiment (Figure 3.3A), but after a maximum on day 3 (Figure 3.3B) rapidly decreased. Soon no living diatom chains were detected in the samples and diatoms vanished completely as the experiment proceeded (Figure 3.3C, D).

Concerning their cell size calcified *E. huxleyi* cells are in the range of small nanoeukaryotes (2-7 μm). Thus, chain-forming diatoms which are larger than *E. huxleyi* cells (compare Figure 3.3) were responsible for the initial peak in Chl *a*. Early after the beginning of the experiment, all different phytoplankton groups contributed to the overall biomass, but with proceeding time the contribution of *E. huxleyi* increased. During the later days (days 12 to 22), due to its cell size in combination with its high abundance, *E. huxleyi* was the main contributor to the total biomass even in those treatments, which displayed a relatively lower cell abundance of 10,000-20,000 cells mL^{-1} . The latter situation also can already be regarded as an *E. huxleyi* bloom.

3.2.2 Bacterial and viral abundance

We determined bacterial and viral abundances (Figure 3.4) to obtain a more complete picture of the community present during the course of the experiment. These microorganisms were of interest, because they might have influenced the other organisms in the phytoplankton community. Further, we were also interested whether the treatments did affect bacteria or viruses. Concerning the metabolome analysis we do not expect that bacterial metabolites did change the outcome of our profiling, because they were not successfully retained on the used filters (GF/F filters, Whatman, Kent, UK, with a pore size of $\sim 0.8 \mu\text{m}$). Nevertheless, they might have influenced metabolite composition in phytoplankton cells due to released exudates.

Bacterial abundance in the fjord water showed only little variation, but commuted around $1.0 \cdot 10^6$ cells mL^{-1} with a pronounced decrease on day 4, between days 15 and 18, and after day 21. In contrast, in the mesocosm enclosures bacterial abundance showed a pattern with three successive peaks (Figure 3.4A). During the

first maximum on day 2 bacterial abundance reached approximately $1.5 \cdot 10^6$ cells mL^{-1} displaying a significant difference between high and low CO_2 on day 1 ($P = 0.04$, ANOVA on ranks, for details on statistical analysis see 6.6.10). Afterwards bacteria decreased until day 4 reaching significantly lower abundances in treatments exposed to elevated CO_2 ($P = 0.042$, ANOVA on ranks). During the second peak with its maximum on day 9 bacterial numbers were higher in treatments exposed to elevated CO_2 than those exposed to ambient CO_2 levels, although this was not significant concerning the effect of CO_2 ($P = 0.1$, ANOVA on ranks). After day 14, bacteria in the low CO_2 treatments grew linearly and peaked for a third time on days 17 and 18 at approximately $1.0 \cdot 10^6$ cells mL^{-1} . In mesocosms exposed to elevated CO_2 , bacteria reached a third maximum at lower abundance on days 17 to 19 (Figure 3.4A). The difference in bacterial abundance between high and low CO_2 treatments was significant on day 18 ($P = 0.041$, ANOVA on ranks).

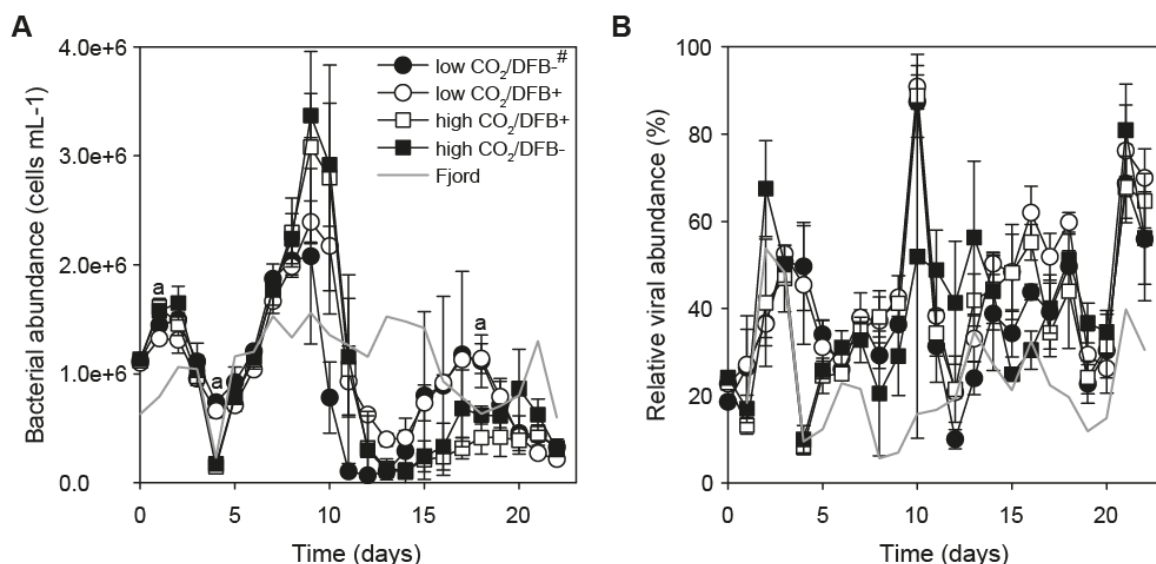


Figure 3.4: Bacterial and viral abundance. (A) Bacterial abundance and (B) abundance of virus-like particles (VLPs) relative to the highest abundance of VLPs detected during the mesocosm experiment (high CO_2 /DFB-, mesocosm 10, day 10) as measured by flow cytometry (mean \pm SD, $n=3$; $^{\#}n=2$). Small letters indicate significant differences between low CO_2 and high CO_2 treatments. Abbreviation: DFB, desferrioxamine B.

Viral samples got defrosted during the transport prior to flow cytometry analysis. This might have affected the real number of viruses present in the samples, because viral capsids are often sensitive when it comes to defrosting effects (W.H. Wilson, personal communication). Since all samples suffered from the same problem during shipment, we assumed that the effect on viral abundance was comparable for

all of them. Thus, the abundance of virus-like particles (VLPs) is given in numbers relative to the highest abundance detected during the mesocosm experiment (highCO₂/DFB- treatment, mesocosm 10 on day 10) to take in account the effect of defrosting on their absolute abundance.

We could not see a clear trend for VLPs in any of the treatments, but in general their abundance was slightly higher in the mesocosm enclosures than in the fjord water during most of the experiment (Figure 3.4B). In the fjord water numbers of VLPs exhibited a rather oscillating pattern. Abundance of VLPs in the mesocosm enclosures showed a moderate increase from day 0 to day 3 and a decrease after day 4. A sharp increase in all treatments except for high CO₂/DFB- was observed on day 10, but numbers of VLPs rapidly decreased afterwards to stay at similar levels between day 12 and 18. After a further slight decrease VLP abundance peaked another time on days 21 and 22 in all treatments (Figure 3.4B).

3.2.3 Experimental additions and nutrient levels

Manipulation of CO₂ concentrations and the addition of the Fe chelating agent DFB necessitated the monitoring of pH, and dissolved and particulate Fe (Figure 3.5A-C). Right after the start of the experiment the pH in treatments exposed to ambient CO₂ conditions lay between 8.0 and 8.1. It increased to 8.3 on day 4 and stayed at this level until day 11, then took on values between 8.1 and 8.2 and remained there for the rest of the experiment (Figure 3.5A). In high CO₂ treatments the initial pH lay at 7.7, but increased to values between 7.8 and nearly 8.0 between days 4 and 10. On day 11 the pH dropped to 7.6 due to another CO₂ addition (see 6.6.1). Levels of pH started to increase again from day 14 onwards reaching a final value of 7.8 on day 22 (Figure 3.5A).

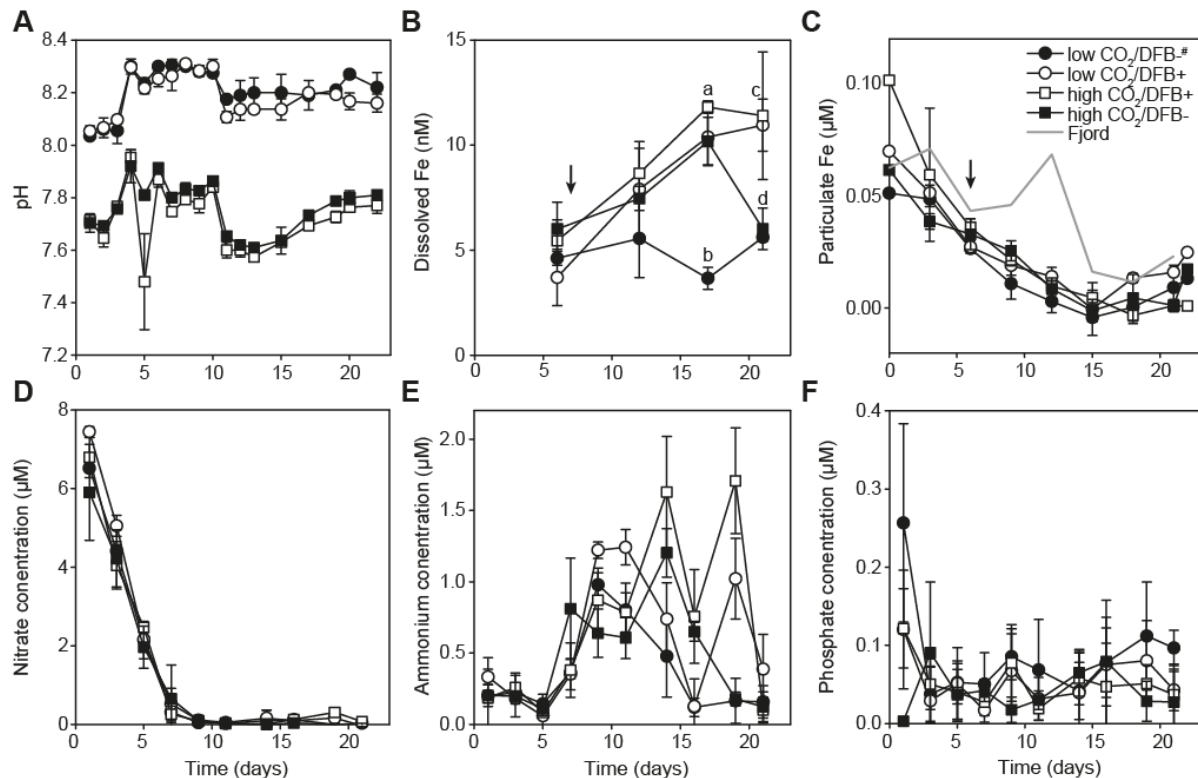


Figure 3.5: Observation of experimental additions and nutrient levels. (A) pH induced by ambient (390 ppm) and elevated (1000 ppm) CO_2 levels. (B) Dissolved iron (Fe) measured by flow injection analysis (FAI) with chemiluminescence detection. (C) Particulate Fe assessed by wavelength dispersive X-ray fluorescence spectroscopy (WDXRF). (D-F) Nutrient concentrations: (D) nitrate, (E) ammonium, and (F) phosphate. Data represent mean \pm SD, $n=3$; $^{\#}n=2$. Small letters indicate significant differences between treatments in dissolved Fe (compare text) and an arrow indicates the day of desferrioxamine B (DFB) addition. Note differences in the y-axis scaling. Data provided by J.A. Fernandez (pH and nutrients), F.J.L. Gordillo (pH), C. Lorenzo (dissolved Fe), and J.K. Egge (particulate Fe).

Dissolved Fe was measured by the extremely sensitive but also material and time intensive method of flow injection analysis (FAI) with chemiluminescence detection. Therefore, this parameter was only assessed at specific time points, the first one prior to the addition of DFB and three more distributed evenly over the remaining experiment. Prior to the addition of the chelating agent (day 6) dissolved Fe concentrations were similar in all mesocosms and, although they slightly increased, remained similar at the first measurement point (day 12) after DFB addition (Figure 3.5B). Except for the control, dissolved Fe concentrations increased in all treatments on day 17 resulting in a significant difference of the control ($P < 0.001$, two way ANOVA with pairwise multiple comparison). On day 21 concentrations of dissolved Fe dropped in the high CO_2 /DFB- treatment leading to a significant separation of treatments with and without DFB addition concerning

dissolved Fe ($P = 0.002$, two way ANOVA with pairwise multiple comparison) (Figure 3.5B). In contrast to dissolved Fe, concentrations of particulate Fe decreased in all treatments until they reached the detection limit around day 15 (Figure 3.5C). It further showed a moderate increase between day 18 and 22, but without any recognizable differences between treatments. Particulate Fe was the only nutrient assessed in the fjord water, because the other parameters were either too expensive or not of specific interest. In general, particulate Fe displayed a similar reduction pattern after the start of the observation in the fjord water, but peaked on day 12 prior to further reduction. As in the mesocosm enclosures particulate Fe concentrations also slightly increased from day 18 to 21 (Figure 3.5C).

Additionally we monitored nutrient concentrations by measuring nitrate, ammonium, and phosphate (Figure 3.5D-F). Nitrate concentrations rapidly decreased between the beginning of the experiment and day 7 in all mesocosms and stayed near the detection limit for the rest of the observation period (Figure 3.5D). Ammonium concentrations were low until day 5 then increased in all mesocosms to levels between 1.0 and 1.5 μM , but without showing specific treatment dependent trends. On day 21 concentrations of ammonium decreased again in all mesocosms (Figure 3.5E). Except for day 1, phosphate levels lay around 0.1 μM during the whole course of the mesocosm experiment and showed no different patterns between treatments (Figure 3.5F).

3.2.4 Separation patterns based on metabolic profiles

The outdoor mesocosms were sampled daily at 9:00 am from a depth of 2.5 m through a 200 μm plankton mesh into 20 L carboys and water from the fjord was taken from ~1 m depth. The carboys were transported on shore and stored in a climate chamber at $\sim 10^{\circ}\text{C}$ (for details on mesocosm sampling see 6.6.4). For extraction of intracellular metabolites, 3-6 L per mesocosm were concentrated on filters with a pore size of $\sim 0.8 \mu\text{m}$ (GF/F, Whatman, Kent, UK) and extracted in 1 mL of a solvent mixture. These samples were later derivatized and measured on a gas chromatograph coupled to a mass spectrometer (GC-MS) (for details see 6.4.1, and 6.6.7 to 6.6.9).

After data normalization using peak sums and a screening for the number of detected peaks per sample, we on average obtained a total of 397.6 ± 73.1 signals in

269 samples. These samples derived from eleven mesocosms and the fjord water (because all 22 samples from mesocosm 3 were excluded from further processing). A complete list of all detected signals per day in each treatment including the fjord water is given in Table 3.1. From the 269 samples ten were excluded as potential outliers, because the number of detected signals was below the selection criterion ($\text{mean} \pm 2 \times \text{SD}$). After data processing 333 signals from 259 mesocosm and fjord water samples remained in the constrained statistical analysis.

Table 3.1: Numbers of detected signals. The list presents the numbers of signals detected by GC-MS for the CO₂ and desferrioxamine B addition (DFB) treatments as well as the fjord water (no replicates) on each day of the mesocosm experiment ($\text{mean} \pm \text{SD}$, $n=3$; $\#n=2$). On day 0 only one mesocosm per treatment was sampled (enclosure 2, 5, 8, and 11).

Time	Treatment				Fjord
	low CO ₂ /DFB- [#]	low CO ₂ /DFB+	high CO ₂ /DFB+	high CO ₂ /DFB-	
Day 0	329	384	364	341	429
Day 1	404.5 \pm 94.0	447.3 \pm 62.1	432.7 \pm 88.5	481.3 \pm 29.1	411
Day 2	470.5 \pm 7.8	386.3 \pm 23.7	455.7 \pm 35.9	489.3 \pm 35.5	459
Day 3	488.0 \pm 31.1	434.7 \pm 83.8	412.0 \pm 60.1	430.3 \pm 83.7	411
Day 4	329.0 \pm 36.8	359.0 \pm 69.4	377.7 \pm 57.3	451.3 \pm 68.5	528
Day 5	430.0 \pm 21.2	379.3 \pm 73.7	459.0 \pm 15.5	466.7 \pm 28.4	469
Day 6	427.5 \pm 79.9	346.7 \pm 121.1	356.0 \pm 101.4	435.0 \pm 36.7	488
Day 7	417.5 \pm 98.3	423.0 \pm 68.1	387.7 \pm 39.7	374.7 \pm 82.4	410
Day 8	422.5 \pm 31.8	343.0 \pm 44.5	443.3 \pm 56.0	465.7 \pm 30.7	352
Day 9	470.0 \pm 22.6	393.3 \pm 82.0	419.7 \pm 101.7	379.0 \pm 102.2	319
Day 10	454.0 \pm 2.8	389.0 \pm 48.8	404.3 \pm 72.0	432.0 \pm 40.0	401
Day 11	366.5 \pm 89.8	404.0 \pm 113.3	412.0 \pm 70.8	352.0 \pm 75.7	476
Day 12	354.0 \pm 33.9	408.0 \pm 59.6	379.7 \pm 37.0	363.3 \pm 75.9	299
Day 13	394.5 \pm 125.2	423.0 \pm 76.9	371.3 \pm 66.1	352.0 \pm 133.8	363
Day 14	409.5 \pm 24.7	399.3 \pm 82.4	347.0 \pm 63.5	270.0 \pm 36.5	382
Day 15	417.5 \pm 29.0	347.7 \pm 78.0	258.3 \pm 52.5	296.3 \pm 80.5	420
Day 16	333.5 \pm 21.9	398.0 \pm 44.2	367.7 \pm 28.0	368.0 \pm 31.7	365
Day 17	431.0 \pm 19.8	402.7 \pm 58.7	376.3 \pm 22.0	363.3 \pm 92.5	220
Day 18	386.5 \pm 46.0	376.3 \pm 37.8	234.7 \pm 87.0	433.7 \pm 22.5	204
Day 19	438.0 \pm 21.2	416.3 \pm 56.4	353.0 \pm 40.8	291.3 \pm 67.4	343
Day 20	418.0 \pm 19.8	472.0 \pm 45.5	439.0 \pm 35.8	439.7 \pm 56.5	449
Day 21	375.0 \pm 59.4	468.7 \pm 13.5	416.0 \pm 74.5	378.0 \pm 39.1	310
Day 22	501.5 \pm 34.6	460.7 \pm 4.0	375.7 \pm 113.6	392.3 \pm 53.3	364

The use of peak sum normalization here might be criticized, but neither normalization by cell number nor biomass was possible, because of the complex mixture of phytoplankton groups present in the mesocosms. Further, normalization by the standard ribitol also was not suitable, as filtered volumes differed and ribitol cannot be used for normalization of such a broad spectrum of compound classes. Thus, independent of the different phytoplankton present, we selected peak sum normalization, because at least towards the second part of the experiment we assumed *E. huxleyi* to contribute most to the metabolic profiles.

Canonical analysis of principal coordinates (CAP) (Anderson and Willis, 2003) was used to determine metabolic differences between the treatments during the course of the mesocosm experiment. When the whole metabolic data set including samples obtained during all 22 days of the experiment was analyzed, fjord water samples were separated from mesocosm samples after the first three days (Figure 3.6), because only data points of days 0-3 lay within the cloud of other data. Analysis of all four treatments over all 22 days resulted in no separation, (Figure 3.6A). Accordingly, CAP diagnostic values did not support a separation of the treatments (Table 3.2). Analysis for one parameter at a time did neither determine an effect of CO₂ levels (Figure 3.6B) nor of DFB addition (Figure 3.6C) during the course of the whole experiment, and axes were not differentiating between groups (Table 3.2).

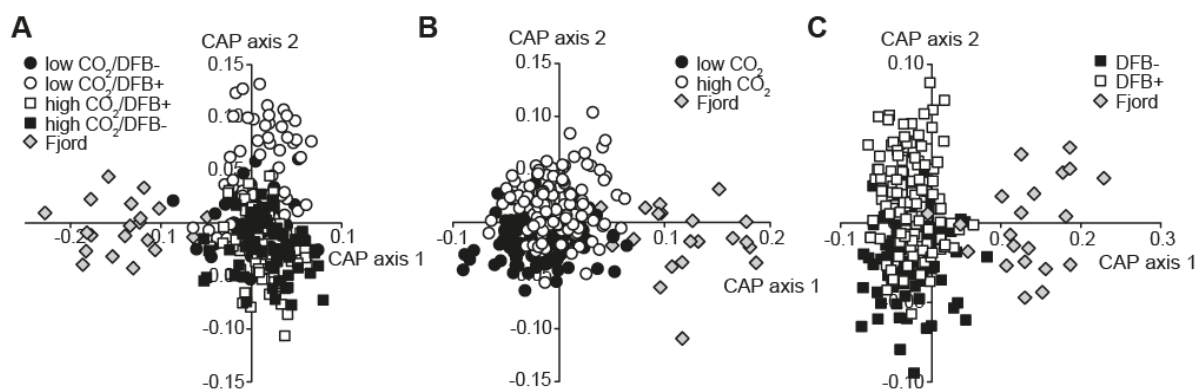


Figure 3.6: Multivariate separation of mesocosms by canonical analysis of principal coordinates (CAP). (A) Separation of all four applied treatments from the fjord water, (B) of the low and high CO₂ treatment from the fjord water, and (C) of the desferrioxamine B (DFB) addition treatments from the fjord water during the 22 days the mesocosm experiment lasted. Note the different scaling of x- and y-axis.

Table 3.2: Statistical diagnostic values of canonical analysis of principal coordinates (CAP). Complete list of statistical support values of the CAP with CO₂ levels and desferrioxamine B (DFB) addition as listed in the column “Parameters” defined as groups. Support values correspond to graphs shown in Figures 3.6, and 3.7. Data present eigenvalues (λ) and squared correlation (Δ^2) for all CAP axes, misclassification error, and P values of the permutation test. A high eigenvalue (> 0.9 for the 1st axis), a low misclassification error and a significant permutation test ($P < 0.05$) indicate a significant separation by the corresponding axis. Abbreviation: M, mesocosm.

Parameters	Time intervals	Constrained canonical axes								Statistics	
		1 st axis		2 nd axis		3 rd axis		4 th axis		Cross validation	Permutation test
		λ	Δ^2	λ	Δ^2	λ	Δ^2	λ	Δ^2	Misclassification error	Trace statistic
CO ₂ , DFB	all	0.80252	0.64404	0.67699	0.45832	0.57172	0.32687	0.37134	0.1379	44.79%	0.0001
CO ₂	all	0.7388	0.54583	0.47541	0.22601	-	-	-	-	33.21%	0.0001
DFB	all	0.79805	0.63689	0.49443	0.24446	-	-	-	-	32.82%	0.0001
CO ₂ , DFB	D0-3	0.70833	0.50174	0.58473	0.34191	0.44556	0.19852	-	-	62.16%	0.3833
	D4-11	0.79775	0.63641	0.5519	0.30459	0.49446	0.24449	-	-	48.28%	0.0001
CO ₂	D12-22*	0.93868	0.88113	0.85195	0.72582	0.55893	0.3124	-	-	21.05%	0.0001
	D0-3 ^a	0.52658 ^d	0.27729 ^d	0.38368 ^e	0.14721 ^e	-	-	-	-	48.78%	0.386
	D4-11 ^a	0.96026 ^d	0.92209 ^d	0.57238 ^e	0.32762 ^e	-	-	-	-	22.11%	0.0001
	D12-22 ^a	0.95182 ^d	0.90597 ^d	0.8782 ^e	0.77124 ^e	-	-	-	-	0.81%	0.0001
	D12-22 ^b	0.92515	0.85591	-	-	-	-	-	-	0.88%	0.0001
DFB	D0-3 ^c	0.35379 ^d	0.12517 ^d	0.16278 ^e	0.0265 ^e	-	-	-	-	58.54%	0.4171
	D4-11 ^c	0.62335 ^d	0.38857 ^d	0.53432 ^e	0.2855 ^e	-	-	-	-	44.21%	0.0001
	D12-22 ^c	0.91655 ^d	0.84006 ^d	0.66763 ^e	0.44573 ^e	-	-	-	-	21.95%	0.0001
	D12-22 ^b	0.6492	0.42146	-	-	-	-	-	-	25.44%	0.0001
low CO ₂ & DFB+/-, high CO ₂	D0-3	0.54954	0.302	0.28881	0.08341	-	-	-	-	51.35%	0.4739
	D4-11	0.71103	0.50556	0.39089	0.1528	-	-	-	-	36.78%	0.0001
	D12-22*	0.91946	0.84541	0.84567	0.71515	-	-	-	-	3.51%	0.0001
low CO ₂ /DFB- (M1+2)	all*	0.9763	0.95317	0.87901	0.77266	-	-	-	-	4.44%	0.0001
low CO ₂ /DFB+ (M4-6)	all	0.89965	0.80936	0.813	0.66097	-	-	-	-	7.58%	0.0001

* Treatments are significantly separated based on metabolic profiles.

^a CAP support values of CO₂ treatments including the fjord water as used for visualization in Figure 3.7D-F. The 2nd axis separates CO₂ treatments.

^b CAP support values of CO₂ or DFB addition treatments excluding the fjord water (1-dimensional analysis) used for identification.

^c CAP support values of DFB addition treatments including the fjord water as used for visualization in Figure 3.7G-I. The 2nd axis separates DFB+/-.

^d CAP support values of the axis separating the treatments from the fjord water.

^e CAP support values of the axis actually contributing more to the separation of the treatments from each other.

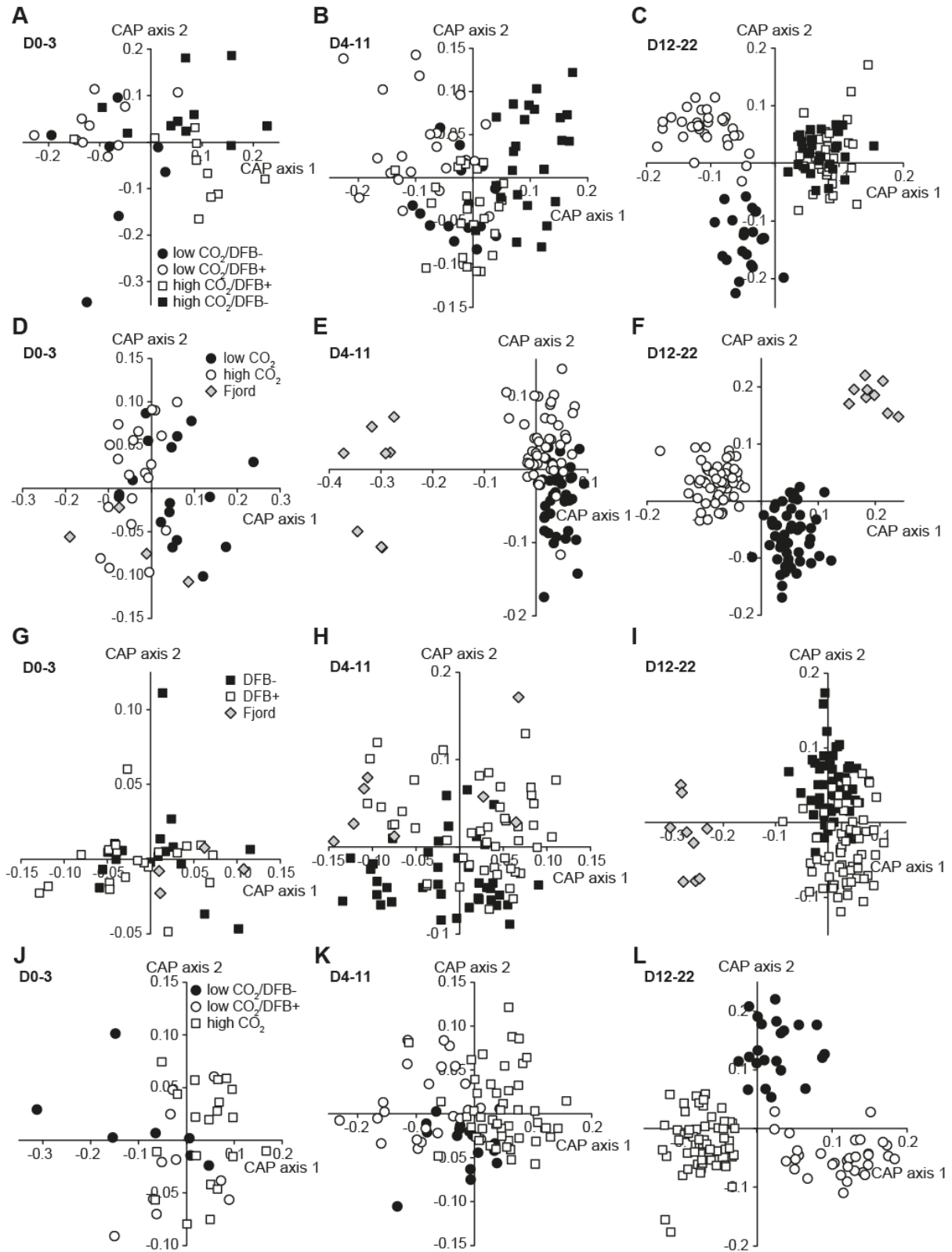


Figure 3.7: Multivariate separation of different treatments in mesocosms by canonical analysis of principal coordinates (CAP) displayed at different time intervals. Separation of all four applied treatments (A) at the beginning (day 0-3), (B) in the middle (day 4-11), and (C) at the end (day 12-22) of the mesocosm experiment. Separation of low and high CO₂ treatments (D) at the beginning (D0-3), (E) in the middle (D4-11), and (F) at the end (D12-22) of the mesocosm experiment. Separation of treatments with and without desferrioxamine B (DFB) addition (G) at the beginning (D0-3), (H) in the middle (D4-11), and (I) at the end

(D12-22) of the mesocosm experiment. For better visualization in form of a 2-dimensional plot, analysis of a single parameter (CO_2 or DFB) is displayed as a separation from the fjord water. Separation of low CO_2 /DFB-, low CO_2 /DFB+, and high CO_2 treatment (J) at the beginning (D0-3), (K) in the middle (D4-11), and (L) at the end (D12-22) of the mesocosm experiment. Note the different scaling of x- and y-axis.

We decided to split the data set into subsets (Figure 3.7). Since the fjord water was separated after three days, the first consisted of days 0 to 3 (D0-3). This subset was assumed to reflect metabolic profiles of the initial fjord water community before a separating effect of the applied treatments. A second subset consisted of days 4 to 11 (D4-11) to allow the detection of signals deriving from the first increase and peaking in *E. huxleyi* cell abundance and of other phytoplankton groups as observed in most of the mesocosms (except treatment low CO_2 /DFB+). Further, this time interval lay around the addition of the chelating agent DFB. The third subset included days 12 to 22 (D12-22), when we observed a beginning differentiation of phytoplankton groups based on the different treatments. Thus, we also expected treatment effects to become apparent in the metabolic profiles.

At D0-3 metabolic profiles showed no statistical separation based on the applied treatments ($P = 0.3833$, permutation test) (Figure 3.7A) and accordingly, the axes were not differentiating between them (Table 3.2). Although at D4-11 first differentiating trends became visible (Figure 3.7B), CAP diagnostic values did not support a separation of treatments (Table 3.2). However, at D12–22 low CO_2 treatments with and without addition of DFB were well separated by the first and second CAP axes (eigenvalue 0.94, and 0.85, correlation Δ^2 0.88, and 0.73) (Figure 3.7C). But with 21%, representing 24 out of 114 samples, the misclassification error was rather high, as the third axis failed to separate between the two DFB treatments under elevated CO_2 levels (Table 3.2). In the case of high CO_2 , 20% of the samples grouped within the high CO_2 /DFB+ treatment by the cross validation test originally presented data from the high CO_2 /DFB- treatment. The other way round, nearly 45% of the high CO_2 /DFB+ profiles were misclassified into high CO_2 /DFB-. Thus, the four groups were only partially separated for D12-22.

In a next step we screened metabolic profiles for effects of CO_2 levels or DFB addition using each of these individual parameters as group. As CAP analysis of 2 groups (low/high CO_2 or DFB+/-) results in a one-dimensional output matrix, we

used the fjord water to enable two-dimensional visualization. This allowed a better graphical differentiation between the treatments as a separation might otherwise be hidden due to the large number of plotted data. Since the fjord population possessed clearly different metabolic profiles at later time intervals (Figure 3.6), and therefore was separated by the first CAP axis, the second axis better resolved differences between the treatments. For D12-22 we repeated CAP analysis using only the treatments without the fjord water, but did not visualize them. Correlation coefficients obtained by this analysis were used for identification of highly correlated metabolites (see 3.2.6, and 3.2.8). CAP diagnostic values obtained by this analysis resembled those obtained for the second axis of the previous analysis including the fjord water and are thus not explicitly mentioned below. All CAP support values for these analyses are given in Table 3.2.

At D0-3, metabolic profiles were not statistically separated based on the exposure to low and high CO₂ levels ($P = 0.386$, permutation test) (Figure 3.7D) as reflected in the CAP diagnostic values (Table 3.2). At D4-11 we saw a first separating trend of CO₂ treatments along the second axis (Figure 3.7E), but it was not statistically supported (2nd axis: eigenvalue 0.57, correlation Δ^2 0.34) (Table 3.2). Exposure to low and high CO₂ had a differentiating effect on metabolic profiles during D12-22 (Figure 3.7F), and accordingly the axes separated between groups (eigenvalues 0.95, and 0.88, correlation Δ^2 0.91, and 0.77) (Table 3.2). Cross validation further resulted in a misclassification error of 0.81%, representing one out of 123 samples, being misclassified (Table 3.2). Hence, during D12-22 metabolic profiles were significantly affected by CO₂ concentrations resulting in a separation of low and high CO₂ treatments.

When we analyzed the metabolic profiles using addition or no addition of DFB (DFB+/-) as groups, samples were located randomly by the CAP during D0-3 (Figure 3.7G) and no statistical support for a differentiation was found ($P = 0.42$, permutation test) (Table 3.2). At D4-11 metabolic profiles also showed no separation based on the DFB treatment (Figure 3.7H), which was reflected in low CAP diagnostic values and a high misclassification error of 44%, resembling 42 out of 95 samples, being misclassified (Table 3.2). Even at D12-22 metabolic profiles were not distinct enough to clearly separate between mesocosms treated with the Fe chelating agent DFB and those without its addition (eigenvalue of the 2nd axis: 0.67)

(Figure 3.7I, Table 3.2). Accordingly, the second axis showed no correlation between the DFB treatments (correlation Δ^2 of the 2nd axis: 0.45) (Table 3.2). Therefore, DFB alone did not exhibit a significant separating effect based on metabolic profiles at any time of the experiment.

Based on the observation that high and low CO₂ treatments could be separated by the CAP during D12-22 (Figure 3.7F) whereas the DFB treatments could not (Figure 3.7I), we assumed that maybe only three parameter combinations actually had an effect on metabolic profiles. This was further supported by the pattern found in the combined analysis of all treatments, which resulted in a differentiation of three instead of four groups (Figure 3.7C). Therefore, we combined metabolic profiles of both DFB treatments (DFB+/-) under elevated CO₂ concentrations and analyzed them in comparison to low CO₂ treatments with and without DFB addition (Figure 3.7J-L). Hence, this analysis combined the treatments: low CO₂/DFB- (control), low CO₂/DFB+, and high CO₂ (consisting of high CO₂/DFB- and high CO₂/DFB+). At D0-3 CAP could not find differences between the three treatment combinations in the metabolic profiles (Figure 3.7J) and accordingly, statistical support ($P = 0.474$, permutation test) and CAP diagnostic values were low (Table 3.2). An initial separating trend in metabolic profiles based on the three treatments became visible at D4-11 (Figure 3.7K), but was not supported by the CAP diagnostic values (Table 3.2). Cross validation resulted in a high misclassification error of 36.8%, representing 32 out of 87 samples, being misclassified (Table 3.2). However, at D12-22 metabolic profiles were resolved well in relation to the treatments (Figure 3.7L) and accordingly, axes differentiated between groups (eigenvalues 0.92, and 0.85, correlation Δ^2 0.85, and 0.72). Further, with 3.5%, representing 4 out of 114 samples, being misclassified the misclassification error was low (Table 3.2). This finding supported our assumption that only three treatments, low CO₂ with and without DFB addition (low CO₂/DFB- and low CO₂/DFB+), and high CO₂ were effectively differentiating metabolic profiles.

3.2.5 Metabolic profiling of specific treatments at different time intervals

In addition to the investigation of treatment effects on metabolism we analyzed changes of metabolic profiles over time within the low CO₂ treatments (Figure 3.8). These were selected as the control (low CO₂/DFB-) best reflected a natural community and the low CO₂/DFB+ treatment led to the strongest induction in the *E. huxleyi* bloom development, comparable to that observed under laboratory conditions. We selected the same time intervals as for the analyses of treatment effects (D0-3, D4-11, and D12-22) and used them as groups, although the low CO₂/DFB+ treatment showed a slightly different growth pattern.

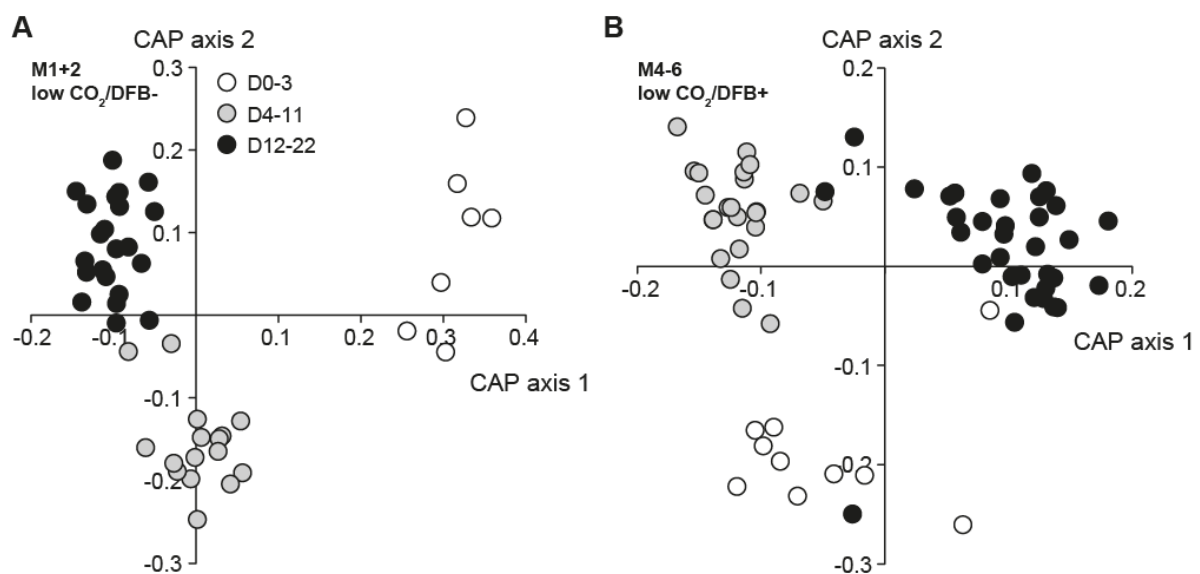


Figure 3.8: Multivariate separation of specific treatments by canonical analysis of principal coordinates (CAP) at different time intervals. Separation of metabolic profiles of (A) the control (low CO₂/DFB-), and (B) the low CO₂/DFB+ treatment by CAP over time using days 0 to 3 (D0-3), 4 to 11 (D4-11), and 12 to 22 (D12-22) as groups. Note the different scaling of x- and y-axis. Abbreviations: DFB, desferrioxamine B, M, mesocosm.

The three assigned time intervals were well separated based on their metabolic profiles in the control (Figure 3.8A), which was reflected in a high correlation especially with the first axis (eigenvalues 0.98, and 0.88, correlation Δ^2 0.95, and 0.77) and a low misclassification error of 4.44%, representing two out of 45 samples, being misclassified (Table 3.2). Metabolic profiles in the low CO₂/DFB+ treatment were resolved based on the three time intervals (Figure 3.8B) and the differentiation supported by CAP diagnostic values (eigenvalues 0.90, and 0.81, correlation Δ^2 0.81, and 0.66) (Table 3.2). Cross validation resulted in a

misclassification error of 7.6%, representing five out of 66 samples, being misclassified (Table 3.2).

From these two analyses we selected the control (low CO₂/DFB-, mesocosms 1 and 2) for further metabolite identification. Reasons for its selection were the slightly better support values (Table 3.2) concerning the significance of separation in both correlated axes and the lower misclassification error. Further, the control better reflected the general growth pattern within most of the mesocosm enclosures and we were more interested in the (semi-)natural, non-manipulated *E. huxleyi* bloom situation. We assumed the latter to be better reflected in the control than one of the treatments.

For identification of metabolites highly correlated with specific treatments during the latest phase (D12-22), we selected the combination of three treatments (low CO₂/DFB-, low CO₂/DFB+, and high CO₂) as well as the low and high CO₂ treatments. Additionally, as mentioned above, we identified metabolites that showed a high correlation to the specified time intervals in the control (low CO₂/DFB-).

3.2.6 General affiliation of metabolic classes to specific treatments

In general, out of the 333 signals that remained in the analysis 193 showed a high correlation to the combination of three treatments during D12-22 (Table 3.3). 67 peaks (~34.7%) were solely correlated with the combination of the three treatments, whereas most were also highly correlated with CO₂. Out of the 128 metabolites significantly related to this parameter only two (phytol, metabolite 242, and an unidentified saccharide, met. 265) were not found among those correlated with the combination of three treatments (Table 3.4). 75 metabolites (~38.9%) correlated with the combination of three treatments could be identified and 47 (~24.3%) were assigned to a metabolic class. Another 71 metabolites (~36.8%) remained unknown. Saccharides (26 signals) and their derivatives (5 complex saccharides, 7 sugar acids, and 13 sugar alcohols) constituted the most abundant metabolic class, but we also detected a high number of fatty acids (17 signals) and sterols (12 signals) (Table 3.3). In the low and high CO₂ treatments we could identify 48 (~37.5%) of the highly correlated metabolites. 34 (~26.6%) signals were successfully assigned to a metabolic class, whereas another 46 peaks (~35.9%)

remained unidentified. Saccharides (20 signals) and related compounds (3 complex sugars, 7 sugar acids, and 7 sugar alcohols) also dominated in the CO₂ treatments, but here carboxylic acids constituted a second abundant group (9 peaks), whereas we only observed 6 fatty acids and 7 sterols (Table 3.3).

In the control mesocosms (low CO₂/DFB-) we found 154 metabolites to be highly correlated with the assigned time intervals. Tentative identification was possible for 56 metabolites (~36.4%) and affiliation to a specific metabolic class could be determined for 49 signals. Another 49 metabolites (~31.8%) remained unidentified. Again carbohydrates (28 saccharides, 5 complex saccharides, 5 sugar acids, and 12 sugar alcohols) constituted the most abundant metabolic class. Additionally, we found a high number of sterols (13 peaks) and different amines (11 signals) (Table 3.3).

Table 3.3: Numbers of detected metabolites important for separation of the different parameters, in different metabolic classes. The list presents the numbers of metabolites detected belonging to different common metabolic classes. Data for three different parameter combinations that received further attention during data analysis (see text for details) are presented and correspond to identified metabolites presented in Tables 3.4, and 3.5. "Others" comprises metabolites that could not be assigned into one of the common groups.

Metabolic class	Parameter		
	low CO ₂ & DFB+/-, high CO ₂	CO ₂	control (low CO ₂ /DFB-)
Amine	5	4	11
Amino acid	7	7	8
Carboxylic acid	12	9	8
Fatty acid	17	6	9
Alcohol	3	2	1
Saccharide	26	20	28
Sugar acid	7	7	5
Sugar alcohol	13	7	12
complex Saccharide	5	3	5
Hydrocarbon	4	2	0
Sterol	12	7	13
Terpene	1	2	1
Others	10	6	4
Unknown	71	46	49
Total	193	128	154

Abbreviation: DFB, desferrioxamine B.

The relation of a metabolite with a specific treatment was determined by visualizing the correlation coefficients as vectors (see 6.4.5). These vectors point in the direction of the treatment the metabolite shows the highest correlation with (Figures 3.9, 3.10, and 3.11).

3.2.7 Combination of low CO₂/DFB-, low CO₂/DFB+, and high CO₂

As presented above, a combination of the three treatments low CO₂/DFB-, low CO₂/DFB+, and high CO₂ best represented the differentiation pattern in the metabolic profiles during the last 11 days of the mesocosm experiment (Figure 3.7C, L). A list of all identified metabolites correlated with this treatment combination is presented in Table 3.4. In general the highest number of metabolites showed an affiliation with the low CO₂/DFB+ treatment. This was especially pronounced among many unidentified compounds which exhibited highest concentrations in this treatment (Figure 3.9A, Appendix Table 3). Saccharides and other carbohydrates displayed an interesting pattern as many were highly correlated with the low CO₂/DFB+ treatment or had vectors pointing between low CO₂/DFB- and high CO₂ (Figure 3.9B). Among saccharides significantly correlated with low CO₂/DFB+ were for example xylose (met. 148), ribose (met. 153), fructose (met. 189, and 190), galactose (met. 193), glucose (met. 194, and 199), and 1-methyl- α -D-glucopyranoside (met. 237) as well as three out of five complex saccharides (lactose, met. 294, and two unidentified disaccharides, met. 298, and 302). The vectors of trehalose (met. 296) and another unidentified disaccharide (met. 289) pointed between low CO₂/DFB- and high CO₂ (Figure 3.9B). The sugar acids glyceric acid, threonic acid, lyxonic acid, and ribonic acid (met. 78, 128, 169, and 173) exhibited highest concentrations in the low CO₂/DFB+ treatment, whereas a hexonic acid (met. 208) was correlated with high CO₂ (Figure 3.9B). *Myo*-inositol (met. 228) and its isomers (met. 205, and 219) also were affiliated to the high CO₂ treatment. In contrast, only two complex sugar alcohols, galactinol and an unidentified one (met. 305, and 309), showed highest concentrations in the low CO₂/DFB+ treatment. All other sugar alcohols such as sorbitol, galactitol, and viburnitol (met. 202, 203, and 204) had vectors pointing between low CO₂/DFB- and high CO₂ (Figure 3.9B).

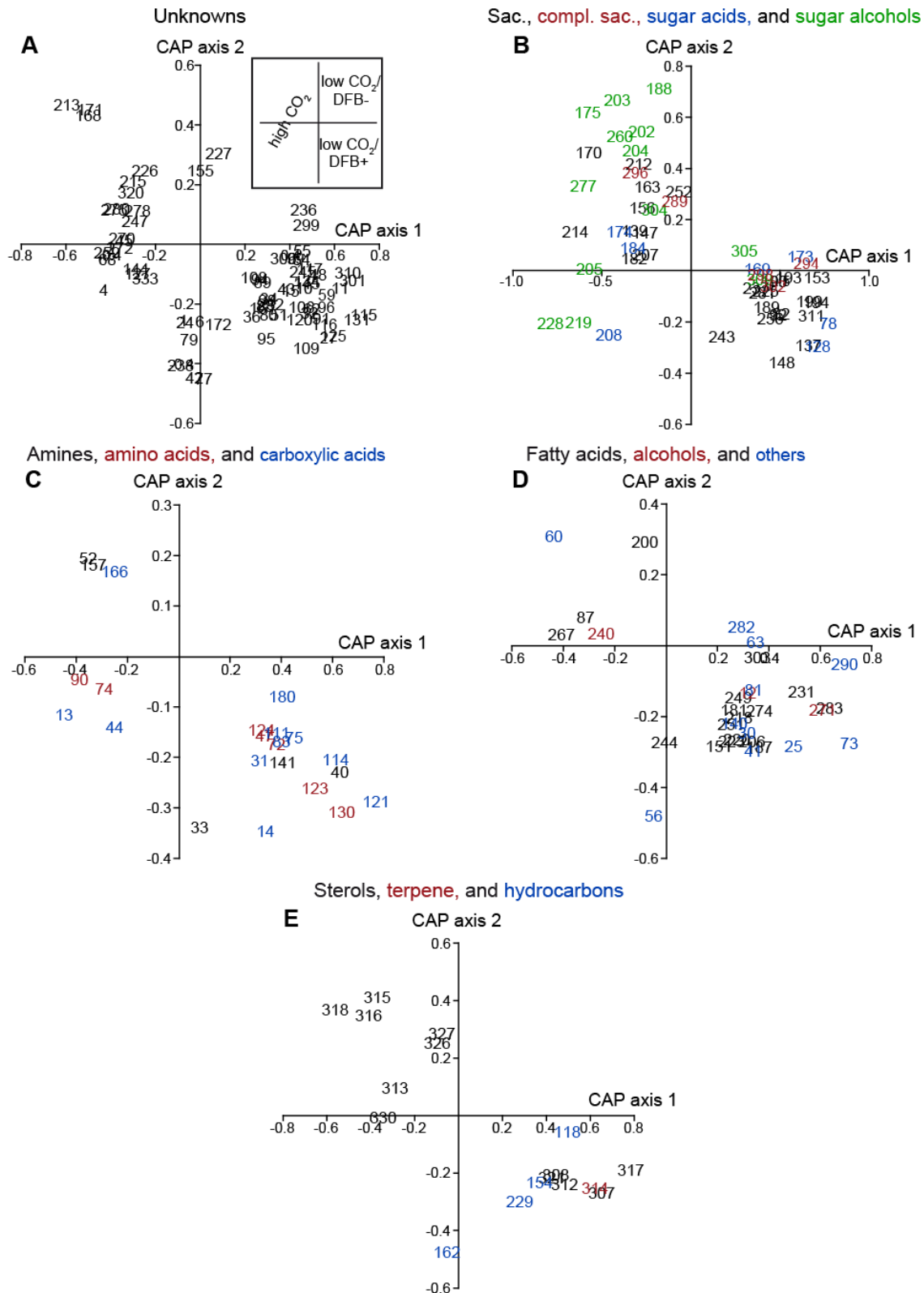


Figure 3.9: Vector plots of metabolites significantly correlated with the combination of low CO_2 /DFB-, low CO_2 /DFB+, and high CO_2 . Vector plots of metabolites significantly correlated with the treatment combination low CO_2 /DFB-, low CO_2 /DFB+, and high CO_2 during days 12 to 22 of the mesocosm experiment assigned to metabolic classes. (A) Unknown metabolites, (B) saccharides and other carbohydrates, (C) amines and small acids, (D) fatty acids, alcohols and metabolites that could not be assigned into one of the other general groups (others), and (E) sterols, a terpene, and hydrocarbons. For better

visualization only the tips of the vectors are presented as indicated by numbers. The insert presents the positioning of the different parameters based on metabolic profiles. Metabolites with positive x- and y-axes values correlate with low CO₂/DFB-, those with a positive x-axis and negative y-axis value correlate with low CO₂/DFB+, and those with a negative x-axis value correlate with the high CO₂ treatment (compare Figure 3.7L). Numbers correspond to metabolites in Table 3.4, and Appendix Table 3. Note the different scaling of x- and y-axis. Abbreviations: compl., complex, DFB, desferrioxamine B, Sac., saccharide.

An amine with the sum formula C₁₀H₁₇NO (met. 33) and two other putative amines (met. 40, and 141) showed highest concentrations in the low CO₂/DFB+ treatment (Figure 3.9C). In contrast, the vectors of ethanolamine (met. 52), and a putative unidentified amine (met. 157) pointed between low CO₂/DFB- and high CO₂. Except for glycine and its derivative (met. 74, and 90), which showed a significant correlation to high CO₂, amino acids exhibited highest concentrations in the low CO₂/DFB+ treatment (Figure 3.9C). These include valine, threonine, N-acetylglutamic acid, phenylalanine, and putative hydroxy-proline (met. 47, 72, 124, 130, and 123). Interestingly, all four detected substrates of the tricarboxylic acid (TCA) cycle, succinic acid, fumaric acid, malic acid, and citric acid (met. 75, 83, 114, and 180), correlated with the low CO₂/DFB+ treatment (Figure 3.9C). Further, 2-hydroxypropanoic acid (met. 14) and three unidentified carboxylic acids (met. 31, 111, and 121) showed the same correlation pattern. Hydroxybutenoic acid (met. 44) and another unidentified carboxylic acid (met. 13) exhibited highest concentrations under high CO₂, whereas the vector of a benzoic acid derivative (met. 166) pointed between this and the low CO₂/DFB- treatment (Figure 3.9C).

As it was the case for carbohydrates, most of the fatty acids displayed a significant correlation to the low CO₂/DFB+ treatment (Figure 3.9D). These were dodecanoic acid, methyl-tridecanoic acid, tetradecanoic acid, pentadecanoic acid, methyl-pentadecanoic acid, hexadecenoic acid, hexadecanoic acid, octadecenoic acid, octadecanoic acid, docosahexaenoic acid (DHA), and putative 1-monooctadecadienoylglycerol (met. 151, 181, 187, 206, 218, 220, 249, 251, 274, and 303) as well as two unidentified, unsaturated fatty acids (met. 231, and 283). An octadecanoic acid derivative (met. 267) showed highest concentrations under high CO₂, whereas methyl-tetradecanoic acid (met. 200) had a vector pointing between this treatment and low CO₂/DFB- (Figure 3.9D).

Propane-1,3-diol and a long chained alcohol (met. 12, and 271) correlated with the low CO₂/DFB+ treatment, whereas putative 1-octadecanol (met. 240) exhibited highest concentrations under high CO₂ (Figure 3.9D). We detected several substrates that could not be assigned to one of the specific metabolic classes. Most of them, as for example glycerol, nicotinic or picolinic acid, lumichrome, trishydroxybenzene, and putative uridine and adenosine (met. 63, 73, 81, 140, 282, and 290) were significantly correlated with the low CO₂/DFB+ treatment (Figure 3.9D). Diethylenglycol (met. 56) had a vector pointing between the low CO₂/DFB+ and high CO₂, whereas the vector of a malonic acid amide was directed between high CO₂ and the low CO₂/DFB- treatment (Figure 3.9D).

Sterols displayed differing patterns. 22E-26,27-dinorergosta-5,22-dien-3 β -ol, epibrassicasterol, stigmasterol (met. 308, 317, and 321), and two unidentified sterols (met. 307, and 312) were correlated with the low CO₂/DFB+ treatment, whereas a sterol with the sum formula C₂₉H₅₄O (met. 330) exhibited its highest concentration under high CO₂. Furthermore, cholesterol, (3 β ,5 α)-cholestan-3-ol, beta-sitosterol, fucosterol, and an unidentified sterol (met. 315, 316, 321, 326, and 318) had vectors pointing between high CO₂ and low CO₂/DFB- (Figure 3.9E). The phenolic terpene alpha-tocopherol (met. 314), and three of the unsaturated hydrocarbons (met. 118, 154, and 229) showed a correlation to the low CO₂/DFB+ treatment, whereas another unsaturated hydrocarbon (met. 162) had a vector pointing between this treatment and high CO₂ (Figure 3.9E).

Table 3.4: Heat map of normalized intensities of identified metabolites correlated with the treatment combination low CO₂/DFB-, low CO₂/DFB+, and high CO₂ or the single parameter CO₂. Metabolites are organized according to their affiliation to one of the three parameters (separated by black lines) and sorted by classes. “#” indicates the correlation of a metabolite solely with the treatment combination low CO₂/DFB-, low CO₂/DFB+, and high CO₂, and “†” indicates the correlation of a metabolite with the parameter CO₂ in the corresponding analyses of metabolic profiles from days 12 to 22 of the mesocosm experiment.

[illegible]

Table 3.4 (continued)[illegible]

Table 3.4 (continued)[illegible]

Table 3.4 (continued)[illegible]

Table 3.4 (continued)

No.	RT	Metabolite	Class	CO2-/DFB-										CO2-/DFB+										CO2+												
				D12	D13	D14	D15	D16	D17	D18	D19	D20	D21	D22	D12	D13	D14	D15	D16	D17	D18	D19	D20	D21	D22	D12	D13	D14	D15	D16	D17	D18	D19	D20	D21	D22
182	13.17	Hexofuranose	S																																	
207	14.05	Monosaccharide ? #	S																																	
214	14.33	Hexofuranose ?	S																																	
265	16.61	Saccharide ? †	S																																	
174	12.81	Sugar acid ?	SA																																	
184	13.25	Pentonic acid ?	SA																																	
208	14.09	Hexonic acid	SA																																	
205	14.01	Inositol isomer	SAc																																	
219	14.48	Inositol isomer	SAc																																	
228	14.90	myo-Inositol*	SAc																																	
277	17.19	Sugar alcohol ?	SAc																																	
330	24.48	Sterol (C ₂₉ H ₅₄ O)	ST																																	

Blue – low metabolite concentration, yellow – high metabolite concentration. If marked by “*”, identification was confirmed by a standard. Metabolites tagged with a “?” had a reverse match of 700 - 800 or, if marked by “??”, of 600 - 700. Abbreviations: A, amine, AA, amino acid, Alc, alcohol, CA, carboxylic acid, CS, complex saccharide, D, day, DFB, desferrioxamine B, FA, fatty acid, HC, hydrocarbon, No., number, O, other, RT, retention time, S, saccharide, SA, sugar acid, SAc, sugar alcohol, ST, sterol, T, terpene, U, unknown.

3.2.8 Low and high CO₂

In general, reducing the parameters to CO₂ (Figure 3.10A) led to similar correlation patterns as observed in the combination of low CO₂/DFB-, low CO₂/DFB+, and high CO₂, with more metabolites showing a high correlation to low CO₂ (Figure 3.10). Further, metabolites that had vectors pointing towards low CO₂/DFB+ in the previous analysis were now correlated with low CO₂ and those with vectors in the direction of high CO₂ were again found to separate for this treatment. Only phytol (met. 242), correlated with high CO₂, and an unidentified saccharide (met. 265), correlated with low CO₂, were not previously discriminating for the combination of low CO₂/DFB-, low CO₂/DFB+, and high CO₂ (Table 3.4, Appendix Table 3).

As in the treatment combination described above, most among the unidentified metabolites exhibited highest concentrations in the low CO₂ treatment (Figure 3.10B, and Appendix Table 3). Most small saccharides such as xylose (met. 148), ribose (met. 153), fructose (met. 189, and 190) or glucose (met. 194, and 199) as well as digalactosylglycerol (met. 311) were significantly correlated with low CO₂, whereas some unidentified penta- and putative hexafuranoses (met. 170, 182, and 214) exhibited higher concentrations under high CO₂ (Figure 3.10C). All three detected complex saccharides, lactose and two unidentified disaccharides (met. 294, 298, and 302), had vectors pointing in the direction of low CO₂. Glyceric acid, threonic acid, lyxonic acid, and ribonic acid (met. 78, 128, 169, and 173) were affiliated with the low CO₂ treatment and another pentonic acid, a hexonic acid, and an unidentified sugar acid (met. 184, 208, and 174) correlated with high CO₂. Among sugar alcohols only *myo*-inositol (met. 228) and its isomers (met. 205, and 219) exhibited highest concentrations under high CO₂, whereas galactinol (met. 305) and three unidentified sugar alcohols (met. 175, 277, and 309) separated for low CO₂ (Figure 3.10C).

Ethanolamine and an unidentified amine (met. 52, and 157), whose vectors had pointed between low CO₂/DFB- and high CO₂ now showed a clear correlation with high CO₂ as did the amino acid glycine and its derivative (met. 74, and 90) (Figure 3.10D). The other detected amino acids, valine, threonine, N-acetylglutamic acid, phenylalanine, and putative hydroxy-proline (met. 47, 72, 124, 130, and 123) separated for low CO₂. The same pattern was also observed for the four detected TCA cycle substrates succinic acid, fumaric acid, malic acid, and citric acid (met. 75,

83, 114, and 180). Carboxylic acids found in higher concentrations under high CO₂ were hydroxybutenoic acid and an unidentified one (met. 44, and 13) (Figure 3.10D).

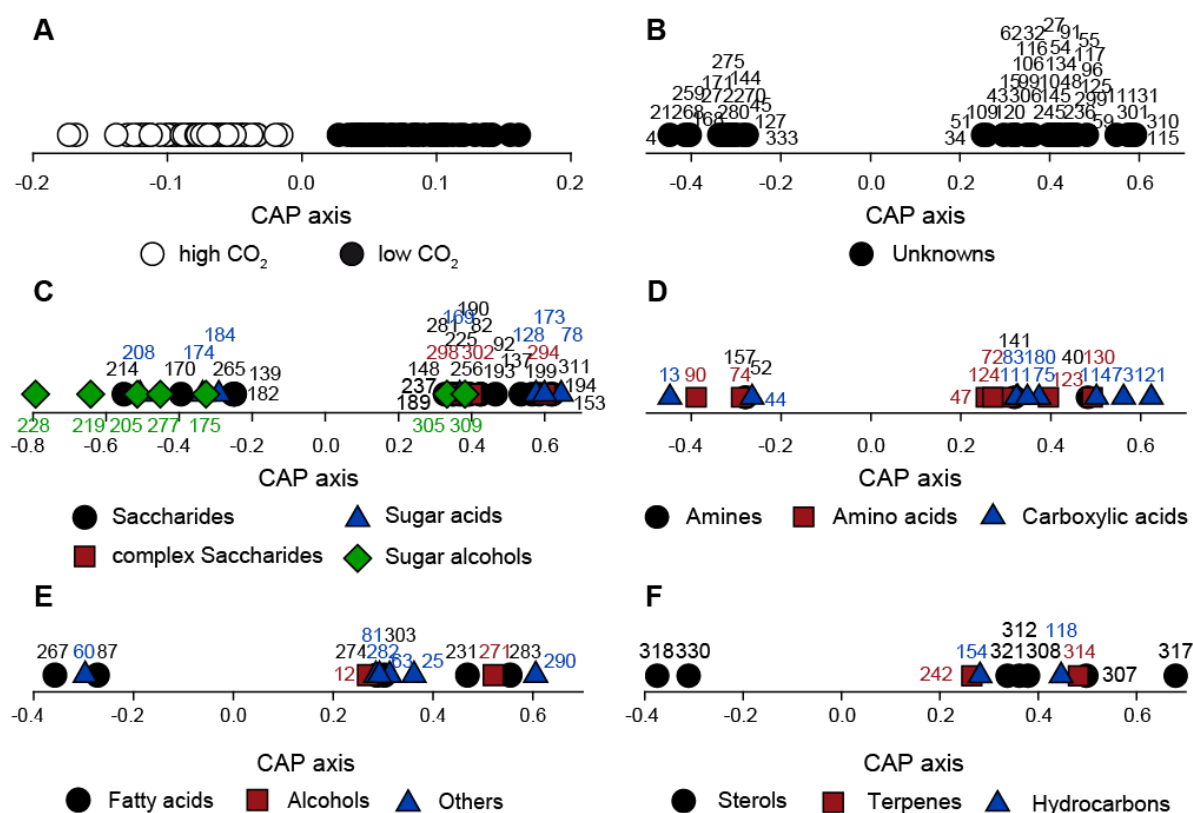


Figure 3.10: Vector plots of metabolites significantly correlated with low or high CO₂. Vector plots of metabolites significantly correlated with the parameter CO₂ during days 12 to 22 (D12-22) of the mesocosm experiment assigned to metabolic classes. (A) Separation of low and high CO₂ treatments on D12-22 by canonical analysis of principal coordinates (CAP) (compare Figure 3.7F, and Table 3.2). (B) Unknown metabolites, (C) saccharides and other carbohydrates, (D) amines and small acids, (E) fatty acids, alcohols and metabolites that could not be assigned into one of the other general groups (others), and (F) sterols, terpenes, and hydrocarbons. For better visualization only the tips of the vectors are presented as indicated by symbols. Metabolites with a positive x-axis value correlate with low CO₂, those with a negative x-axis value correlate with high CO₂ as indicated in (A). Numbers correspond to metabolites in Table 3.4, and Appendix Table 3. Note the different scaling of x- and y-axis.

Whereas many fatty acids were discriminating for the combination of three treatments, only DHA, 1-monooctadecadienoylglycerol, and two unidentified unsaturated fatty acids (met. 274, 303, 231, and 283) were significantly correlated with low CO₂. Further, an octadecanoic acid derivative, and an unidentified fatty acid (met. 267, and 87) correlated with high CO₂ (Figure 3.10E). Both alcohols, propane-1,3-diol and an unidentified long-chained one (met. 2, and 271), exhibited highest concentrations under low CO₂ (Figure 3.10E). Other metabolites correlated

with this treatment were a pyrazine or hydroquinone derivative, glycerol, lumichrome, and putative uridine and adenosine (met. 25, 63, 81, 282, and 290), whereas a malonic acid amide had a vector pointing towards high CO₂ (Figure 3.10E).

Among sterols we found 22E-26,27-dinorergosta-5,22-dien-3 β -ol, epibrassicasterol, stigmasterol (met. 308, 317, and 321), and two unidentified sterols (met. 307, and 312) previously correlated with the low CO₂/DFB+ treatment separating for low CO₂ (Figure 3.10F). Correlated with high CO₂ were a sterol with the sum formula C₂₉H₅₄O, and an unidentified one (met. 330, and 318). Phytol and the phenolic terpene alpha-tocopherol (met. 242, and 314) had vectors pointing towards low CO₂ as did two unsaturated hydrocarbons (met. 118, and 154) (Figure 3.10F).

3.2.9 Dynamic changes in metabolic profiles in the control (low CO₂/DFB-) over time

When we analyzed one specific treatment (the control) and assigned several time intervals resembling different phases during the experiment as groups (days 0-3, 4-11, and 12-22), we observed a complex distribution of metabolites among the specified time phases (Figure 3.11, Table 3.5). Many metabolites could not be identified, most of them correlating with D4-11 (Figure 3.11A, Appendix Table 4).

Saccharides exhibited a complex pattern with several showing a correlation to D0-3 (Figure 3.11B). Among them were xylose (met. 148), three pentafuranoses (met. 135, 136, and 143), 2-O-glycerol- α -d-galactopyranoside (met. 256), digalactosylglycerol (met. 311), and three unidentified saccharides (met. 92, 137, and 243) as well as the complex saccharides maltose (met. 295), a di- and a trisaccharide (297, and 302). Furthermore, threonic acid and a hexonic acid (met. 128, and 208) were affiliated with D0-3. A pentafuranose, a hexofuranose, and a hexose (met. 147, 182, and 212) as well as two unidentified saccharides (met. 276, and 293) exhibited highest concentrations on D4-11 as did ribonic acid (met. 173) (Figure 3.11B). In contrast, the vector of lyxonic acid (met. 169) pointed between D0-3 and D4-11, but no sugar acid showed a correlation to D12-22. During these days other saccharides such as ribose (met. 153), fructose (met. 189, and 190), galactosylglycerol (met. 252), a putative hexofuranose (met. 214), and two unidentified

monosaccharides (met. 104, and 139) together with the complex saccharides trehalose (met. 296), and a disaccharide (met. 302) exhibited highest concentrations. While sorbitol and an unidentified sugar alcohol (met. 260) separated between D4-11 and D12-22, most other sugar alcohols, among them mannitol, viburnitol, *myo*-inositol and one of its isomers (met. 201, 204, 228, and 205), were affiliated with D12-22. In contrast, galactose (met. 193), and glucose (met. 194, and 199) had vectors pointing between D0-3 and D12-22 (Figure 3.11B).

We observed a relatively large number of amines, most of which showed a significant correlation to D4-11 as for example ethanolamine, cadaverine and putrescine (met. 52, 101, and 167) (Figure 3.11C). Hydroxylamine, $C_{10}H_{17}NO$, and an unidentified amine (met. 26, 33, and 40) were affiliated to D12-22. The amino acids alanine, valine, isoleucine, glycine, threonine, beta-alanine, N-acetylglutamic acid, and phenylalanine (met. 22, 47, 71, 74, 93, 105, 124, and 130) exhibited highest concentrations during D4-11 (Figure 3.11C). Further, hydroxybutenoic acid and malic acid (met. 44, and 114) were highly correlated with this time phase, whereas fumaric acid (met. 83), pyrrole-2-carboxylic acid in two different silylation stages (met. 66, and 84), and two unidentified carboxylic acids (met. 13, and 121) had vectors pointing towards D0-3, and an unidentified carboxylic acid was correlated with D12-22 (Figure 3.11C).

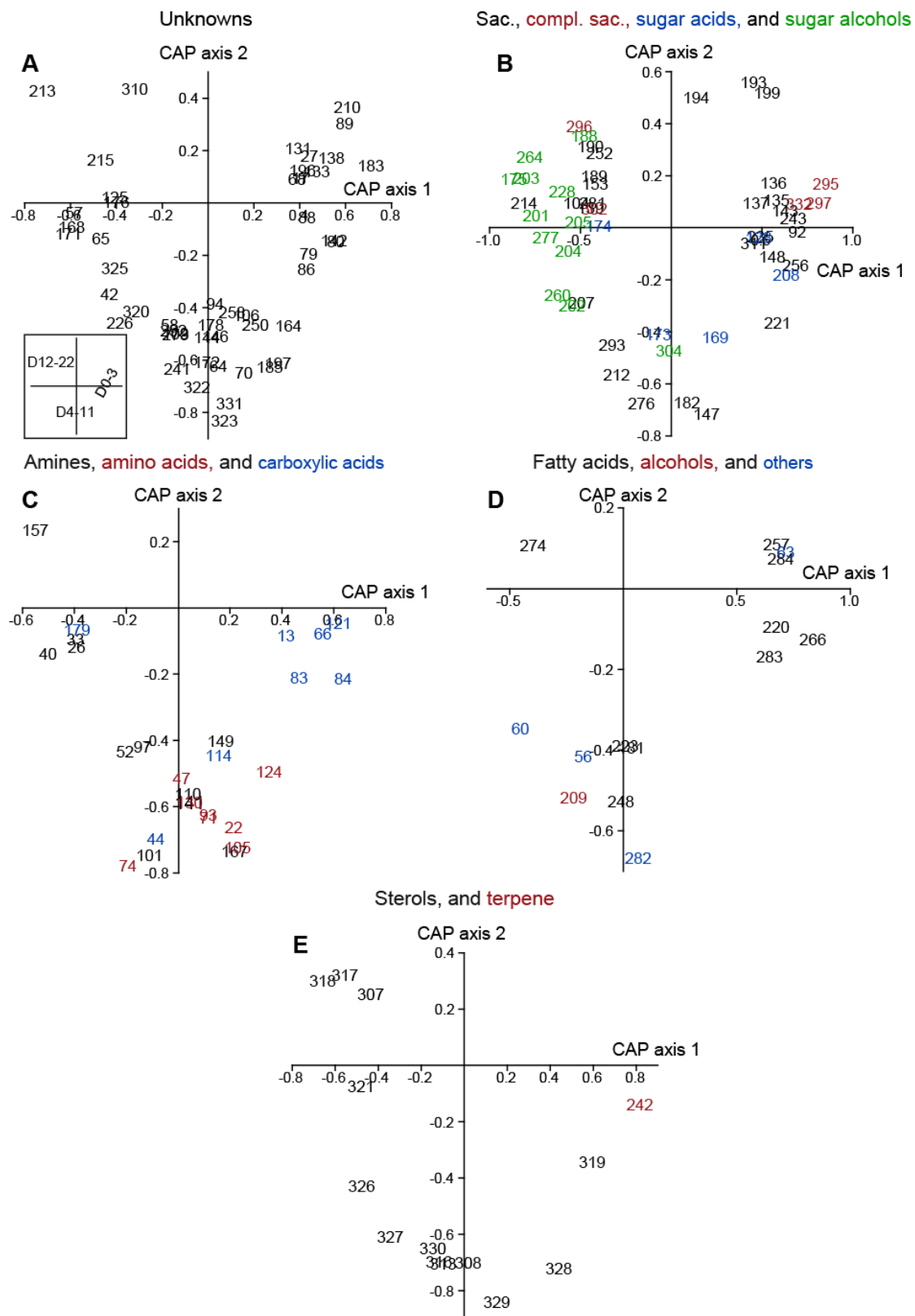


Figure 3.11: Vector plots of metabolites significantly correlated with different time intervals in the control. Vector plots of metabolites significantly correlated with the beginning (D0-3), the middle (D4-11), and the end of the experiment (D12-22). (A) Unknown metabolites, (B) saccharides and other carbohydrates, (C) amines and small acids, (D) fatty acids, alcohols and metabolites that could not be assigned into one of the other general groups (others), and (E) sterols and a terpene. For better visualization only the tips of the

vectors are presented as indicated by numbers. The insert presents the positioning of the different parameters. Metabolites with positive x-axis value correlate with D0-3, those with a negative y-axis value correlate with D4-11, and those with negative x- and positive y-axes values correlate with D12-22 (compare Figure 3.8A). Numbers correspond to metabolites in Table 3.5, and Appendix Table 4. Note the different scaling of x- and y-axis. Abbreviations: compl., complex, Sac., saccharide.

Fatty acids did not show a specific correlation pattern (Figure 3.11D). Hexadecenoic acid, arachidonic acid, 1-monohexadecanoylglycerol (met. 220, 266, and 284), and two unidentified unsaturated fatty acids (met. 257, and 283) exhibited highest concentrations during D0-3. In contrast, methyl-tridecanoic acid, hexadecanoic acid, and an unidentified unsaturated fatty acid (met. 181, 223, and 248) were affiliated to D4-11 and the vector of DHA (met. 274) pointed towards D12-22. The alcohol hexadecan-1-ol (met. 209) showed a significant correlation to D4-11 (Figure 3.11D). Further, we found the vector of glycerol (met. 63) pointing in the direction of D0-3, and those of diethylenglycol, a malonic acid amide and uridine (met. 56, 60, and 282) towards D4-11 (Figure 3.11D).

Sterols either correlated with D4-11 or D12-22 (Figure 3.11E). The sterols 22*E*-26,27-dinorergosta-5,22-dien-3 β -ol, (3 β ,5 α)-cholestan-3-ol, fucosterol, beta-sitosterol, C₂₉H₅₂O, C₂₉H₅₄O (met. 308, 316, 326, 327, 328, and 330), and three unidentified ones (met. 313, 319, and 329) exhibited highest concentrations during D4-11. In contrast, epibrassicasterol, and two unidentified sterols (met. 317, 307, and 318) separated for D12-22. The vector of stigmasterol (met. 321) pointed between D4-11 and D12-22, and thus was positioned apart from the other three sterols correlated with D12-22, although its concentration was highest during this time interval (Table 3.5). The oxo-terpene phytol was significantly correlated with D0-3 (Figure 3.11E).

Table 3.5: Heat map of normalized intensities of identified metabolites correlated with metabolic profiles of the control over time. Metabolites are organized according to their affiliation to one of the three time phases (separated by black lines) and sorted by classes.

[illegible]

Table 3.5 (continued)[illegible]

Table 3.5 (continued)

No.	RT	Metabolite	Class	Day 0-3				Day 4-11								Day 12-22									
				D0	D1	D2	D3	D4	D5	D6	D7	D8	D9	D10	D11	D12	D13	D14	D15	D16	D17	D18	D19	D20	D21
260	16.33	Sugar alcohol ?	SAC																						
304	19.55	Sugar alcohol ?	SAC																						
308	20.13	22E-26,27-Dinorergosta-5,22-dien-3β-ol	ST																						
313	21.18	Sterol, Isomer of RT 21.04	ST																						
316	21.66	(3β,5α)-Cholestan-3-ol	ST																						
326	23.49	Fucosterol	ST																						
327	23.51	beta-Sitosterol*	ST																						
328	23.70	Sterol (C ₂₉ H ₅₂ O)	ST																						
329	23.95	Sterol ??	ST																						
330	24.48	Sterol (C ₂₉ H ₅₄ O)	ST																						
26	7.10	Hydroxylamine	A																						
33	7.46	C ₁₀ H ₁₇ NO	A																						
157	12.16	Amine ?	A																						
179	13.03	Carboxylic acid	CA																						
274	17.11	Docosahexaenoic acid	FA																						
104	10.02	Monosaccharide	S																						
139	11.44	Monosaccharide ?	S																						
153	12.00	Ribose*	S																						
189	13.41	Fructose*	S																						
190	13.47	Fructose*	S																						
214	14.33	Hexofuranose ?	S																						
252	15.96	Galactosylglycerol	S																						
281	17.44	Saccharide	S																						
174	12.81	Sugar acid ?	SA																						
175	12.89	Sugar alcohol	SAC																						
188	13.38	Sugar alcohol	SAC																						
201	13.83	Mannitol*	SAC																						
203	13.91	Galactitol	SAC																						
204	13.94	Viburnitol	SAC																						
205	14.01	Inositol isomer	SAC																						
228	14.90	myo-Inositol*	SAC																						
264	16.56	Sugar alcohol	SAC																						
277	17.19	Sugar alcohol ?	SAC																						
296	18.46	Trehalose*	CS																						

Table 3.5 (continued)

No.	RT	Metabolite	Class	Day 0-3				Day 4-11								Day 12-22									
				D0	D1	D2	D3	D4	D5	D6	D7	D8	D9	D10	D11	D12	D13	D14	D15	D16	D17	D18	D19	D20	D21
302	18.96	Disaccharide ??	CS																						
307	20.07	Sterol ??	ST																						
317	21.90	Epibrassicasterol	ST																						
318	22.02	Sterol ??	ST																						
321	22.81	Stigmasterol*	ST																						

Days 0-3, D4-11, and D12-22 were assigned as groups. Blue – low metabolite concentration, yellow – high metabolite concentration. If marked by “*”, identification was confirmed by a standard. Metabolites tagged with a “?” had a reverse match of 700 - 800 or, if marked by “??”, of 600 - 700. Abbreviations: A, amine, AA, amino acid, Alc, alcohol, CA, carboxylic acid, CS, complex saccharide, D, day, FA, fatty acid, HC, hydrocarbon, No., number, O, other, RT, retention time, S, saccharide, SA, sugar acid, SAc, sugar alcohol, ST, sterol, T, terpene, TMS, trimethylsilyl, U, unknown.

3.3 Discussion

After the successful induction of the desired *E. huxleyi* bloom (Figure 3.2B) in a large scale mesocosm experiment, we observed a differentiating development in the mesocosm enclosures relative to the fjord concerning the overall phytoplankton community. We further detected changes in metabolic profiles in correlation with different CO₂ concentrations over the progression of the mesocosm experiment. Ecosystem level effects of the parameter CO₂ manifested themselves in the mesocosms and thus could be assessed. In general, mesocosm studies allow the observation of such effects (Connon et al., 2012). The detected influence of CO₂ conditions on phytoplankton, visible by the changes of the community composition or metabolic profiles, in general reflects the effects of a projected future forcing due to increasing atmospheric CO₂ levels on natural aquatic ecosystems (Riebesell et al., 2000b). In contrast, Fe only affected the metabolic profiles in dependence of CO₂ levels and so constitutes an interacting effect under changed future ocean conditions.

Data interpretation of a mesocosm study is disproportionately more difficult than of a culture. Due to the high number of different species present in the phytoplankton community, as also observed in the present study (Figure 3.2), the attribution of effects to a specific group is hampered. Further, results are often obscured by confounding factors and high variability between replicates (Connon et al., 2012). This is especially true for metabolic profiling, as it is difficult to identify the contributor of a specific metabolite in a complex community. Thus, instead of targeting the whole metabolome many studies rather quantified effects of a specific compound class such as polyunsaturated aldehydes, where the potential producer was known (Vidoudez and Pohnert, 2008; Paul et al., 2012), or targeted the effect of toxicants (Liess and Beketov, 2011) or inhibitor addition (Knauert et al., 2008) at the community level. Hence, this lack of reference metabolic profiles deriving from mesocosm studies necessitates the discussion of our results in the light of culture derived studies, although we thus might overlook the real complexity of the effects.

A previously mentioned statement also remains valid for mesocosm experiments: metadata describing the biological performance of the organism under investigation are necessary to validate and understand the obtained results (Fiehn et al., 2007). Therefore, we monitored growth of the most abundant phytoplankton

groups and collected data on parameters that validate the manifestation of the performed treatments. Exposure of half of our mesocosm enclosures to an elevated CO₂ concentration of 1000 ppm resulted in a decrease of the pH in comparison to the non-treated enclosures. The slight increase in pH levels in all treatments during the course of the experiment is in accord to other studies applying CO₂ manipulation (Engel et al., 2005). Further, by covering of the mesocosms with lids combined with continuous fumigation via airlifts we established a continuous increased CO₂ concentration in part of our mesocosm enclosures throughout the experiment. Hence, our set-up was suitable to study the effect of CO₂ changes on the phytoplankton community during the bloom event.

Addition of the fungal siderophore desferrioxamine B resulted in a higher concentration of dissolved Fe in treated mesocosms, but did not affect particulate Fe. The addition of DFB is supposed to sequester ambient Fe(III) and thereby markedly decrease its availability to phytoplankton, leading to an artificial Fe limitation (Hutchins et al., 1999). This was successfully performed in previous studies, where DFB addition resulted in a decrease of total chlorophyll (Eldridge et al., 2004) and changed nutrient concentration, biomass, and other biological parameters in a way indicative for Fe-limitation (Hutchins et al., 1999). Therefore, the observed effect of a higher dissolved Fe content in mesocosm enclosures treated with DFB was unexpected. The same was true for the observation that complexation made Fe better bioavailable for *E. huxleyi*, as demonstrated by its enhanced growth in the low CO₂/DFB+ treatment. The reason for this unforeseen bioavailability possibly lies in the possession of a transmembrane reductase that is able to catalyze the release of Fe from FeDFB (Shi et al., 2010) as described from *Thalassiosira oceanica* (Maldonado and Price, 2001). A previous study even demonstrated that *E. huxleyi* is able to take up Fe from FeDFB, although FeEDTA is preferred (Shaked and Lis, 2012). Consequently, *E. huxleyi* could have experienced a competitive advantage over other phytoplankton taxa, because they might not have been able to mobilize FeDFB. Thus, our DFB addition treatments have to be regarded as enriched in bioavailable Fe favoring phytoplankton growth at least in the case of *E. huxleyi*.

Most other nutrients such as nitrate and phosphate rapidly decreased with accumulation of biomass without showing different effects in the applied treatments. Concomitantly, Engel et al. (2005) observed no effect on nutrient uptake during a

mesocosm experiment with elevated CO₂ levels. The onset of the *E. huxleyi* bloom occurred after nutrient levels were already depleted. This is not contradicting as by their small cell size and low Chl *a* content even a dense coastal bloom of *E. huxleyi* does usually not consume more nutrients in respect to nitrate and phosphate than are initially present in non-enriched seawater (Paasche, 2002).

To understand the Chl *a* concentration pattern, which did not reflect the flow cytometry-based overall growth behavior of phytoplankton, it is necessary to regard all information on phytoplankton groups present during the experiment. The small phytoplankton groups detected by flow cytometry (Figure 3.2B-F) all increased later during the experiment, but preliminary flow cam data indicated a short diatom bloom right after the onset of the experiment. The Chl *a* content of diatoms, with values ranging from 0.35 pg Chl *a* cell⁻¹ in *Thalassiosira pseudonana* to 2.37 pg Chl *a* cell⁻¹ in *Coscinodiscus wailesii* (Hitchcock, 1982), is large in comparison to *E. huxleyi* with only 0.1 pg Chl *a* cell⁻¹ (Stolte et al., 2000). Thus, the observed Chl *a* concentration pattern can be explained by an initial peaking of diatoms followed by their decrease, while the treatment-dependent increase in *E. huxleyi*, the dominant phytoplankton taxon, is reflected in the Chl *a* concentration only later. This second increase of Chl *a* further represents the increase in cell abundance of *Synechococcus* spp., and small and big nanoeukaryotes. Hence, Chl *a* is not a suitable parameter to estimate abundance of small phytoplankton groups in a natural community.

E. huxleyi constituted the dominant phytoplankton taxon during the mesocosm experiment (Figure 3.2B). The growth pattern of this species was clearly treatment-dependent as it showed differences between low and high CO₂ treatments. This is especially true as low CO₂ levels and addition of the Fe chelating agent DFB led to strongly elevated growth exceeding 60.000 cells mL⁻¹. In contrast, Fe manipulation under high CO₂ conditions did not affect growth. Such strongly induced *E. huxleyi* growth is in accord with previous mesocosm studies conducted at the same facility (Delille et al., 2005; Martínez-Martínez et al., 2006). Our observation of the strongest growth in the Fe manipulation treatment might hint for an initial Fe limitation in the fjord water as documented to occur sporadically in the Trondheim fjord (Öztürk et al., 2002). Fe limitation can lead to significantly diminished growth rates (Schulz et al., 2007). Consequently, the high amount of bioavailable iron in the low CO₂/DFB+ treatment resulted in the opposite effect by increasing the growth rate of *E. huxleyi*.

Concerning the effect of CO₂, in contrast to our findings a previous study detected that induced CO₂ concentrations lead to a slight increase in *E. huxleyi* cell abundance, although this effect was not significant during most days of the mesocosm experiment (Paulino et al., 2008). *Synechococcus* spp. and picoeukaryotes preceded *E. huxleyi* and thus reflected a succession pattern of these groups (Martínez-Martínez et al., 2006). The second maximum in other phytoplankton groups observed by us, however, did not coincide with the decline in *E. huxleyi* cell abundance as it was the case in other experiments (Delille et al., 2005; Martínez-Martínez et al., 2006). We found *Synechococcus* spp. to be affected by high CO₂ leading to slightly reduced growth during the second half of the experiment. This is in accord with Paulino et al. (2008), who also recorded lower *Synechococcus* abundance under elevated CO₂ conditions towards the end of their experiment. In contrast, an induction in picoeukaryote abundance at high CO₂ levels (Paulino et al., 2008) was only partly reflected by our cell counts. Abundance patterns of nanoeukaryotes and *Synechococcus* spp. might have been shaped by grazing, since microzooplankton grazers such as dinoflagellates and ciliates prefer cyanobacteria over the dominant phytoplankton groups such as coccolithophores or diatoms and potentially remove 20-65% of the standing stock per day (Suffrian et al., 2008).

The growth pattern of heterotrophic bacteria might reflect a shift in community composition. Heterotrophic bacteria as well as the cyanobacterial population underwent a rapid decrease shortly after the beginning of the experiment. Therefore, the initial nutrient addition might have resulted in a community shift from small (heterotrophic bacteria, *Synechococcus* spp.) to intermediate (diatoms, *E. huxleyi* and nanoeukaryotes) (phyto)planktonic groups as documented by Paulino et al. (2008). In general, our bacterial population showed a similar growth pattern as reported in this study, although the authors documented a non-significant trend for higher bacterial abundance under elevated CO₂ during the last days of the experiment (Paulino et al., 2008). In contrast, we detected the opposite pattern with slightly higher bacterial numbers under ambient CO₂ conditions from days 14 to 19 and a significant support on day 18. Viral abundance data did not reflect a regular infection pattern. We detected oscillating numbers of viruses throughout the experiment that lacked the specific maximum following the peak of the dominant phytoplankton group and that coincides with the diminish of this group as reported from infected blooms (Martínez-Martínez et al., 2007; Pagarete et al., 2009). Further,

we also did not document a decline in *E. huxleyi* abundance but an increase during most time of the experiment. Therefore, we can state that a big viral infection event of *E. huxleyi* as the dominant phytoplankton group did not occur.

Most metabolites showed a high correlation to low CO₂/DFB+, a treatment that probably reflects good growth conditions for *E. huxleyi*. This assumption is supported by the continuous *E. huxleyi* growth observed in all corresponding mesocosms and might be due to the higher amount of dissolved Fe, a micronutrient that potentially diminishes growth rates in *E. huxleyi*, if limited (Schulz et al., 2007). That we did not observe an enhancement in *E. huxleyi* abundance under high CO₂/DFB+, a treatment that actually could not be resolved from the other high CO₂ treatment, probably resulted from a CO₂ effect independent of the increase in dissolved Fe, which was also supported by low CO₂/DFB- and high CO₂/DFB-. The net specific growth rate of *E. huxleyi* was affected by partial pressure of gas CO₂ (pCO₂) in a previous mesocosm experiment (Engel et al., 2005). Further, as the vectors of many metabolites pointed between low CO₂/DFB- and high CO₂ they were contributing to the separation of these two groups, although not being clearly assignable to one or the other. This differentiation was well reflected in the separation pattern, if CO₂ constituted the sole analyzed parameter. Since manipulation in pCO₂ significantly affected the composition of dissolved and particulate carbon species (Engel et al., 2005), it is approvable to assume this change to be reflected in the intracellular metabolite composition.

The complex pattern we found for carbohydrates might reflect high photosynthetic activity and the production of building blocks for cell growth and division. We assume that the high abundance of monosaccharides correlated with low CO₂/DFB+ or low CO₂ in general results from their accumulation in the cells due to carbon assimilation (Raven and Beardall, 2003). During an Fe limitation experiment observed concentration increases in cellular glucose and intermediate saccharides, as detected by us, were interpreted as indicators for a conversion of polysaccharides to glucose fueling increased glycolytic activity (Allen et al., 2008a). Thus, we suggest that induced glycolytic activity is also needed for energy production to facilitate downstream metabolic reactions and to favor cell growth in mesocosm communities under ambient CO₂ conditions. Another indication for high photosynthetic activity is provided by the accumulation of sugar acids, in particular

glyceric acid. It is produced in the chloroplasts during photosynthesis. Glycerate formation leading to its accumulation is favored over further conversion under high levels of reducing capacity from photosynthesis (Tolbert, 1979). Glyceric acid can also be transformed to glycerol, which we also found accumulating in low CO₂ treatments. Under Fe limitation the opposite effect occurred in the centric diatom *Phaeodactylum tricornutum*, because glycerol showed a reduction in concentration (Allen et al., 2008a).

Most of the observed sugar alcohols showed a correlation to high CO₂. This might indicate a higher stress level of these cells because sugar alcohols can function as scavengers for free radicals (Raven and Beardall, 2003). Prominent among sugar alcohols was the glycolytic derivative *myo*-inositol and its isomers, which all showed induced concentrations under high CO₂ conditions. It is assumed that the existence of an inositol dehydrogenase in haptophytes allows putative usage of an inositol/inosase shuttle system for reducing equivalents between mitochondrion and cytosol (Gross and Meyer, 2003). This mechanism to exchange reducing power was suggested to be especially important under the light of an intensified glycine and serine metabolism (Allen et al., 2008a) as seen in higher concentrations of glycine and a glycine derivative under high CO₂, because it can mitigate the production of reactive oxygen species (Allen et al., 2008a).

Amino acids were reflecting high productivity as, except for glycine, all were correlated with low CO₂/DFB+ or the low CO₂ treatment in general and they are assumed to be indicative of the nitrogen nutrition state in phytoplankton (Admiraal et al., 1986). With valine and phenylalanine we observed two amino acids deriving from the glycolysis products pyruvate and phosphoenolpyruvate, respectively. N-acetylglutamic acid, which is formed in an enzymatically triggered reaction from glutamic acid and acetyl-CoA (Maas et al., 1953), threonine, and hydroxy-proline are descended from the TCA cycle. Hydroxy-proline is even formed via a proteolytic reaction. As the TCA cycle receives pyruvate via glycolysis this again indicates a high carbon fixation rate and glycolytic activity necessary to sustain high growth. Interestingly, all four detected TCA cycle substrates grouped together. A possible explanation for their correlation to low CO₂/DFB+ might be that aconitase, a key enzyme in the TCA cycle, requires Fe as a co-factor (Gray et al., 1993). Thus, due to

the high amount of bioavailable Fe this treatment provided better conditions for energy production via TCA cycle activity.

Among amines the only tentatively identified one, ethanolamine, was correlated with high CO₂. Why this head group of phosphatidylethanolamine displayed higher concentrations in high CO₂ is not completely comprehensive, but in an nitrogen limitation experiment changes in phosphatidylethanolamine were observed only under high CO₂ but not under atmospheric CO₂ (Gordillo et al., 1998). The explanation by the authors that it was related to carbon availability does not fit the correlation patterns of our metabolic profiles, because almost all free fatty acids needed as potential reaction partners to form phosphatidylethanolamine showed highest concentrations under low CO₂/DFB+ and low CO₂, respectively. With increasing CO₂ concentrations Riebesell et al. (2000a) report an increase in the total fatty acid content per cell for most fatty acids with the exception of highly unsaturated ones (C18:5 and C22:6). Thus, the iron effect probably overruled a potential CO₂ effect and we may assume that the high abundance of free fatty acids found in the well growing low CO₂/DFB+ treatment reflects the general high content of storage lipids in algae (Griffiths and Harrison, 2009), although we have to mention that free fatty acids cannot be directly compared to such storage lipids.

The reported high complexity of sterols (Volkman, 2003 and references within) was confirmed in our metabolic profiles and might be related to dominant sterols deriving from different phytoplankton groups. For example the main sterol of *E. huxleyi*, epibrassicasterol, also referred to as (24S)-24-methylcholesta-5,22E-dien-3 β -ol (Maxwell et al., 1980), showed its highest concentration in the low CO₂/DFB+ treatment, which nearly represented a monoculture of this alga, and was also high in the other low CO₂ treatment. A higher content of this sterol under low CO₂ probably only reflects the better performance of *E. huxleyi* under this conditions as a previous laboratory-based study did not see tremendous changes in epibrassicasterol concentration under varying CO₂ levels (Riebesell et al., 2000a). These authors also detected no change in phytol concentrations when exposed to the same changing CO₂ concentrations (Riebesell et al., 2000a), which contrasts its correlation to low CO₂ within our mesocosm study. Nevertheless, phytol, the esterified side chain of chlorophyll *a* and part of chlorophyll *c* in some haptophytes (Rontani and Volkman, 2003 and references within), might be expected to show a correlation to mesocosms

with high photosynthetic activity as was generally observed under low CO₂. This high reactivity might also explain why we detected the powerful radical-trapping antioxidant alpha-tocopherol (Palozza and Krinsky, 1992) related to low CO₂/DFB+ and low CO₂, respectively. The induction of alpha-tocopherol probably reduced the stress experienced by the algae as reported for plants (Munne-Bosch, 2005).

Detected metabolites such as uridine, adenosine, and the pyridine derivative nicotinic or picolinic acid might hint for induced pyridine and purine biosynthesis for incorporation into nucleotides. We suppose that nucleic acid and nucleotide synthesis are high in a growing culture as assessment of nucleic acid concentrations is used to quantify growth (e.g. Karl et al., 1981; Moriarty and Pollard, 1981).

Changes in metabolic profiles over time in the control mesocosm enclosures 1 and 2 seem to best reflect metabolic characteristics of a natural *E. huxleyi*-dominated bloom community. Right after the onset of the experimental manipulation (D0-3) our metabolic profiles most likely documented metabolic patterns of diatoms, because they had a short pre-bloom during this period. Since all observed phytoplankton groups showed high abundances during the intermediate D4-11, we suggest it best represents the metabolic complexity of a mixed phytoplankton community, although *E. huxleyi* was already abundant. Later on during the second half of the experiment (D12-22), the highly abundant *E. huxleyi* should be the main contributor to metabolic profiles. This high variation limits direct comparison with laboratory data deriving from the observation of diploid and haploid *E. huxleyi* cultures (2.2.3, and 2.2.4). Nevertheless, we will carefully make such attempts.

Carbohydrate patterns probably represent several different aspects. A significant correlation of a number of monosaccharides to D0-3 and D4-11 might reflect a high carbon fixation rate (Raven and Beardall, 2003) enabled by high nutrient availability during the onset of the phytoplankton bloom. These monosaccharides can then be incorporated into polysaccharides explaining the correlation pattern for disaccharides such as maltose and trisaccharides to D0-3. Similar patterns were visible in our laboratory experiment targeting haploid *E. huxleyi* cells during the exponential growth phase (2.2.4) and have been reported for diatoms by Vidoudez and Pohnert (2012). As main storage compound of *E. huxleyi* (Obata et al., 2013), mannitol accumulated during D12-22 and reflects the dominance of this alga. Further, induction of many other sugar alcohols during this time period might

indicate increasing stress as these metabolites can function as free radical scavengers (Raven and Beardall, 2003). During laboratory experiments, we documented their concentration increase during the declining phase (2.2.4). Vectors of glucose pointing between the time intervals D0-3 and D12-22 indicate that glycolysis and energy production in the control were no longer at their maximum. Since most of the nutritional resources have been used up at the last days of the experiment, glucose could accumulate as it was no longer consumed in downstream glycolytic reactions. The separating positioning of glucose concerning D0-3 becomes comprehensive regarding that glucose is among the main respiratory substrates in the diatom *S. costatum* and observed to make up the highest content among monosaccharides in this alga (Handa, 1969). In contrast, in *E. huxleyi* a similar function is performed by mannitol (Obata et al., 2013).

Polyamine metabolism reportedly is extremely sensitive to environmental challenges (Bouchereau et al., 1999). We detected high concentrations of the two polyamines putrescine and cadaverine during D4-11. Since putrescine levels reportedly increased with progressing senescence for example in carnation flowers (Serrano et al., 2001), this molecule might be indicative for the decay of cells as the community shifted from diatoms to pico- and nanoeukaryotes and later on to an *E. huxleyi*-dominated bloom. An involvement of putrescine accumulation has also been reported for potassium deficiency, originally observed in barley plants (Richards and Coleman, 1952). Nevertheless, the sensitive role of putrescine in maintaining the cation-anion balance as in tissues of higher plants (Bouchereau et al., 1999 and references within) is unlikely to be important in algae growing in seawater. Further, putrescine and cadaverine have both been detected in the green alga *Chlorella* sp. followed by an increase in putrescine levels but a reduction in cadaverine, if viral infection set in (Kaiser et al., 1999). Although so far this pattern is not generally validated, we might interpret the lack of such a diverging pattern in polyamines as further indication that our mesocosm experiment was not affected by viral infection, as is also reflected in viral counts. None of these polyamines were detected in *E. huxleyi* lab cultures (2.2.3, and 2.2.4). Instead, we observed ethanolamine, the head group of phosphatidylethanolamine accumulating in cells infected by a lytic virus (4.2.4). Accumulation of ethanolamine during D4-11 of the mesocosm experiment fits a report of a high concentration of the membrane lipid phosphatidylethanolamine during exponential and stationary phase samplings in

E. huxleyi (Bell and Pond, 1996). Together with the important role of lipids during viral reproduction (4.2.4), this finding supports the assumption that the high abundance of ethanolamine is associated with lipid production in *E. huxleyi* cells.

Potentially, nitrogen was not yet limiting for phytoplankton growth during D4-11 as all detected amino acids correlated with this period. A cellular pool of free amino acids was suggested to serve as significant nitrogen buffer (Admiraal et al., 1986) and accordingly, amino acid production should be high, as long as nitrogen is not limited (Admiraal et al., 1986; Haberstroh and Ahmed, 1986). In general, we observed a higher variety among amino acids than during the laboratory study (2.2.3, and 2.2.4), but as community composition was complex during the days of their highest concentration, other phytoplankton species than *E. huxleyi* might constitute the source of a part of these amino acids. On the other hand, except for beta-alanine, which we also found in laboratory cultures (2.2.4, and 4.2.4), and N-acetylglutamic acid, all amino acids detected in the mesocosm experiment were previously reported from *E. huxleyi* by Obata and co-workers (2013).

We could not find a distinct pattern in polar low molecular weight carboxylic acids over time. Out of the two TCA cycle substrates, fumaric acid correlated with D0-3, whereas malic acid separated for D4-11. Therefore, we cannot directly explain this pattern by TCA cycle activity. On the other hand, pyrrole-2-carboxylic acid, which also correlated with D0-3, can derive via an enzymatic or non-enzymatic reaction from hydroxy-proline (Radhakrishnan and Meister, 1957) and as mentioned above the production of this amino acid is dependent on TCA cycle activity. Carboxylic acids differed from those correlated with growth phases in haploid *E. huxleyi* cells (2.2.4), so they could either derive from other phytoplankton groups or differences in carboxylic acids between diploid and haploid life phases are larger than we assumed based on our laboratory metabolic profiles.

The complex correlation pattern of free fatty acids to the assigned time intervals in the control might reflect the changing community composition. The best correlation to D12-22, and therefore probably also to *E. huxleyi*, showed DHA. A previous report described it as one of the major fatty acids in this alga (Pond and Harris, 1996) and in laboratory cultures we detected it in highest concentration during the stationary growth phase (2.2.4). In contrast, 1-monohexadecanoylglycerol separating D0-3 was neither detected in diploid nor haploid *E. huxleyi* cultures

(2.2.3), but has been previously found in a benthic diatom (Nappo et al., 2009). Thus, this compound might constitute an example of a fatty acid produced by another member of the phytoplankton community.

A similar situation as for fatty acids was detected in sterols. Epibrassicasterol showed a high correlation to D12-22 and thus to the *E. huxleyi*-dominated phytoplankton community. This pattern reflects the laboratory observation as epibrassicasterol constituted the most abundant sterol in diploid cells (2.2.3). In contrast, other sterols such as (3 β ,5 α)-cholestan-3-ol, beta-sitosterol, or fucosterol potentially derived from other phytoplankton groups showing high abundances during D4-11 and, hence, reflected the high variability of this compound class in marine microalgae (Volkman, 2003). Fucosterol for instance is the dominant sterol in brown algae (Patterson, 1971) and sitosterol was found in high concentrations in the haptophyte *Diacronema (Monochrysis) lutheri* (Lin et al., 1982). The slightly separate positioning of stigmasterol is more difficult to explain. We did not detect this sterol in our laboratory study (2.2.3, and 2.2.4), but it has been described to present a major sterol of haptophytes and together with brassicasterol to account for more than 75% of total sterols in this group (Véron et al., 1996). Thus, we assume that the producers belong to the nanoplankton groups and were present during both D4-11 and D12-22.

As a conclusion we should point out the unexpected good growth conditions in the low CO₂/DFB+ treatment resulting in high photosynthetic activity and carbon fixation. The resulting high metabolic activity induced by a sufficient supply of bioavailable Fe could be documented in our metabolic profiles. In general, cells in this treatment distinguished themselves by a high glycolytic activity, active energy production via the TCA cycle reflected in four detected substrates as well as high amino acid and fatty acid biosynthesis. Analysis of the control treatment allowed to distinguish metabolites associated to a (semi-)natural phytoplankton bloom. Further, we were able to compare metabolites showing high correlations to the last time interval (D12-22) assumed to reflect an *E. huxleyi*-dominated bloom with our previous laboratory-based findings. Thus, the metabolic profiles presented here should help future studies to interpret the complexity of mesocosm- or field-based metabolic profiles deriving from mixed phytoplankton communities. This is especially true as yet investigations on metabolic reactions at community level are rare as is our understanding of the complicated metabolic interactions in natural communities.

4 Rewiring of host metabolism by large viruses infecting the cosmopolitan bloom-forming alga *Emiliania huxleyi*²

The experiments presented in this chapter were conducted in a close cooperation at the laboratory of A. Vardi, Plant Sciences Department, Weizmann Institute of Science, Rehovot, Israel, especially together with S. Rosenwasser. Data deriving from the cooperation, but essential for the understanding of the experiment, are indicated in the figure legends. Pharmacological inhibition experiments of fatty acid and terpene biosynthesis pathways were conducted and analyzed together with S. Rosenwasser.

4.1 Experimental design

In the previous chapters metabolic differences between diploid and haploid life phases of the coccolithophore *Emiliania huxleyi* together with changes in metabolic profiles during growth were presented. Further, a bloom of this alga could be induced and monitored under semi-natural conditions during a mesocosm study. Besides metabolic reactions to future ocean conditions we documented how metabolic profiles of a natural *E. huxleyi*-dominated bloom in the control changed during the course of the experiment and related these data to the results obtained for the laboratory cultures. In all these cases the alga displayed complex metabolic patterns either deriving from changes during growth or complex interactions in a semi-natural community. In a further step, specific viruses are now included to our study-system functioning as interaction partners and triggering a complex metabolic remodeling of the host metabolism.

² Parts of this chapter are based on the manuscript: Rosenwasser, S.*, Mausz, M.A.*, Schatz, D., Sheyn, U., Malitsky, S., Aharoni, A., Weinstock, E., Tzfadia, O., Ben-Dor, S., Feldmesser, E., Pohnert, G., and A. Vardi. Rewiring host lipid metabolism by large viruses determines the fate of *Emiliania huxleyi*, a bloom-forming alga in the ocean. This manuscript was accepted for publication in Plant Cell. (The “*” indicates that authors contributed equally.)

Recent studies documented a reduction of the unsaturation degree in fatty acids (Evans et al., 2009) or changes in pigment composition during infection of *E. huxleyi* by its specific virus EhV86 (Llewellyn et al., 2007). Further, transcriptomic (Pagarete et al., 2011) and expressed sequence tag (EST) approaches (Kegel et al., 2010) found indication for manipulation of the lipid and carbohydrate metabolism during viral infection. Additionally, viral glycosphingolipids reportedly play an essential role in the induction of host cell death after lytic infection of *E. huxleyi* cells (Vardi et al., 2009). However, our understanding of the processes ultimately leading to host cell lysis is hitherto still limited.

In this chapter we present a novel model culture system consisting of *E. huxleyi*, which is successfully infected either by a lytic or non-lytic virus. By monitoring the metabolome and relating the metabolic profiles to gene expression patterns observed at the transcriptome level in comparison to non-infected controls, we detected metabolic changes triggering cell lysis in the host. This was achieved using triplicates of 20 L cultures of the non-calcified *E. huxleyi* strain CCMP2090 infected by the lytic *Emiliania huxleyi* virus 201 (EhV201) or the non-lytic EhV163 as well as non-infected controls (Figure 4.1). Cultures were sampled for intracellular metabolites at several time points during the course of infection (Figure 4.1, bottom left). Metabolite samples were analyzed by a metabolomic approach based on gas chromatography coupled to mass spectrometry (GC-MS) (Figure 4.1, center) described in chapters 6.4, and 6.7.3. Subsequently, metabolic profiles were correlated with a RNA-seq based transcriptome (Figure 4.1, right) allowing the assignment of metabolic pathways. Specific determination of metabolites undergoing drastic concentration changes in lytic infected host cells compared to the control draw our attention to highly regulated metabolic pathways. These pathways undergoing the most intense changes are described in the following sections. Further, we provide a complete description of the system documenting host abundance and cell death, intra- and extracellular viral abundance, and origin of RNA counts. To confirm differences between the two viral replication strategies, transmission electron microscopy (TEM) was used. Although obtained by others, the latter data are essential for the understanding of the outcome of this study and their origin is thus indicated in the figure legends.

Metabolic data that enable conclusions about how the virus actively remodeled host metabolism to provide building blocks for viral progeny production and putative host defense mechanisms shall be presented and discussed in relation to transcriptomic gene expression patterns. Together with recent literature on metabolic changes in human cell lines during infection by human viruses, this allows a more complete picture of processes involved in cell lysis in the marine alga *E. huxleyi*.

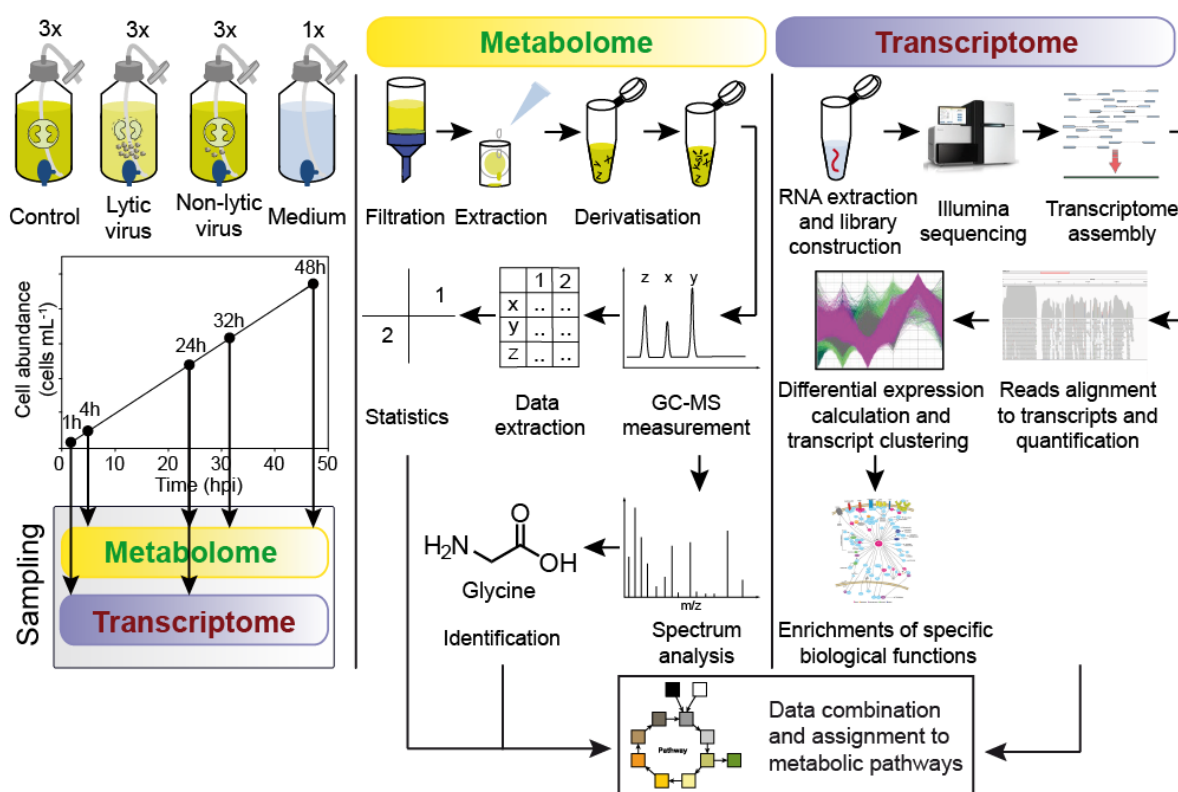


Figure 4.1: Scheme of the experimental design with metabolomic and transcriptomic workflow. Upper left: triplicates of 20 L cultures of the non-calcified *E. huxleyi* strain CCMP2090 were infected with a lytic (EhV201) or non-lytic (EhV163) virus. Cultures of non-infected cells served as control and a carboy containing blank medium was added for metabolic data correction. Lower left: cells were sampled as indicated by the arrows in the sampling schedule. Mid: workflow of metabolome analysis from cell extraction via gas chromatography-mass spectrometry (GC-MS) measurement to metabolite identification. Right: workflow of the RNA-seq based transcriptomic approach. Bottom: combination of transcriptome and metabolome data for mapping of metabolic pathways. Abbreviation: hpi, hours post infection.

4.2 Results

4.2.1 *Infection dynamics of *Emiliana huxleyi* and its specific viruses*

In this experiment we used an experimental set-up in which a single *E. huxleyi* host was either infected by the lytic virus EhV201 or the non-lytic virus EhV163. Cultures infected by the lytic virus displayed no growth and decreased in abundance 32 hours post infection (hpi) due to host cell lysis. In contrast, cultures infected by the non-lytic virus EhV163 grew exponentially and exhibited similar cell abundances as the control (Figure 4.2A, B). This pattern was reflected by induction of cell death as measured by Sytox® green fluorescence, which was only detectable in cultures infected by the lytic EhV201 but not in non-lytic infected cultures (Figure 4.2C). Transmission electron microscopy (TEM) images revealed viral particles 48 hpi only in lytic infected cells accompanied by shrinkage of the nucleus and degradation of the chloroplast (Figure 4.2E), whereas control cells or cells infected by the non-lytic virus exhibited no structural changes (Figure 4.2D, F). Intracellular viral DNA accumulated in lytic infected cells 4 hpi onwards, peaking already at 24 hpi, and decreased as the infection further progressed (Figure 4.2G). Viral DNA accumulation was followed by viral release due to host cell lysis with its maximum reached at 32 hpi (Figure 4.2H). Neither non-infected control cells nor cells infected by the non-lytic virus EhV163 showed cell death, viral DNA replication or viral release (Figure 4.2C, G, H).

This approach was further used to investigate GC-MS-based metabolic data in relation to gene expression patterns based on transcriptomic analysis. The latter documented rapid remodeling of host metabolism by the lytic virus reflected in a drastic increase in viral-derived RNA transcripts from 1 to 24 hpi. At 1 hpi only 5% of the total reads were aligned with the EhV201 genome, whereas at 24 hpi 80% of the total reads aligned to the viral genome (Figure 4.2I). No induction of viral RNA transcripts was observed for the non-lytic virus EhV163.

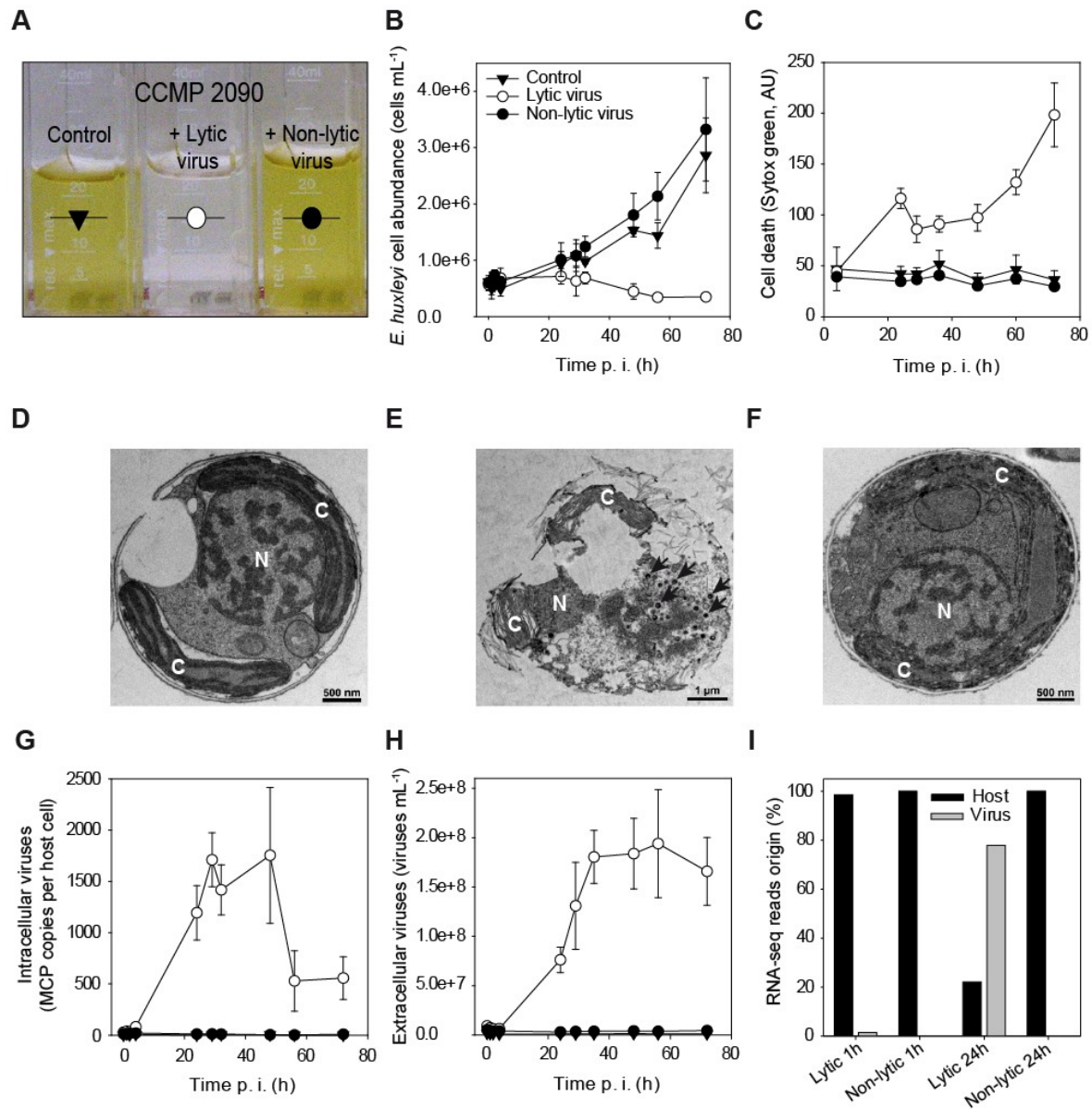


Figure 4.2: Infection dynamics and ultrastructural analysis of *E. huxleyi* and its specific viruses. (A) Cultures of *E. huxleyi* host cells monitored during infection by the lytic virus EhV201 or the non-lytic virus EhV163 and compared to non-infected control cells. Images were taken at 72 hpi. (B) Host cell abundance, (C) and host cell death, the latter assessed by Sytox® green fluorescence, measured by flow cytometry (mean \pm SD, $n=3$). (D-F) Transmission electron microscopy (TEM) images show (D) a non-infected control cell, (E) a cell infected by the lytic, and (F) the non-lytic virus at 48 hpi. Viral particles, indicated by arrows, were only detected in lytic infected cells. (G) Intracellular viral abundance as determined by qPCR of the viral DNA within the cellular fraction by probing for the major capsid protein (MCP) gene. Data present the mean of biological triplicates and technical duplicates. (H) Abundance of extracellular viruses measured by flow cytometry (mean \pm SD, $n=3$). (I) Relative abundance of RNA reads mapped to host or virus genomes at 1 and 24 hpi. Data were provided by U. Sheyn (flow cytometry), D. Schatz (TEM images), and S. Rosenwasser (qPCR and RNA reads). Abbreviations: AU, arbitrary unit, C, chloroplast, N, nucleus, p. i., post infection.

4.2.2 Dynamic modulation of metabolism with proceeding viral infection

At 4, 24, 32, and 48 hpi 2 L of culture and blank medium were sampled from triplicates of 20 L cultures containing *E. huxleyi* infected by the lytic or non-lytic virus or non-infected control cells. Afterwards, duplicates of 100 mL sub-sample per biological replicate were concentrated on filters with a pore size of $\sim 1.2 \mu\text{m}$ (GF/C, Whatman, Kent, UK) followed by metabolite extraction using a solvent mixture (for details see 6.4.2, 6.7.2, and 6.7.3). Later, samples were derivatized and a GC-MS based metabolomic analysis (see 6.4.2) was used to determine global changes in host cell metabolism. All biological replicates derived from the same culture, thus, the assumption of constant metabolic intensity was assumed to be fulfilled and data were normalized by the peak sum.

In total, we observed 185 signals at four time points (4, 24, 32, and 48 hpi). A detailed list of the numbers of signals detected for each time point is given in Table 4.1. Nearly half of the detected peaks (86 signals) could be identified as specific metabolites by library comparison and/or co-injection with authentic standards. Of the remaining signals, 47 ($\sim 25.4\%$) were tentatively assigned to a metabolite class based on their mass spectra, and 52 signals ($\sim 28.1\%$) remained unknown. The largest compound class consisted of saccharides (54 signals) and related metabolites (five sugar acids, nine sugar alcohols). Eleven fatty acids and eight fatty acid derivatives constituted a second large group, whereas we found only two amino acids and two amino acid derivatives. Among several other substances we further detected five terpenes and eight sterols. Metabolite concentrations varied between cells infected by the lytic or non-lytic virus in comparison to non-infected control cells depicting different metabolic profiles of infected cells (Table 4.2, and Appendix Table 5).

Table 4.1: Average number of detected metabolites. The table shows the actual number of metabolites detected by automated AMDIS processing (see 6.4.4 for details) at each time point (4, 24, 32, and 48 hpi) in control cells or cells infected by the lytic virus EhV201 or the non-lytic virus EhV163 (mean \pm SD, $n=3$).

Time	Control	Lytic virus	Non-lytic virus
4 hpi	145.0 \pm 6.6	139.7 \pm 10.0	144.7 \pm 7.7
24 hpi	144.6 \pm 8.2	134.5 \pm 12.3	151.8 \pm 8.4
32 hpi	160.5 \pm 14.3	156.2 \pm 9.9	175.0 \pm 14.0
48 hpi	138.3 \pm 21.9	128.5 \pm 13.7	152.3 \pm 18.5

Abbreviation: hpi, hours post infection.

Table 4.2: Fold changes of identified metabolites detected during viral infection. List of identified metabolites detected in *E. huxleyi* cells infected by the lytic (EhV201) or non-lytic (EhV163) virus relative to the control visualized as fold change (n=3). Metabolites are organized by metabolic classes. Colors indicate the intensity of the concentration change. Dark green: 0.0 – 0.329, green: 0.33 – 0.659, lime-green: 0.66 – 0.99, yellow: 1.0 – 4.99, beige: 5.0 – 9.99, and orange: >10.

RT	Metabolite	Class	Fold change							
			Lytic				Non-lytic			
			4 hpi	24 hpi	32 hpi	48 hpi	4 hpi	24 hpi	32 hpi	48 hpi
6.65	Ethanolamine*	A	n.d.	6.64	20.67	24.05	n.d.	4.68	4.57	3.53
7.35	Amine ?	A	n.d.	9.26	29.80	n.d.	n.d.	6.50	5.18	n.d.
12.16	Amine	A	n.d.	n.d.	n.d.	0.00	n.d.	n.d.	n.d.	1.55
6.10	Alanine ?	AA	1.10	1.07	0.77	0.60	1.16	1.65	0.90	0.73
8.11	Glycine*	AA	1.78	1.50	1.60	2.51	1.42	1.62	1.49	1.98
8.73	Glycine deriv. ?	AA	0.62	0.50	1.60	n.d.	0.76	0.59	0.64	n.d.
10.05	Pyroglutamic acid	AA	n.d.	n.d.	1.68	0.00	n.d.	n.d.	6.06	2.57
11.87	n-Tetradecan-1-ol	Alc	0.94	n.d.	n.d.	n.d.	0.44	n.d.	n.d.	n.d.
5.67	Lactic acid ?	CA	0.96	0.87	0.56	0.00	1.08	0.62	0.37	0.00
6.57	unidentified Carboxylic acid ?	CA	n.d.	n.d.	20.87	1.82	n.d.	n.d.	39.54	1.62
7.63	Benzoic acid	CA	n.d.	n.d.	n.c.	n.d.	n.d.	n.c.	n.d.	n.d.
8.19	Succinic acid*	CA	n.d.	n.d.	7.49	0.00	n.d.	n.d.	7.24	2.26
12.25	Citric acid	CA	9.05	0.50	0.29	0.04	5.12	2.56	4.31	2.27
5.86	Hexanoic acid	FA	0.00	0.28	1.05	0.00	0.14	2.55	1.30	1.11
7.73	Octanoic acid	FA	1.11	n.d.	2.39	0.00	1.06	n.c.	1.87	1.64
8.61	Nonanoic acid*	FA	1.25	0.86	2.16	0.39	0.84	2.35	1.03	0.93
10.17	2,4,5-Trihydroxypentanoic acid ??	FA	1.13	0.65	1.08	0.55	1.05	0.84	0.81	0.77
11.63	Tetradecanoic acid deriv.	FA	n.d.	n.d.	n.d.	0.38	n.d.	n.d.	n.d.	0.61
12.35	Pentadecanoic acid deriv.	FA	1.23	n.d.	n.d.	0.16	1.27	n.d.	n.d.	0.51
12.48	Tetradecanoic acid*	FA	1.51	2.72	1.70	0.28	1.91	2.27	2.29	1.47
13.03	Hexadecanoic acid deriv.	FA	1.20	n.d.	n.d.	n.d.	1.38	n.d.	n.d.	n.d.
13.15	Pentadecanoic acid*	FA	n.d.	n.d.	1.10	0.07	n.d.	n.d.	2.48	1.18
13.79	Hexadecanoic acid*	FA	1.37	2.22	1.25	0.24	1.44	2.94	3.08	1.14
14.19	Fatty acid	FA	1.15	0.00	1.19	1.30	1.54	0.57	0.86	0.70
15.01	Octadecanoic acid	FA	1.63	1.19	0.74	0.17	1.30	0.66	1.35	0.97
15.85	Tetradecanoic acid deriv.	FA	n.d.	n.d.	4.92	10.99	n.d.	n.d.	1.53	0.79
15.87	Octadecanoic acid deriv. ?	FA	n.d.	1.25	n.d.	n.d.	n.d.	1.17	n.d.	n.d.
16.05	Fatty acid	FA	n.d.	0.81	0.61	0.26	n.d.	1.99	0.95	1.20
16.25	Docosahexaenoic acid	FA	1.19	0.57	0.57	0.24	1.34	1.13	0.82	0.58
16.89	Hexadecanoic acid deriv.	FA	0.00	0.00	2.58	2.22	2.51	1.45	1.87	0.69
17.86	Octadecanoic acid deriv. ?	FA	n.d.	0.00	0.00	47.34	n.c.	0.34	5.99	0.00
21.47	Fatty acid	FA	1.22	1.00	1.26	1.01	1.23	0.93	1.15	1.06
7.29	Glyceraldehyde*	O	1.32	0.14	0.60	0.36	1.14	0.95	0.69	1.03
7.82	Glycerol	O	n.d.	n.c.	9.60	5.03	n.d.	n.c.	7.73	3.59
8.39	Lumichrome	O	1.13	0.31	1.88	2.39	1.53	0.47	0.79	4.51
11.33	Heptadecenone	O	n.d.	n.d.	n.d.	0.48	n.d.	n.d.	n.d.	0.77
11.93	D(-)-Galactono-1,4-lactone ??	O	n.d.	n.d.	0.32	0.00	n.c.	n.d.	0.80	1.26
13.23	Glucono-1,5-lactone*	O	0.95	0.88	0.89	0.90	1.18	0.88	0.78	0.85
14.12	Oleanitrile	O	n.d.	0.93	n.d.	n.d.	n.d.	1.11	n.d.	n.d.
17.15	Adenosine ??	O	n.d.	n.d.	n.d.	1.40	n.d.	n.d.	n.d.	1.55
9.17	Erythrose ?	S	2.73	0.57	0.54	0.09	5.48	0.76	0.83	0.17
9.23	Monosaccharide ?	S	n.d.	0.53	0.62	0.12	n.d.	0.90	0.84	0.49

Table 4.2 (continued)

RT	Metabolite	Class	Fold change							
			Lytic				Non-lytic			
			4 hpi	24 hpi	32 hpi	48 hpi	4 hpi	24 hpi	32 hpi	48 hpi
9.63	Monosaccharide	S	2.72	0.48	0.57	n.d.	5.45	0.84	0.95	n.d.
10.49	(Arabino-)Pentafuranose	S	1.26	n.d.	1.32	n.d.	1.03	n.d.	1.10	n.d.
10.59	Pentafuranose	S	1.23	1.32	1.47	0.87	1.65	1.23	1.27	1.35
10.63	Sugar deriv.	S	n.d.	0.74	0.46	n.d.	n.d.	1.44	0.81	n.d.
10.65	Pentafuranose ?	S	1.47	n.d.	n.d.	1.10	1.38	n.d.	n.d.	1.60
10.73	Sugar deriv.	S	n.d.	0.73	0.48	n.d.	n.d.	1.01	0.70	n.d.
10.77	Pentafuranose	S	1.24	1.71	1.40	0.81	1.01	1.14	1.38	1.55
10.87	Pentapyranoside ??	S	1.00	0.90	n.d.	n.d.	0.97	0.75	n.d.	n.d.
10.93	2-Deoxyribose ?	S	1.57	n.d.	n.d.	n.d.	0.00	n.d.	n.d.	n.d.
11.07	Arabinose*	S	1.03	1.47	2.89	2.65	0.98	0.81	0.71	0.61
11.11	Monosaccharide (Pentapyranose?)	S	0.98	1.07	1.56	0.74	0.99	0.64	0.63	0.64
11.19	Monosaccharide (Pentapyranose?)	S	1.08	0.43	0.94	n.d.	1.02	0.79	0.83	n.d.
11.23	Ribose*	S	1.03	0.64	1.12	0.80	0.88	1.03	0.90	0.99
11.41	Xylulose ?	S	0.98	0.67	0.74	0.28	1.04	0.82	0.64	0.71
11.81	Monosaccharide ?	S	n.d.	1.99	7.51	n.d.	n.d.	0.80	0.67	n.d.
11.89	Glucopyranose ?	S	n.d.	1.54	n.d.	n.d.	n.d.	0.17	n.d.	n.d.
11.95	Monosaccharide	S	n.d.	1.29	0.92	n.d.	n.d.	1.28	1.12	n.d.
12.09	Saccharide	S	n.d.	n.d.	0.60	n.d.	n.d.	n.d.	1.47	n.d.
12.23	Monosaccharide	S	1.13	0.54	n.d.	0.68	0.95	0.56	n.d.	0.83
12.37	unidentified Sugar deriv. ?	S	n.d.	0.59	0.26	n.d.	n.d.	1.40	0.92	n.d.
12.57	Glucopyranose	S	1.10	0.75	0.74	0.38	1.09	1.20	1.06	1.10
12.63	Fructose*	S	1.35	0.62	0.59	0.45	1.33	1.47	0.98	1.41
12.69	Fructose*	S	1.12	0.11	0.94	0.60	1.07	0.80	1.21	1.32
12.77	Galactose*	S	n.d.	n.d.	0.99	1.15	n.d.	n.d.	1.15	1.25
12.83	Glucose*	S	1.06	1.11	1.77	1.30	1.04	1.12	1.05	1.38
12.97	Glucose*	S	1.02	1.17	1.69	1.22	0.97	1.36	1.07	1.44
13.37	β -D-Galactofuranose ?	S	1.39	1.18	0.95	0.55	1.27	2.62	1.00	1.18
13.99	Hexose	S	1.16	0.61	0.40	0.28	1.32	1.16	1.35	1.42
14.27	Sedoheptulose	S	0.86	0.09	0.71	0.61	0.97	0.75	0.72	1.09
14.31	Hexose	S	0.97	0.62	0.37	n.d.	1.20	1.36	1.01	n.d.
14.39	Hexose	S	n.d.	n.d.	1.06	0.47	n.d.	n.d.	1.00	1.24
14.68	Saccharide	S	0.81	0.66	0.92	0.69	1.02	0.92	0.82	0.99
15.29	Saccharide deriv.	S	1.01	0.85	0.78	1.07	1.05	1.00	0.83	0.75
15.32	Saccharide	S	n.d.	n.d.	0.68	0.62	n.d.	n.d.	0.72	1.13
15.41	Galactosylglycerol	S	1.06	0.75	0.86	0.61	0.94	1.56	0.99	1.61
15.71	Galactosylglycerol	S	n.d.	n.d.	0.79	0.37	n.d.	n.d.	1.58	1.47
8.35	Glyceric acid*	SA	4.06	0.33	0.45	0.30	4.76	2.31	2.45	1.62
10.31	Threonic acid	SA	1.12	0.84	0.59	0.09	1.14	1.42	1.05	1.46
10.90	Uronic acid ?	SA	n.d.	n.d.	n.d.	0.06	n.d.	n.d.	n.d.	6.49
13.42	Hexoaldonic acid ?	SA	2.37	n.d.	0.74	0.51	1.64	n.d.	1.50	0.54
13.55	Gluconic acid*	SA	n.d.	n.d.	0.99	0.37	n.d.	n.d.	0.90	0.95
8.99	Erythritol ?	SAC	1.29	1.08	1.10	0.48	1.31	1.54	1.07	0.90
12.60	Sugar alcohol ?	SAC	1.16	n.d.	n.d.	n.d.	1.07	n.d.	n.d.	n.d.
13.08	Mannitol*	SAC	0.81	1.25	1.09	1.63	0.87	0.95	0.97	1.06
13.15	Viburnitol	SAC	1.06	1.01	1.17	1.66	0.90	0.79	0.97	0.99
13.47	myo-Inositol deriv. ?	SAC	n.d.	n.d.	0.62	0.47	n.d.	n.d.	0.81	1.21
13.63	Inositol iso. ?	SAC	0.97	0.92	0.99	n.d.	1.19	1.67	0.93	n.d.

Table 4.2 (continued)

RT	Metabolite	Class	Fold change							
			Lytic				Non-lytic			
			4 hpi	24 hpi	32 hpi	48 hpi	4 hpi	24 hpi	32 hpi	48 hpi
13.70	Inositol iso.	SAC	1.20	0.62	0.83	0.51	0.66	0.75	0.88	0.70
14.13	myo-Inositol*	SAC	1.17	0.88	0.91	0.91	1.05	0.77	0.74	0.73
19.40	Galactinol ??	SAC	1.07	0.75	0.72	0.65	1.08	1.86	1.08	1.41
16.63	complex Saccharide	CS	1.18	0.84	0.80	0.12	1.29	1.58	0.98	1.34
17.10	D-Xylobiose	CS	n.d.	n.d.	n.d.	0.51	n.d.	n.d.	n.d.	2.02
17.17	complex Saccharide	CS	n.d.	n.d.	0.69	n.d.	n.d.	n.d.	0.55	n.d.
17.22	Sucrose*	CS	1.01	n.d.	n.d.	n.d.	0.78	n.c.	n.d.	n.d.
17.67	Maltose*	CS	n.d.	0.82	0.00	2.01	n.d.	0.90	0.00	2.61
17.75	Trehalose, alpha,alpha'-, D-*	CS	1.27	1.35	3.69	7.78	1.58	1.16	1.48	4.47
18.11	Disaccharide	CS	n.d.	n.d.	0.81	0.56	n.d.	n.d.	0.79	1.81
18.21	Disaccharide	CS	n.d.	n.d.	1.05	n.d.	n.d.	n.d.	0.95	n.d.
18.29	Disaccharide	CS	n.d.	n.d.	0.90	n.d.	n.d.	n.d.	0.81	n.d.
18.93	Melibiose	CS	1.05	0.78	0.57	0.34	1.33	1.49	1.23	1.34
19.99	Digalactosylglycerol	CS	1.04	1.16	0.94	0.40	0.96	2.26	1.22	1.42
20.33	Disaccharide ?	CS	n.d.	n.d.	1.94	4.08	n.d.	n.d.	0.03	20.79
21.93	Disaccharide	CS	0.65	0.87	0.66	0.71	0.62	0.84	0.91	1.19
22.40	complex Saccharide deriv.	CS	0.91	0.83	0.67	0.47	0.97	1.43	1.14	1.12
22.71	Disaccharide	CS	0.96	0.81	0.56	n.d.	1.17	0.74	0.63	n.d.
27.02	Trisaccharide	CS	n.d.	n.d.	1.06	0.31	n.d.	n.d.	0.87	2.02
13.57	unsat. Hydrocarbon, iso. RT 13.81	H	1.04	0.86	0.94	0.48	1.10	1.06	0.70	0.67
13.81	unsat. Hydrocarbon, iso. RT 13.57	H	0.97	0.80	0.72	0.29	1.08	0.91	0.66	0.70
13.91	unsat. Hydrocarbon	H	1.10	0.85	0.83	0.47	1.21	1.14	0.82	0.69
14.10	unsat. Hydrocarbon	H	0.96	0.60	0.63	0.30	0.91	1.40	0.92	0.63
15.09	unsat. Hydrocarbon	H	1.39	2.47	0.76	0.25	1.81	4.39	0.92	1.17
15.47	unsat. Hydrocarbon	H	1.13	0.68	0.70	0.34	1.25	1.50	1.30	1.08
16.49	unsat. Hydrocarbon	H	n.d.	1.01	1.94	0.43	n.d.	1.01	0.82	1.10
18.47	unsat. Hydrocarbon	H	1.20	1.64	1.54	0.59	1.30	2.58	1.23	1.07
19.68	C ₃₁ H ₆₀ , 2DBE, iso. RT 19.90	H	1.15	0.77	1.02	0.70	1.16	1.05	0.96	0.78
19.90	C ₃₁ H ₆₀ , 2 DBE, iso. RT 19.68	H	1.07	0.71	1.06	0.59	1.13	0.98	0.87	0.66
21.36	C ₃₃ H ₆₂ , 3DBE, iso. RT 21.66	H	1.18	1.01	1.21	0.98	1.23	1.17	1.10	0.99
21.66	C ₃₃ H ₆₂ , 3DBE, iso. RT 21.36	H	1.05	0.79	1.05	0.62	1.12	0.97	0.91	0.86
18.27	Ergostatriene iso. ?	ST	n.d.	0.60	0.92	0.31	n.d.	1.13	1.17	0.90
18.79	Ergostatriene iso.	ST	0.89	0.51	1.00	0.43	1.07	1.10	1.24	0.98
19.02	Ergostatriene iso.	ST	0.93	0.50	0.99	0.39	1.08	0.95	1.15	0.74
19.20	Sterol	ST	0.99	0.89	0.64	0.50	1.03	0.96	1.12	1.12
20.67	Epibrassicasterol	ST	1.24	0.74	0.68	0.53	1.20	1.08	0.80	0.66
20.91	Sterol	ST	1.23	0.84	0.55	0.00	1.25	1.08	1.01	1.01
21.18	Sterol	ST	1.53	6.34	19.43	5.06	2.01	1.68	1.58	0.90
21.84	Ergostadienone ??	ST	n.d.	n.d.	0.30	0.19	n.d.	n.d.	1.76	1.66
12.43	Neophytadiene ⁺	T	1.16	0.71	0.67	0.40	1.25	1.18	1.04	0.75
12.59	(Z)-1,3-Phytadiene	T	1.05	0.68	0.72	0.56	1.18	1.07	0.92	0.76
12.73	(E)-1,3-Phytadiene	T	1.17	0.66	0.64	0.48	1.28	1.02	0.91	0.78
14.59	(E)-Phytol*	T	n.d.	n.d.	0.84	0.67	n.d.	n.d.	1.22	0.92
20.17	alpha-Tocopherol	T	0.88	1.09	1.33	0.66	0.61	0.90	0.91	0.89

Metabolites with a reverse match between 800 and 700 are indicated by "?", or by "??", if the reverse match lay between 700 and 600. "*" indicates metabolite identification confirmed by a standard or "+" an authentic, natural sample (see 6.4.3). Abbreviations: A, amine, AA, amino acid, Alc, alcohol, CA,

carboxylic acid, CS, complex saccharide, DBE, double bond equivalent, deriv., derivative, FA, fatty acid, HC, hydrocarbon, hpi, hours post infection, iso., isomer, n.c., not calculable, n.d., not detected, O, other, RT, retention time, S, saccharide, SA, sugar acid, SAc, sugar alcohol, ST, sterol, T, terpene, unsat., unsaturated.

Differential metabolomic analysis indicated a profound rewiring of host metabolism during viral infection (Table 4.2, and Appendix Table 5). We used canonical analysis of principal coordinates (CAP) (Anderson and Willis, 2003) to get a general overview of metabolic differences between the treatments. Cells infected by the lytic EhV201 or the non-lytic EhV163 and non-infected control cells were assigned as groups and each time point was analyzed separately. At 4 hpi treatments showed no statistical separation ($P = 0.7275$, permutation test) (Figure 4.3A) and accordingly axes were not differentiating between groups (Table 4.3). However, as viral infection progressed, metabolic profiles of all treatments at all later time points were resolved statistically (24 hpi: $P = 0.0058$, 32 hpi: $P = 0.0215$, and 48 hpi: $P = 0.01$, permutation test) (Figure 4.3B-D) and supported by CAP diagnostic values (Table 4.3). Infection with the non-lytic virus resulted in a temporal separation of metabolic profiles, as at 24 hpi this group showed a higher similarity to the lytic group (Figure 4.3B) but subsequently resembled the control (Figure 4.3C, D) (as was confirmed by cross validation). This trend suggested a critical phase of metabolite production impaired in the non-lytic infection. In contrast, the three biological replicates of the lytic infection were at all time points well separated from the other groups.

Table 4.3: Statistical support values of canonical analysis of principle coordinates (CAP). Complete list of statistical support values of CAP with non-infected control cells, lytic infected and non-lytic infected cells defined as groups. Data present eigenvalues (λ) and squared correlation (Δ^2) for the first two axes, misclassification error, and P values of the permutation test. An eigenvalue of > 0.9 , together with a high squared correlation, and a low misclassification error indicates a significant separation by the corresponding axis. Further, a $P \leq 0.05$ was regarded as significant.

Time	Constrained canonical axes				Statistics	
	1 st axis		2 nd axis		Cross validation	Permutation test
	λ	Δ^2	λ	Δ^2	Misclassification error	Trace statistic
4 hpi	0.4805	0.23088	0.30301	0.09182	44.44%	0.7275
24 hpi	0.96694	0.93497	0.9112	0.83029	22.22%	0.0058
32 hpi	0.94203	0.88743	0.67244	0.45217	22.22%	0.0215
48 hpi	0.98114	0.96263	0.67807	0.45978	22.22%	0.01

Abbreviation: hpi, hour post infection.

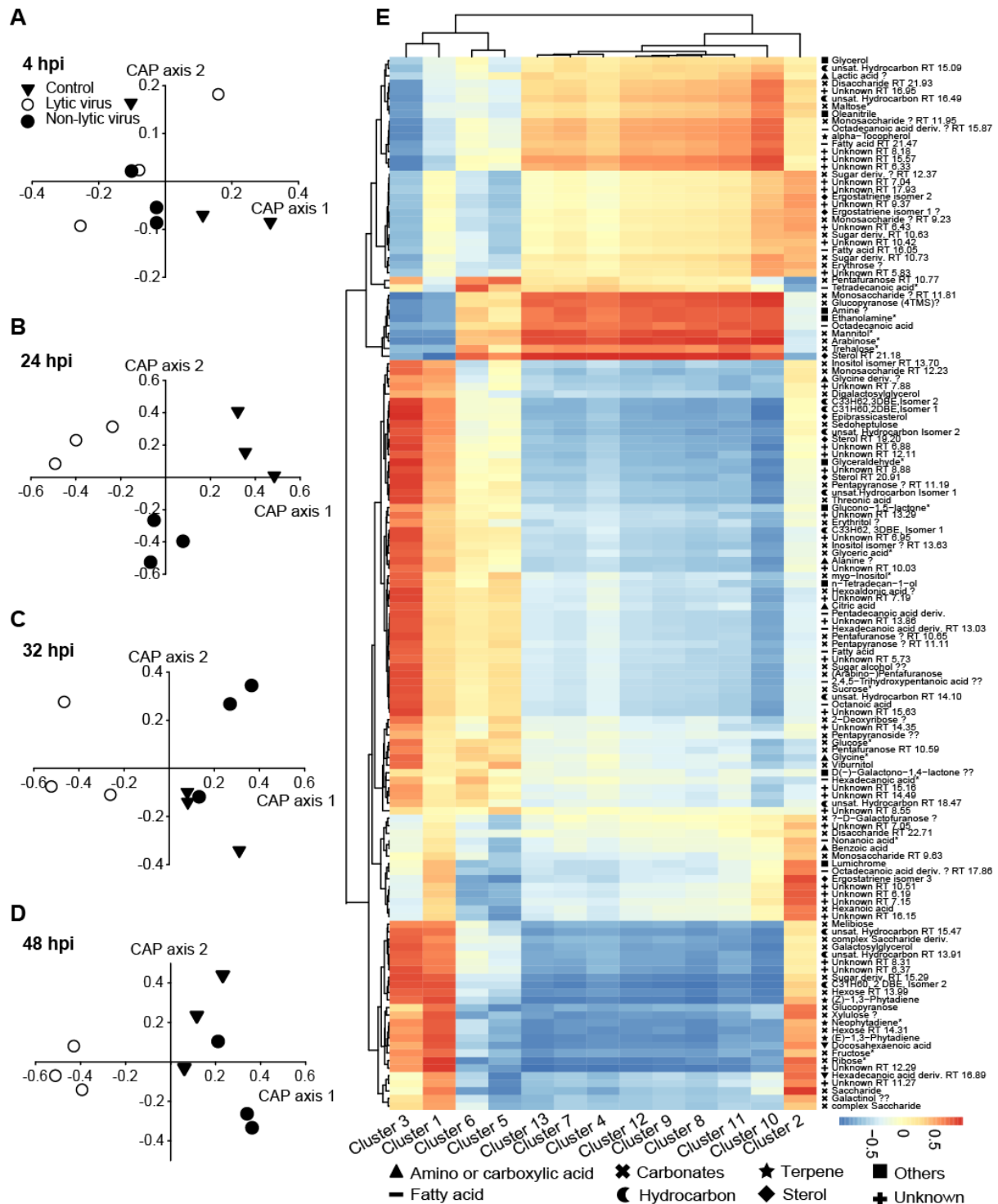


Figure 4.3: Viral-induced remodeling of host metabolism during infection. (A-D) Canonical analysis of principle coordinates (CAP) of metabolic profiles derived from control cells compared to cells infected by the lytic or non-lytic virus at (A) 4, (B) 24, (C) 32, and (D) 48 hpi (n=3). (E) Correlation of transcriptomic gene expression patterns (1 and 24 hpi), which are assigned into different clusters (columns), with metabolite abundance (4 and 24 hpi) (lines) based on weighted correlation network analysis (WGCNA). Symbols indicate the affiliation of metabolites to specific metabolic classes. Blue – low correlation; red – high correlation between transcriptome and metabolome. Transcriptomic data provided by S. Rosenwasser, WGCNA performed by O. Tzfadia. Abbreviation: hpi, hours post infection.

4.2.3 Correlation of metabolome and transcriptome profiles

For a direct comparison of metabolic levels with gene cluster profiles deriving from transcriptomic data under the same conditions and at comparable sampling times we used weighted correlation network analysis (WGCNA) (Langfelder and Horvath, 2008). As quickly changing gene expression patterns detected at 1 hpi were assumed to have an influence down-stream on the slower reacting metabolome at 4 hpi, these data sets were combined for the earlier time point and analyzed together with data deriving from 24 hpi. This analysis approach indicated a high correlation of many identified metabolites with gene expression patterns for several among the host gene clusters (Figure 4.3E).

Most prominent was this pattern for host gene cluster 3, which showed correlations to carbohydrates especially monosaccharides, amino acids and several among the fatty acids. This metabolic pattern fits well as genes aligned to this cluster involved biological functions related to glycolysis, fatty acid, and amino acid biosynthesis. Further, a high correlation with metabolic profiles was also observed for host gene cluster 1. Here, metabolites showing concentration patterns correlated with gene expression levels additionally involved carbohydrates, terpenoids, and sterols. Accordingly, host gene cluster 1 was enriched in biological functions such as photosynthesis, but also terpenoid and sterol metabolism.

4.2.4 The effect of viral infection on amino acids and small amines

We detected two different amino acids deriving from different metabolic amino acid synthesis pathways. Alanine, which descends from the glycolysis end product pyruvate, displayed similar concentrations as the control (fold change ~1.1) at 4 and 24 hpi, but gradually decreased with progressing lytic infection (fold change 0.8 at 32 hpi and 0.6 at 48 hpi). In cells infected by the non-lytic virus the pattern was nearly identical except for an induction relative to the control 24 hpi (fold change 1.7) (Figure 4.4, and Table 4.2). In contrast, levels of glycine were induced at all time points both during lytic and non-lytic infection in comparison to non-infected cells (fold change 1.5-2.5 for lytic infected cells and 1.4-2.0 for non-lytic infected cells) exhibiting highest concentrations 48 hpi (Figure 4.4A, and Table 4.2).

Two small amines, ethanolamine and an unidentified one, were among the metabolites exhibiting the strongest induction of all detected metabolites. Ethanolamine, which was detected 24 hpi onwards, gradually increased in lytic infected cells relative to the control from 6.6-fold to 24.1-fold with progressing infection. In contrast, although still displaying high concentrations in non-lytic infected cells, induction levels of ethanolamine gradually became weaker (from 4.7-fold to 3.5-fold at 48 hpi) relative to control cells (Table 4.2). Exactly the same pattern was observed in the unidentified amine (Table 4.2), indicating accumulation of small amines during infection independent of the replication strategy.

4.2.5 Effects of viral infection on glycolysis

Glucose exhibited increased concentrations in cells infected by the lytic virus at all time points (fold change > 1.0-1.7) relative to control cells, suggesting a breakdown of macromolecules such as glycolipids and storage carbohydrates which support glycolytic activity. Further, slightly increased glucose levels were also observed in non-lytic infected cells (fold change > 1.0-1.4). Non-phosphorylated forms of glycolysis products such as fructose, glyceraldehyde, and glyceric acid were all more abundant 4 hpi in cells infected by the lytic virus, with the most pronounced increase in glyceric acid (4.1-fold). At later time points (24 hpi onwards) these metabolites showed decreased concentrations in comparison to non-infected cells, suggesting their rapid consumption by downstream metabolic reactions. In cells infected by the non-lytic virus, fructose and glyceric acid were generally more abundant, whereas glyceraldehyde was slightly decreased 24 and 32 hpi (fold change < 1.0 and 0.7, respectively) (Figure 4.4A, and Table 4.2).

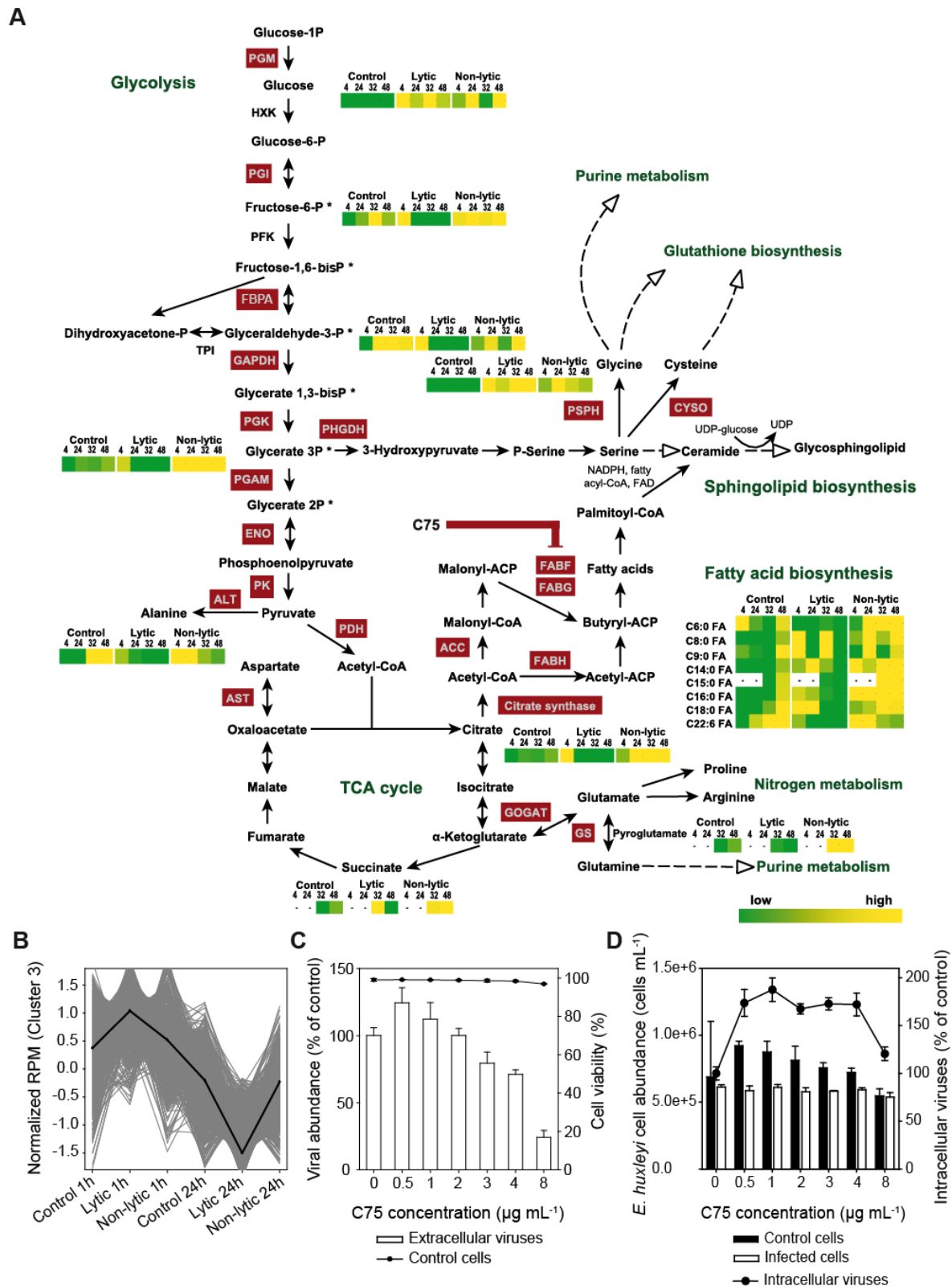


Figure 4.4: Viral-induced rewiring of host glycolysis facilitating fatty acid biosynthesis. (A) Integrated metabolic map of glycolysis, the tricarboxylic acid (TCA) cycle, fatty acid biosynthesis, and some steps of sphingolipid biosynthesis during infection by the lytic virus EhV201 or the non-lytic virus EhV163 compared to non-infected control cells. Inserted heat maps present normalized intensities (mean, $n=3$) of specific metabolites associated to this pathways in *E. huxleyi* control cells, and cells infected by the lytic or non-lytic virus at 4, 24,

32, and 48 hpi. Genes associated to these metabolic pathways and detected during transcriptome analysis are marked in dark red. The dark red bar indicates inhibition of fatty acid biosynthesis by C75. Metabolites marked by an “*” were detected in the non-phosphorylated form and a “-” sign indicates the absence of a metabolite at a specific time point. Dashed lines refer to connections via a known metabolic pathway. Green – low metabolite concentration; yellow – high metabolite concentration. For corresponding fold change data of the depicted metabolites see Table 4.2. (B) Gene expression pattern of host genes (cluster 3) associated with these metabolic pathways. Expression normalized values of each gene are presented as gray lines and the average is indicated by a thick black line. Transcriptomic data were provided by S. Rosenwasser. (C) The effect of inhibition of fatty acid biosynthesis by various concentrations of C75 on extracellular virus abundance at 72 hpi relative to viruses released from infected cells without addition of the inhibitor (% of control) (mean \pm SD, n=3), and the percentage of viable *E. huxleyi* cells at 24 hpi as measured by flow cytometry (mean \pm 3·SD, n=3). (D) The effect of inhibition of fatty acid biosynthesis by various C75 concentrations on host abundance at 72 hpi (mean \pm SD, n=3) measured by flow cytometry and intracellular viral DNA production at 24 hpi relative to viral DNA production in lytic infected cells without addition of the inhibitor (% of control). Intracellular viral DNA production was measured by qPCR of the major capsid protein (MCP) gene using biological triplicates and technical duplicates. Note the different scaling of x- and y-axis. Abbreviations: ACC, acetyl-CoA carboxylase, ALT, alanine transferase, AST, aspartate transaminase, CYSO, cysteine synthase/O-phosphoserine sulfhydrylase/cystathionine beta-synthase, ENO, enolase, FA, fatty acid, FABF-H, β -ketoacyl-[acyl-carrier-protein] synthase I-III, FAD, flavin adenine dinucleotide, FBPA, fructose-bisphosphate aldolase, GAPDH, glyceraldehyde phosphate dehydrogenase, GOGAT, glutamate synthase, GS, glutamine synthase, hpi, hours post infection, HXK, hexokinase, NADPH, nicotinamide adenine dinucleotide phosphate (reduced form), P, phosphate, PDH, pyruvate dehydrogenase complex, PFK, 6-phosphofructokinase, PGAM, phosphoglycerate mutase, PGI, phosphoglucosomerase, PGK, phosphoglycerate kinase, PGM, glucose-1-phosphate phosphodismutase, PHGDH, 3-phosphoglycerate dehydrogenase, PK, pyruvate kinase, PSPH, phosphoserine phosphatase, RPM, reads per million, TPI, triose phosphate isomerase, UDP, uridine diphosphate.

4.2.6 The role of fatty acid biosynthesis in viral infection

Metabolic levels of citrate, the initial molecule of the tricarboxylic acid cycle which receives acetyl coenzyme A (acetyl-CoA) derived from pyruvate out of glycolysis, were significantly induced in lytic infected cells 4 hpi (9.1-fold) and decreased afterwards (Figure 4.4A). A less pronounced increase in citrate concentration (fold change >2.3) was detected during non-lytic infection. Succinic acid, the only other detected tricarboxylic acid (TCA) cycle substrate and only present at 32 and 48 hpi, showed a strong induction in cells infected by the lytic virus (7.5-fold) in comparison to non-infected control cells at 32 hpi, but was completely depleted 48 hpi. At 32 hpi this pattern was represented in cells infected by the non-lytic virus, but concentrations also remained high during the later time point (fold change 2.3) (Figure 4.4A, and Table 4.2). As no further compounds involved in the TCA cycle were observed, citrate might alternatively feed the “citrate shuttle”, enhancing fatty acid biosynthesis. In cells infected by the lytic virus, most free fatty acids (C8-C16) showed higher concentrations at 4 and 32 hpi (fold change 1.1-2.4) relative to control cells, whereas long chain fatty acids (C18, C22:6) decreased at 32 hpi (docosahexaenoic acid, DHA, already at 24 hpi) (Figure 4.4A, and Table 4.2). In contrast, non-lytic infected cells displayed higher concentrations of fatty acids at almost all time points, with a slight reduction in DHA at 32 and 48 hpi when compared to control cells.

Gene expression of enzymes involved in glycolysis and fatty acid biosynthesis (host gene cluster 3) as well as the gene encoding citrate synthase were up-regulated at 1 hpi, but exhibited a strong down-regulation 24 hpi (Figure 4.4A, B).

If in an additional experiment *E. huxleyi* cells were treated with the fatty acid synthase (FAS) inhibitor C75 (4-methylene-2-octyl-5-oxotetrahydrofuran-3-carboxylic acid) (Pizer et al., 1998), extracellular viral production was reduced in a dose-dependent manner (Figure 4.4C). In contrast, inhibition of fatty acid biosynthesis did not reduce intracellular viral DNA production (Figure 4.4D). Inhibitor concentrations reducing extracellular viral production exhibited no toxicity for *E. huxleyi* cells as >90% of the cells were viable (Figure 4.4C, D). These findings indicate a dependence of successful viral production and release on fatty acid production.

4.2.7 Induction of the pentose phosphate pathway during late viral infection

Besides supporting glycolysis, glucose can facilitate the pentose phosphate pathway (PPP). In general, we detected lower concentrations of non-phosphorylated forms of metabolites involved in this pathway in lytic infected than control cells (Figure 4.5A, and Table 4.2). The initial product, glucono-1,5-lactone was only slightly reduced at all time points (fold change ~0.9) as was gluconic acid at 32 hpi. Cells infected by the non-lytic virus showed a similar pattern except for a moderate increase of glucono-1,5-lactone 4 hpi (1.2-fold). In lytic infected cells ribose, which can stimulate nucleotide biosynthesis, either reflected the control (fold change 1.0 at 4 and 1.1 at 32 hpi) or showed depletion at 24 hpi (0.6-fold) and 48 hpi (0.8-fold). The downstream PPP products xylulose and sedoheptulose displayed lower concentrations in lytic infected cells relative to non-infected cells at all time points with a very strong down-regulation of sedoheptulose 24 hpi (fold change 0.1). Although induced at 4 hpi (2.7-fold), this reduction was reflected in erythrose from 24 hpi onwards (fold changes 0.6, 0.5, and 0.1 at 24, 32, and 48 hpi, respectively). These patterns indicate an induction of upstream PPP substrates facilitating nucleotide biosynthesis accompanied by depletion in downstream products in lytic infected cells. In contrast, during the observation period ribose levels of non-lytic infected cells nearly reflected concentrations observed in control cells (fold change 0.9-1.0), and xylulose and sedoheptulose were slightly reduced or exhibited the same concentrations as control cells at 4 hpi (sedoheptulose also at 48 hpi). Only erythrose showed a similar concentration pattern in non-lytic infected cells as observed during the course of lytic infection but with a stronger induction at 4 hpi (5.5-fold) and a slighter reduction later on (fold change 0.8 at 24, and 48 hpi). At 48 hpi erythrose exhibited a strong concentration decrease (0.2-fold) in non-lytic infected compared to non-infected control cells.

Genes related to the PPP and to nucleotide biosynthesis (gene cluster 4) displayed a moderate up-regulation at 1 hpi and gradually increased at 24 hpi during lytic infection (Figure 4.5A, B).

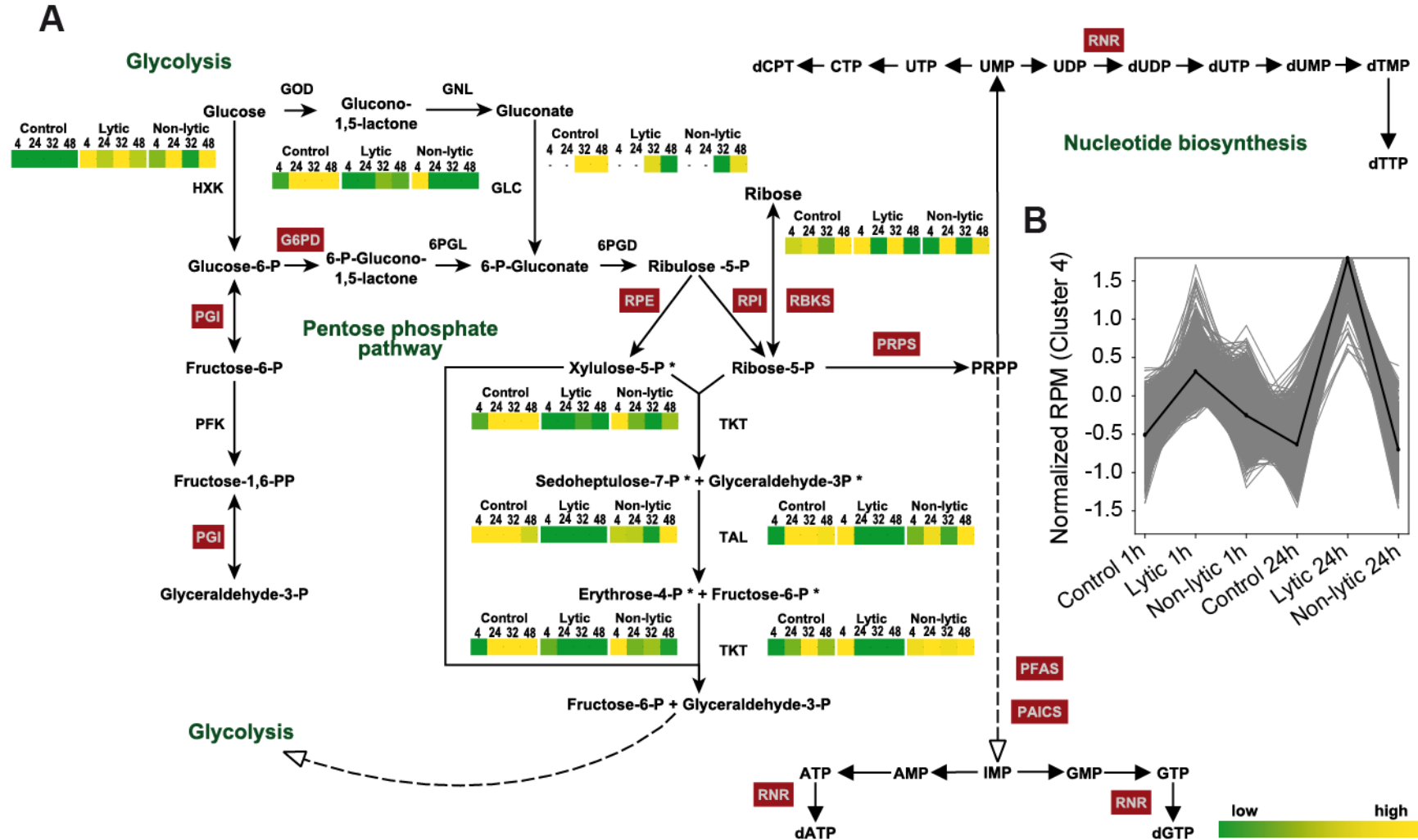


Figure 4.5: Induction of the pentose phosphate pathway and nucleotide biosynthesis during viral infection. (A) Integrated metabolic map of the pentose phosphate pathway and nucleotide biosynthesis during infection by the lytic virus EhV201 or the non-lytic virus EhV163 compared to non-infected control cells. Inserted heat maps present normalized intensities (mean, $n=3$) of specific metabolites associated with these

pathways in *E. huxleyi* control cells, and cells infected by the lytic or non-lytic virus at 4, 24, 32, and 48 hpi. Genes associated to these metabolic pathways and detected during transcriptome analysis are marked in dark red. Metabolites marked by an “*” were detected in non-phosphorylated form and “-” sign indicates the absence of a metabolite at a specific time point. Green – low metabolite concentration; yellow – high metabolite concentration. For corresponding fold change data of the depicted metabolites see Table 4.2. (B) Gene expression pattern of host genes (cluster 4) associated with these metabolic pathways. Expression normalized values of each gene are presented as gray lines and the average indicated by a thick black line. Transcriptomic data were provided by S. Rosenwasser. Abbreviations: 6PGD, 6-phosphogluconic dehydrogenase, 6PGL, 6-phosphogluconolactonase, AMP, adenosine monophosphate, ATP, adenosine triphosphate, CTP, cytidine triphosphate, dATP, deoxyadenosine triphosphate, dCTP, deoxycytidine triphosphate, dGTP, deoxyguanosine triphosphate, dTMP, deoxythymidine monophosphate, dTTP, deoxythymidine triphosphate, dUDP, deoxyuridine diphosphate, dUMP, deoxyuridine monophosphate, dUTP, deoxyuridine triphosphate, G6PD, glucono-6-phosphate dehydrogenase, GLC, glucokinase, GMP, guanosine monophosphate, GNC, gluconokinase, GNL, gluconolactonase, GOD, glucose 1-dehydrogenase, GTP, guanosine triphosphate, hpi, hours post infection, HKK, hexokinase, IMP, inosine monophosphate, P, phosphate, PAICS, phosphoribosylaminoimidazole carboxylase, PFAS, phosphoribosylformylglycinamide synthase, PGI, phosphoglucoisomerase, PGK, phosphoglycerate kinase, PRPP, 5-phospho-D-ribose α -1-pyrophosphate, PRPS, ribose-5-phosphate to PRPP synthase, RBKS, ribokinase, RNR, ribonucleotide reductase, RPE, ribulose-phosphate 3-epimerase, RPI, ribose-5-phosphate isomerase, RPM, reads per million, TAL, transaldolase, TKT, transketolase, UDP, uridine diphosphate, UMP, uridine monophosphate, UTP, uridine triphosphate.

4.2.8 The role of terpene and sterol biosynthesis in viral progeny assembly

Metabolic analysis indicated severe concentration depletion in several products of the terpene and sterol biosynthesis pathways exclusively during lytic infection (Figure 4.6A, and Table 4.2). At 4 hpi the detected diterpenes, neophytadiene and two phytadiene isomers, in cells infected by the lytic EhV201 displayed moderately increased or similar levels as the control (fold change 1.0-1.2). But as the lytic infection progressed all diterpenes, including phytol which was detected at 32 hpi onwards, experienced a profound reduction in abundance (Figure 4.6A, and Table 4.2). This pattern was most drastic for neophytadiene showing a 0.4-fold reduction 48 hpi (Table 4.2). Accordingly, sterols, among which we detected epibrassicasterol, three putative isomers of $\Delta^{5,22}$ ergostatriene (sterols 1-3), and probably ergostadienone (sterol 4), at 4 hpi also showed similar concentrations as the control (fold change 0.9-1.2), but like diterpenes depleted later during lytic infection (Figure 4.6A, and Table 4.2). Among sterols experiencing the most expressed abundance reduction during lytic infection were an isomer of ergostatriene and putative ergostadienone (fold change 0.3 and 0.2 at 48 hpi). An unidentified sterol even experienced complete shutdown 48 hpi in lytic infected cells (Table 4.2). In contrast, cells infected by the non-lytic virus displayed similar or only slightly changed terpene and sterol levels in comparison to the control (Figure 4.6A, and Table 4.2).

Expression patterns of all detected genes encoding enzymes involved in the mevalonate (MVA) or the methylerythritol phosphate (MEP) pathway of terpene biosynthesis (host gene cluster 1) were down-regulated in lytic infected cells 24 hpi, whereas they showed no expression change compared to the control at 4 hpi (Figure 4.6A, B).

As two different pathways are involved in terpene biosynthesis, we specifically inhibited each to determine the effect on viral production and decipher, whether both or only one among them are involved. Treatment of *E. huxleyi* cells with cerivastatin, which specifically inhibits the rate limiting enzyme of the MVA pathway 3-hydroxy-3-methylglutaryl-CoA reductase (HMGR) (Mason, 2006), 2 h prior to lytic viral infection led to a reduction in extracellular viral production (Figure 4.6C). Interestingly, intracellular viral DNA production was not significantly different from the control at the various cerivastatin concentrations tested ($P = 0.317$, one-way ANOVA)

(Figure 4.6D). In contrast, inhibition with fosmidomycin, a specific inhibitor of 1-deoxy-D-xylulose-5-phosphate reductoisomerase (DXR) involved in the MEP route (Yeh and DeRisi, 2011), did not affect viral production at any of the tested concentrations (Figure 4.6E). None of the used inhibitors was toxic to *E. huxleyi* cells as >95% of the cells were viable (Figure 4.6C-E). These observations indicate that the MVA-branch of terpene biosynthesis is crucial during viral replication.

Since we assumed sterol depletion to be essential for the production of the released viruses, we further analyzed the metabolic profile of isolated, purified EhV201 virions (Table 4.4). Indeed, together with three fatty acids and a few other host derived molecules we detected (24S)-24-methylcholesta-5,22E-diene-3 β -ol, also called epibrassicasterol, the dominant sterol of *E. huxleyi* (Figure 4.6F) in extracts of isolated virions (Figure 4.6G). This suggests that this sterol constitutes a part of the viral lipid membranes.

Table 4.4: List of identified metabolites in EhV201 virions. The table presents all identified metabolites isolated from purified, concentrated EhV201 virions and indicates whether they were also found among the metabolites of the host (compare Table 4.2).

Model-Ion	RT	Metabolite	Class	Presence in host
129.1	10.77	Carboxylic acid	Carboxylic acid	no
285.2	13.06	Tetradecanoic acid*	Fatty acid	yes
313	14.36	Hexadecanoic acid*	Fatty acid	yes
117	15.57	Octadecanoic acid*	Fatty acid	yes
72	16.34	Oleic acid amide ?	Amide	no
122.1	17.03	unsaturated Hydrocarbon	Hydrocarbon	yes
221.1	17.09	Fatty acid derivative ??	Fatty acid derivative	no
248.1	17.75	Carboxylic acid	Carboxylic acid	no
399.3	18.36	Octadecanoic acid derivate	Fatty acid derivative	yes
380.3	21.33	Epibrassicasterol	Sterol	yes

Metabolites with a reverse match between 800 and 700 are indicated by a "?" or by "??", if the reverse match lay between 700 and 600. "*" indicates metabolite identification confirmed by a standard. Abbreviation: RT, retention time.

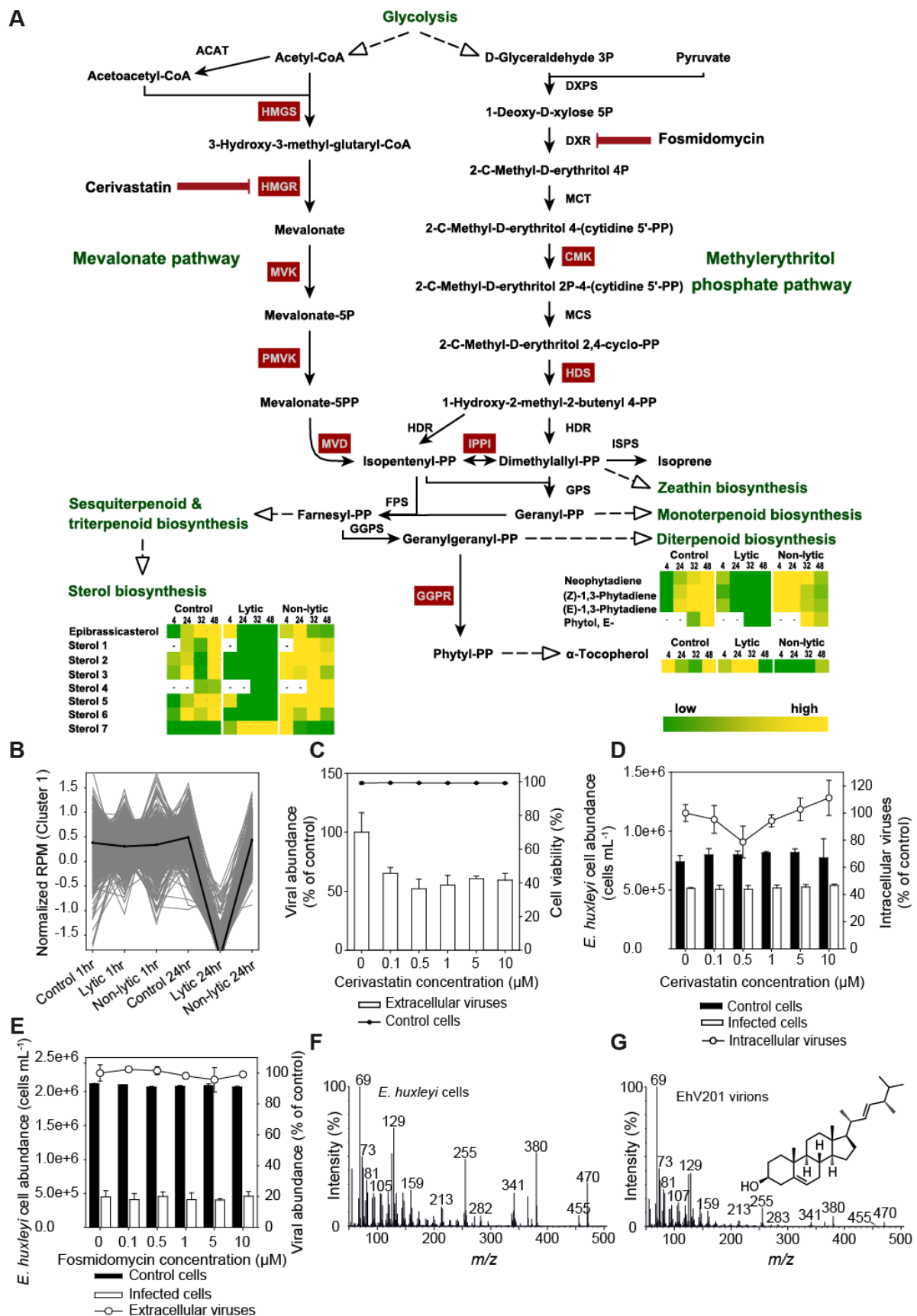


Figure 4.6: Terpene and sterol biosynthesis via the mevalonate pathway is required for viral replication. (A) Enzymatic and metabolic patterns of terpenoid and sterol biosynthesis during infection by the lytic virus EhV201 or the non-lytic virus EhV163 compared to non-infected control cells. Inserted heat maps present normalized intensities (mean, $n=3$) of

specific metabolites associated to this pathway in *E. huxleyi* control cells, and cells infected by the lytic or non-lytic virus at 4, 24, 32, and 48 hpi. Genes associated with these metabolic pathways and detected during transcriptome analysis are marked in dark red. Dark red bars indicate inhibition of the mevalonate (MVA) pathway by cerivastatin and of the methylerythritol phosphate (MEP) pathway by fosmidomycin. Sterols 1-3 are probably isomers of ergostatriene, sterol 4 is putative ergostadienone, sterols 5-7 remain unidentified. “-” indicates the absence of a metabolite at a specific time point. Dashed lines refer to connections via a known metabolic pathway. Green – low metabolite concentration; yellow – high metabolite concentration. For corresponding fold change values of the depicted metabolites see Table 4.2. (B) Gene expression pattern of host genes (cluster 1) associated with these metabolic pathways. Expression normalized values of each gene are presented as gray lines and the average indicated by a thick black line. Transcriptomic data were provided by S. Rosenwasser. (C) The effect of inhibition of the MVA pathway by various cerivastatin concentrations on extracellular virus abundance at 72 hpi relative to viruses released from infected cells without addition of the inhibitor (% of control) (mean \pm SD, $n=3$), and on the percentage of viable *E. huxleyi* cells at 24 hpi as measured by flow cytometry (mean \pm 3·SD, $n=3$). (D) The effect of inhibition of the MVA pathway by various cerivastatin concentrations on host abundance at 72 hpi (mean \pm SD, $n=3$) measured by flow cytometry and intracellular viral DNA production at 24 hpi relative to viral DNA production in infected cells without addition of the inhibitor (% of control). Intracellular viral DNA production was measured by qPCR targeting the major capsid protein (MCP) gene using biological triplicates and technical duplicates and was not significantly different at the various cerivastatin concentrations ($P = 0.317$, one-way ANOVA). (E) The effect of inhibition of the MEP pathway by various fosmidomycin concentrations on host cell abundance and on extracellular virus abundance (both at 72 hpi) relative to viruses released from infected cells without addition of the inhibitor (% of control) (mean \pm SD, $n=3$). Note the different scaling of x- and y-axis. (F) Mass spectrum of epibrassicasterol, the main sterol detected in *E. huxleyi* cells. (G) Mass spectrum of epibrassicasterol isolated from concentrated, purified EhV201 virions. The insert displays the structure of the compound. Abbreviations: ACAT, acetyl-CoA C-acetyltransferase, CMK, 4-(cytidine 5'-diphospho)-2-C-methyl-D-erythritol kinase, DXPS, 1-deoxy-D-xylulose-5-phosphate synthase, DXR, 1-deoxy-D-xylulose-5-phosphate reductoisomerase, FPS, 2,6-farnesyl-diphosphate synthase, GGPR, geranylgeranyl diphosphate reductase, GGPS, geranylgeranyl diphosphate synthase, GPS, geranyl-diphosphate synthase, HDR, 4-hydroxy-3-methylbut-2-enyl-diphosphate reductase, HDS, (E)-4-hydroxy-3-methylbut-2-enyl-diphosphate synthase, HMGR, 3-hydroxy-3-methylglutaryl-CoA reductase, HMGS, 3-hydroxy-3-methylglutaryl-CoA synthase, hpi, hours post infection, IPPI, isopentenyl-diphosphate delta-isomerase, ISPS, isoprene synthase, MCS, 2-C-methyl-D-erythritol 4-phosphate cytidyltransferase, MCT, 2-C-methyl-D-erythritol 4-phosphate cytidyltransferase, MVK, mevalonate kinase, MVD, diphosphomevalonate decarboxylase, m/z , mass to charge ratio, P, phosphate, PMVK, phosphomevalonate kinase, PP, pyrophosphate, RPM, reads per million.

4.2.9 Effect of viral challenge of virus-resistant *E. huxleyi* host strains on terpene and sterol biosynthesis

We tested whether the phenomenon of depletion of products deriving from the terpene biosynthesis pathway during infection is unique for strains susceptible to viruses. Therefore, we challenged two pre-grown resistant *E. huxleyi* strains, CCMP373 and CCMP379, with the lytic virus (EhV201). Before (0 h) and 32 h after virus addition we screened the intracellular metabolites of the resistant host cell cultures for terpenes and sterols. Both resistant strains showed a slightly arrested growth directly after they were challenged with the virus, but grew linearly after 32 h until 72 h, when the observation period ended (Figure 4.7A). In contrast, strain CCMP2090, which is susceptible to viral infection, decreased in abundance 24 hpi (Figure 4.7A). Since we had already analyzed the metabolic profile of the virus-susceptible strain in the previous experiment, we did not extract metabolites from this control.

Peak areas of metabolites of interest (terpenes and sterols) were normalized by cell numbers, because other normalization methods were not suitable. We detected several diterpenes, neophytadiene, and two phytadiene isomers, alpha-tocopherol, and sterols, among them epibrassicasterol, three isomers of $\Delta^{5,22}$ ergostatriene and three unidentified sterols. In strain CCMP373 the three phytadiene species although showed lower concentrations 32 h after virus addition, alpha-tocopherol and all sterols increased in comparison to concentrations before the viruses were added (Figure 4.7B black and white). When strain CCMP379 was examined all detected products of the terpene biosynthesis pathways showed induced levels 32 h after virus addition (Figure 4.7B color). This further indicates the importance of this pathway during lytic infection in cells susceptible to viruses.

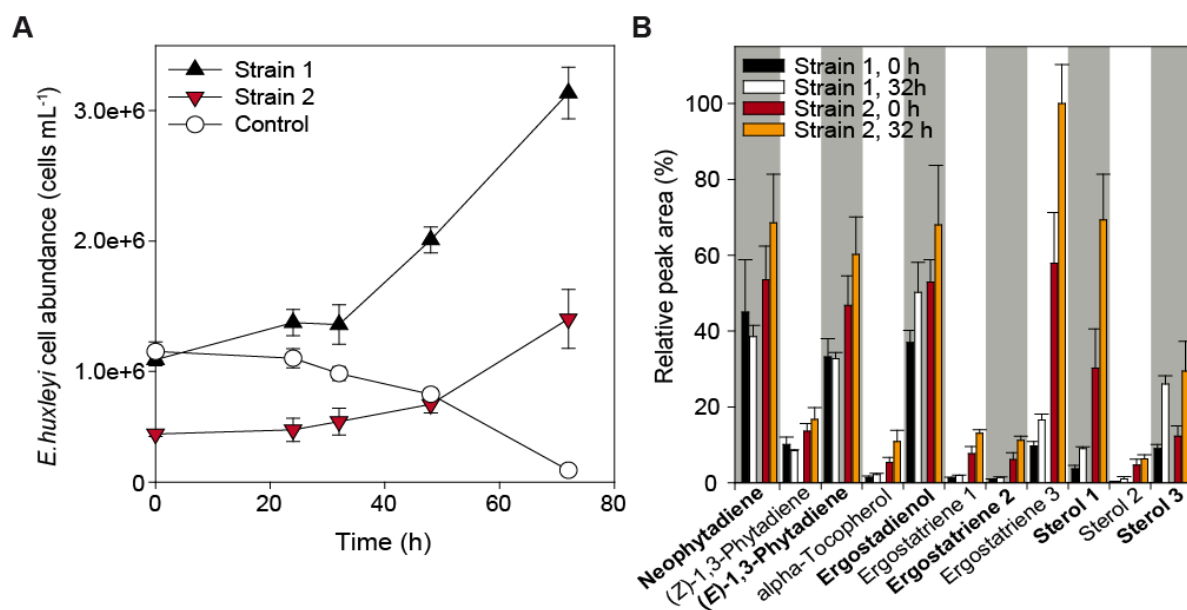


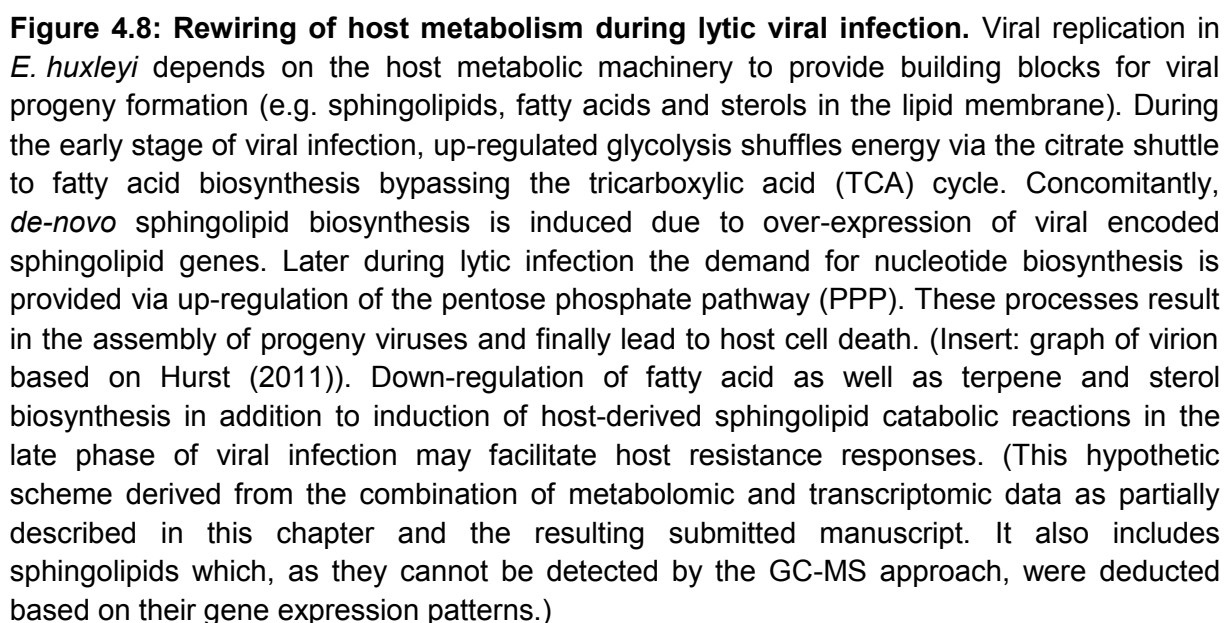
Figure 4.7: Viral challenging of resistant host strains. (A) Host cell abundance after challenging of the two virus-resistant strains and a strain susceptible to viral infection used as a control with the lytic virus (EhV201) (mean \pm SD, $n=3$). (B) Relative intensities of detected terpenes and sterols in cells of the resistant strains before (0 h) and after (32 h) cells were challenged with the lytic virus. Strain 1: CCMP373, strain 2: CCMP379, control: CCMP2090. Ergostatriene 1-3 indicate three different isomers of $\Delta^{5,22}$ ergostatriene and sterol 1-3 refer to unidentified sterols. Data represent means of biological triplicates of integrated peak area relative to the largest detected peak (ergostatriene isomer 3 in strain CCMP379 32 h after addition of viruses).

4.3 Discussion

Our combined metabolomic, transcriptomic and pharmacological approaches proved a sophisticated tool to investigate host-virus interactions in the unique system of one *E. huxleyi* host being infected by a specific lytic and non-lytic virus. This unique viral combination together with the extensive analysis tools allowed us to determine key metabolic processes constituting specific host responses to viral infection. This was possible as we could successfully link rapid transcriptomic gene regulation within 1 hpi to the resulting metabolic changes manifested later within infected host cells. Thus, we could finally identify those metabolic pathways that are essential for successful viral replication and release during infection of an *E. huxleyi* host. Uniquely, this led to a comprehensive picture of the essential regulation processes during viral infection of an algal host.

We present here data on a rapid rewiring of host metabolism to fulfill viral demands. The algal host was forced to provide building blocks for viral progeny formation such as lipids for viral membranes and synthesized nucleotides. We could show that glycolysis activity increased early during lytic infection. Further, high gene expression of the pyruvate dehydrogenase already 1 hpi indicated that energy was fed via the citrate shuttle into fatty acid biosynthesis, thereby bypassing the TCA cycle (Figure 4.8). These fatty acids can be incorporated into viral membranes and become parts of viral glycosphingolipids, which constitute an important fraction of EhV virions (Vardi et al., 2009, 2012; Fulton et al., 2014). Additionally, sterols represent another important building block of viral membranes. Only later, energy was transferred via the PPP to nucleotide biosynthesis, clearly indicating that production of lipid membranes precedes DNA synthesis in EhV. Depletion of fatty acids, terpenes and sterols accompanied by a down-regulation of genes encoding for enzymes involved in these pathways with progressing infection can therefore be interpreted as host defense mechanisms to prevent viral progeny formation (Figure 4.8).

It was necessary to document the performance of both, host and viruses, during the experimental period. In general, the observed infection pattern by the lytic EhV201 well reflected those detected in coccolithovirus infection as documented in the laboratory (Schroeder et al., 2002) or in natural populations (Pagarete et al., 2009, 2012). Further, ultrastructural changes such as chloroplast degradation indicate a reduction of photosynthesis efficiency during the lytic phase in EhV, which is in accordance with previous findings (Bidle et al., 2007; Vardi et al., 2009). Although EhV163 has been observed to be lytic in CCMP1516, a strain closely related to CCMP2090 (Schroeder et al., 2002), it did not display a lytic infection pattern during the study described here. Instead, our data clearly indicate different replication strategies with one virus behaving lytic and the other non-lytic.



The strong gradual increase of ethanolamine concentration with progressing lytic infection drew our attention to this small amine, although we had no supporting gene regulation patterns deriving from transcriptome data. Ethanolamine constitutes the head group of phosphatidylethanolamine, a lipid species which accumulated during infection of a human hepatoma cell line by Hepatitis C virus (HCV) at the time when viral replication was observed (Diamond et al., 2010). Phosphatidylethanolamine assumingly is involved in the formation of cytosolic lipid droplets and modified membrane compartments that promote replication and assembly of infectious viruses (Diamond et al., 2010). Therefore, elevated ethanolamine concentrations probably hint for accelerated lipid production needed for viral replication.

As amino acids constitute the major building blocks of proteins, the demand for these compounds increases during lytic viral infection. Proteomic analysis revealed at least 28 proteins including 23 putative membrane proteins in EhV86 virions (Allen et al., 2008b), which have to be produced by the host during viral assembly. Therefore, a moderate induction followed by depletion in alanine might reflect downstream processing of this free amino acid and its incorporation into viral proteins. This is in accord with induced amino acid metabolism during infection of human endothelial cells by Kaposi's Sarcoma-associated herpesvirus (KSHV) (Delgado et al., 2012). The detection of only a few amino acids or their derivatives in the metabolome further might indicate a rapid binding into proteins preventing the observation of free amino acids. The seemingly contradicting increased concentration pattern displayed by glycine, the second identified amino acid, can probably be explained by its incorporation into glutathione (Johnston and Bloch, 1951). EhV was reported to trigger the production of reactive oxygen species (ROS) such as hydrogen peroxide as a result of elevated oxidative stress in infected *E. huxleyi* cultures in the laboratory (Evans et al., 2006). Glutathione in turn functions as sensor and response regulator for stress in microalgae (Janknegt et al., 2009) and can detoxify ROS via an ascorbate-glutathione cycle (Shiu and Lee, 2005). In this scenario, glycine production is increased resulting in the observed induction until ROS concentration reaches a threshold level. Afterwards glycine is enzymatically adjoined to γ -glutamyl-cysteine to produce glutathione (Dupont et al., 2004), which then functions in detoxification of these virally induced ROS. Support for this scenario

is further found in the transcriptome data, where we observed a significant up-regulation of glutathione metabolism genes at 24 hpi during lytic infection.

We detected slightly elevated glucose levels throughout lytic infection, although genes encoding glycolysis proteins were up-regulated at the onset of infection but showed a strong down-regulation 24 hpi. But instead of directly reflecting glycolysis activity, meaning that high glycolysis would rapidly reduce glucose levels and thus prevent its accumulation, induced glucose concentration might derive from a breakdown of storage molecules. These might include glycolipids and storage carbohydrates such as beta-D-glucan, a common storage compound accumulating in *E. huxleyi* cells (Varum et al., 1986). Therefore, glycolytic activity is probably indirectly supported. Further, glucose provides a suitable head group for glucosyl ceramides needed for the formation of viral glycosphingolipids, which constitute a part of viral membranes (Vardi et al., 2009, 2012). So instead of contradicting glycolysis induction, a slight accumulation of glucose might instead indicate elevated production or release rates due to multiple downstream target reactions, which involve glucose.

The predicted increase in glycolytic activity right after the onset of lytic infection based on an up-regulation of transcriptomic gene expression profiles 1 hpi provides an energy source for molecules needed during viral assembly. In fact, transcriptomic data indicated that pyruvate hydrolase (PDH) transferred this energy to acetyl-CoA which in turn stimulated fatty acid biosynthesis thereby circumventing the TCA cycle via the citrate shuttle. This process induced *de-novo* fatty acid synthesis and finally led to elevated concentrations of saturated C8-C16 free fatty acids, while the unsaturated DHA got depleted. Concomitantly, concentrations of saturated and monounsaturated fatty acids were found to increase during infection of laboratory cultures with EhV86, whereas intracellular levels of structurally more complex polyunsaturated fatty acids decreased (Evans et al., 2009). Further, hints for induction of glycolysis and lipid metabolism during viral infection of *E. huxleyi* cells were also reported from EST and microarray analysis (Kegel et al., 2010) and a transcriptomic analysis of mesocosm samples (Pagarete et al., 2011). This overall pattern of induced glycolysis facilitating fatty acid biosynthesis was further reported as a strategy in several enveloped human viruses. Up-regulation of central carbon metabolism including glycolysis early during lytic infection in human cytomegalovirus

(HCMV) (Munger et al., 2008) shuffled energy via a shortcut in the TCA cycle to the fatty acid biosynthesis pathway (Vastag et al., 2011). A similar pattern with induced glycolysis and elevation of metabolites involved in the synthesis of fatty acids was found in human endothelial cells infected by KSHV (Delgado et al., 2012). While inhibition of fatty acid biosynthesis led to a reduction in EhV release during lytic infection of *E. huxleyi* cells, it even provoked apoptosis of KSHV-infected endothelial cells (Delgado et al., 2012) indicating the requirement of this synthesis pathway for viral survival and release. Therefore, we suspect that the reduction in gene expression at 24 hpi reflected in fatty acid concentrations during late lytic infection of *E. huxleyi* constitutes a host defense mechanism to prevent successful viral release.

Successful viral assembly is dependent on fatty acid biosynthesis as seen from the reduction of viral production following fatty acid biosynthesis inhibition. As three fatty acids were detected in the metabolic profile of purified virions, fatty acids are supposedly needed as part of viral membranes. EhV possesses a lipid membrane (Mackinder et al., 2009) partially built-up by glycosphingolipids containing a C14 fatty acid side chain (Vardi et al., 2009). A siRNA screening determined an involvement of multiple long chain acyl-CoA synthetases and fatty acid elongases in HCMV replication and observed enrichment of C26-C34 saturated fatty acids in virion envelopes (Koyuncu et al., 2013). Our GC-MS approach did not allow the detection of free fatty acids larger than DHA, but we might assume the existence of fatty acids in EhV membranes, especially because we detected three fatty acids of a mid chain length in isolated virions. Nevertheless, further analysis would need to reveal the specific composition and chain lengths of fatty acids in viral membranes. An alternative explanation for the importance of fatty acids derives from Herpes Simplex virus-1 (HSV-1), where saturated and monounsaturated fatty acids proved essential for RNA replication (Kapadia and Chisari, 2005). Nevertheless, as viral DNA production was not affected by inhibition of fatty acid biosynthesis this is unlikely to be the case in EhV.

Both metabolic profiles and transcriptomic data clearly indicated that lipid formation preceded viral DNA replication during lytic infection of *E. huxleyi* cells. We observed a depletion of down-stream PPP products accompanied by up-regulation of genes encoding enzymes involved in this pathway 24 hpi. Our data is in agreement with induction of the PPP in KSHV-infected endothelial cells at 48 hpi (Delgado et al.,

2012). Ribose-5-phosphate might be consumed in nucleotide biosynthesis, which could explain the slight reduction in up-stream PPP products accompanied by a stronger depletion of down-stream products. Concomitantly, HSV-1 redirected central carbon metabolism towards the production of nucleotide components when infecting fibroblasts (Vastag et al., 2011). A similar strategy is pursued by some cyanophages as they carry a Calvin cycle inhibitor, whose expression gears the carbon flux to the PPP (Thompson et al., 2011). This supposedly augments NADPH and ribose-5-phosphate production and therefore probably enables a larger viral burst size due to *de-novo* nucleotide biosynthesis (Thompson et al., 2011).

Our metabolic data revealed a drastic depletion in terpenes and sterols, drawing our attention to a pathway hitherto unrecognized in the context of host-virus interactions in marine algae like *E. huxleyi* and its specific viruses. Metabolic data were well supported by the transcriptome data which detected a down-regulation of terpene and sterol biosynthesis 24 hpi, probably induced by the host to prevent successful viral replication. Two major pathways for terpenoid biosynthesis, the cytosolic MVA and the plastidic MEP pathway, lead to the formation of terpenoids and consequently sterols in plants (Lohr et al., 2012 and references within) and algae (Disch et al., 1998). Both are encoded in the *E. huxleyi* genome (Read et al., 2013). Nevertheless, only specific inhibition of the MVA pathway led to a significant reduction in viral release clearly indicating the importance of this specific metabolic route for successful viral assembly and release. Why specifically the MVA pathway is of such importance is not clear, but it might be explained by its cytosolic location. Alternatively, triterpenoids, the building blocks of sterols, specifically derive from the MVA pathway in algae (Disch et al., 1998). Sterols constitute parts of cellular membranes (Hartmann, 1998) including viral envelopes (e.g. Bates and Rothblat, 1972; Selstam and Jackson, 1983). Therefore, the reduction in sterol concentrations during lytic viral infection can result from its consumption by newly produced viruses. Indeed, we detected epibrassicasterol, the dominant sterol of *E. huxleyi* (Maxwell et al., 1980) and deriving from the MVA pathway (Disch et al., 1998), in isolated, purified EhV201 virions. This specific sterol differentiates the sterol composition of virus-susceptible diploid and resistant haploid cells in *E. huxleyi* (2.2.3). Concomitant to this data, West Nile virus (WNV) modulates host cell cholesterol homeostasis by up-regulating cholesterol biosynthesis and redistributing this sterol to viral replication membranes, while inhibition of HMGR, the key enzyme in the MVA pathway,

drastically hampered virus replication (Mackenzie et al., 2007). A reduction in cholesterol biosynthesis at transcriptional and metabolic level regulated by an interferon regulatory loop mechanism upon infection was also reported for cells infected by HCMV (Blanc et al., 2011). In HCMV infected cells inhibition of the MVA pathway reduced viral infectivity, an effect which could be circumvented by substitution with the diterpene geranylgeraniol (Blanc et al., 2011). These data well reflect our detection of the main host sterol in viral membranes and the crucial role of the MVA pathway solely observed in lytic infected *E. huxleyi* cells. Neither non-lytic infected cells nor cells of virus-challenged resistant strains exhibited a reduction in terpene or sterol concentrations, but even showed increased levels of these compounds, which rather reflects patterns related to growth (compare 2.2.4). Thus, this further emphasizes the importance of host-derived terpene and sterol metabolism for viral production and release. In this context, the near shutdown of the whole terpene biosynthesis pathway 24 hpi can be interpreted as a host defense mechanism preventing the ongoing formation of essential viral membrane compounds.

In addition to the central role of sterols in virion membranes smaller terpenes themselves might also contribute to the importance of this metabolic pathway. Besides anchoring proteins within cell membranes (Pechlivanis and Kuhlmann, 2006) post-translational isoprenylation of viral proteins even participates in the regulation of viral replication. This was emphasized as geranylgeranylated proteins are required for the incorporation of newly synthesized proteins into virions in Murine leukemia virus (Overmeyer and Maltese, 1992) and for RNA replication in HCV (Ye et al., 2003; Kapadia and Chisari, 2005). As metabolic levels and gene expression patterns showed a reduction of terpene biosynthesis within 24 hpi, a similar regulatory mechanism via protein prenylation might be assumed. If isoprenylation indeed plays a functional role in regulation of viral proteins during EhV infection, will need to be determined by future studies.

The strong depletion during lytic infection in unfunctionalized hydrocarbons such as neophytadiene and two phytadiene isomers, which often derive from the plastidic MEP pathway in algae (Lohr et al., 2012), might further indicate a shift in the balance of hydrophobic metabolites in the host. Consequently, this could affect membrane stability thereby facilitating viral release. However, in this scenario

inhibition of terpene biosynthesis should also reduce membrane stability resulting in increased host mortality. In contrast to this hypothesis, we did not observe any effect on host mortality or membrane stability during inhibition by either inhibitor of the terpene biosynthesis pathways. An explanation why the MEP pathway is less effectively involved in viral replication, although in algae intermediate compounds can be exchanged with the MVA pathway (Lohr et al., 2012), might be its localization in the chloroplast. Loss of the apicoplast, an endosymbiotic organelle deriving from cyanobacteria and containing the MEP pathway in the parasitic protist group Apicomplexa, results in the death of the human parasite *Plasmodium falciparum* (Coppens, 2013). The apicoplast is similar to the chloroplast of algae concerning its origin and the localization of the MEP pathway. Since our ultrastructural images clearly indicate a degradation of the chloroplast in lytic infected *E. huxleyi* cells probably resulting in a loss of its efficiency, this compromised organelle might be a reason, why the MVA and not the MEP pathway is crucial during EhV infection.

It might be mentioned here that neophytadiene and phytadiene isomers can constitute phytol degradation products (Hites, 1974) and their artificial formation from phytol during extraction was previously discussed (Grossi et al., 1996). Nevertheless, this is unlikely in the current report. Our extraction method differs from those leading to potential artifact formation and phytol was derivatized prior to GC-MS analysis preventing its degradation during measurement (Grossi et al., 1996). Consequently, measurements of a phytol standard did not result in the formation of phytadienes. Several additional reasons argue against their origin as artifacts. First, they showed a distinct pattern of correlation with lytic infection. Second, although found in *E. huxleyi* metabolic profiles, these metabolites correlated with the exponential phase of haploid cells (2.2.4), which, since cells were sampled in the same growth phase, contradicts their reduction during viral infection. Further, neither of these metabolites was detected in the comparative approaches in the mesocosm experiment (3.2.7 to 3.2.9). Additionally, these phytadiene species have also been described from the cyanobacterium *Synechocystis* sp. (Plaza et al., 2010) and fresh water algae (Zhang and Sachs, 2007). In both cases the authors could exclude their artificial origin from phytol (Zhang and Sachs, 2007; Plaza et al., 2010).

To conclude, our data clearly show the central role of lipid metabolism, might it be fatty acid, sphingolipid, or terpene and sterol metabolism, during infection of the cosmopolitan, bloom-forming alga *E. huxleyi* by its specific lytic virus. We further found indication that lipid formation precedes nucleotide biosynthesis contradicting the general assumption that the viral nucleotide core is assembled before the capsid. Specific inhibition could decipher that mainly the MVA-route of terpene biosynthesis is essential for viral release, a pathway which previously has not received much attention in this host. We assume this data to give directions for future studies on how large dsDNA viruses manipulate their host and rewire central metabolic reactions in order to provide the essential building blocks for viral replication.

5 Conclusion

My PhD research aimed to investigate metabolic reactions of the ecologically important coccolithophore alga *Emiliania huxleyi* under different aspects. Therefore, I adapted a protocol for intracellular metabolite profiling for diatoms and successfully applied the approach to laboratory cultures and under semi-natural conditions. This investigation led to the metabolic characterization of diploid and haploid cultures and detected metabolic patterns in an *E. huxleyi*-dominated phytoplankton bloom. We conducted one of the first studies that successfully link metabolic profiles with transcriptomic gene expression patterns. This allowed to clearly identify and follow changes in pathways critically involved in lytic viral infection.

The metabolome reflected the reported transcriptomic variation between diploid and haploid life phases. A limited number of metabolites accounted for a separation of these life phases during exponential growth. Most of the molecules were produced in higher concentrations in the less studied haploid life phase, whereas only five metabolites were indicative for diploid cells: mannitol and an unidentified saccharide, epibrassicasterol, putative adenosine, and an unknown metabolite. Choosing the thus metabolically more productive haploid cells allowed us to get a better insight into metabolic changes during the course of growth resulting in this hypothetical scenario: In exponential phase, photosynthetic activity led to the production of saccharides and the storage molecule mannitol. A dynamic primary metabolism was further reflected in the formation of several polar low molecular weight carboxylic acids. The stationary phase was characterized by high fatty acid biosynthesis and the accumulation of galactosyl- and digalactosylglycerol due to lipid mobilization. As conditions became limiting, glycolytic activity decreased leading to glucose accumulation and amino acid production abated in the transition to the declining phase probably due to reduced nitrogen availability. Finally, breakdown of structural polysaccharides resulted in the accumulation of mono- and disaccharides. With increasing stress levels sugar alcohols and the powerful antioxidant α -tocopherol were produced as radical scavengers. Increases in sterol concentrations probably reflect attempts of the decaying cells to maintain membrane integrity.

The application of the metabolomic approach during an *E. huxleyi*-dominated phytoplankton bloom allowed tracking changes in metabolic profiles of the phytoplankton community over time. Thereby, metabolic changes reflected the succession pattern observed in the composition of phytoplankton groups. Applied carbon dioxide and iron manipulation showed a manifestation at the metabolic level during the second half of the experiment. Whereas differences in dissolved iron only affected the phytoplankton community under low carbon dioxide levels, variation in the latter parameter affected *E. huxleyi* growth and allowed a strong differentiation between metabolic profiles. Metabolic activity was most pronounced under low carbon dioxide and increased bioavailable iron. These conditions led to a high glycolytic activity, active energy transfer via the tricarboxylic acid cycle, and high amino acid and fatty acid biosynthesis. Metabolic changes as observed during this mesocosm experiment demonstrate the potential of an *E. huxleyi*-dominated phytoplankton community to react to changes they might encounter in the ocean within this century and which will definitely affect community ecology.

Combination of transcriptome and metabolome data allowed the extensive study of lytic viral infection resulting in a conclusive picture on the rewiring of host metabolism. At the onset of lytic infection, glycolysis was induced resulting in high energy production, which was shuffled into fatty acid biosynthesis thereby circumventing the tricarboxylic acid cycle via the citric acid shuttle. In parallel, sterols were synthesized for their integration into viral membranes, but without affecting metabolic levels. Only later during lytic infection the high energy demand for nucleic acid biosynthesis to provide nucleotides for viral DNA replication was met by an induction of the pentose phosphate pathway. Lipid production accompanied by nucleotide synthesis led to the assembly of progeny viruses inside the host cell and finally resulted in host cell lysis and death. Long after the onset of infection surviving host cells down-regulated fatty acid, terpene and sterol biosynthesis to prevent successful viral assembly and release (compare Figure 4.8). These findings allow us to better understand the complex metabolic reactions within host *E. huxleyi* cells to viral infection.

Regarding all results obtained during this study, it is conspicuous that sterols repeatedly showed up in metabolic profiles of the coccolithophore *E. huxleyi*. They were accounting for the separation between diploid and haploid life phases, highly correlated with the declining phase, displayed a specificity concerning succession patterns reflecting differences in the phytoplankton community and played an essential role during lytic viral infection. We can therefore assume that lipid metabolism is essential in this host species affecting it at several levels. Further studies are thus needed to better understand aspects of sterol biosynthesis and their regulating functions in phytoplankton. In this context it should also be mentioned that neophytadiene and the two phytadiene isomers that were tremendously reduced during lytic viral infection were always detected in our metabolic profiles. Interestingly, they decreased during lytic infection, whereas they showed highest concentrations during the exponential growth phase of haploid cells, for which they also discriminated. Since the sampling for the viral infection experiment was also conducted during exponential growth, this further supports the importance of the reduction in terpene biosynthesis during viral infection and its physiologically indicative role. Maybe this pattern could even be used to metabolically trace viral infection within the environment, although viral counts constitute an easier but less specific method. Fatty acids constituted a second interesting group, although their separation potential under the investigated aspects was not as explicit as for sterols. Nevertheless, the crucial involvement in viral infection would justify further attention to this metabolic class. Another compound detected several times in our metabolic profiles was ethanolamine. Although speculatively involved in lipid metabolism as potential head group of phosphatidylethanolamine, its function in the multiple contexts presented in this study as for example during viral infection is not completely clear.

Finally, it should be mentioned that only the combination of metabolic profiles and transcriptomic gene expression patterns really allowed conclusions concerning the regulation of metabolic pathways. Targeting metabolites without enzymatic support lacks the possibility to draw final conclusions as a concentration reduction in a molecule could derive either from the consumption of a metabolite in downstream metabolic reactions or by a decrease of the related pathway. The biological significance and consequences of these oppositional scenarios are completely different. Therefore, if the sequence of the organism is available, I recommend

accompanying metabolic profiling by transcriptomic approaches, as was partly done in this study, or by proteomic analysis. Alternatively, without a sequence being available, carbon assimilation rate can be analyzed or pathways of specific interest targeted by flux analysis.

6 Experimental procedures

6.1 Solvents

All solvents used in this study were HPLC grade or higher, but their origin depended on the country the experiment was conducted in. In general, the following solvents were used for extraction and sample preparation: methanol, pyridine, water (all Chromasolv® Plus, Sigma-Aldrich, Munich, Germany), ethanol (LiChrosolv, Merck, Darmstadt, Germany), and chloroform (HiPerSolv, VWR, Dresden, Germany). For samplings conducted in other countries equivalent solvents of local distributors were used. During the mesocosm experiment (Chapter 3) in Espegrend, Norway, the following solvents were used: methanol (Chromasolv® Plus, Sigma-Aldrich, Oslo, Norway), ethanol (Chromasolv®, Sigma-Aldrich, Oslo, Norway), and chloroform (HiPerSolv, VWR, Bergen, Norway). For sampling and extraction during the viral infection experiment (Chapter 4) in Rehovot, Israel, the solvents used were: methanol (Chromasolv® Plus, Sigma-Aldrich, Rehovot, Israel), ethanol, and chloroform (both HPLC grade, JT Baker, Ra'anana, Israel).

6.2 Cultivation

6.2.1 *Phytoplankton cultures and viruses*

Diploid (2N) and haploid (1N) strains of *Emiliania huxleyi* as well as strains used to provide viral lysate after infection were obtained from the Roscoff Culture Collection, France, (2N: RCC1216, 1N: RCC1217, RCC1242, RCC1259). Strains challenged by viruses originated from the Provasoli-Guillard National Center for Marine Algae and Microbiota (NCMA), USA, (non-resistant strain: CCMP2090, resistant strains: CCMP373, CCMP379). Viruses used in this study were obtained from Dr. Mike Allen at the Plymouth Marine Laboratory, Great Britain. EhV201 was isolated from the English Channel in 2001 and EhV163 isolated from a Norwegian fjord in 2000 (Allen et al., 2007). While EhV201 is lytic for CCMP2090, EhV163 is not.

If not otherwise specified, cultures were grown in sterile K/2 (see 6.2.3) at 18-20°C with a light/dark regime of 14/10 h and 80 $\mu\text{mol photons m}^{-2} \text{ s}^{-1}$ (measured

as photosynthetic active radiation, PAR) provided from the top by Osram Biolux lamps. Stock cultures were kept under sterile conditions in preservation jars (100-200 mL), which were heated up to 250°C for 8 h prior to use, or sterile plastic cell culture flasks (40 mL, Carl-Roth, Karlsruhe, Germany). Inoculation cultures were grown under sterile conditions using autoclaved (121°C, 20 min) Erlenmeyer flasks or sterile plastic cell culture flasks (40 mL, 250 mL, and 500 mL Carl-Roth, Karlsruhe, Germany).

6.2.2 Preparation of viral lysate and storage conditions

To obtain viral lysate defined 20 mL cultures of strains RCC1242 or RCC1259 were infected by addition of viral lysate at a ratio of 1:50 (v:v) equaling a multiplicity of infection (MOI) of about 1:1 viral particles per cell at regular intervals. Cultures were grown for 3-5 days until cells were lysed under conditions as specified above. Then, cells were filtered off using 0.22 or 0.45 µm sterile syringe filters (polyethersulfone, PES or polyvinylidene difluoride, PVDF) and stored at 4°C or at -80°C after cryofixation.

For cryofixation glycerol or dimethyl sulfoxide (DMSO) were added to viral lysate at a final concentration of 10%. Therefore, 2 mL of glycerol or DMSO were mixed with 8 mL of K/2 (lacking Tris and Si) and this mixture added to viral lysate at a ratio of 1:1. Then aliquots of 1.5 mL were pipetted into sterile 2 mL cryo-vials (VWR, Darmstadt, Germany), which were transferred into a cryo-freezing container (Mr. Frosty, Nalgene via VWR, Darmstadt, Germany). The container was filled with isopropanol as specified by the manufacturer and stored at -80°C for 24 h during which samples were cooled down at a speed of ~1°C min⁻¹. Afterwards, cryo-vials containing viral lysate could be stored at -80°C.

If cryofixed lysate was used for infection, a lysate-containing vial was thawed for ~5 min at 35°C. Lysate was then added to defined 20 mL cultures at a ratio of 1:25 (v:v) to even out the dilution and proceeded as described above.

To estimate the MOI *E. huxleyi* cells or viral abundance were counted using a hemocytometer (host cells only) or by flow cytometry (for details see the specific sections, host cells: 6.5.2, and 6.7.6, viruses: 6.6.6, and 6.7.7).

6.2.3 Medium

K/2 medium (lacking Tris and Si) (Keller et al., 1987) was used for cultivation in all experiments. For medium preparation natural sea water (NSW) was obtained from the Biological Institute Helgoland (BAH), Germany, and kept at 19°C for at least 2 month. Afterwards, NSW was filtered through 0.22 µm PES membrane filters, filled into 1 L bottles (polypropylene, PPL, Nalgene® via VWR, Darmstadt, Germany) and autoclaved (121°C, 30 min). Previously autoclaved or sterile filtered nutrients and vitamins (f/2 vitamin solution) were added under sterile conditions reaching final concentrations of 18 µM phosphate, 288 µM nitrate, and 5 µM ammonium (optional, only used for stock cultures). After nutrient addition, medium was heated up to 80°C for 2 h, cooled to room temperature and sterile filtered (0.22 µm, PES) to ensure sterility of the medium after all manipulation steps.

6.3 Large volume cultures (20 L)

6.3.1 Design of 20 L culture vessels

Design and preparation of large volume culture vessels was adapted from Vidoudez (2010). For large volume cultures used to examine growth phases of haploid *E. huxleyi* cells (Chapter 2) 20 L culture vessels (polycarbonate, PC, Nalgene via VWR, Darmstadt, Germany) (Figure 6.1A) were used. A scheme of the culture vessel is presented in Figure 6.1. At the cap three tubes were connected, two presenting outlet tubes (Figure 6.1D, F) and one was used as inlet. Inside the vessel the sampling outlet (Figure 6.1D) was connected to a long Teflon tube (Ø 1 mm) (Figure 6.1C) and outside to a “dropping chamber” (Figure 6.1E). The latter consisted of a 1 mL syringe inserted into a 2.5 mL syringe (both PC). To close the sampling outlet a piece of silicon tubing was connected to the syringe and a Luer stop lock applied to it. The second outlet constituting the air outlet was covered by autoclaved aluminum foil (Figure 6.1F). The inlet tube was connected to a glass tube (Duran glass, Ø 4 mm) inside the vessel (Figure 6.1B), which ended above the level of the culture. The inlet was divided by a cross piece and consisted of three separate parts: one culture inlet (Figure 6.1G), one for medium (Figure 6.1H), and one for air. Two sterile filters (Figure 6.1I) in line at the medium inlet enabled sterilization of the culture medium while filling (for details see 6.3.2). The tubing of the air inlet was

attached to an autoclaved, glass wool containing pre-filter (Figure 6.1L) and a HEPA-Vent filter (\varnothing 50 mm, Whatman, Kent, UK) (Figure 6.1K) to enable sterile air flow from an aquarium pump (Figure 6.1M) into the culture vessel. A hose clamp (Figure 6.1J) enabled regulation of the airflow. Cultures were not permanently bubbled as exposure to permanent bubbling was reported to reduce growth of haploid *E. huxleyi* cultures (von Dassow et al., 2009). The air inlet was thus only used for sampling purpose (see 6.3.3). Mixing of the cultures was assured by regular agitation prior to sampling. Eight fluorescent tubes (Osram Biolux lamps) placed above the culture vessels provided illumination ($80 \mu\text{mol photons m}^{-2} \text{ s}^{-1}$, measured as PAR) at a 14/10 h light/dark regime (Figure 6.1O). Heating of the cultures during the experiment was prevented by a constant air flow provided by fans (Figure 6.1N).

6.3.2 Culture vessel preparation

Prior to usage, vessels were washed with ~ 3 L of 1% acetic acid in deionized water with repeated shaking and left in acid overnight. The next day, vessels were thoroughly rinsed 3x with deionized water and left standing with ~ 5 L of deionized water for a whole day. Then, they were again rinsed 3x with deionized water, covered with aluminum foil and autoclaved (121°C , 20 min). Caps with all tubing attached were autoclaved separately in plastic bags. Culture vessels with caps and tubing were assembled under a vertical flow sterile bench (BDK, Sonnenbühl-Genkingen, Germany) directly before filling with medium. For this purpose two sterile filters ($0.22 \mu\text{m}$, PES) were put in line at the medium inlet (Figure 6.1H) to enable sterile filling of the culture vessel outside the sterile bench. Vessels were then filled by pumping autoclaved medium through the liquid inlet with a peristaltic pump (MV-GES, Ismatec, Glattbrugg, Switzerland). If the filling speed strongly decreased the external sterile filter was changed. After filling was completed, both sterile filters were disassembled under the sterile bench and the outlet permanently closed with an autoclaved Luer lock stopper. 2 L of inoculation culture (approximately $2.07 \cdot 10^5$ cells mL^{-1} , haploid *E. huxleyi* strain RCC1217, compare 6.5.1) contained in autoclaved glass bottles were connected by silicon tubing in the cap of the bottle to the sterile culture inlet (Figure 6.1G). The culture was pumped in via the sterile culture inlet by the use of the peristaltic pump. After complete inoculation the culture inlet was permanently closed via an autoclaved Luer lock stopper.

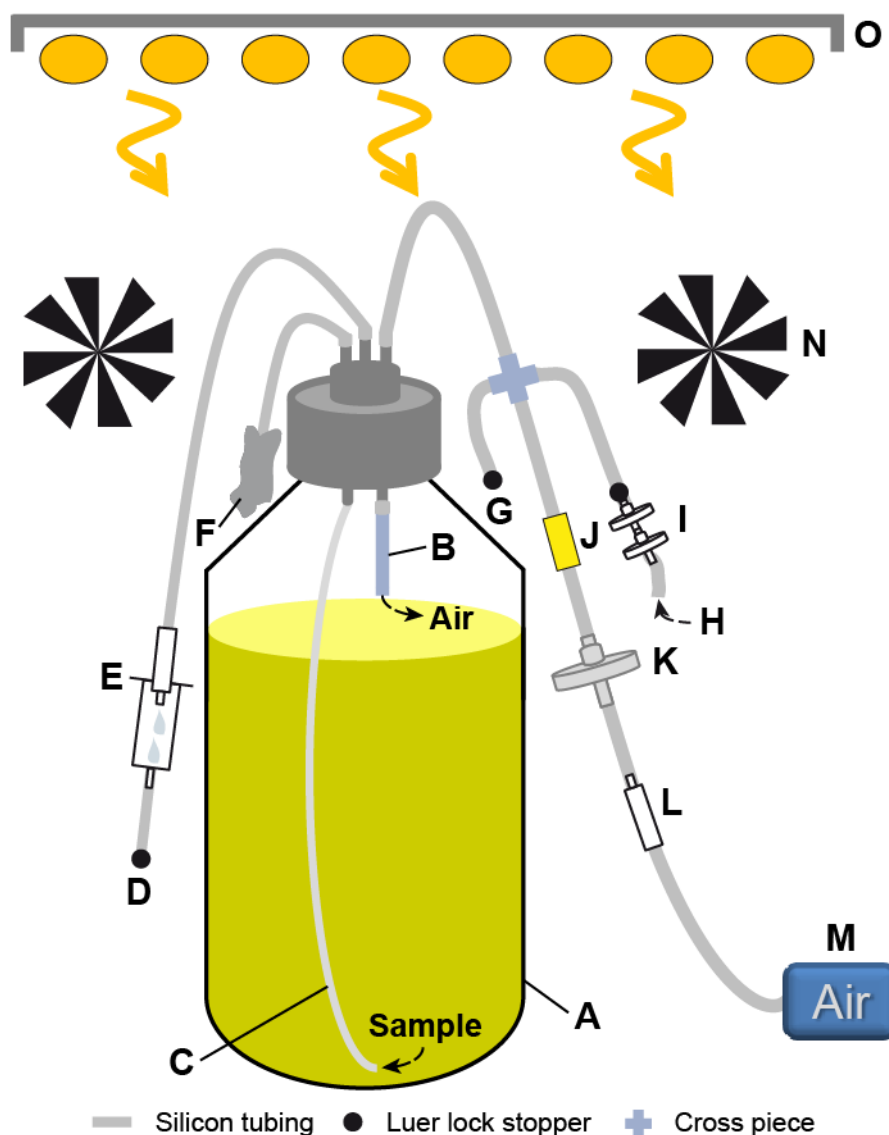


Figure 6.1: Scheme of the 20 L culture vessel. Set-up of a 20 L culture vessel as used for metabolomics of growth phases of haploid *E. huxleyi* cells. (A) 20 L culture vessel (PC, Nalgene), (B) air tube (Duran glass, Ø 4 mm) to produce pressure for sampling, (C) sampling tube (Teflon, Ø 1 mm), (D) sampling outlet, (E) dripping chamber, consisting of a 1 mL syringe inserted into a 2.5 mL syringe (both PC), (F) air outlet covered by aluminum foil, (G) sterile culture inlet, (H) non-sterile media inlet, (I) line of 2 sterile filters (0.22 µm, PES), (J) hose clamp to control the air flow from the pump, (K) sterile HEPA-Vent filter (Whatman), (L) air pre-filter consisting of a 1 mL syringe (PC) filled with glass wool, (M) aquarium air pump, (N) fans for cooling, (O) light source (Osram Biolux lamps).

6.3.3 Sampling process

Bottles were agitated to ensure homogenous mixing. Then sampling of the cultures could be achieved by the following procedure: the aquarium pump was turned on and the hose clamp loosened to enable a regular airflow. Next, the air outlet was closed by a clamp, leading to the establishment of a slight overpressure inside the culture vessel. Consequently, when the sampling outlet was now opened, culture was pushed out due to the overpressure. For all samplings approximately the first 20 mL were discarded, because a few mL of culture from the previous day always remained in the tubing and the “dropping chamber” after sampling. Then cultures were collected either in 15 mL falcon tubes (monitoring of daily growth behavior) or in 2 L Erlenmeyer bottles (metabolomics sampling). After sampling the sampling outlet was closed again by the Luer lock stopper, the hose clamp closed and the aquarium pump turned off. At last the clamp blocking the air outlet was slowly opened and taken off to release the overpressure.

6.3.4 Remarks

20 L culture vessels used during viral infection (Chapter 4) were prepared and filled by D. Schatz at the laboratory of A. Vardi, Plant Sciences Department, Weizmann Institute of Science, Rehovot, Israel. In principal, the set-up to provide sterile conditions during the experiment was similar as described above, but the vessels were autoclaved containing the medium (K/2 medium, without Tris and Si) covered by a lid. Inoculation was performed by pouring the cultures in through the opening in a sterile area in the laboratory and viral lysate for the infection was added the same way (see 6.7.1). Diploid cultures were constantly mixed by air bubbling and sampling performed via an outlet at the bottom of the culture vessel.

6.4 Metabolomics – general method

6.4.1 *Metabolite extraction and derivatization*

The metabolite extraction procedure from wet, cells containing GF/C filters (Whatman, Kent, UK) and further work-up was based on a protocol by Vidoudez and Pohnert (2012). (For details about the sampling of metabolites see method sections specific for each chapter, 6.5.3, 6.6.7, and 6.7.2) In brief: Wet, cell containing filters were transferred to 25 mL beakers and extracted in 1 mL freshly prepared and cooled (-20°C) extraction mix (methanol:ethanol:chloroform, 1:3:1, v:v). Thereby, as no washing step was included, the extraction of some surface associated exudates alongside the intracellular metabolites cannot be excluded. Nevertheless, we refer to intracellular metabolites in the whole text meaning metabolites associated with the cells instead of being extracted from the medium. Next, samples were transferred to 1.5 mL eppendorf centrifuge tubes, vortexed for 10 s and 5 µL of ribitol solution (20 nmol in water, Sigma-Aldrich, Munich, Germany) were added as internal standard. Samples were not quenched prior to filtration. Instead they were quickly transferred on ice and stored at -80°C until further processing (for one month: life phase experiment, and mesocosm experiment, see chapters 2, and 3, or for three months; growth phase experiment, and viral infection, see chapters 2, and 4). For sample processing random batches were warmed to room temperature and extracts corresponding to an equivalent of $\sim 50 \cdot 10^6$ cells were aliquoted into eppendorf centrifuge tubes. After adjusting the total volume to 1 mL with extraction mix (see above), samples were treated in an ultrasound bath for 10 min and centrifuged for 15 min at 30.000 g at 4°C. The supernatant was transferred into a 1.5 mL glass vial and evaporated to dryness under reduced pressure (stepwise decreased to ~ 30 mbar) for approximately 5 h. These samples were derivatized by adding 50 µL of methoxyamine solution (20 mg methoxyamine hydrochloride in 1 mL pyridine, Sigma Aldrich, Munich, Germany), sealed with PTFE-butyl-PTFE septa and vortexed for 1 min. After incubation at 60°C for 1 h followed by 9 h at room temperature 50 µL N-methyl-N-(trimethylsilyl)trifluoroacetamide (MSTFA, Macherey-Nagel, Düren, Germany) containing a retention time index solution (40 µL in 1 mL of MSTFA) consisting of decane, pentadecane, nonadecane, docosane, octacosane, dotriacontane (all 40 µM final concentration within 1 mL of MSTFA), and hexatriacontane (20 µM final concentration within 1 mL of MSTFA in hexane, all

> 99%, Sigma-Aldrich, Munich, Germany) were added with a gas tight Hamilton glass syringe. Samples were then incubated at 40°C for 1 h, transferred into 200 µL glass inserts and centrifuged for 5 min at 8,000 g. The supernatant was transferred into a new glass insert, and measured within 12 h by GC-MS to ensure sample stability (compare Gunnar et al., 2005).

6.4.2 GC-MS analysis

Metabolic samples and solvent controls, the latter from all used solvents as well as extraction mix at the beginning and the end of the experiment, were measured randomly on an Agilent 6890N gas chromatograph (GC) equipped with a 30 m DB-5 ms column (0.25 mm internal diameter, 0.25 µm film thickness, with 10 m Duraguard pre-column, Agilent, Waldbronn, Germany). Solvent controls were only used to identify potential contaminations in the sample sets. For carrier gas I used He 5.0 with a constant flow rate of 1 mL min⁻¹ and for each experiment a new deactivated, glass wool containing glass liner (4 × 6.3 × 78.5 mm inner Ø × outer Ø × length, Agilent, Waldbronn, Germany) was used and regularly exchanged (for details on frequency see specific sections, 6.5.4, 6.6.8, and 6.7.3). For detection a GCT premier (Waters, Manchester, UK) orthogonal reflectron time-of-flight mass spectrometer (MS) was coupled to the GC. 1 µL per sample was injected at 300°C in split 1 or 5 mode. GC parameters were: initial temperature of 60°C for 1 min followed by an increase of 15°C min⁻¹ to a final temperature of 310°C (held for 10 min). The MS scan rate was set to 5 scans s⁻¹ in dynamic range extension (DRE) mode and the electron impact source was set at 70 eV. The resolution of the tune was ≥5800 at *m/z* 501.97. Instrument performance was monitored by measuring a quality control standard (test standard, DB-5ms (Capillary/Megabore), ordering number 200-0185, Agilent, Waldbronn, Germany) containing n-tetradecane, n-tridecane, 1-undecanol, 1,6-hexanediol, 2-ethylhexanoic acid, 4-chlorophenol, dicyclohexylamine, and 1-methylnaphthalene before and after every batch.

6.4.3 *Measurement of standards*

Standard compounds (in total 120 standards) were dissolved in different concentrations in water or tetrahydrofuran (HiPerSolv, VWR, Dresden, Germany). 25 μ L of 4 mM or 20 mM standards were evaporated to dryness and derivatized as described above. Each standard was then measured by the above described GC-MS protocol, but the split was varied from split 5 mode to split 150 mode depending on the standard concentration and metabolite class.

As for neophytadiene no standard was available, but it was reported to be highly abundant in tobacco (Ellington et al., 1978). Thus, I used an authentic, natural sample for comparison. Therefore, I extracted approximately 20 mg of dried tobacco from a cigarette (f6 fine flavor, Cigarettenfabrik Dresden GmbH, Germany) in 1 mL of hexane over night. Further processing of this natural sample was as described above, but for measurement 100 μ L of tobacco extract were used.

6.4.4 *Data processing*

Data processing was based on a published protocol (Vidoudez and Pohnert, 2012). In brief, for background-noise correction the Component Detection Algorithm (CODA) implemented in MassLynxTM (version 4.1, Waters, Manchester, UK) with Mass Chromatographic Quality (MCQ) set to 0.65 and a smoothing window of 3 scans was used. Chromatograms were then converted to netCDF files by MassLynxTM DataBridge and each experiment was run as a batch job in AMDIS (Automated Mass Spectral Deconvolution and Identification System, version 2.71, NIST, <http://chemdata.nist.gov/>, 2012) using the following parameters: minimum match factor: 30; analysis type: simple; high and low m/z : auto; component width: 10; omitted m/z : 147, 176, 193, 207, 219; adjacent peak subtraction: 2, resolution: low; sensitivity: medium; shape requirement: low. As target compound library a GMD mass spectrum reference library (Golm Metabolome Database, see 6.4.6) (Wagner et al., 2003) was used. To quantify detected metabolites netCDF and corresponding AMDIS output files were fed into MET-IDEA (Metabolomics Ion-based Data Extraction Algorithm, version 2.08, <http://bioinfo.noble.org/download/>, 2012) (Lei et al., 2012). The applied parameters were: chromatography type: GC; average peak width: 0.08; minimum peak width: 0.5; maximum peak width: 2; peak start/stop slope:

1.5; adjusted retention time accuracy: 0.25; peak overload factor: 0.9; MS type: TOF; mass accuracy: 0.1; mass range: 0.3; excluded ions: 73, 147, 193, 281, 341, 415; lower mass limit: 100; ion per component: 1. In a few cases where no suitable ion above the mass limit was found, a mass limit of 50 was accepted or the ion selected manually. Borders of each peak were manually inspected and integration was corrected, if necessary. Resulting datasets containing peak areas and suggested identity of each component were copied into Excel 2010 (Microsoft, Redmont, USA). Signals of the retention time index, ribitol and a few badly annotatable peaks were excluded. Further, if a signal in the extract of the medium control was detected, it was subtracted 3x from the corresponding peak area of a compound in all samples to exclude potential contaminations. If after this procedure all the corresponding peak areas of a compound were below zero, it was deleted from the dataset. If not specified otherwise in the corresponding sections I performed a sum-normalization by dividing each peak area by the sum of all peak areas within one sample for metabolomics data. Final data matrices were exported as text files for statistical analysis.

6.4.5 Statistical analysis

To evaluate the difference between metabolic profiles the constrained method of canonical analysis of principal coordinates (CAP) was used, applying the software CAP12 (<http://www.stat.auckland.ac.nz/~mja/prog/>) (Anderson and Willis, 2003). This method uses a principal coordinate analysis (PCO) to define axes followed either by a discriminant analysis, which was used in the present study, or a canonical correlation analysis. Parameters were: transformation: none; standardization: none; similarity measure: Bray-Curtis; analysis mode: discriminant analysis; number of principal coordinate axes: chosen by the program; random permutations: 9999. Resulting CAP axes and coordinates were visualized graphically using SigmaPlot™ (version 11.0, Systat Software, San Jose, USA). For the comparative approach correlations of metabolites with the CAP axes were considered significant, if above a threshold correlation coefficient determined by t-distribution with corresponding degrees of freedom and a $P = 0.01$. The relation with a specific group was determined by visualizing these correlation coefficients as vectors, which point in the direction of a specific group.

6.4.6 Metabolite identification

Mass spectra of metabolites correlated with the CAP axes were manually examined for identification using the software MS Search (version 2.0 d, NIST). The libraries implemented in the software are listed in Table 6.1. The in-house library contained entries of 175 derivatized compounds from several metabolic classes including natural algae extracts.

Table 6.1: MS spectra libraries used for metabolite identification.

Name	Origin	Version	Link	Reference
NIST	NIST	2005		(Ausloos et al., 1999)
GOLM	Golm Metabolome Database	T_MSRI_ID 2004-03-01	http://csbdb.mpimp-golm.mpg.de/csbdb/gmd/msri/gmd_msri.html	(Wagner et al., 2003)
MPI	MPI of Molecular Plant Physiology	Q_MSRI_ID 2004-03-01		
GMD	Golm Metabolome Database	GMD_20111 121_VAR5_ ALK_MSP	http://gmd.mpimp-golm.mpg.de/	(Hummel et al., 2010)
Terpenoids Library*	MassFinder 4.0		http://massfinder.com/wiki/Terpenoids_Library_List	(König et al., 2008)
Essential Oil Components*	Adams			(Adams, 2007)
Metabo	In-house library			(Vidoudez, 2010)

* Commercial libraries available at the Max Planck Institute for Chemical Ecology, Jena, and used by Dr. Stefan Bartram to try to identify a few potential terpenoids of specific interest during the viral infection experiment (see 4).

A structure was accepted, if several criteria were fulfilled: the reverse match factor, a normalized score indicating how well the submitted spectrum fits the library spectrum that disregards elements not present in the library spectrum, had to be >800, the retention index of the structure suggested in the library had to be close to the retention index of the compound and, if a standard was available, retention times of compound and standard had to be the same, and the spectrum had to show an identical fragmentation pattern. Structures confirmed by a standard were indicated by “*” and “+” indicates confirmation by a natural sample. Metabolites tagged with “?” showed a reverse match between 700 and 800 and those with “??” one between 600 and 700. Such metabolites were referred to as “putative” in the text.

6.4.7 Data availability

Data of all individual experiments were deposited locally on a storage device within the Institute of Inorganic and Analytical Chemistry of the Friedrich Schiller University, Jena.

6.5 *Emiliana huxleyi* life and growth phases (method of Chapter 2)

6.5.1 Experimental setup and culture preparation

Life phase experiment: Non-axenic diploid (2N) and haploid (1N) strains of *Emiliana huxleyi* were obtained from the Roscoff Culture Collection (2N: RCC1216, 1N: RCC1217). The haploid strain RCC1217 was isolated from the diploid strain, thus these strains represent two genetically identical life phases of a single strain. They were grown in K/2 (lacking Tris and Si) medium (Keller et al., 1987) at a temperature of 20°C with a light/dark regime of 14/10 h and 80 $\mu\text{mol photons m}^{-2} \text{s}^{-1}$. Previous to the experiment two cultures (12 mL of growing culture, respectively) of each life phase were diluted 5x in fresh medium resulting in two 60 mL cultures per life phase. This was performed two more times on every other day producing two 1.5 L cultures in 2 L Erlenmeyer flasks per life phase. One week after the first dilution the two pre-cultures of each life phase were combined to a 3 L culture, from which I generated ten biological replicates per life phase by diluting 300 mL of the combined culture 5x with medium. This resulted in a total volume of 1.5 L for each biological replicate contained in a 2 L Erlenmeyer flask. All pre-cultures remained stable concerning their ploidy level during this preparation. Inoculation resulted in cell abundances of approximately $9 \cdot 10^3 \text{ cells mL}^{-1}$ (2N) and $8 \cdot 10^4 \text{ cells mL}^{-1}$ (1N) as pre-cultures were growing differently resulting in different total cell abundances. 4x 1.5 L of medium were used as blank (one per sampling, see 6.5.3). Among the diploid cultures three out of ten replicates did not grow, resulting in three biological replicates for early and four for late exponential phase sampling (see 6.5.3). Cultures were shaken daily and 2x 1 mL was sampled under sterile conditions for estimation of cell abundance, chlorophyll *a* (Chl *a*) fluorescence and photosystem II (PSII) efficiency (see 6.5.2). Samples of these parameters were taken 3 h after onset of illumination.

Growth phase experiment: 20 L cultures of RCC1217 (1N) were grown from five cultures (16 mL each) diluted 5x in fresh medium resulting in five 80 mL cultures. Dilution was repeated every other day in total 3x resulting in five 2 L cultures that were combined to a 10 L inoculation culture. Four 20 L culture vessels (polycarbonate, Nalgene) were filled with 18 L of sterile filtered medium and 2 L of the inoculation culture were added resulting in a cell abundance of approximately $2 \cdot 10^4$ cells mL⁻¹. Culture conditions were as described above. Culture vessels were agitated daily by rolling and 10 mL were sampled immediately afterwards to estimate cell and bacterial abundance, Chl *a* fluorescence, and PSII efficiency (see 6.5.2). Samples of these parameters were taken 3 h after the lights turned on.

6.5.2 Monitoring of growth parameters and photosynthetic activity

Life phase experiment: To estimate cell abundance in the life phase experiment 1 mL of sample was fixed by addition of 10 µL 25% aqueous glutaraldehyde (electron microscopy grade, Sigma Aldrich, Munich, Germany) resulting in a final concentration of 0.25%, vortexed and incubated in the dark at 4°C for 30 min. To 100 µL of these samples 100 µL of a calibration standard (see below) and 300 µL of sterile filtered (0.22 µm, PES) ultra-pure water were added. Measurement was performed immediately afterwards on a Cytomics FC 500 flow cytometer (Beckman Coulter, Krefeld, Germany) equipped with CXP-software, a 20 mW 488 nm air-cooled argon-ion laser and standard filters. The side scatter was used as discriminator and samples were run for 1 min at a flow rate of 30 µL min⁻¹. Polystyrene fluorospheres (3.6 µm in diameter; Beckman Coulter, Krefeld, Germany) measured at 620 nm were used for data calibration and samples were measured in triplicates.

Growth phase experiment: In the growth phase experiment at least 400 haploid cells per replicate were counted 3x using a Fuchs-Rosenthal hemocytometer with an upright microscope (magnification: 400x; Leica DM 2000, Heerbrugg, Switzerland), whereas bacterial abundance was determined by flow cytometry. Therefore, samples were fixed as described above, immediately frozen in liquid nitrogen and stored at -80°C. For further analysis a protocol originally optimized for viruses (Marie et al., 1999; Brussaard, 2004b) was adapted. In brief: samples

were thawed for approximately 5 min in a water bath at 35°C, so that when taken out of the water bath the samples were still cool. Next, 10 µL of SYBR® Gold Nucleic Acid Gel Stain (Invitrogen, Carlsbad, CA, USA) (final concentration 10^{-4} of commercial stock) were added and samples were stained for 10 min at 80°C in the dark. To avoid coincidence (two or more particles being simultaneously present in the sensor zone) samples were diluted 10- or 20-fold in sterile filtered TE buffer (10 mM Tris-HCl and 1 mM EDTA, pH 8.0) in later growth phases. Afterwards, samples were measured on the flow cytometer as described above but with the discriminator on green fluorescence and calibration with latex fluorospheres at 525 nm (1.0 µm in diameter; Polysciences Inc., Eppelheim, Germany).

In both experiments to obtain Chl *a* fluorescence 3x 200 µL of each culture were pipetted on black 96 well plates and measured on a Mithras LB 940 plate reader using a 430 nm excitation and a 665 nm emission filter (Berthold Technologies, Bad Wildbad, Germany). For PSII efficiency the same plates were incubated in the dark at 15°C for 30 min and then initial fluorescence (F_0) was measured using the same parameters as for Chl *a* fluorescence. To obtain maximum fluorescence (F_m) 15 µL of aqueous 3'-(3,4-dichlorophenyl)-1',1'-dimethylurea (71.7 µM; Sigma-Aldrich, Munich, Germany) were added reaching a final concentration of 5 µM and the fluorescence measurement was repeated immediately with 90 s of shaking prior to measurement. Finally, PSII efficiency was calculated based on the equation $(F_m - F_0)/F_m$ (Roy and Legendre, 1979).

6.5.3 Sampling of intracellular metabolites

All samples for metabolome analysis were taken 5 h after onset of illumination. In the diploid and haploid life phase experiment metabolites were sampled during exponential growth when $3 \cdot 10^5$ cells mL⁻¹ (2N: day 3, 1N: day 2) and a second time when $8 \cdot 10^5$ cells mL⁻¹ (2N: day 6, 1N: day 4) were exceeded using the entire 1.5 L culture. From the 20 L haploid cultures samples were taken 2x during each growth phase (exponential phase: day 5 and 7, stationary phase: day 10 and 12, and declining phase: day 17 and 22). In both experiments 500 mL aliquots of culture were concentrated at daylight illumination on 47 mm GF/C filters (pore size ~1.2 µm, Whatman, Kent, UK) under vacuum (~500 mbar) within less than 5 min per sample.

6.5.4 Analysis of intracellular metabolites

Metabolites were extracted from wet filters, derivatized and measured as described above (see 6.4.1). The biomass of filtered diploid and haploid cells was the same, because the same number of cells equal in size was used. The following modifications were applied to the general method: samples were measured on the GC equipped with a 30 m DB-5ms column without Duraguard pre-column (Agilent, Waldbronn, Germany). For data processing life and growth phase experiment were analyzed separately and the MCQ for background subtraction set to 0.7. Metabolic data for the life phase experiment were normalized only by cell numbers, because they derived from different strains, whereas data of the growth phase experiment were sum-normalized. Correlations of metabolites with the CAP axes were considered significant, if above a threshold correlation coefficient determined by t-distribution with corresponding degrees of freedom and a $P = 0.05$ (life phases) or $P = 0.01$ (growth phases).

6.5.5 Statistical analysis

Differences in cell growth were statistically analyzed using a paired t-test (between the first and last sampling point within a life or growth phase) or a Mann-Whitney Rank Sum test (between diploid and haploid life phase), because a test for normal distribution showed that this criterion was not fulfilled for the latter data. These statistical analyses were performed using SigmaPlotTM 11 (Systat Software, San Jose, USA).

6.6 Mesocosm (method of Chapter 3)

The mesocosm experiment was conducted at the Norwegian National Mesocosm Centre, Esperend, Norway, between the 5th (day 0) and 27th (day 22) of June, 2012 in a close international collaboration. To observe as many of the complex variables in this semi-natural experiment as possible many people collecting data on different parameters were necessary. In this section only those methods conducted in connection with the general set-up, daily sampling, intracellular metabolomics, or viral and bacterial abundance counts during the mesocosm experiment shall be described. All further methods performed by other participants in the mesocosm experiment like flow cytometry and flow cam cell abundance counts, measurements of nutrients and other additions are not described here, but will be subject of a publication (Segovia et al., to be submitted).

6.6.1 *Set-up of the mesocosms*

In total 12 mesocosm enclosures (bags consisting of glass fiber enforced polyethylene, PE, Ø 2 m, depth 4.5 m) floating alongside a raft in Raunefjorden, Norway, were filled with the natural, local plankton community (see 6.6.2) and exposed to CO₂ and iron manipulation. The material of the enclosures allowed the penetration of the natural irradiance (including PAR, UVA, and UVB, see Table 6.2). To ensure mixing mesocosms were exhibited to permanent bubbling via airlifts reaching to a depth of 4 m. In mesocosm enclosures 2, 5, 8, and 12 HOBO Pendant® Temperature/Light Data Logger 64K – UA-002-64 (Onset, Bourne, USA) were attached to the airlifts in a depth of 0, 1, 2, and 3 m. Further, the airlifts were connected to the aeration system to avoid CO₂ dilution and therefore took air at the desired CO₂ levels. Dissolved gas CO₂ levels were 390 ppm (low CO₂) and 1000 ppm (high CO₂). The value for low CO₂ represents the ambient CO₂ concentration and the high CO₂ level is based on the prediction of the IPCC's "business as usual" scenario IS92a for the year 2100 (IPCC, 2007). Increased CO₂ concentrations were initially reached by addition of pre-equilibrated water enriched in CO₂ to the mesocosm enclosures via silicon tubing at a depth of 4 m. The addition was repeated 1x as CO₂ levels strongly decreased (day 11). This procedure was conducted and observed by J. A. Fernandez, University of Malaga, Spain. To manipulate bioavailable iron the fungal siderophore desferrioxamine B (DFB) (see

Figure 6.2) that complexes Fe(III) was added as an Fe chelating agent on day 7 (12th of June, 2012). In total 100 mL of 70 μ M DFB resulting in a final concentration of ~63.6 nM in the mesocosms were added to enclosures number 4-9 (DFB+), whereas enclosures number 1-3 and 10-12 were not treated with DFB (DFB-). For the experimental design compare also chapter 3.1.

Table 6.2: Irradiance through the bags of the mesocosm enclosures and lids. Data for the bags refer to the sun and those of the lids were measured referred to a Qpanel lamp used for UVA and UVB control. Data were measured using a SM S-500 (Ocean Optics LLC, Ostfildern, Germany) spectroradiometer between 200-800 nm. Specifications provided by M. Segovia.

Irradiance	Sun (%)	Bag (%)	Lamp (%)	Lids (%)
UVA (320-400)	100	67.04	100	80.32
UVA (315-400)	100	66.86	100	80.92
UVB (280-320)	100	53.93	100	83.58
UVB (280-315)	100	50.15	100	83.64
PAR	100	73.33	100	90.45

Abbreviations: UV, ultraviolet, PAR, photosynthetically active radiation.

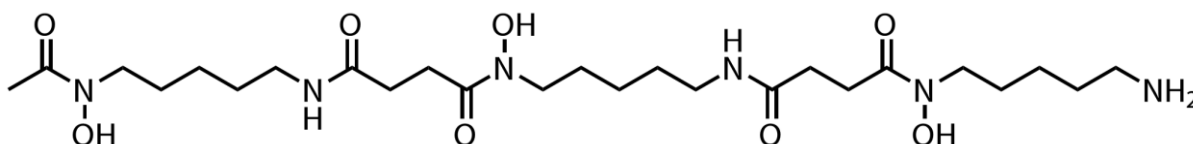


Figure 6.2: Structure of the fungal siderophore desferrioxamine B (DFB). DFB was used for chelating of bioavailable iron, Fe(III), during the mesocosm experiment.

Mesocosms were filled on day -1 (4th of June, 2012) and covered with lids consisting of low density polyethylene (LDPE), which allowed the penetration of >80% of the full solar spectrum (e.g. PAR, UVA, and UVB, see Table 6.2), to cover them against CO₂ loss and external iron sources. On day 0 (5th of June, 2012) enclosures number 2, 5, 8, and 11 were sampled along with water from the fjord (for sampling procedure see 6.6.4). After sampling CO₂ enriched seawater (see above) and nutrients were directly added into the seawater. The applied ratio of nitrogen to phosphorus (N:P) of 30:1 is supposed to be favorable for the initiation of a coccolithophore bloom (Engel et al., 2004). Regular sampling of all mesocosms was started on day 1 (6th of June, 2012).

6.6.2 Filling of mesocosms

Enclosures were filled with the natural plankton community from the fjord. Therefore, water was brought up by a submersible pump (CS-3085.182, ITT Flygt, Sundbyberg, Sweden) located in 7 m depth corresponding to the chlorophyll maximum and distributed between the 12 bags via a hose at a flow rate of approximately $1.5 \text{ m}^3 \text{ min}^{-1}$. First all 12 enclosures were filled for 5 min starting with bag number 1, then starting again with enclosure 1 they were filled for another 3.7 min (total filling time $\sim 8 \text{ min } 40 \text{ s}$) to ensure equal filling volumes. Afterwards each mesocosm contained a total volume of approximately 11,000 L.

6.6.3 Preparation of sampling equipment

As we intended to apply an iron-limited treatment, special care was taken to exclude all sources of potential iron contamination. Four sampling carboys plus an additional carboy for fjord water sampling, and twelve 25 L cans supposed to contain the samples after collection (all PPL, Nalgene, borrowed from the University of Bergen, Norway) underwent a daily cleaning protocol. Therefore, all containers were rinsed 3x with deionized water, filled with approximately 2 L of 10% HCl, shaken rigorously and left standing in HCl overnight. Prior to sampling in the morning sampling containers were thoroughly shaken again, rinsed 3x with deionized water followed by 3x rinsing with fresh Milli-Q water. The same acid and rinsing protocol was also conducted for all tubing involved in sampling.

Bottles, glass beakers, and filtration units used for sub-sample collection or filtration of cells for intracellular metabolite analysis, and for bacterial and viral abundance counts were not treated for exclusion of iron, because the short time the phytoplankton community was exposed to this equipment was not regarded critical in regard of changing their metabolism due to different iron availability. Instead, each piece of the equipment was only used for a defined mesocosm. Measurement cylinders temporarily used to estimate volumes smaller than 1 L were attributed to iron treatment using one cylinder for samples with addition of the iron chelating agent (DFB+) and one for samples without its addition (DFB-). All equipment was daily rinsed rigorously in deionized water after sampling and filtration.

6.6.4 *Sampling of mesocosms*

All mesocosms were sampled daily at 9:00 am over 22 days by application of reduced pressure (>500 mbar) from a depth of 2.5 m through a 200 µm plankton mesh into 20 L carboys. All manipulations of tubing, lids of the sampling carboys, and inside the mesocosms necessary for sample collection were performed with gloves and under precautions against introduction of iron into the mesocosms. The four treatments were sampled in parallel using one carboy per treatment and sampling one replicate after the other. Additionally, fjord water was taken from approximately 1 m depth by direct deposition of the sampling carboy into the fjord. A 200 µm plankton mesh was applied to this carboy after sampling. Obtained water samples were filled into 25 L cans, transported on shore and stored for further processing in a climate chamber set to the same temperature as the fjord water (~10°C). Sampling of all 12 mesocosms and the fjord water took approximately 1-1.5 h. All samples for subsequent analyses were taken from these 25 L can.

6.6.5 *Sampling for bacterial and viral abundance measurements*

Samples for bacterial and viral abundance were all collected at the same time from the 25 L can into 50 mL beakers. Therefore, 13 beakers (one per mesocosm plus one for fjord water) were first rinsed 1x with water from the corresponding can and then ~10 mL of the sample taken. From this sub-sample 2x 1 mL were pipetted into cryo-vials, fixed with 20 µL of 25% aqueous glutaraldehyde (electron microscopy grade, Sigma Aldrich, Oslo, Norway) resulting in a final concentration of 0.5%, vortexed and incubated in the dark at 4°C for 30 min. Then, vials were filled into nylon stockings and deposited in a liquid nitrogen container with the end of the nylon stocking tucked to the outside of the container for sample retrieving. Cryo-vials were left in liquid nitrogen until I found time to transfer them to the -80°C freezer, which was approximately 3 min of walk away. Samples were later shipped at -80°C and after arrival immediately stored at -80°C.

6.6.6 Bacterial and viral enumeration

Bacterial and viral abundances were determined one after the other from the same sample by flow cytometry based on a protocol optimized for quantification of marine viruses (Marie et al., 1999; Brussaard, 2004b). In brief: batches of 10 samples were thawed for approximately 5 min in a water bath at 35°C. SYBR® Gold Nucleic Acid Gel Stain (10.000x concentrated in DMSO, Invitrogen, Carlsbad, CA, USA) was diluted 1:100 (v:v) in sterile filtered TE buffer (10 mM Tris-HCl and 1 mM EDTA, pH 8.0) and stored at -20°C. 10 µL of diluted SYBR® Gold were added to samples resulting in a final concentration of 10^{-4} of the commercial stock. Next, samples were stained for 10 min at 80°C in the dark. Then, samples were prepared separately for determining bacterial and viral enumeration. Depending on bacterial abundance samples were measured undiluted or diluted 5x in sterile filtered TE buffer to avoid coincidence (two or more particles being simultaneously present in the sensor zone). All samples measured for viral abundance were diluted 10x. 100 µL of diluted samples, 100 µL of a calibration standard (see below), and 300 µL of sterile filtered TE buffer were pipetted into test tubes and immediately measured.

For sample measurement a Cytomics FC 500 flow cytometer (Beckman Coulter, Krefeld, Germany) equipped with CXP-software, a 20 mW 488 nm air-cooled argon-ion laser and standard filters was used. The discriminator was set on green fluorescence (emission at 525 nm) and samples run for 1 min at a flow rate of 30 µL min⁻¹. Latex fluorospheres (1.0 µm in diameter; Polysciences Inc., Eppelheim, Germany) measured at 525 nm were used for data calibration and samples measured in triplicates. Since the viral signal was nearly at the detection limit, a blank was subtracted from the number of counted viral like particles. Therefore, TE buffer was stained like the samples and measured in triplicates. Then the mean of the detected signals was subtracted from the estimated numbers for viral like particles.

6.6.7 Sampling of intracellular metabolites

After agitation to ensure a homogenous distribution of phytoplankton in the 25 L can, samples for intracellular metabolites were collected into 1 L plastic bottles (PP, Nalgene® via VWR, Darmstadt, Germany). Depending on *E. huxleyi* abundance 3-6 L per mesocosm were concentrated on GF/F filters (pore size ~0.8 µm, Whatman, Kent, UK) under vacuum (>600 mbar). To prevent temperature stress all filtrations were performed under artificial light in a climate chamber at a temperature equivalent to that of the fjord water (~10°C). Filtration was performed for samples of six mesocosm enclosures in parallel starting with low CO₂ treatments without and with addition of DFB (mesocosms 1-3, and 4-6, respectively) followed by high CO₂ treatments with and without DFB (mesocosms 7-8, and 9-12, respectively). The fjord water sample was concentrated in parallel with low CO₂ treatments. Cell filtration took between 3-5 h per treatment.

Metabolites were extracted from wet filters as described above (see 6.4.1). Extracts were then stored at -20°C during filtration and transferred to -80°C at the end of each day. Samples were shipped at -80°C for further processing.

6.6.8 Analysis of intracellular metabolites

The following modifications of the general metabolomics method for derivatization and GC-MS measurement were used: after ~5 h of drying under reduced pressure (>30 mbar) samples were additionally dried for another 1-2 h under further reduced pressure (<1 mbar) to ensure absolute dryness. The incubation temperature was increased from 40°C to 60°C for derivatization with MSTFA to accelerate the reaction. Further, batches of 19 samples were measured on the GC-MS using a new glass wool containing liner after every 4th batch and the injector set to split mode 5. Data analysis did not lead to exclusion of signals due to co-occurrence with signals from media, because fjord water representing a natural community by itself was not suitable as a blank and thus could not be used to exclude potential contaminations. Instead, it was treated as an additional sample. Further, solvent blanks did not show contaminating peaks that would justify the exclusion of compounds from the data set.

6.6.9 Identification of intracellular metabolites

Three data sets were selected for identification of intracellular metabolites. A combination of the treatments low CO₂/DFB-, low CO₂/DFB+, and high CO₂ was created based on the CAP separation pattern which rather reflected three instead of four treatments (for details see 3.2.4-3.2.7). Further, we identified metabolites highly correlated with low and high CO₂ (see 3.2.8) or correlated with one among three time phases (D0-3, D4-11, and D12-22) in the control (low CO₂/DFB-) (see 3.2.9).

6.6.10 Statistical analysis

Statistical analyses were performed using SigmaPlot™ 11 (Systat Software, San Jose, USA). Two outliers were excluded from the *E. huxleyi* cell abundance data (data provided by A. Larson) and the data set was tested for normality (Shapiro-Wilk test) and for equal variances. As both conditions were fulfilled, differences in *E. huxleyi* cell abundance were statistically analyzed using a one way analysis of variance (ANOVA) with the Holm-Sidak method for pairwise multiple comparisons between the four treatments. As the low CO₂/DFB+ treatment showed a much higher growth than the other treatments, it was excluded to determine differences in *E. huxleyi* cell abundance between low CO₂/DFB-, high CO₂/DFB+, and high CO₂/DFB-. Therefore, a two way ANOVA using a general linear model without interactions followed by the Holm-Sidak method for pairwise multiple comparisons was applied.

Bacterial abundance data did not fulfill the normality and equal variance requirements necessary to use ANOVA. Consequently, a Kruskal-Wallis rank sum test was used to assess differences in bacterial abundance between CO₂ and DFB treatments.

6.6.11 Remarks

Mesocosm enclosure number 1 (low CO₂/DFB-) was overfilled, because we overestimated the necessary filling time. Hence, part of its volume had to be pumped out using a drain pump. Some water also had to be taken out from enclosure number 7 (high CO₂/DFB+), but the volume was not relevant in comparison to the total filling volume. Further, the deposition of a Ramses PAR/UV spectrometer (TrioS Optical GmbH, Oldenburg, Germany) in mesocosm 3 (low CO₂/DFB-) resulted in the introduction of iron from the screws attached to the instrument. Although we did not analyze iron availability in the fjord water, it seemed to have been limited in iron at the start of the experiment (compare 3.3). Therefore, due to iron fertilization enclosure number 3 developed independently from the others and had to be excluded from all further analyses.

Due to a delay at customs samples originally intended to be sent on dry ice (-80°C), arrived melted although still cool (<10°C). This neither affected intracellular metabolites, which are usually shipped at ~4°C, nor bacterial abundance. The latter was tested by comparing bacterial counts of regular samples with samples that were melted and refrozen. Since viral capsids are more fragile than bacterial cells, we expected the melting to reduce absolute viral numbers and, therefore, visualized viral counts using relative numbers (see 3.2.2).

6.7 Viral infection (method of Chapter 4)

This experiment was conducted in a close cooperation with the laboratory of A. Vardi, Weizmann Institute of Science, Rehovot, Israel. Therefore, only methods applied by myself are described, focusing on the metabolic analysis during viral infection and on a pharmacological approach to inhibit biosynthesis pathways of specific metabolite classes.

6.7.1 *Experimental set-up and infection*

Nine 20 L cultures of the non-calcifying *E. huxleyi* strain CCMP2090 were cultured in K/2 medium (Keller et al., 1987) at 18°C and a light/dark cycle of 16:8 h provided by illumination with white fluorescent lights at 100 $\mu\text{M photons m}^{-2} \text{ s}^{-1}$. Cultures in exponential phase ($5 \cdot 10^5$ - 10^6 cells mL^{-1}) were used for the experiment. Triplicates of cultures were infected by adding viral lysate of the lytic virus EhV201 and the non-lytic virus EhV163 at a ratio of 1:50 (v:v) equaling a MOI of about 1:1 viral particles per cell. Non-infected culture triplicates were used as control and supplemented with virus-free 0.22 μm filtered medium originating from a non-infected culture to simulate a potential addition of nutrients or exudates via the viral lysate. An additional 20 L carboy containing medium was used as control to exclude putative contamination.

6.7.2 *Sampling of infected and non-infected E. huxleyi cultures*

2 L of culture and blank medium were sampled from triplicates of 20 L culture vessels containing *E. huxleyi* cells infected by the lytic or non-lytic virus or healthy control cultures at 4, 24, 32, and 48 hours post infection (hpi). For analysis of intracellular metabolites 2x 100 mL (two analytical replicates) of each sample were quickly concentrated at daylight illumination on 47 mm GF/C filters (pore size $\sim 1.2 \mu\text{m}$, Whatman, Kent, UK) applying vacuum (~ 500 mbar). Filtration and extraction of one biological replicate of all three treatments was performed in parallel and took approximately 20 min.

6.7.3 Analysis of intracellular metabolites

Metabolites were extracted from wet glass fiber filters (GF/C filters, Whatman, Kent, UK), derivatized and measured as described above (see 6.4.1) with the following modifications: for derivatization only 25 μ L of methoxyamine solution (10 mg methoxyamine hydrochloride in 0.5 mL pyridine, Sigma-Aldrich, Munich, Germany) was added, samples vortexed for 1 min and incubated at 60°C for 1 h followed by 10 h at room temperature. The retention time index solution did not contain docosane. Samples of each sampling point (4, 24, 32, and 48 hpi) and solvent controls were measured in random order on the GC-MS equipped with a 30 m DB-5ms column with 8 m Duraguard pre-column (Agilent, Waldbronn, Germany) and a liner without glass wool that was changed after every batch (20 samples). Samples were injected in split mode 1 and the MS scan rate was set to 2 scans s^{-1} in DRE mode. For data analysis each sampling point (4, 24, 32, and 48 hpi) was analyzed separately, the component width in the AMDIS settings was modified to 20, which is recommended for broader peaks as obtained in this experiment, and peaks with a retention time earlier than 5 min were excluded from the final data matrix. All detected metabolites were manually examined in MS Search (version 2.0 d, NIST) to determine their identity, statistically analyzed by CAP but without the application of a comparative approach.

Additionally, screening for standard based metabolites of specific interest resulted in the detection of a few compounds that were not found by AMDIS with the general settings. Therefore, the peak area of these metabolites was manually integrated using a selected trace ion and the QuanLynx tool incorporated in MassLynxTM (version 4.1, Waters). After processing as described above peak areas were added to the constrained analysis.

6.7.4 Inhibition of fatty acid biosynthesis

To test the influence of *de-novo* fatty acid biosynthesis on viral production we added 4-methylene-2-octyl-5-oxotetrahydrofuran-3-carboxylic acid (C75) (Sigma-Aldrich, Rehovot, Israel), which inhibits fatty acid synthase (FAS) to *E. huxleyi* CCMP2090 infected by the lytic virus EhV201 or non-infected control cells. Therefore, three biological replicates of exponentially growing 300 mL cultures

(approximately $5 \cdot 10^5$ cells·mL⁻¹) were each divided into 14x 20 mL cultures contained in 40 mL plastic cell culture flasks (greiner bio-one, Rosh Haayin, Israel). C75 was dissolved in DMSO (5 mg mL⁻¹), diluted 1:10 and 1:100 (v:v) in DMSO and added to the cultures reaching final concentrations of 0, 0.5, 1, 2, 3, 4, and 8 µg mL⁻¹. Half of the cultures were directly infected with EhV201 as described above (see 6.7.1). Culture conditions were identical to those described above (see 6.7.1). Samples for *E. huxleyi* cell counts, cell death counts, intra-, and extracellular viruses were taken at 4, 24, 48, and 72 hpi.

6.7.5 Inhibition of terpene biosynthesis

Since two pathways are potentially involved in terpenoid biosynthesis, we specifically inhibited both to determine, which has an influence on viral production. Two biological replicates of 100 mL exponentially growing *E. huxleyi* cultures (approximately $4 \cdot 10^5$ cells·mL⁻¹) were pipetted on two sterile 24 well plates (Thermo Scientific via Danyel Biotech, Rehovot, Israel) using 2 mL per well (one plate per inhibitor). To inhibit terpenoid biosynthesis cerivastatin (mevalonate pathway) and fosmidomycin (methylerythritol phosphate pathway) (both 5 mg mL⁻¹ in double distilled water, ddW, Sigma-Aldrich, Rehovot, Israel) were diluted at ratios of 1:10 and 1:100 (v:v) and added in duplicates at 6 different concentrations resulting in final concentrations of 0, 0.1, 0.5, 1, 5, and 10 µM. After incubation for 2 h half of the cultures were infected by the lytic virus at a ratio of 1:50 (v:v). Cultures were left to grow for 72 h under conditions as described above (see 6.7.1) and then sampled for *E. huxleyi* and extracellular viral abundance. The same set-up was repeated for inhibition with fosmidomycin using three biological replicates and sampled for the same parameters 72 hpi.

To investigate the effect of inhibition of the MVA pathway in more detail, three biological replicates of exponentially growing 250 mL cultures (approximately $4 \cdot 10^5$ cells·mL⁻¹) were divided into 12x 20 mL cultures contained in 40 mL plastic cell culture flasks (Nalgene). Next, cerivastatin was added and cultures infected and cultivated as described above. Samples for *E. huxleyi* cell counts, cell death counts, intra-, and extracellular viruses were taken at 4, 24, 48, and 72 hpi.

6.7.6 Enumeration of life and dead *E. huxleyi* cells

For *E. huxleyi* cell abundance 250 μ L of culture were pipetted on a 96 well plate and quantified using an Eclipse (iCyt) flow cytometer (Sony Biotechnology Inc., Champaign, USA) equipped with 405 and 488 nm solid state air cooled lasers, both with 25 mW on the flowCell, and standard filters. Algae were identified by plotting of chlorophyll fluorescence (red channel, 737-663 nm) against green fluorescence (500-550 nm) or side scatter. The 488 nm laser was used for excitation.

Cell death analysis enumerating lysed cells was used to determine whether the added inhibitors were toxic for *E. huxleyi* cells. Therefore, cells were stained by adding 2 μ L of SYTOX® Green Nucleic Acid Stain (Invitrogen, Carlsbad, CA, USA) in DMSO to 250 μ L of culture resulting in a final concentration of 1 μ M. After incubation in the dark for approximately 1 h, samples were counted on the flow cytometer in the green fluorescence channel at an emission of 525 nm using the 488 nm excitation laser.

6.7.7 Intra- and extracellular viral abundance

Viral abundance was measured using flow cytometry (extracellular viruses) or quantitative polymerase chain reaction (qPCR) of the viral major capsid protein (MCP, intracellular viruses).

To determine the abundance of extracellular viruses 700 μ L of each culture were filtered through a 0.45 μ m Millex-HV filter (PVDF, Millipore, Rosh Haayin, Israel). 100 μ L of cell free lysate were transferred to a 100 μ L ELISA-plate (Thermo Scientific via Danyel Biotech, Rehovot, Israel) and fixed by adding 2 μ L 25% aqueous glutaraldehyde (electron microscopy grade, Sigma Aldrich, Rehovot, Israel) resulting in a final concentration of 0.5%. Samples were vortexed and incubated at 4°C in the dark for 30 min. After fixation, samples were shock frozen in liquid nitrogen and stored at -80°C. For enumeration, samples were thawed at room temperature, diluted 40x in sterile filtered TE buffer (10 mM Tris-HCl and 1 mM EDTA, pH 8.0) containing SYBR® Gold Nucleic Acid Gel Stain (Invitrogen, Carlsbad, CA, USA) (final concentration 10^{-4} of commercial stock) and incubated at 80°C for 20 min. Samples were cooled to room temperature and measured on the flow cytometer using the 488 nm excitation laser and an emission of 525 nm.

For qPCR of intracellular viruses 1 mL of sample was pelleted by centrifugation at 30.000 g for 1 min at 4°C, the pellet washed 2x with autoclaved, filtered NSW and frozen in liquid nitrogen. To estimate viral DNA inside the host cells REDExtract-N-AmpPlant PCR kit (Sigma Aldrich, Rehovot, Israel) was used according to the manufacturer's instructions. In short, 10 µL XNAP extraction buffer were added to the pellet, the sample transferred to a PCR tube and incubated at 95°C for 10 min. Next, 10 µL of XNAP dilution buffer were added and the volume filled up to ~200 µL with ddW. Samples were diluted 100x and 1 µL used for the qPCR reaction in a total volume of 20 µL. qPCR reagent Platinum® SYBR® Green qPCR Super Mix-UDG with ROX (Invitrogen, Carlsbad, CA, USA) was used according to the manufacturer's instructions and 8 pmol per reaction of the following primers were added: MCP1-Fw (5'-ACGCACCCTCAATGTATGGAAGG-3') and MCP90-Rv (5'-AGCCAACTCAGCAGTCGTTC-3') (both Sigma-Aldrich, Rehovot, Israel) (Pagarete et al., 2009). qPCR reactions were performed on StepOnePlus™ real-time PCR Systems (Applied Biosystems, Foster City, USA) as follows: 50°C for 2 min, 95°C for 2 min, 40 cycles of 95°C for 15 s, 60°C for 30 s, followed by melting curve analysis. Results were calibrated against serial dilutions (10^{-2} - 10^{-8}) of EhV201 DNA at known concentrations, enabling exact quantification of viral abundance.

6.7.8 Analysis of free metabolites in viral capsids

Purified, concentrated viral lysate resuspended in 200 µL of phosphate buffer saline was shipped at 4°C for analysis of metabolites in the virion capsids. Virions were retained on 25 mm Anodisc 25 filters (pore size 0.02 µm, Whatman, Kent, UK) and extracted as described above (see 6.4.1) with slight modifications: 500 µL extraction mix were used, samples processed within less than one month, and the whole sample evaporated to dryness and derivatized. The same procedure was performed with a sample of medium. Resulting chromatograms of viral metabolites were screened and spectra for all detected signals compared to library entries using MS Search as described above.

6.7.9 Virus-resistant *E. huxleyi* strains

To confirm the influence of lytic viral infection on terpenoid and sterol biosynthesis we extracted metabolites from two resistant *E. huxleyi* strains challenged with viruses. *E. huxleyi* strains CCMP373, CCMP379 (both resistant to EhV201) and CCMP2090 (non-resistant) used in this experiment were obtained from NCMA. Cultures were grown in K/2 (lacking Tris and Si) medium (Keller et al., 1987) at a temperature of ~20°C under a light/dark regime of 14/10 h with ~48 $\mu\text{mol photons m}^{-2} \text{s}^{-1}$ irradiance. Before the start of the experiment, cultures of all strains were diluted 5x in new medium for a total of 3x every two days. After the last transfer, cultures were grown for 4 days before division of the resistant cultures into three 250 mL replicates contained in Erlenmeyer flasks. 100 mL of each replicate were sampled immediately and intracellular metabolites extracted as described above (see 6.4.1). To the remaining 150 mL cultures lysate of EhV201 was added at a ratio of 1:20 (v:v). As a control EhV201 was also added to 150 mL of the non-resistant strain and the same procedure applied to 250 mL medium. 32 hpi another 100 mL were sampled for extraction of intracellular metabolites as previously described (see 6.4.1). All extracts were stored at -20°C for further processing (see 6.4.4), but only $\sim 25 \cdot 10^6$ cells were used and measured by GC-MS (within two weeks after the experiment) using the settings described above (see 6.4.2).

For analysis of terpene and sterol regulation, chromatograms were screened for specific ion traces of these compounds. Peak areas were obtained by manual integration as described above (see 6.7.3) and transferred into Excel 2010 (Microsoft, Redmont, USA). Since different strains were used for metabolite extraction and, thus, the assumption of constant metabolite intensity probably not fulfilled, data were normalized by cell number. Further, of the total metabolites only terpenes and sterols were analyzed, which further does not allow for peak sum normalization.

For all counts 1 mL of culture was sampled under sterile conditions to monitor growth at 0, 24, 32, 48, and 72 hpi. *E. huxleyi* abundance was determined by counting at least 400 cells in triplicates using a Fuchs-Rosenthal hemocytometer with an upright microscope (magnification: 400x, Leica DM 2000, Heerbrugg, Switzerland).

References

- Adams, R.P. (2007). Identification of essential oil components by gas chromatography/mass spectrometry. (Allured Publishing Corporation: Carol Stream), p. 804.
- Admiraal, W., Peletier, H., and Laane, R.W.P.M. (1986). Nitrogen metabolism of marine planktonic diatoms; extraction, assimilation and cellular pools of free amino acids in seven species with different cell size. *J. Exp. Mar. Biol. Ecol.* 98: 241-263.
- Allen, A.E., LaRoche, J., Maheswari, U., Lommer, M., Schauer, N., Lopez, P.J., Finazzi, G., Fernie, A.R., and Bowler, C. (2008a). Whole-cell response of the pennate diatom *Phaeodactylum tricornutum* to iron starvation. *Proc. Nat. Acad. Sci. USA* 105: 10438-10443.
- Allen, M., Howard, J., Lilley, K., and Wilson, W. (2008b). Proteomic analysis of the EhV-86 virion. *Proteome Sci.* 6: 11.
- Allen, M.J., Martinez-Martinez, J., Schroeder, D.C., Somerfield, P.J., and Wilson, W.H. (2007). Use of microarrays to assess viral diversity: from genotype to phenotype. *Environ. Microbiol.* 9: 971-982.
- Anderson, M.J., and Willis, T.J. (2003). Canonical analysis of principal coordinates: a useful method of constrained ordination for ecology. *Ecology* 84: 511-525.
- Ausloos, P., Clifton, C.L., Lias, S.G., Mikaya, A.I., Stein, S.E., Tchekhovskoi, D.V., Sparkman, O.D., Zaikin, V., and Zhu, D. (1999). The critical evaluation of a comprehensive mass spectral library. *J. Am. Soc. Mass. Spectr.* 10: 287-299.
- Azam, F., Fenchel, T., Field, J.G., Gray, J.S., Meyer-Reil, L.A., and Thingstad, F. (1983). The ecological role of water-column microbes in the sea. *Mar. Ecol. Prog. Ser.* 10: 257-262.
- Balch, W.M., Holligan, P.M., Ackleson, S.G., and Voss, K.J. (1991). Biological and optical properties of mesoscale coccolithophore blooms in the Gulf of Maine. *Limnol. Oceanogr.* 36: 629-643.
- Barofsky, A., Vidoudez, C., and Pohnert, G. (2009). Metabolic profiling reveals growth stage variability in diatom exudates. *Limnol. Oceanogr.-Meth.* 7: 382-390.
- Barofsky, A., Simonelli, P., Vidoudez, C., Troedsson, C., Nejstgaard, J.C., Jakobsen, H.H., and Pohnert, G. (2010). Growth phase of the diatom *Skeletonema marinoi* influences the metabolic profile of the cells and the selective feeding of the copepod *Calanus* spp. *J. Plankton Res.* 32: 263-272.
- Bates, S.R., and Rothblat, G.H. (1972). Incorporation of L cell sterols into vesicular stomatitis virus. *J. Virol.* 9: 883.
- Bell, M.V., and Pond, D. (1996). Lipid composition during growth of motile and coccolith forms of *Emilinia huxleyi*. *Phytochemistry* 41: 465-471.
- Bergh, Ø., Børsheim, K.Y., Bratbak, G., and Haldal, M. (1989). High abundance of viruses found in aquatic environments. *Nature* 340: 467-468.
- Bidle, K.D., Haramaty, L., e Ramos, J.B., and Falkowski, P. (2007). Viral activation and recruitment of metacaspases in the unicellular coccolithophore, *Emiliana huxleyi*. *Proc. Natl. Acad. Sci. USA* 104: 6049-6054.
- Billard, C., and Inouye, I. (2004). Cell biology and biochemistry. In Coccolithophores: From Molecular Processes to Global Impact, H.R. Thierstein and J.R. Young, eds (Springer-Verlag: Berlin Heidelberg), pp. 1-29.
- Blanc, M., Hsieh, W.Y., Robertson, K.A., Watterson, S., Shui, G., Lacaze, P., Khondoker, M., Dickinson, P., Sing, G., Rodríguez-Martín, S., Phelan, P., Forster, T., Strobl, B., Müller, M., Riemersma, R., Osborne, T., Wenk, M.R., Angulo, A., and Ghazal, P. (2011). Host defense against viral infection involves interferon mediated down-regulation of sterol biosynthesis. *PLOS Biol.* 9: e1000598.
- Bölling, C., and Fiehn, O. (2005). Metabolite profiling of *Chlamydomonas reinhardtii* under nutrient deprivation. *Plant Physiol.* 139: 1995-2005.

- Bouchereau, A., Aziz, A., Larher, F., and Martin-Tanguy, J. (1999). Polyamines and environmental challenges: recent development. *Plant Sci.* 140: 103-125.
- Bratbak, G., Egge, J.K., and Haldal, M. (1993). Viral mortality of the marine alga *Emiliania huxleyi* (Haptophyceae) and termination of algal blooms. *Mar. Ecol. Prog. Ser.* 93: 39-48.
- Breitbart, M. (2012). Marine viruses: truth or dare. *Annu. Rev. Marine Sci.* 4: 425-448.
- Brown, C.W., and Yoder, J.A. (1994). Distribution pattern of coccolithophorid blooms in the western North Atlantic Ocean. *Cont. Shelf Res.* 14: 175-197.
- Brussaard, C.P.D. (2004a). Viral control of phytoplankton populations - a review. *J. Eukaryot. Microbiol.* 51: 125-138.
- Brussaard, C.P.D. (2004b). Optimization of procedures for counting viruses by flow cytometry. *Appl. Environ. Microb.* 70: 1506-1513.
- Brussaard, C.P.D., Riegman, R., Noordeloos, A.A.M., Cadée, G.C., Witte, H., Kop, A.J., Nieuwland, G., van Duyl, F.C., and Bak, R.P.M. (1995). Effects of grazing, sedimentation and phytoplankton cell lysis on the structure of a coastal pelagic food web. *Mar. Ecol. Prog. Ser.* 123: 259-271.
- Caldeira, K., and Wicket, M.E. (2003). Anthropogenic carbon and ocean pH. *Nature* 425: 365.
- Chuecas, L., and Riley, J.P. (1969). Component fatty acids of the total lipids of some marine phytoplankton. *J. Mar. Biol. Ass. UK* 49: 97-116.
- Colombini, M.P., Modugno, F., and Giacomelli, A. (1999). Two procedures for suppressing interference from inorganic pigments in the analysis by gas chromatography-mass spectrometry of proteinaceous binders in paintings. *J. Chromatogr. A* 846: 101-111.
- Connon, R.E., Geist, J., and Werner, I. (2012). Effect-based tools for monitoring and predicting the ecotoxicological effects of chemicals in the aquatic environment. *Sensors* 12: 12741-12771.
- Coppens, I. (2013). Targeting lipid biosynthesis and salvage in apicomplexan parasites for improved chemotherapies. *Nat. Rev. Micro.* 11: 823-835.
- de Vargas, C., Aubry, M.-P., Probert, I., and Young, J. (2007). Origin and evolution of coccolithophores: from coastal hunters to oceanic farmers. In *Evolution of Aquatic Photoautotrophs*, P. Falkowski and A.H. Knoll, eds (Elsevier Academic Press: New York, USA), pp. 251-285.
- Delgado, T., Sanchez, E.L., Camarda, R., and Lagunoff, M. (2012). Global metabolic profiling of infection by an oncogenic virus: KSHV induces and requires lipogenesis for survival of latent infection. *PLOS Pathog.* 8: e1002866.
- Delille, B., Harlay, J., Zondervan, I., Jacquet, S., Chou, L., Wollast, R., Bellerby, R.G.J., Frankignoulle, M., Borges, A.V., Riebesell, U., and Gattuso, J.-P. (2005). Response of primary production and calcification to changes of pCO₂ during experimental blooms of the coccolithophorid *Emiliania huxleyi*. *Global Biogeochem. Cy.* 19: GB2023.
- Diamond, D.L., Syder, A.J., Jacobs, J.M., Sorensen, C.M., Walters, K.-A., Proll, S.C., McDermott, J.E., Gritsenko, M.A., Zhang, Q., Zhao, R., Metz, T.O., Camp, D.G.I., Waters, K.M., Smith, R.D., Rice, C.M., and Katze, M.G. (2010). Temporal proteome and lipidome profiles reveal hepatitis C virus-associated reprogramming of hepatocellular metabolism and bioenergetics. *PLOS Pathog.* 6: e1000719.
- Disch, A., Schwender, J., Müller, C., Lichtenthaler, H.K., and Rohmer, M. (1998). Distribution of the mevalonate and glyceraldehyde phosphate/pyruvate pathways for isoprenoid biosynthesis in unicellular algae and the cyanobacterium *Synechocystis* PCC 6714. *Biochem. J.* 333: 381-388.
- Ducklow, H.W., Steinberg, D.K., and Buesseler, K.O. (2001). Upper ocean carbon export and the biological pump. *Oceanography* 14: 50-58.
- Dunlap, W.C., and Susic, M. (1986). Photochemical decomposition rates of pteridines and flavins in seawater exposed to surface solar radiation. *Mar. Chem.* 19: 99-107.
- Dupont, C.L., Goepfert, T.J., Lo, P., Wei, L., and Ahner, B.A. (2004). Diurnal cycling of glutathione in marine phytoplankton: field and culture studies. *Limnol. Oceanogr.* 49: 991-996.
- Eldridge, M.L., Trick, C.G., Alm, M.B., DiTullio, G.R., Rue, E.L., Bruland, K.W., Hutchins, D.A., and Wilhelm, S.W. (2004). Phytoplankton community response to a manipulation of bioavailable iron in HNLC waters of the subtropical Pacific Ocean. *Aquat. Microb. Ecol.* 35: 79-91.

- Ellington, J.J., Schlotzhauer, P.F., and Schepartz, A.I. (1978). Quantitation of hexane-extractable lipids in serial samples of flue-cured tobaccos. *J. Agric. Food Chem.* 26: 270-273.
- Engel, A., Delille, B., Jacquet, S., Riebesell, U., Rochelle-Newall, E., Terbrüggen, A., and Zondervan, I. (2004). Transparent exopolymer particles and dissolved organic carbon production by *Emiliana huxleyi* exposed to different CO₂ concentrations: a mesocosm experiment. *Aquat. Microb. Ecol.* 34: 93-104.
- Engel, A., Zondervan, I., Aerts, K., Beaufort, L., Benthien, A., Chou, L., Delille, B., Gattuso, J.-P., Harlay, J., Heemann, C., Hoffmann, L., Jacquet, S., Nejstgaard, J., Pizay, M.-D., Rochelle-Newall, E., Schneider, U., Terbrueggen, A., and Riebesell, U. (2005). Testing the direct effect of CO₂ concentration on a bloom of the coccolithophore *Emiliana huxleyi* in mesocosm experiments. *Limnol. Oceanogr.* 50: 493-507.
- Evans, C., Pond, D.W., and Wilson, W.H. (2009). Changes in *Emiliana huxleyi* fatty acid profiles during infection with *E. huxleyi* virus 86: physiological and ecological implications. *Aquat. Microb. Ecol.* 55: 219-228.
- Evans, C., Malin, G., Mills, G.P., and Wilson, W.H. (2006). Viral infection of *Emiliana huxleyi* (Prymnesiophyceae) leads to elevated production of reactive oxygen species. *J. Phycol.* 42: 1040-1047.
- Falkowski, P.G., Barber, R.T., and Smetacek, V. (1998). Biogeochemical controls and feedbacks on ocean primary production. *Science* 281: 200-206.
- Fernández, E., Balch, W.M., Marañón, E., and Holligan, P.M. (1994). High rates of lipid biosynthesis in cultured, mesocosm and coastal populations of the coccolithophore *Emiliana huxleyi*. *Mar. Ecol. Prog. Ser.* 114: 13-22.
- Fiehn, O. (2002). Metabolomics - the link between the genotypes and phenotypes. *Plant Mol. Biol.* 48: 155-171.
- Fiehn, O. (2008). Extending the breadth of metabolite profiling by gas chromatography coupled to mass spectrometry. *Trends Anal. Chem.* 27: 261-269.
- Fiehn, O., Kopka, J., Dörmann, P., Altmann, T., Trethewey, R.N., and Willmitzer, L. (2000). Metabolite profiling for plant functional genomics. *Nat. Biotechnol.* 18: 1157-1161.
- Fiehn, O., Sumner, L.W., Rhee, S.Y., Ward, J., Dickerson, J., Lange, B.M., Lane, G., Roessner, U., Last, R., and Nikolau, B. (2007). Minimum reporting standard for plant biology context information in metabolomic studies. *Metabolomics* 3: 195-201.
- Field, C.B., Behrenfeld, M.J., Randerson, J.T., and Falkowski, P. (1998). Primary production of the biosphere: integrating terrestrial and oceanic components. *Science* 281: 237-240.
- Frada, M., Probert, I., Allen, M.J., Wilson, W.H., and de Vargas, C. (2008). The "Cheshire Cat" escape strategy of the coccolithophore *Emiliana huxleyi* in response to viral infection. *Proc. Natl. Acad. Sci. USA* 105: 15944-15949.
- Frada, M.J., Bidle, K.D., Probert, I., and de Vargas, C. (2012). *In situ* survey of life cycle phases of the coccolithophore *Emiliana huxleyi* (Haptophyta). *Environ. Microbiol.* 14: 1558-1569.
- Fredholm, B.B. (2007). Adenosine, an endogenous distress signal, modulates tissue damage and repair. *Cell Death Differ.* 14: 1315-1323.
- Fuhrman, J.A. (1999). Marine viruses and their biogeochemical and ecological effects. *Nature* 399: 541-548.
- Fulton, J.M., Fredricks, H.F., Bidle, K.D., Vardi, A., Kendrick, B.J., DiTullio, G.R., and Van Mooy, B.A.S. (2014). Novel molecular determinants of viral susceptibility and resistance in the lipidome of *Emiliana huxleyi*. *Environ. Microbiol.*: doi:10.1111/1462-2920.12358.
- Gordillo, F.L., Goutx, M., Figueroa, F., and Niell, F.X. (1998). Effects of light intensity, CO₂ and nitrogen supply on lipid class composition of *Dunaliella viridis*. *J. Appl. Phycol.* 10: 135-144.
- Goulitquer, S., Potin, P., and Tonon, T. (2012). Mass spectrometry-based metabolomics to elucidate functions in marine organisms and ecosystems. *Mar. Drugs* 10: 849-880.
- Gray, N.K., Quick, S., Goossen, B., Constable, A., Hirling, H., Kühn, L.C., and Hentze, M.W. (1993). Recombinant iron-regulatory factor functions as an iron-responsive-element-binding protein, a translational repressor and an aconitase. *Eur. J. Biochem.* 218: 657-667.

- Green, J.C., Course, P.A., and Tarran, G.A. (1996). The life-cycle of *Emiliania huxleyi*: a brief review and a study of relative ploidy levels analysed by flow cytometry. *J. Mar. Syst.* 9: 33-44.
- Gregg, W.W., and Casey, N.W. (2007). Modeling coccolithophores in the global oceans. *Deep-Sea Res. Pt. II* 54: 447-477.
- Griffiths, M.J., and Harrison, S.T.L. (2009). Lipid productivity as a key characteristic for choosing algal species for biodiesel production. *J. Appl. Phycol.* 21: 493-507.
- Gross, W., and Meyer, A. (2003). Distribution of *myo*-inositol dehydrogenase in algae. *Eur. J. Phycol.* 38: 191-194.
- Grossi, V., Baas, M., Schogt, N., Klein Breteler, W.C.M., De Leeuw, J.W., and Rontani, J.-F. (1996). Formation of phytadienes in the water column: myth or reality? *Org. Geochem.* 24: 833-839.
- Gunnar, T., Ariniemi, K., and Lillsunde, P. (2005). Determination of 14 benzodiazepines and hydroxy metabolites, zaleplon and zolpidem astert-butyl dimethylsilyl derivatives compared with other common silylating reagents in whole blood by gas chromatography-mass spectrometry. *J. Chromatogr. B* 818: 175-189.
- Haberstroh, P.R., and Ahmed, S.I. (1986). Resolution by high pressure liquid chromatography of intracellular and extracellular free amino acids of a nitrogen deficient marine diatom, *Skeletonema costatum* (Grev.) Cleve, pulsed with nitrate or ammonium. *J. Exp. Mar. Biol. Ecol.* 101: 101-117.
- Handa, N. (1969). Carbohydrate metabolism in the marine diatom *Skeletonema costatum*. *Mar. Biol.* 4: 208-214.
- Hartmann, M.-A. (1998). Plant sterols and the membrane environment. *Trends Plant Sci.* 3: 170-175.
- Helsper, J.P., and Loewus, F.A. (1982). Metabolism of L-threonic acid in *Rumex x acutus* L. and *Pelargonium crispum* (L.) L'Hér. *Plant Physiol.* 69: 1365-1368.
- Hitchcock, G.L. (1982). A comparative study of the size-dependent organic composition of marine diatoms and dinoflagellates. *J. Plankton Res.* 4: 363-377.
- Hites, R.A. (1974). Phytadienes from the pyrolysis of pheophytin a. *J. Org. Chem.* 39: 2634-2635.
- Holligan, P.M., Viollier, M., Harbour, D.S., Camus, P., and Champagne-Philippe, M. (1983). Satellite and ship studies of coccolithophore production along a continental shelf edge. *Nature* 304: 339-342.
- Holligan, P.M., Fernández, E., Aiken, J., Balch, W.M., Boyd, P., Burkill, P.H., Finch, M., Groom, S.B., Malin, G., Muller, K., Purdie, D.A., Robinson, C., Trees, C.C., Turner, S.M., and van der Wal, P. (1993). A biogeochemical study of the coccolithophore, *Emiliania huxleyi*, in the North Atlantic. *Global Biogeochem. Cy.* 7: 879-900.
- Honjo, S., Manganini, S.J., Krishfield, R.A., and Francois, R. (2008). Particulate organic carbon fluxes to the ocean interior and factors controlling the biological pump: a synthesis of global sediment trap programs since 1983. *Prog. Oceanogr.* 76: 217-285.
- Houdan, A., Probert, I., Lenning, K.V., and Lefebvre, S. (2005). Comparison of photosynthetic responses in diploid and haploid life-cycle phases of *Emiliania huxleyi* (Prymnesiophyceae). *Mar. Ecol. Prog. Ser.* 292: 139-146.
- Houdan, A., Billard, C., Marie, D., Not, F., Sáez, A.G., Young, J.R., and Probert, I. (2004). Holococcolithophore-heterococcolithophore (Haptophyta) life cycles: flow cytometric analysis of relative ploidy levels. *Syst. Biodivers.* 1: 453-465.
- Hummel, J., Strehmel, N., Selbig, J., Walther, D., and Kopka, J. (2010). Decision tree supported substructure prediction of metabolites from GC-MS profiles. *Metabolomics* 6: 322-333.
- Hurst, C.J. (2011). An introduction to viral taxonomy with emphasis on microbial and botanical hosts and the proposal of Akamara, a potential domain for the genomic acellular agents. In *Studies in Viral Ecology: Microbial and Botanical Host Systems*, J.C. Hurst, ed (John Wiley & Sons, Inc.: Hoboken, New Jersey), pp. 41-65.
- Huseby, S., Degerlund, M., Zingone, A., and Hansen, E. (2012). Metabolic fingerprinting reveals differences between northern and southern strains of the cryptic diatom *Chaetoceros socialis*. *Eur. J. Phycol.* 47: 480-489.

- Hutchins, D.A., Franck, V.M., Brzezinski, M.A., and Bruland, K.W. (1999). Inducing phytoplankton iron limitation in iron-replete coastal waters with a strong chelating ligand. *Limnol. Oceanogr.* 44: 1009-1018.
- Iglesias-Rodriguez, M.D., Brown, C.W., Doney, S.C., Kleypas, J., Kolber, D., Kolber, Z., Hayes, P.K., and Falkowski, P.G. (2002). Representing key phytoplankton functional groups in ocean carbon cycle models: coccolithophorids. *Global Biogeochem. Cy.* 16: 47-41–47-20.
- Iglesias-Rodriguez, M.D., Halloran, P.R., Rickaby, R.E.M., Hall, I.R., Colmenero-Hidalgo, E., Gittins, J.R., Green, D.R.H., Tyrell, T., Gibbs, S.J., von Dassow, P., Rehm, E., Armbrust, E.V., and Boessenkool, K.P. (2008). Phytoplankton calcification in a high-CO₂ world. *Science* 320: 336-340.
- IPCC. (2007). Climate Change 2007: The Physical Science Basis. Contribution of Working Group I to the Fourth Assessment Report of the Intergovernmental Panel on Climate Change. (Cambridge University Press: Cambridge, United Kingdom and New York, NY, USA), p. 996.
- Jacquet, S., Heldal, M., Iglesias-Rodriguez, D., Larsen, A., Wilson, W., and Bratbak, G. (2002). Flow cytometric analysis of an *Emiliana huxleyi* bloom terminated by viral infection. *Aquat. Microb. Ecol.* 27: 111-124.
- Jamers, A., Blust, R., and De Coen, W. (2009). Omics in algae: paving the way for a systems biological understanding of algal stress phenomena? *Aquat. Toxicol.* 92: 114-121.
- Janknegt, P.J., de Graaff, C.M., van de Poll, W.H., Visser, R.J.W., Rijstenbil, J.W., and Buma, A.G.J. (2009). Short-term antioxidative responses of 15 microalgae exposed to excessive irradiance including ultraviolet radiation. *Eur. J. Phycol.* 44: 525-539.
- Jansen, J.J., Smit, S., Hoefsloot, H.C.J., and Smilde, A.K. (2009). The photographer and the greenhouse: how to analyse plant metabolomics data. *Phytochem. Anal.* 21: 48-60.
- Johnston, R.B., and Bloch, K. (1951). Enzymatic synthesis of glutathione. *J. Biol. Chem.* 188: 221-240.
- Jordan, R.J., Cros, L., and Young, J.R. (2004). A revised classification scheme for living haptophytes. *Micropaleontology* 50: 55-79.
- Kaiser, A., Vollmert, M., Tholl, D., Graves, M.V., Gurnon, J.R., Xing, W., Lisec, A.D., Nickerson, K.W., and Van Etten, J.L. (1999). Chlorella virus PBCV-1 encodes a functional homospermidine synthase. *Virology* 263: 254-262.
- Kapadia, S.B., and Chisari, F.V. (2005). Hepatitis C virus RNA replication is regulated by host geranylgeranylation and fatty acids. *Proc. Natl. Acad. Sci. USA* 102: 2561-2566.
- Karl, D.M., Winn, C.D., and Wong, D.C.L. (1981). RNA synthesis as a measure of microbial growth in aquatic environments. I. Evaluation, verification and optimization of methods. *Mar. Biol.* 64: 1-12.
- Kegel, J.U., Blaxter, M., Allen, M.J., Metfies, K., Wilson, W.H., and Valentin, K. (2010). Transcriptional host-virus interaction of *Emiliana huxleyi* (Haptophyceae) and EhV-86 deduced from combined analysis of expressed sequence tags and microarrays. *Eur. J. Phycol.* 48: 1-12.
- Keller, M.D., Selvin, R.C., Claus, W., and Guillard, R.R.L. (1987). Media for the culture of oceanic ultraphytoplankton. *J. Phycol.* 23: 633-638.
- Klaveness, D. (1972). *Coccolithus huxleyi* (Lohm.) Kamptn II. The flagellate cell, aberrant cell types, vegetative propagation and life cycles. *Br. phycol. J.* 7: 309-318.
- Kluender, C., Sans-Piché, F., Riedl, J., Altenburger, R., Härtig, C., Laue, G., and Schmitt-Jansen, M. (2009). A metabolomics approach to assessing phytotoxic effects on the green alga *Scenedesmus vacuolatus*. *Metabolomics* 5: 59-71.
- Knauert, S., Escher, B., Singer, H., Hollender, J., and Knauer, K. (2008). Mixture toxicity of three photosystem II inhibitors (antrazine, isoproturon, and diuron) toward photosynthesis of freshwater phytoplankton studied in outdoor mesocosms. *Environ. Sci. Technol.* 42: 6424-6430.
- Koek, M.M., Muilwijk, B., van der Werf, M.J., and Hankemeier, T. (2006). Microbial metabolomics with gas chromatography/mass spectrometry. *Anal. Chem.* 78: 1272-1281.

- König, W.A., Joulain, D., Robertet, S., Grasse, A., and Hochmuth, D.H. (2008). Terpenoids and related constituents of essential oils, Library of MassFinder 4.0. (University of Hamburg, Hochmuth Scientific Consulting: Hamburg, Germany).
- Koyuncu, E., Purdy, J.G., Rabinowitz, J.D., and Shenk, T. (2013). Saturated very long chain fatty acids are required for the production of infectious human cytomegalovirus progeny. *PLOS Pathog.* 9: e1003333.
- Krug, S.A., Schulz, K.G., and Riebesell, U. (2011). Effects of CO₂-induced changes in seawater carbonate chemistry speciation on *Coccolithus braarudii*: a conceptual model of coccolithophorid sensitivities. *Biogeosciences* 8: 771-777.
- Kruskopf, M., and Flynn, K.J. (2006). Chlorophyll content and fluorescence responses cannot be used to gauge reliably phytoplankton biomass, nutrient status or growth rate. *New Phytol.* 169: 525-536.
- La Scola, B., Desnues, C., Pagnier, I., Robert, C., Barrassi, L., Fournous, G., Merchat, M., Suzan-Monti, M., Forterre, P., Koonin, E., and Raoult, D. (2008). The virophage as a unique parasite of the giant mimivirus. *Nature* 455: 100-105.
- Langfelder, P., and Horvath, S. (2008). WGCNA: an R package for weighted correlation network analysis. *BMC Bioinformatics* 9: 559.
- Lee, D.Y., and Fiehn, O. (2008). High quality metabolomic data for *Chlamydomonas reinhardtii*. *Plant Methods* 4: 7.
- Lei, Z., Li, H., Chang, J., Zhao, P.X., and Sumner, L.W. (2012). MET-IDEA version 2.06; improved efficiency and additional functions for mass spectrometry-based metabolomics data processing. *Metabolomics* 8: 105-110.
- Liang, H., Yao, N., Song, J.T., Luo, S., Lu, H., and Greenberg, J.T. (2003). Ceramides modulate programmed cell death in plants. *Gene Dev.* 17: 2636-2641.
- Liess, M., and Beketov, M. (2011). Traits and stress: keys to identify community effects of low levels of toxicants in test systems. *Ecotoxicology* 20: 1328-1340.
- Lin, D., Ilias, A., Connor, W., Caldwell, R., Cory, H.T., and Doyle, G.D.J. (1982). Composition and biosynthesis of sterols in selected marine phytoplankton. *Lipids* 17: 818-824.
- Lindell, D., Jaffe, J.D., Johnson, Z.I., Church, G.M., and Chisholm, S.W. (2005). Photosynthesis genes in marine viruses yield proteins during host infection. *Nature* 438: 86-89.
- Link, J. (2002). Does food web theory work for marine ecosystems? *Mar. Ecol. Prog. Ser.* 230: 1-9.
- Lippemeier, S., Hintze, R., Vanselow, K.H., Hartig, P., and Colijn, F. (2001). In-line recording of PAM fluorescence of phytoplankton cultures as a new tool for studying effects of fluctuating nutrient supply on photosynthesis. *Eur. J. Phycol.* 36: 89-100.
- Lisec, J., Schauer, N., Kopka, J., Willmitzer, L., and Fernie, A.R. (2006). Gas chromatography mass spectrometry-based metabolite profiling in plants. *Nat. Protoc.* 1: 387-396.
- Llewellyn, C.A., Evans, C.A., Airs, R.L., Cook, I., Bale, N., and Wilson, W.H. (2007). The response of carotenoids and chlorophylls during virus infection of *Emiliania huxleyi* (Prymnesiophyceae). *J. Exp. Mar. Biol. Ecol.* 344: 101-112.
- Lohr, M., Schwender, J., and Polle, J.E.W. (2012). Isoprenoid biosynthesis in eukaryotic phototrophs: a spotlight on algae. *Plant Sci.* 185-186: 9-22.
- Maas, W.K., Novelli, G.D., and Lipmann, F. (1953). Acetylation of glutamic acid by extracts of *Escherichia coli*. *Proc. Nat. Acad. Sci. USA* 39: 1004-1008.
- Mackenzie, J.M., Khromykh, A.A., and Parton, R.G. (2007). Cholesterol manipulation by West Nile Virus perturbs the cellular immune response. *Cell Host Microbe* 2: 229-239.
- Mackinder, L.C.M., Worthy, C.A., Biggi, G., Hall, M., Ryan, K.P., Varsani, A., Harper, G.M., Wilson, W.H., Brownlee, C., and Schroeder, D.C. (2009). A unicellular algal virus, *Emiliania huxleyi* virus 86, exploits an animal-like infection strategy. *J. gen. Virol.* 90: 2306-2316.
- Madigan, M.T., Martinko, J.M., and Parker, J. (2000). Brock Biology of Microorganisms. (Prentice Hall: Upper Saddle River, NJ), p. 992.
- Maldonado, M.T., and Price, N.M. (2001). Reduction and transport of organically bound iron by *Thalassiosira oceanica* (Bacillariophyceae). *J. Phycol.* 37: 298-310.

- Malin, G., and Steinke, M. (2004). Dimethyl sulfide production: what is the contribution of the coccolithophores? In *Coccolithophores: From Molecular Processes to Global Impact*, H.R. Thierstein and J.R. Young, eds (Springer-Verlag: Berlin Heidelberg), pp. 127-164.
- Marie, D., Brussaard, C.P.D., Thyrhaug, R., Bratbak, G., and Vaultot, D. (1999). Enumeration of marine viruses in culture and natural samples by flow cytometry. *Appl. Environ. Microbiol.* 65: 45-52.
- Martin, J.H., and Fitzwater, S.E. (1988). Iron deficiency limits phytoplankton growth in the north-east Pacific subarctic. *Nature* 331: 341-343.
- Martínez-Martínez, J., Norland, S., Thingstad, T.F., Schroeder, D.C., Bratbak, G., Wilson, W.H., and Larsen, A. (2006). Variability in microbial population dynamics between similarly perturbed mesocosms. *J. Plankton Res.* 28: 783-791.
- Martinez Martinez, J., Schroeder, D.C., Larsen, A., Bratbak, G., and Wilson, W.H. (2007). Molecular dynamics of *Emiliana huxleyi* and cooccurring viruses during two separate mesocosm studies. *Appl. Environ. Microbiol.* 73: 554-562.
- Mason, R.P. (2006). Molecular basis of differences among statins and a comparison with antioxidant vitamins. *Am. J. Cardiol.* 98: S34-S41.
- Maxwell, J.R., Mackenzie, A.S., and Volkman, J.K. (1980). Configuration at C-24 in steranes and sterols. *Nature* 286: 694-697.
- Milliman, J.D. (1993). Production and accumulation of calcium carbonate in the ocean: budget of a nonsteady state. *Global Biogeochem. Cy.* 7: 927-957.
- Moreira, D., and López-García, P. (2009). Ten reasons to exclude viruses from the tree of life. *Nat. Rev. Microbiol.* 7: 306-311.
- Moriarty, D.J.W., and Pollard, P.C. (1981). DNA synthesis as a measure of bacterial productivity in seagrass sediments. *Mar. Ecol. Prog. Ser.* 5: 151-156.
- Munger, J., Bennett, B.D., Parikh, A., Feng, X.-J., McArdle, J., Rabitz, H.A., Shenk, T., and Rabinowith, J.D. (2008). Systems-level metabolic flux profiling identifies fatty acid synthesis as a target for antiviral therapy. *Nat. Biotechnol.* 26: 1179-1186.
- Munne-Bosch. (2005). The role of α -tocopherol in plant stress tolerance. *J. Plant Physiol.* 162: 743-748.
- Nappo, M., Berkov, S., Codina, C., Avila, C., Messina, P., Zupo, V., and Bastida, J. (2009). Metabolite profiling of the benthic diatom *Cocconeis scutellum* by GC-MS. *J. Appl. Phycol.* 21: 295-306.
- Nissimov, J.I., Worthy, C.A., Rooks, P., Napier, J.A., Kimmance, S.A., Henn, M.R., Ogata, H., and Allen, M.J. (2012). Draft genome sequence of four Coccolithoviruses: *Emiliana huxleyi* virus EhV-88, EhV-201, EhV-207, and EhV-208. *J. Virol.* 86: 2896-2897.
- Nylund, G.M., Weinberger, F., Rempt, M., and Pohnert, G. (2011). Metabolomic assessment of induced and activated chemical defence in the invasive red alga *Gracilaria vermiculophylla*. *PLOS One* 6: e29359.
- Obata, T., Schoenefeld, S., Krahnert, I., Bergmann, S., Scheffel, A., and Fernie, A.R. (2013). Gas-chromatography mass-spectrometry (GC-MS) based metabolite profiling reveals mannitol as a major storage carbohydrate in the coccolithophorid alga *Emiliana huxleyi*. *Metabolites* 3: 168-184.
- Oliver, S.G., Winson, M.K., Kell, D.B., and Baganz, F. (1998). Systematic functional analysis of the yeast genome. *Trends Biotechnol.* 16: 373-378.
- Overmeyer, J.H., and Maltese, W.A. (1992). Isoprenoid requirement for intracellular transport and processing of murine leukemia virus envelope protein. *J. Biol. Chem.* 267: 22686-22692.
- Öztürk, M., Steinnes, E., and Sakshaug, E. (2002). Iron speciation in the Trondheim Fjord from the perspective of iron limitation for phytoplankton. *Estuar. Coast. Mar. Sci.* 55: 197-212.
- Paasche, E. (2002). A review of the coccolithophorid *Emiliana huxleyi* (Prymnesiophyceae) with particular reference to growth, coccolith formation, and calcification-photosynthesis interactions. *Phycologia* 40: 503-529.
- Pagarete, A., Allen, M.J., Wilson, W.H., Kimmance, S.A., and de Vargas, C. (2009). Host-virus shift of the sphingolipid pathway along an *Emiliana huxleyi* bloom: survival of the fattest. *Environ. Microbiol.* 11: 2840-2848.

- Pagarete, A., Corguille, G.L., Tiwari, B., Ogata, H., de Vargas, C., Wilson, W.H., and Allen, M.J. (2011). Unveiling the transcriptional features associated with coccolithovirus infection of natural *Emiliana huxleyi* blooms. *FEMS Microbiol. Ecol.* 78: 555-564.
- Paloza, P., and Krinsky, N.I. (1992). β -Carotene and α -tocopherol are synergistic antioxidants. *Arch. Biochem. Biophys.* 297: 184-187.
- Patterson, G. (1971). The distribution of sterols in algae. *Lipids* 6: 120-127.
- Patti, G.J., Yanes, O., and Siuzdak, G. (2012). Metabolomics: the apogee of the omics trilogy. *Nat. Rev. Mol. Cell Bio.* 13: 263-269.
- Paul, C., Mausz, M.A., and Pohnert, G. (2013). A co-culturing/metabolomics approach to investigate chemically mediated interactions of planktonic organisms reveals influence of bacteria on diatom metabolism. *Metabolomics* 9: 349-359.
- Paul, C., Barofsky, A., Vidoudez, C., and Pohnert, G. (2009). Diatom exudates influence metabolism and cell growth of co-cultured diatom species. *Mar. Ecol. Prog. Ser.* 389: 61-70.
- Paul, C., Reunamo, A., Lindehoff, E., Bergkvist, J., Mausz, M.A., Larsson, H., Richter, H., Wängberg, S.-Å., Leskinen, P., Båmstedt, U., and Pohnert, G. (2012). Diatom derived polyunsaturated aldehydes do not structure the planktonic microbial community in a mesocosm study. *Mar. Drugs* 10: 775-792.
- Paulino, A.I., Egge, J.K., and Larsen, A. (2008). Effects of increased atmospheric CO₂ on small and intermediate sized osmotrophs during a nutrient induced phytoplankton bloom. *Biogeosciences* 5: 739-748.
- Pechlivanis, M., and Kuhlmann, J. (2006). Hydrophobic modifications of Ras proteins by isoprenoid groups and fatty acids - more than just membrane anchoring. *Biochim. Biophys. Acta* 1764: 1914-1931.
- Pizer, E.S., Chrest, F.J., DiGiuseppe, J.A., and Han, W.F. (1998). Pharmacological inhibitors of mammalian fatty acid synthase suppress DNA replication and induce apoptosis in tumor cell lines. *Cancer Res.* 58: 4611-4615.
- Plaza, M., Santoyo, S., Jaime, L., García-Blairsy Reina, G., Herrero, M., Señoráns, F.J., and Ibáñez, E. (2010). Screening for bioactive compounds from algae. *J. Pharmaceut. Biomed.* 51: 450-455.
- Pond, D.W., and Harris, R.P. (1996). The lipid composition of the coccolithophore *Emiliana huxleyi* and its possible ecophysiological significance. *J. Mar. Biol. Ass. UK* 76: 579-594.
- Radhakrishnan, A.N., and Meister, A. (1957). Conversion of hydroxyproline to pyrrole-2-carboxylic acid. *J. Biol. Chem.* 226: 559-571.
- Rajamani, S., Bauer, W.D., Robinson, J.B., Farrow, J.M.^{3rd}, Pesci, E.C., Teplitski, M., Gao, M., Sayre, R.T., and Phillips, D.A. (2008). The vitamin riboflavin and its derivative lumichrome activate the LasR bacterial Quorum-Sensing receptor. *Mol. Plant-Microbe Interact.* 21: 1184-1192.
- Raoult, D., and Forterre, P. (2008). Redefining viruses: lessons from Mimivirus. *Nat. Rev. Microbiol.* 6: 315-319.
- Raven, J.A., and Beardall, J. (2003). Carbohydrate metabolism and respiration in algae. In *Photosynthesis in Algae*, A.W.D. Larkum, S.E. Douglas, and J.A. Raven, eds (Springer Netherlands: Dordrecht), pp. 205-224.
- Read, B.A., Kegel, J., Klute, M.J., Kuo, A., Lefebvre, S., Maumus, F., Mayer, C., Miller, J., Monier, A., Salamov, A., Young, J., Aguilar, M., Claverie, J.-M., Frickenhaus, S., Gonzalez, K., Herman, E.K., Lin, Y.-C., Napier, J., Ogata, H., Sarno, A.F., Shmutz, J., Schroeder, D., de Vargas, C., Verret, F., von Dassow, P., Valentin, K., Van de Peer, Y., Wheeler, G., Consortium, E.h.A., Dacks, J.B., Delwiche, C.F., Dyhrman, S.T., Glöckner, G., John, U., Richards, T., Worden, A.Z., Zhang, X., and Grigoriev, I.V. (2013). Pan genome of the phytoplankton *Emiliana* underpins its global distribution. *Nature* 499: 209-213.
- Richards, F.J., and Coleman, R.G. (1952). Occurrence of putrescine in potassium-deficient barley. *Nature* 170: 460-460.
- Riebesell, U., Revill, A.T., Holdsworth, D.G., and Volkman, J.K. (2000a). The effects of varying CO₂ concentration on lipid composition and carbon isotope fractionation in *Emiliana huxleyi*. *Geochim. Cosmochim. Ac.* 64: 4179-4192.

- Riebesell, U., Zondervan, I., Rost, B., Tortell, P.D., Zeebe, R.E., and Morel, F.M.M. (2000b). Reduced calcification of marine plankton in response to increased atmospheric CO₂. *Nature* 407: 364-367.
- Riebesell, U., Bellerby, R.G.J., Engel, A., Fabry, V., Hutchins, D.A., Reusch, T.B.H., Schulz, K.G., and Morel, F.M.M. (2008). Comment on "Phytoplankton calcification in a high-CO₂ world". *Science* 322: 1466b.
- Robertson, J.E., Robinson, C., Turner, D.R., Holligan, P., Watson, A.J., Boyd, P., Fernandez, E., and Finch, M. (1994). The impact of a coccolithophore bloom on oceanic carbon uptake in the northeast Atlantic during summer 1991. *Deep-Sea Res. Pt. I* 41: 297-314.
- Rohwer, F., and Thurber, R.V. (2009). Viruses manipulate the marine environment. *Nature* 459: 207-212.
- Rokitta, S.D., de Nooijer, L.J., Trimborn, S., de Vargas, C., Rost, B., and John, U. (2011). Transcriptome analyses reveal differential gene expression patterns between the life-cycle stages of *Emiliania huxleyi* (Haptophyta) and reflect specialization to different ecological niches. *J. Phycol.* 47: 829-838.
- Rontani, J.-F., and Volkman, J.K. (2003). Phytol degradation products as biogeochemical tracers in aquatic environments. *Org. Geochem.* 34: 1-35.
- Rost, B., and Riebesell, U. (2004). Coccolithophores and the biological pump: responses to environmental changes. In *Coccolithophores: From Molecular Processes to Global Impact*, H.R. Thierstein and J.R. Young, eds (Springer-Verlag: Berlin Heidelberg), pp. 99-126.
- Roy, S., and Legendre, L. (1979). DCMU-enhanced fluorescence as an index of photosynthetic activity in phytoplankton. *Marine Biol.* 55: 93-101.
- Schauer, N., and Fernie, A.R. (2006). Plant metabolomics: towards biological function and mechanism. *Trends Plant Sci.* 11: 508-516.
- Schroeder, D.C., Oke, J., Malin, G., and Wilson, W.H. (2002). Coccolithovirus (*Phycodnaviridae*): characterisation of a new large dsDNA algal virus that infects *Emiliania huxleyi*. *Arch. Virol.* 147: 1685-1698.
- Schulz, K.G., Rost, B., Burkhardt, S., Riebesell, U., Thoms, S., and Wolf-Gladrow, D.A. (2007). The effect of iron availability on the regulation of inorganic carbon acquisition in the coccolithophore *Emiliania huxleyi* and the significance of cellular compartmentation for stable carbon isotope fractionation. *Geochim. Cosmochim. Ac.* 71: 5301-5312.
- Selstam, E., and Jackson, A.O. (1983). Lipid composition of sonchus yellow net virus. *J. gen. Virol.* 64: 1607-1613.
- Seritti, A., Morelli, E., Nannicini, L., and Del Vecchio, R. (1994). Production of hydrophobic fluorescent organic matter by the marine diatom *Phaeodactylum tricornutum*. *Chemosphere* 28: 117-129.
- Serrano, M., Amorós, A., Pretel, M.T., Martínez-Madrid, M.C., and Romojaro, F. (2001). Preservative solutions containing boric acid delay senescence of carnation flowers. *Postharvest Biol. Tec.* 23: 133-142.
- Seyedsayamdost, M.R., Case, R.J., Kolter, R., and Clardy, J. (2011). The Jekyll-and-Hyde chemistry of *Phaeobacter gallaeciensis*. *Nat. Chem.* 3: 331-335.
- Shaked, Y., and Lis, H. (2012). Disassembling iron availability to phytoplankton. *Front. Microbio.* 3: 123.
- Shi, D., Xu, Y., Hopkinson, B.M., and Morel, F.M.M. (2010). Effect of ocean acidification on iron availability to marine phytoplankton. *Science* 327: 676-679.
- Shiu, C.-T., and Lee, T.-M. (2005). Ultraviolet-B-induced oxidative stress and responses of the ascorbate-glutathione cycle in a marine macroalga *Ulva fasciata*. *J. Exp. Bot.* 56: 2851-2865.
- Simo, R. (2001). Production of atmospheric sulfur by oceanic plankton: biogeochemical, ecological and evolutionary links. *Trends Ecol. Evol.* 16: 287-294.
- Souchet, N., and Laplante, S. (2007). Seasonal and geographical variations of sterol composition in snow crab hepatopancreas and pelagic fish viscera from Eastern Quebec. *Comp. Biochem. Phys. B* 147: 378-386.

- Stebbins, G.L., and Hill, G.J.C.** (1980). Did multicellular plants invade the land? *Am. Nat.* 115: 342-353.
- Stolte, W., Kraay, G.W., Noordeloos, A.A.M., and Riegman, R.** (2000). Genetic and physiological variation in pigment composition of *Emiliana huxleyi* (Prymnesiophyceae) and the potential use of pigment ratios as a quantitative physiological marker. *J. Phycol.* 36: 529-539.
- Stringer, K.A., Serkova, N.J., Karnovsky, A., Guire, K., Paine, R.3rd, and Standiford, T.J.** (2011). Metabolic consequences of sepsis-induced acute lung injury revealed by plasma ¹H-nuclear magnetic resonance quantitative metabolomics and computational analysis. *Am. J. Physiol. Lung Cell. Mol. Physiol.* 300: L4-L11.
- Suffrian, K., Simonelli, P., Nejstgaard, J.C., Putzeys, S., Carotenuto, Y., and Antia, A.N.** (2008). Microzooplankton grazing and phytoplankton growth in marine mesocosms with increased CO₂ levels. *Biogeosciences* 5: 1145-1156.
- Sullivan, M.B., Colman, M.L., Weigle, P., Rowher, F., and Chisholm, S.W.** (2005). Three *Prochlorococcus* cyanophage genomes: signature features and ecological interpretation. *PLOS Biol.* 3: e144.
- Suttle, C.A.** (2005a). The virosphere: the greatest biological diversity on Earth and driver of global processes. *Environm. Microbiol.* 7: 481-482.
- Suttle, C.A.** (2005b). Viruses in the sea. *Nature* 437: 356-361.
- Suttle, C.A.** (2007). Marine viruses - major players in the global ecosystem. *Nat. Rev. Microbiol.* 5: 801-812.
- Thompson, L.R., Zeng, Q., Kelly, L., Huang, K.H., Singer, A.U., Stubbe, J.A., and Chisholm, S.W.** (2011). Phage auxiliary metabolic genes and the redirection of cyanobacterial host carbon metabolism. *Proc. Natl. Acad. Sci. USA* 108: E757-E764.
- Tolbert, N.E.** (1979). Glycolate metabolism by higher plants and algae. In *Photosynthesis II*, M. Gibbs and E. Latzko, eds (Springer Verlag: Berlin Heidelberg), pp. 338-352.
- Tyrell, T., and Merico, A.** (2004). *Emiliana huxleyi*: bloom observations and the conditions that induce them. In *Coccolithophores: From Molecular Processes to Global Impact*, H.R. Thierstein and J.R. Young, eds (Springer-Verlag: Berlin Heidelberg), pp. 75-98.
- van Hummel, H.C.** (1975). Chemistry and biosynthesis of plant galactolipids. In *Fortschritte der Chemie organischer Naturstoffe / Progress in the chemistry of organic natural products*, L. Zechmeister, W. Herz, H. Grisebach, and G.W. Kirby, eds (Springer Verlag: Wien), pp. 267-295.
- Vardi, A., van Mooy, B.A.S., Fredricks, H.F., Pendorf, K.J., Ossolinski, J.E., Haramaty, L., and Bidle, K.D.** (2009). Viral glycosphingolipids induce lytic infection and cell death in marine phytoplankton. *Science* 326: 861-865.
- Vardi, A., Haramaty, L., Van Mooy, B.A.S., Fredricks, H.F., Kimmance, S.A., Larsen, A., and Bidle, K.D.** (2012). Host-virus dynamics and subcellular controls of cell fate in a natural coccolithophore population. *Proc. Natl. Acad. Sci. USA* 109: 19327-19332.
- Varum, K.M., Kvam, B.J., Myklestad, S., and Paulsen, B.S.** (1986). Structure of a food-reserve β -D-glucane produced by the haptophyte alga *Emiliana huxleyi* (Lohmann) Hay and Mohler. *Carbohydr. Res.* 152: 243-248.
- Vastag, L., Koyuncu, E., Grady, S.L., Shenk, T.E., and Rabinowitz, J.D.** (2011). Divergent effects of human cytomegalovirus and herpes simplex virus-1 on cellular metabolism. *PLOS Pathog.* 7: e1002124.
- Véron, B., Dauquet, J.-C., and Billard, C.** (1996). Sterolic biomarkers in marine phytoplankton. I. Free and conjugated sterols of *Pavlova lutheri* (Haptophyta). *Eur. J. Phycol.* 31: 211-215.
- Vidoudez, C.** (2010). Diatom metabolomics. PhD-Thesis. (Friedrich Schiller University Jena: Jena), p. 183.
- Vidoudez, C., and Pohnert, G.** (2008). Growth phase-specific release of polyunsaturated aldehydes by the diatom *Skeletonema marinoi*. *J. Plankton Res.* 30: 1305-1313.
- Vidoudez, C., and Pohnert, G.** (2012). Comparative metabolomics of the diatom *Skeletonema marinoi* in different growth phases. *Metabolomics* 8: 654-669.

- Viso, A.-C., and Marty, J.-C.** (1993). Fatty acids from 28 marine microalgae. *Phytochemistry* 34: 1521-1533.
- Volkman, J.K.** (2003). Sterols in microorganisms. *Appl. Microbiol. Biotechnol.* 60: 495-506.
- von Dassow, P., Ogata, H., Probert, I., Wincker, P., Da Silva, C., Audic, S., Claverie, J.-M., and de Vargas, C.** (2009). Transcriptome analysis of functional differentiation between haploid and diploid cells of *Emiliana huxleyi*, a globally significant photosynthetic calcifying cell. *Genome Biol.* 10: R114.111-R114.133.
- Wagner, C., Sefkow, M., and Kopka, J.** (2003). Construction and application of a mass spectral and retention time index database generated from plant GC/EI-TOF-MS metabolite profiles. *Phytochemistry* 62: 887-900.
- Weitz, J.S., and Wilhelm, S.W.** (2012). Ocean viruses and their effects on microbial communities and biogeochemical cycles. *F1000 Biol. Rep.* 4: 17.
- Westbroek, P., Young, J.R., and Linschooten, K.** (1989). Coccolith production (biomineralization) in the marine alga *Emiliana huxleyi*. *J. Protozool.* 36: 368-373.
- Wilhelm, S.W., and Suttle, C.A.** (1999). Viruses and nutrient cycles in the sea. *BioScience* 49: 781-788.
- Wilson, W.H., Van Etten, J.L., and Allen, M.J.** (2009). The *Phycodnaviridae*: the story of how tiny giants rule the world. *Curr. Top. Microbiol. Immunol.* 328: 1-42.
- Wilson, W.H., Tarran, G.A., Schroeder, D.C., Cox, M., Oke, J., and Malin, G.** (2002). Isolation of viruses responsible for the demise of an *Emiliana huxleyi* bloom in the English Channel. *J. Mar. Biol. Assoc. U.K.* 82: 369-377.
- Wilson, W.H., Schroeder, D.C., Allen, M.J., Holden, M.T.G., Parkhill, J., Barrell, B.G., Churcher, C., Hamlin, N., Mungall, K., Norbertczak, H., Quail, M.A., Price, C., Rabinowitsch, E., Walker, D., Craigon, M., Roy, D., and Ghazal, P.** (2005). Complete genome sequence and lytic phase transcription profile of a *Coccolithovirus*. *Science* 309: 1090-1092.
- Wommack, K.E., and Colwell, R.R.** (2000). Virioplankton: viruses in aquatic ecosystems. *Microbiol. Mol. Biol. Rev.* 64: 69-114.
- Ye, J., Wang, C., Sumpter, R., Brown, M.S., Goldstein, J.L., and Gale, M.J.** (2003). Disruption of hepatitis C virus RNA replication through inhibition of host protein geranylgeranylation. *Proc. Natl. Acad. Sci. USA* 100: 15865-15870.
- Yeh, E., and DeRisi, J.L.** (2011). Chemical rescue of malaria parasites lacking an apicoplast defines organelle function in blood-stage *Plasmodium falciparum*. *PLOS Biol.* 9: e1001138.
- Young, J.R.** (1987). Possible functional interpretations of coccolith morphology. *Abh. Geol. B.-A.* 39: 305-313.
- Zhang, Z., and Sachs, J.P.** (2007). Hydrogen isotope fractionation in freshwater algae: I. Variations among lipids and species. *Org. Geochem.* 38: 582-608.

Appendices

Appendix Table 1: Heat map of relative intensities of all intracellular metabolites significantly correlated with the CAP axis separating diploid and haploid life phase of exponentially growing *E. huxleyi* cultures.

No.	Model-Ion	RT	Metabolite	Molecular formula	Class	Library	Diploid life phase	Haploid life phase
1	163.1	4.90	Unknown	-	?	-		
5	155.1	5.14	Unknown	-	?	-		
16	102.1	5.71	Unknown	-	?	-		
32	177.1	6.25	3-Hydroxypropanoic acid	C ₃ H ₆ O ₃	Carboxylic acid	NIST		
64	158.1	7.68	Isoleucine*	C ₆ H ₁₃ NO ₂	Amino acid	GOLM		
66	129.1	7.75	Unknown	-	?	-		
67	103.1	7.78	Unknown	-	?	-		
77	184	8.08	Lumichrome	C ₁₂ H ₁₀ N ₄ O ₂	Other	GMD2011		
78	215.1	8.11	Unknown	-	?	-		
85	117.1	8.44	unidentified Carboxylic acid ?	-	Carboxylic acid	GOLM		
110	145.1	9.27	Unknown	-	?	-		
111	234.1	9.30	unidentified Monosaccharide	-	Saccharide	GOLM		
120	248.1	9.71	unidentified Carboxylic acid ?	-	Carboxylic acid	NIST		
127	117.1	9.92	Unknown	-	?	-		
128	292.1	9.96	Threonic acid	C ₄ H ₈ O ₅	Sugar acid	NIST		
133	217.1	10.13	Unknown	-	?	-		
137	217.1	10.25	unidentified Monosaccharide	-	Saccharide	GOLM		
150	229.1	10.60	Unknown	-	?	-		
153	103.1	10.72	Xylose*	C ₅ H ₁₀ O ₅	Saccharide	GOLM		
161	204.1	10.99	unidentified Monosaccharide	-	Saccharide	GOLM		
189	273.1	11.96	Citric acid*	C ₆ H ₈ O ₇	Carboxylic acid	GOLM		
200	307.2	12.30	Fructose*	C ₆ H ₁₂ O ₆	Saccharide	GOLM		
209	205.1	12.72	Mannitol†*	C ₆ H ₁₄ O ₆	Sugar alcohol	GOLM		
224	121.1	13.33	unidentified Hydrocarbon or Terpene	-	Hydrocarbon	NIST		
232	105.1	13.58	unidentified Hydrocarbon or Terpene	-	Hydrocarbon	NIST		
233	165.1	13.62	unidentified Saccharide	-	Saccharide	GOLM		

Appendix Table 1 (continued)

Appendix Table 1 (continued)																																																																																																																																																																																																																																																																																																																																																																																																																																																																																																																																																																																																																																																																																																																																																																																																																																																																																																																																																																																																																																																																																																																																																																																																																																																																																																																																																																							
No.	Model-Ion		RT	Metabolite	Molecular formula	Class	Library	Diploid life phase								Haploid life phase																																																																																																																																																																																																																																																																																																																																																																																																																																																																																																																																																																																																																																																																																																																																																																																																																																																																																																																																																																																																																																																																																																																																																																																																																																																																																																																																																							
243	179.1	13.99	Octadecenoic acid derivative	C ₁₉ H ₃₆ O ₂	Fatty acid derivative	GMD2011																																																																																																																																																																																																																																																																																																																																																																																																																																																																																																																																																																																																																																																																																																																																																																																																																																																																																																																																																																																																																																																																																																																																																																																																																																																																																																																																																																	

Gray coloring reflects the intensities of the metabolites with light gray for low and dark gray for high intensities. Metabolites tagged with "†" are highly correlated with the diploid life phase. If marked by "*", identification was confirmed by a standard. Metabolites tagged with a "?" had a reverse match of 700 - 800 or, if marked by "??", of 600 - 700. Used libraries were: Nist library version 2005 (NIST), T_MSRI_ID 2004-03-01 (GOLM), and GMD_20111121_VAR5_ALK_MSP (GMD2011) (both Golm Metabolome Database) (compare 6.4.6). Abbreviation: compl., complex, deriv., derivative, No., number, RT, retention time.

Appendix Table 2: Heat map of relative intensities of all intracellular metabolites significantly correlated with the first two CAP axes separating growth phases in haploid *E. huxleyi* cultures.

No.	Model- ion	RT	Metabolite	Molecular formula	Class	Library	Exp.	Stat.	Decl.
3	165	5.00	C ₃ H ₈ NCI	C ₃ H ₈ NCI	Amine	-			
5	113.1	5.06	Unknown	-	?	-			
7	155.1	5.15	Unknown	-	?	-			
8	152	5.19	Pyridine, 2-hydroxy-	C ₅ H ₅ NO	Other	GOLM			
10	155.1	5.31	Unknown	-	?	-			
11	117.1	5.40	2-Hydroxypropanoic acid	C ₃ H ₆ O ₃	Carboxylic acid	NIST			
13	136	5.50	Unknown	-	?	-			
15	173.1	5.56	Hexanoic acid	C ₆ H ₁₂ O ₂	Fatty acid	GOLM			
19	173.1	5.79	Unknown	-	?	-			
20	105	5.82	Unknown	-	?	-			
22	167.1	5.89	Pyrazine or Hydroquinone deriv.	-	Other	NIST			
24	228.1	6.01	Unknown	-	?	-			
25	117	6.03	2,3-Butanediol, monoacetate ?	C ₆ H ₁₂ O ₃	Alcohol	NIST			
27	103.1	6.12	Glycerol	C ₃ H ₈ O ₃	Other	NIST			
29	177.1	6.26	3-Hydroxypropanoic acid	C ₃ H ₆ O ₃	Carboxylic acid	NIST			
31	152.1	6.31	Pyridine, 3-hydroxy-	C ₅ H ₅ NO	Other	GMD2011			
40	210.1	6.73	Unknown	-	?	-			
44	103.1	6.84	2,3-Dihydroxypropanal	C ₃ H ₆ O ₃	Other	NIST			
46	247.1	6.90	3-Hydroxyisovaleric acid	C ₅ H ₁₀ O ₃	Fatty acid deriv.	NIST			
47	186	6.96	Unknown	-	?	-			
51	174.1	7.09	unidentified Amine	-	Amine	GOLM			
52	110	7.20	Unknown	-	?	-			
56	129	7.41	Unknown	-	?	-			
59	182.1	7.54	Unknown	-	?	-			
70	116.1	7.86	Unknown	-	?	-			
76	184	8.08	Lumichrome	C ₁₂ H ₁₀ N ₄ O ₂	Other	GMD2011			
80	245.1	8.23	Unknown	-	?	-			
81	240.1	8.25	Pyrrole-2-carboxylic acid	C ₅ H ₅ NO ₂	Carboxylic acid	GOLM			

Appendix Table 2 (continued)

No.	Model- ion	RT	Metabolite	Molecular formula	Class	Library	Exp.	Stat.	Decl.
82	186.1	8.26	Unknown	-	?	-			
84	221.1	8.30	Unknown	-	?	-			
85	117	8.35	Nonanoic acid	C ₉ H ₁₈ O ₂	Fatty acid	NIST			
87	247.1	8.46	Threonic acid-1,4-lactone, <i>trans</i> -	C ₄ H ₆ O ₄	Lactone	GOLM			
91	255.1	8.58	Carboxylic acid ?	-	Carboxylic acid	GDM2003			
95	239.1	8.70	Dihydroxybenzene ?	C ₆ H ₆ O ₂	Other	NIST			
98	154.1	8.83	Unknown	-	?	-			
99	205.1	8.85	Monosaccharide	-	Saccharide	NIST			
100	201.1	8.90	Monosaccharide ?	-	Saccharide	GOLM			
101	174.1	8.92	beta-Alanine ?	C ₃ H ₇ NO ₂	Amino acid	GOLM			
104	238.1	9.09	Unknown	-	?	-			
106	318.2	9.14	Unknown	-	?	-			
109	227.1	9.24	Unknown	-	?	-			
112	234.1	9.30	Monosaccharide	-	Saccharide	GOLM			
114	103.1	9.37	2,4-Bishydroxybutanoic acid ?	C ₄ H ₈ O ₄	Fatty acid deriv.	GOLM			
115	129.1	9.43	Unknown	-	?	-			
117	154.1	9.53	Unknown	-	?	-			
118	217.1	9.63	Unknown	-	?	-			
119	155.1	9.65	Unknown	-	?	-			
120	248.1	9.71	Carboxylic acid ?	-	Carboxylic acid	NIST			
121	237.1	9.75	Hydroxy-proline ?	C ₅ H ₉ NO ₃	Amino acid	IHL			
122	183.1	9.79	Unknown	-	?	-			
125	103.1	9.86	Unknown	-	?	-			
127	140	9.92	Unknown	-	?	-			
128	292.1	9.96	Threonic acid	C ₄ H ₈ O ₅	Sugar acid	MPI			
134	205.1	10.20	Monosaccharide	-	Saccharide	GOLM			
136	328.1	10.27	Unknown	-	?	-			
137	242	10.29	Unknown	-	?	-			
139	258.1	10.32	Monosaccharide	-	Saccharide	GOLM			

Appendix Table 2 (continued)

No.	Model- ion	RT	Metabolite	Molecular formula	Class	Library	Exp.	Stat.	Decl.
141	142.1	10.37	Unknown	-	?	-			
143	140	10.44	Unknown	-	?	-			
144	257.1	10.49	Unknown	-	?	-			
146	142.1	10.58	Unknown	-	?	-			
148	257.1	10.66	Unknown	-	?	-			
149	103.1	10.72	Xylose*	C ₅ H ₁₀ O ₅	Saccharide	MPI			
152	217.1	10.82	1,6-Anhydroglucose ?	C ₆ H ₁₀ O ₅	Saccharide	GOLM			
154	103.1	10.89	Ribose*	C ₅ H ₁₀ O ₅	Saccharide	GOLM			
155	217.1	10.91	Pentapyranose ?	C ₅ H ₁₀ O ₅	Saccharide	GOLM			
156	205.1	10.93	Monosaccharide ?	-	Saccharide	GOLM			
158	204.1	10.99	Monosaccharide ?	-	Saccharide	GOLM			
159	279.2	11.02	Unknown	-	?	-			
160	129	11.07	Unknown	-	?	-			
162	129	11.12	3,4,5-Trihydroxypentanoic acid ?	C ₅ H ₁₀ O ₅	Fatty acid deriv.	NIST			
163	133.1	11.20	Sugar alcohol ?	-	Sugar alcohol	GOLM			
166	302.1	11.33	Unknown	-	?	-			
167	143.1	11.38	Tetradecanoic acid ME	C ₁₅ H ₃₀ O ₂	Fatty acid	NIST			
172	392.2	11.52	Unknown	-	?	-			
175	129.1	11.59	D(-)-Galactono-1,4-lactone ?	C ₆ H ₁₀ O ₆	Lactone	GOLM			
176	302.1	11.65	Unknown	-	?	-			
178	129.1	11.71	Unknown	-	?	-			
179	392.2	11.74	Unknown	-	?	-			
180	392.2	11.79	Unknown	-	?	-			
181	295.1	11.83	1,3-Benzenedicarboxylic acid, ester deriv.	C ₈ H ₆ O ₄ + ?	Other	NIST			
183	217.1	11.87	Monosaccharide ??	-	Saccharide	GOLM			
185	217.1	11.94	Monosaccharide (Pentafuranose) ?	(C ₅ H ₁₀ O ₅)	Saccharide	GOLM			
188	256.2	12.11	Pentadecanoic acid ME	C ₁₆ H ₃₂ O ₂	Fatty acid	MPI			
191	123.1	12.19	Neophytadiene ⁺	C ₂₀ H ₃₈	Terpene	-			
193	117	12.24	Tetradecanoic acid *	C ₁₄ H ₂₈ O ₂	Fatty acid	NIST			

Appendix Table 2 (continued)

No.	Model- ion	RT	Metabolite	Molecular formula	Class	Library	Exp.	Stat.	Decl.
197	123.1	12.36	(Z)-1,3-Phytadiene	C ₂₀ H ₃₈	Terpene	-			
198	362.2	12.42	Galactose*	C ₆ H ₁₂ O ₆	Saccharide	GOLM			
200	123.1	12.49	(E)-1,3-Phytadiene	C ₂₀ H ₃₈	Terpene	-			
201	117	12.52	Unknown	-	?	-			
202	217.1	12.55	Sugar alcohol	-	Sugar alcohol	GOLM			
203	319.2	12.61	Glucose*	C ₆ H ₁₂ O ₆	Saccharide	NIST			
204	117	12.67	Fatty acid	-	Fatty acid	NIST			
205	205.1	12.71	Mannitol*	C ₆ H ₁₄ O ₆	Sugar alcohol	MPI			
206	204.1	12.76	Hexose	C ₆ H ₁₂ O ₆	Saccharide	IHL			
207	143.1	12.80	Hexadecanoic acid ME	C ₁₇ H ₃₄ O ₂	Fatty acid	MPI			
208	204.1	12.85	Hexose	C ₆ H ₁₂ O ₆	Saccharide	IHL			
209	117	12.91	Pentadecanoic acid*	C ₁₅ H ₃₀ O ₂	Fatty acid	NIST			
211	205.1	12.97	Saccharide deriv.	-	Saccharide	GOLM			
212	239	13.05	Unknown	-	?	-			
217	217.1	13.21	Saccharide deriv.	-	Saccharide	GOLM			
218	293.2	13.26	Unknown	-	?	-			
222	121.1	13.33	unsaturated Hydrocarbon	-	Hydrocarbon	-			
223	217	13.37	Inositol isomer	C ₆ H ₁₂ O ₆	Sugar alcohol	NIST			
226	217.1	13.47	Monosaccharide	-	Saccharide	GOLM			
228	117	13.56	Hexadecanoic acid*	C ₁₆ H ₃₂ O ₂	Fatty acid	NIST			
233	204.1	13.70	Hexose	-	Saccharide	IHL			
238	122.1	13.86	Oleanitrile	C ₁₈ H ₃₃ N	Other	NIST			
240	116.1	13.94	Unknown	-	?	-			
241	108.1	13.96	Octadecatrienoic acid ME	C ₁₉ H ₃₂ O ₂	Fatty acid	MPI			
246	204.1	14.11	Hexose	C ₆ H ₁₂ O ₆	Saccharide	IHL			
247	239.2	14.14	Unknown	-	?	-			
249	204.1	14.27	Saccharide ?	-	Saccharide	GOLM			
251	319.2	14.37	Saccharide ?	-	Saccharide	GOLM			
253	148.1	14.50	Unknown	-	?	-			

Appendix Table 2 (continued)

No.	Model- ion	RT	Metabolite	Molecular formula	Class	Library	Exp.	Stat.	Decl.
254	108.1	14.53	Unknown	-	?	-			
256	117	14.63	9-Octadecenoic acid	C ₁₈ H ₃₄ O ₂	Fatty acid	NIST			
257	117	14.67	Octadecenoic acid	C ₁₈ H ₃₄ O ₂	Fatty acid	NIST			
258	117	14.78	Octadecanoic acid*	C ₁₈ H ₃₆ O ₂	Fatty acid	NIST			
259	358.2	14.93	Sugar alcohol ?	-	Sugar alcohol	GOLM			
260	204.1	14.94	Saccharide ?	-	Saccharide	GOLM			
261	170.1	14.97	Unknown	-	?	-			
263	204.1	15.08	Galactosylglycerol	C ₉ H ₁₈ O ₈	Saccharide	GOLM			
264	370.2	15.18	Saccharide ?	-	Saccharide	GOLM			
265	180.1	15.22	unsaturated Hydrocarbon	-	Hydrocarbon	-			
267	106	15.33	Unknown	-	?	-			
268	167	15.35	Unknown	-	?	-			
269	204.1	15.41	Saccharide	-	Saccharide	GOLM			
270	285.3	15.63	Octadecanoic acid deriv. ??	C ₁₈ H ₃₆ O ₂ + ?	Fatty acid	NIST			
271	204.1	15.75	Unknown	-	?	-			
272	108.1	15.80	long-chained Alcohol	-	Alcohol	GOLM			
274	105.1	16.02	Docosahexaenoic acid	C ₂₂ H ₃₂ O ₂	Fatty acid	NIST			
276	204.1	16.36	Saccharide	-	Saccharide	GOLM			
278	204.1	16.48	Disaccharide	C ₁₂ H ₂₂ O ₁₁	compl. Saccharide	GOLM			
279	156.1	16.54	Unknown	-	?	-			
280	361.2	16.63	Disaccharide	C ₁₂ H ₂₂ O ₁₁	compl. Saccharide	GOLM			
281	116.1	16.70	Unknown	-	?	-			
284	236.1	16.89	Adenosine ??	C ₁₀ H ₁₃ N ₅ O ₄	Other	GOLM			
286	217.1	17.25	Unknown	-	?	-			
289	108.1	17.42	Unknown	-	?	-			
290	204.1	17.56	Unknown	-	?	-			
292	204.1	17.86	Saccharide ?	-	Saccharide	GOLM			
293	204.1	17.95	Unknown	-	?	-			
296	253.2	18.21	Cycloergostatriene ?	C ₂₈ H ₄₂	Sterol	NIST			

Appendix Table 2 (continued)

No.	Model- ion	RT	Metabolite	Molecular formula	Class	Library	Exp.	Stat.	Decl.
299	204.1	18.52	Galactinol ?	C ₁₂ H ₂₂ O ₁₁	Sugar alcohol	GOLM			
300	478.3	18.64	Unknown	-	?	-			
301	380.4	18.69	Ergostatriene	C ₂₈ H ₄₄	Sterol	NIST			
303	204.1	18.97	Unknown	-	?	-			
304	378.3	19.06	Sterol ?	-	Sterol	NIST			
305	204.1	19.44	Digalactosylglycerol	C ₁₅ H ₂₈ O ₁₃	Saccharide	GOLM			
307	227.2	19.52	Unknown	-	?	-			
309	237.1	19.75	alpha-Tocopherol *	C ₂₉ H ₅₀ O ₂	Terpene	NIST			
310	251.2	20.22	Epibrassicasterol	C ₂₈ H ₄₆ O	Sterol	NIST			
314	204.1	21.31	beta-D-Methylgalactopyranoside ?	C ₇ H ₁₄ O ₆	compl. Saccharide	GOLM			
315	204.1	21.73	Disaccharide ?	C ₁₂ H ₂₂ O ₁₁	compl. Saccharide	GOLM			
317	604.4	23.66	Unknown	-	?	-			
319	647.5	24.28	Unknown	-	?	-			
321	292.3	25.69	unsaturated Hydrocarbon	-	Hydrocarbon	-			

Gray coloring reflects the intensities of the metabolites with light gray for low and dark gray for high intensities. If marked by “*”, identification was confirmed by a standard. Metabolites tagged with a “?” had a reverse match of 700 - 800 or, if marked by “??”, of 600 - 700. Used libraries were: Nist library version 2005 (NIST), T_MSRI_ID 2004-03-01 (GOLM), GMD_20111121_VAR5_ALK_MSP (GMD2011) (both Golm Metabolome Database), Q_MSRI_ID 2004-03-01 (MPI, Max Plank Institute of Molecular Plant Physiology), and an in-house library (IHL) (compare 6.4.6). Abbreviations: compl., complex, Decl., declining, deriv., derivative, Exp., exponential, ME, methyl ester, No., number, RT, retention time, Stat., stationary.

Appendix Table 3: Heat map of normalized intensities of metabolites highly correlated with the treatment combination low CO₂/DFB-, low CO₂/DFB+, and high CO₂ as well as low and high CO₂ in the analysis of these parameter combinations. “#” indicates metabolites deriving from the analysis of the combination of the three treatments, and “†” indicates metabolites specific for the CO₂ treatment.

[illegible]

Appendix Table 3 (continued)

No.	RT	Metabolite	Class	CO2-/DFB-										CO2-/DFB+										CO2+																																																																																																																																																																																																																																																																																																																																																																																																																																																																																																																																																																																																																																																																																																																																																																																																																																																																																																																																																																																																																																																																																																																																																																																																																																																																																																																				
				D 12	D 13	D 14	D 15	D 16	D 17	D 18	D 19	D 20	D 21	D 22	D 12	D 13	D 14	D 15	D 16	D 17	D 18	D 19	D 20	D 21	D 22	D 12	D 13	D 14	D 15	D 16	D 17	D 18	D 19	D 20	D 21	D 22																																																																																																																																																																																																																																																																																																																																																																																																																																																																																																																																																																																																																																																																																																																																																																																																																																																																																																																																																																																																																																																																																																																																																																																																																																																																																																								
47	8.08	Valine*	AA																																																																																																																																																																																																																																																																																																																																																																																																																																																																																																																																																																																																																																																																																																																																																																																																																																																																																																																																																																																																																																																																																																																																																																																																																																																																																																																																									</

Appendix Table 3 (continued)

[illegible]

Appendix Table 3 (continued)

[illegible]

Appendix Table 3 (continued)

[illegible]

Appendix Table 3 (continued)

[illegible]

Appendix Table 3 (continued)

[illegible]

Appendix Table 3 (continued)

No.	RT	Metabolite	Class	CO2-/DFB-										CO2-/DFB+										CO2+												
				D12	D13	D14	D15	D16	D17	D18	D19	D20	D21	D22	D12	D13	D14	D15	D16	D17	D18	D19	D20	D21	D22	D12	D13	D14	D15	D16	D17	D18	D19	D20	D21	D22
326	23.49	Fucosterol #	ST																																	
327	23.51	beta-Sitosterol* #	ST																																	
330	24.48	Sterol (C ₂₉ H ₅₄ O)	ST																																	
333	26.93	Unknown	U																																	

Gray coloring reflects the intensities of the metabolites with light gray for low and dark gray for high intensities. If marked by “*”, identification was confirmed by a standard. Metabolites tagged with a “?” had a reverse match of 700 - 800 or, if marked by “??”, of 600 - 700. Abbreviations: A, amine, AA, amino acid, Alc, alcohol, CA, carboxylic acid, CS, complex saccharide, D, day, DFB, desferrioxamine B, FA, fatty acid, HC, hydrocarbon, No., number, O, other, RT, retention time, S, saccharide, SA, sugar acid, SAc, sugar alcohol, ST, sterol, T, terpene, U, unknown.

Appendix Table 4: Heat map of normalized intensities of metabolites correlated with metabolic profiles of the control over time.
Days 0-3, D4-11, and D12-22 were assigned as groups.

[illegible]

Appendix Table 4 (continued)

[illegible]

Appendix Table 4 (continued)

[illegible]

Appendix Table 4 (continued)

[illegible]

Appendix Table 4 (continued)

				Day 0-3				Day 4-11								Day 12-22											
No.	RT	Metabolite	Class	D0	D1	D2	D3	D4	D5	D6	D7	D8	D9	D10	D11	D12	D13	D14	D15	D16	D17	D18	D19	D20	D21	D22	
308	20.13	22E-26,27-Dinorergosta-5,22-dien-3β-ol	ST	
310	20.27	Unknown	U	
311	20.83	Digalactosylglycerol	S	
313	21.18	Sterol, Isomer of RT 21.04	ST	
316	21.66	(3β,5α)-Cholestan-3-ol	ST	
317	21.90	Epibrassicasterol	ST	
318	22.02	Sterol ??	ST	
319	22.48	Sterol	ST	
320	22.63	Unknown	U	
321	22.81	Stigmasterol*	ST	
322	22.88	Unknown	U	
323	23.00	Unknown	U	
325	23.47	Unknown	U	
326	23.49	Fucosterol	ST	
327	23.51	beta-Sitosterol*	ST	
328	23.70	Sterol (C ₂₉ H ₅₂ O)	ST	
329	23.95	Sterol ??	ST	
330	24.48	Sterol (C ₂₉ H ₅₄ O)	ST	
331	24.59	Unknown	U	
332	26.54	Trisaccharide	CS	

Gray coloring reflects the intensities of the metabolites with light gray for low and dark gray for high intensities. If marked by “*”, identification was confirmed by a standard. Metabolites tagged with a “?” had a reverse match of 700 - 800 or, if marked by “??”, of 600 - 700. Abbreviations: A, amine, AA, amino acid, Alc, alcohol, CA, carboxylic acid, CS, complex saccharide, D, day, FA, fatty acid, HC, hydrocarbon, No, number, O, other, RT, retention time, S, saccharide, SA, sugar acid, SAc, sugar alcohol, ST, sterol, T, terpene, TMS, trimethylsilyl, U, unknown.

Appendix Table 5: Fold changes of metabolites detected during viral infection. Complete list of metabolites detected in cells infected by the lytic or non-lytic virus relative to the control visualized as fold change (n=3). Grey colors indicate the intensity of the concentration change.

Model-Ion	RT	Metabolite	Class	Fold change								Fold change
				Lytic				Non-lytic				
				4 hpi	24 hpi	32 hpi	48 hpi	4 hpi	24 hpi	32 hpi	48 hpi	
112.1	5.61	Unknown	?	n.d.	n.d.	n.d.	1.13	n.d.	n.d.	n.d.	1.44	0.0-0.329
168	5.67	Lactic acid ?	Carboxylic acid	0.96	0.87	0.56	0.00	1.08	0.62	0.37	0.00	0.33-0.659
221.1	5.73	Unknown	?	0.86	n.d.	1.44	0.70	1.22	n.d.	0.77	1.69	0.66-0.99
192.1	5.82	Unknown	?	n.d.	0.44	n.d.	n.d.	n.d.	0.21	n.d.	n.d.	1.0-4.99
173.1	5.86	Hexanoic acid	Fatty acid	0.00	0.28	1.05	0.00	0.14	2.55	1.30	1.11	5.0-9.99
116.1	6.10	Alanine ?	Amino acid	1.10	1.07	0.77	0.60	1.16	1.65	0.90	0.73	> 10.0
244	6.19	Unknown	?	n.d.	0.00	6.68	n.d.	n.d.	0.46	3.56	n.d.	
167	6.33	Unknown	?	n.d.	1.25	n.d.	1.92	n.d.	0.96	n.d.	4.56	
117,228.10	6.37	Unknown	?	1.24	0.65	0.76	0.71	1.38	1.01	1.27	1.04	
116.1	6.43	Unknown	?	n.d.	0.54	n.d.	n.d.	n.d.	1.04	n.d.	n.d.	
133.1	6.57	unidentified Carboxylic acid ?	Carboxylic acid	n.d.	n.d.	20.87	1.82	n.d.	n.d.	39.54	1.62	
174.1	6.65	Ethanolamine*	Amine	n.d.	6.64	20.67	24.05	n.d.	4.68	4.57	3.53	
159.1	6.73	Unknown	?	n.d.	n.d.	1.19	1.00	n.d.	n.d.	1.37	1.05	
159.1	6.88	Unknown	?	1.06	0.83	0.92	0.40	1.06	1.23	0.99	0.95	
129	6.95	Unknown	?	1.32	0.94	0.97	0.59	1.40	1.44	1.18	0.94	
189.1	7.04	Unknown	?	n.d.	0.64	n.d.	n.d.	n.d.	1.59	n.d.	n.d.	
140,210.1,224	7.05	Unknown	?	4.35	0.70	3.75	0.58	2.12	1.86	2.40	7.50	
140	7.15	Unknown	?	n.d.	0.09	n.d.	0.76	n.d.	0.60	n.d.	2.12	
132.1	7.19	Unknown	?	2.01	n.d.	n.d.	n.d.	1.65	n.d.	n.d.	n.d.	
186	7.23	Unknown	?	n.d.	n.d.	n.d.	0.68	n.d.	n.d.	n.d.	7.44	
160.1	7.29	Glyceraldehyde*	Other	1.32	0.14	0.60	0.36	1.14	0.95	0.69	1.03	
174.1	7.35	unidentified Amine ?	Amine	n.d.	9.26	29.80	n.d.	n.d.	6.50	5.18	n.d.	
265	7.49	Unknown	?	n.d.	n.d.	n.d.	0.44	n.d.	n.d.	n.d.	2.06	
179.1	7.63	Benzoic acid	Carboxylic acid	n.d.	n.d.	n.c.	n.d.	n.d.	n.c.	n.d.	n.d.	
201.1	7.73	Octanoic acid	Fatty acid	1.11	n.d.	2.39	0.00	1.06	n.c.	1.87	1.64	
205.1	7.82	Glycerol	Other	n.d.	n.c.	9.60	5.03	n.d.	n.c.	7.73	3.59	
186.1	7.88	Unknown	?	0.65	0.63	1.85	0.12	0.80	0.75	0.76	0.93	

Appendix Table 5 (continued)

Model-Ion	RT	Metabolite	Class	Fold change							
				Lytic				Non-lytic			
				4 hpi	24 hpi	32 hpi	48 hpi	4 hpi	24 hpi	32 hpi	48 hpi
174.1	8.11	Glycine*	Amino acid	1.78	1.50	1.60	2.51	1.42	1.62	1.49	1.98
429.1	8.18	Unknown	?	n.d.	0.83	n.d.	n.d.	n.d.	0.35	n.d.	n.d.
247.1	8.19	Succinic acid*	Carboxylic acid	n.d.	n.d.	7.49	0.00	n.d.	n.d.	7.24	2.26
196.1	8.31	Unknown	?	1.13	0.55	0.72	0.47	1.48	1.10	0.85	0.77
189.1	8.35	Glyceric acid*	Sugar acid	4.06	0.33	0.45	0.30	4.76	2.31	2.45	1.62
184	8.39	Lumichrome	Other	1.13	0.31	1.88	2.39	1.53	0.47	0.79	4.51
217.1	8.48	Unknown	?	n.d.	n.d.	n.d.	0.23	n.d.	n.d.	n.d.	2.66
243.1,429.1	8.55	Unknown	?	1.12	0.69	1.56	n.d.	1.12	0.21	0.51	n.d.
215.1	8.61	Nonanoic acid*	Fatty acid	1.25	0.86	2.16	0.39	0.84	2.35	1.03	0.93
158.1	8.73	Glycine deriv. ?	Amino acid deriv.	0.62	0.50	1.60	n.d.	0.76	0.59	0.64	n.d.
242.1	8.81	Unknown	?	n.d.	n.d.	n.d.	0.59	n.d.	n.d.	n.d.	1.24
213.1	8.88	Unknown	?	0.97	0.87	n.d.	n.d.	0.95	1.36	n.d.	n.d.
204.1	8.99	Erythritol ?	Sugar alcohol	1.29	1.08	1.10	0.48	1.31	1.54	1.07	0.90
205.1	9.17	Erythrose ?	Saccharide	2.73	0.57	0.54	0.09	5.48	0.76	0.83	0.17
205.1	9.23	Monosaccharide ?	Saccharide	n.d.	0.53	0.62	0.12	n.d.	0.90	0.84	0.49
238.1	9.37	Unknown	?	n.d.	0.51	0.52	0.10	n.d.	1.09	1.15	0.97
103.1	9.53	Unknown	?	n.d.	n.d.	0.49	n.d.	n.d.	n.d.	0.83	n.d.
113,318.20	9.57	Unknown	?	n.d.	n.d.	1.09	0.78	n.d.	n.d.	1.58	1.67
234.1	9.63	Monosaccharide	Saccharide	2.72	0.48	0.57	n.d.	5.45	0.84	0.95	n.d.
228.1	9.80	Unknown	?	n.d.	n.d.	0.58	0.42	n.d.	n.d.	1.16	1.65
283.2	10.03	Unknown	?	1.00	1.23	1.27	0.73	1.09	2.44	1.02	1.42
156	10.05	Pyroglutamic acid	Amino acid deriv.	n.d.	n.d.	1.68	0.00	n.d.	n.d.	6.06	2.57
200	10.11	Unknown	?	n.d.	n.d.	0.35	n.d.	n.d.	n.d.	1.07	n.d.
245.1	10.17	2,4,5-Trihydroxypentanoic acid ??	Fatty acid deriv.	1.13	0.65	1.08	0.55	1.05	0.84	0.81	0.77
117,292.10	10.31	Threonic acid	Sugar acid	1.12	0.84	0.59	0.09	1.14	1.42	1.05	1.46
157	10.42	Unknown	?	n.d.	0.90	0.61	0.06	n.d.	1.95	1.33	1.17
217.1	10.49	(Arabino-)Pentafuranose	Saccharide	1.26	n.d.	1.32	n.d.	1.03	n.d.	1.10	n.d.
242	10.51	Unknown	?	n.d.	0.02	0.54	0.83	n.d.	0.48	0.47	3.96

Appendix Table 5 (continued)

Model-Ion	RT	Metabolite	Class	Fold change							
				Lytic				Non-lytic			
				4 hpi	24 hpi	32 hpi	48 hpi	4 hpi	24 hpi	32 hpi	48 hpi
217.1	10.59	Pentafuranose	Saccharide	1.23	1.32	1.47	0.87	1.65	1.23	1.27	1.35
258.1	10.63	Sugar deriv.	Saccharide	n.d.	0.74	0.46	n.d.	n.d.	1.44	0.81	n.d.
217.1	10.65	Pentafuranose ?	Saccharide	1.47	n.d.	n.d.	1.10	1.38	n.d.	n.d.	1.60
258.1	10.73	Sugar deriv.	Saccharide	n.d.	0.73	0.48	n.d.	n.d.	1.01	0.70	n.d.
217.1	10.77	Pentafuranose	Saccharide	1.24	1.71	1.40	0.81	1.01	1.14	1.38	1.55
82.1	10.83	Unknown	?	n.d.	n.d.	n.d.	0.14	n.d.	n.d.	n.d.	1.15
129.1	10.87	Pentapyranoside ??	Saccharide	1.00	0.90	n.d.	n.d.	0.97	0.75	n.d.	n.d.
333.1	10.90	Uronic acid ?	Sugar acid	n.d.	n.d.	n.d.	0.06	n.d.	n.d.	n.d.	6.49
191.1	10.93	2-Deoxyribose ?	Saccharide	1.57	n.d.	n.d.	n.d.	0.00	n.d.	n.d.	n.d.
103.1	11.07	Arabinose*	Saccharide	1.03	1.47	2.89	2.65	0.98	0.81	0.71	0.61
217.1	11.11	Monosaccharide (Pentapyranose?)	Saccharide	0.98	1.07	1.56	0.74	0.99	0.64	0.63	0.64
217.1	11.19	Monosaccharide (Pentapyranose?)	Saccharide	1.08	0.43	0.94	n.d.	1.02	0.79	0.83	n.d.
103.1	11.23	Ribose*	Saccharide	1.03	0.64	1.12	0.80	0.88	1.03	0.90	0.99
279.2	11.27	Unknown	?	2.11	0.19	1.18	0.37	4.26	1.44	1.46	0.91
111.1	11.33	Heptadecanone	Oxo-Hydrocarbon	n.d.	n.d.	n.d.	0.48	n.d.	n.d.	n.d.	0.77
129	11.41	Xylulose ?	Saccharide	0.98	0.67	0.74	0.28	1.04	0.82	0.64	0.71
199.1	11.63	Tetradecanoic acid deriv.	Fatty acid deriv.	n.d.	n.d.	n.d.	0.38	n.d.	n.d.	n.d.	0.61
217.1	11.81	Monosaccharide ?	Saccharide	n.d.	1.99	7.51	n.d.	n.d.	0.80	0.67	n.d.
271.2	11.87	n-Tetradecan-1-ol	Alcohol	0.94	n.d.	n.d.	n.d.	0.44	n.d.	n.d.	n.d.
217.1	11.89	Glucopyranose ?	Saccharide	n.d.	1.54	n.d.	n.d.	n.d.	0.17	n.d.	n.d.
103.1,129.1	11.93	D(-)-Galactono-1,4-lactone ??	Other	n.d.	n.d.	0.32	0.00	n.c.	n.d.	0.80	1.26
217.1	11.95	Monosaccharide	Saccharide	n.d.	1.29	0.92	n.d.	n.d.	1.28	1.12	n.d.
276.1	12.03	Unknown, Isomer RT 12.15	?	n.d.	n.d.	0.57	n.d.	n.d.	n.d.	1.19	n.d.
204.1	12.09	Saccharide	Saccharide	n.d.	n.d.	0.60	n.d.	n.d.	n.d.	1.47	n.d.
101,393	12.11	Unknown	?	1.45	0.32	n.d.	n.d.	1.97	0.88	n.d.	n.d.
276.1	12.15	Unknown, Isomer RT 12.03	?	n.d.	n.d.	0.13	n.d.	n.d.	n.d.	1.63	n.d.
144	12.16	Amine	Amine	n.d.	n.d.	n.d.	0.00	n.d.	n.d.	n.d.	1.55
217.1	12.23	Monosaccharide	Saccharide	1.13	0.54	n.d.	0.68	0.95	0.56	n.d.	0.83

Appendix Table 5 (continued)

Model-Ion	RT	Metabolite	Class	Fold change							
				Lytic				Non-lytic			
				4 hpi	24 hpi	32 hpi	48 hpi	4 hpi	24 hpi	32 hpi	48 hpi
273.1	12.25	Citric acid	Carboxylic acid	9.05	0.50	0.29	0.04	5.12	2.56	4.31	2.27
253.1	12.29	Unknown	?	1.02	0.50	n.d.	n.d.	1.11	1.17	n.d.	n.d.
143.1	12.35	Pentadecanoic acid deriv.	Fatty acid deriv.	1.23	n.d.	n.d.	0.16	1.27	n.d.	n.d.	0.51
205.1	12.37	? unidentified Sugar deriv.	Saccharide	n.d.	0.59	0.26	n.d.	n.d.	1.40	0.92	n.d.
123.1	12.43	Neophytadiene ⁺	Terpene	1.16	0.71	0.67	0.40	1.25	1.18	1.04	0.75
285.2	12.48	Tetradecanoic acid*	Fatty acid	1.51	2.72	1.70	0.28	1.91	2.27	2.29	1.47
204.1	12.57	Glucopyranose	Saccharide	1.10	0.75	0.74	0.38	1.09	1.20	1.06	1.10
217.1	12.60	Sugar alcohol ?	Sugar alcohol	1.16	n.d.	n.d.	n.d.	1.07	n.d.	n.d.	n.d.
123.1	12.59	(Z)-1,3-Phytadiene	Terpene	1.05	0.68	0.72	0.56	1.18	1.07	0.92	0.76
103.1	12.63	Fructose*	Saccharide	1.35	0.62	0.59	0.45	1.33	1.47	0.98	1.41
103.1	12.69	Fructose*	Saccharide	1.12	0.11	0.94	0.60	1.07	0.80	1.21	1.32
123.1	12.73	(E)-1,3-Phytadiene	Terpene	1.17	0.66	0.64	0.48	1.28	1.02	0.91	0.78
205.1	12.77	Galactose*	Saccharide	n.d.	n.d.	0.99	1.15	n.d.	n.d.	1.15	1.25
319.2	12.83	Glucose*	Saccharide	1.06	1.11	1.77	1.30	1.04	1.12	1.05	1.38
319.2	12.97	Glucose*	Saccharide	1.02	1.17	1.69	1.22	0.97	1.36	1.07	1.44
227.2	13.03	Hexadecanoic acid deriv.	Fatty acid deriv.	1.20	n.d.	n.d.	n.d.	1.38	n.d.	n.d.	n.d.
319	13.08	Mannitol*	Sugar alcohol	0.81	1.25	1.09	1.63	0.87	0.95	0.97	1.06
217.1	13.15	Viburnitol	Sugar alcohol	1.06	1.01	1.17	1.66	0.90	0.79	0.97	0.99
299.2	13.15	Pentadecanoic acid*	Fatty acid	n.d.	n.d.	1.10	0.07	n.d.	n.d.	2.48	1.18
319.2	13.23	Glucono-1,5-lactone*	Other	0.95	0.88	0.89	0.90	1.18	0.88	0.78	0.85
205.1	13.29	Unknown	?	0.83	1.16	1.26	0.32	0.85	1.47	0.83	0.62
217.1	13.37	β -D-Galactofuranose ?	Saccharide	1.39	1.18	0.95	0.55	1.27	2.62	1.00	1.18
217.1	13.42	Hexoaldonic acid ?	Sugar acid	2.37	n.d.	0.74	0.51	1.64	n.d.	1.50	0.54
217.1	13.47	myo-Inositol deriv. ?	Sugar alcohol	n.d.	n.d.	0.62	0.47	n.d.	n.d.	0.81	1.21
333.1	13.55	Gluconic acid*	Sugar acid	n.d.	n.d.	0.99	0.37	n.d.	n.d.	0.90	0.95
105.1	13.57	unsat. Hydrocarbon, Isomer RT 13.81	Hydrocarbon	1.04	0.86	0.94	0.48	1.10	1.06	0.70	0.67
305.1	13.63	Inositol isomer ?	Sugar alcohol	0.97	0.92	0.99	n.d.	1.19	1.67	0.93	n.d.
318	13.70	Inositol isomer	Sugar alcohol	1.20	0.62	0.83	0.51	0.66	0.75	0.88	0.70

Appendix Table 5 (continued)

Model-Ion	RT	Metabolite	Class	Fold change							
				Lytic				Non-lytic			
				4 hpi	24 hpi	32 hpi	48 hpi	4 hpi	24 hpi	32 hpi	48 hpi
393.2	13.75	Unknown	?	n.d.	n.d.	0.80	0.66	n.d.	n.d.	0.93	0.76
313	13.79	Hexadecanoic acid*	Fatty acid	1.37	2.22	1.25	0.24	1.44	2.94	3.08	1.14
105.1	13.81	unsat. Hydrocarbon, Isomer RT 13.57	Hydrocarbon	0.97	0.80	0.72	0.29	1.08	0.91	0.66	0.70
211.2	13.86	Unknown	?	1.16	n.d.	n.d.	n.d.	1.23	n.d.	n.d.	n.d.
105.1,108.1	13.91	unsat. Hydrocarbon	Hydrocarbon	1.10	0.85	0.83	0.47	1.21	1.14	0.82	0.69
204.1	13.99	Hexose	Saccharide	1.16	0.61	0.40	0.28	1.32	1.16	1.35	1.42
105.1	14.10	unsat. Hydrocarbon	Hydrocarbon	0.96	0.60	0.63	0.30	0.91	1.40	0.92	0.63
122.1	14.12	Oleanitrile	Other	n.d.	0.93	n.d.	n.d.	n.d.	1.11	n.d.	n.d.
305.1	14.13	myo-Inositol*	Sugar alcohol	1.17	0.88	0.91	0.91	1.05	0.77	0.74	0.73
108.1,112.1	14.19	Fatty acid	Fatty acid	1.15	0.00	1.19	1.30	1.54	0.57	0.86	0.70
319.2	14.27	Sedoheptulose	Saccharide	0.86	0.09	0.71	0.61	0.97	0.75	0.72	1.09
204.1	14.31	Hexose	Saccharide	0.97	0.62	0.37	n.d.	1.20	1.36	1.01	n.d.
151	14.35	Unknown	?	0.74	n.d.	n.d.	n.d.	0.00	n.d.	n.d.	n.d.
204.1	14.39	Hexose	Saccharide	n.d.	n.d.	1.06	0.47	n.d.	n.d.	1.00	1.24
327.3	14.49	Unknown	?	n.c.	0.95	0.00	n.d.	n.c.	0.42	0.00	n.d.
143.1	14.59	(E)-Phytol*	Terpene	n.d.	n.d.	0.84	0.67	n.d.	n.d.	1.22	0.92
319.2	14.68	Saccharide	Saccharide	0.81	0.66	0.92	0.69	1.02	0.92	0.82	0.99
167	14.73	Unknown	?	n.d.	n.d.	n.d.	1.24	n.d.	n.d.	n.d.	0.70
117	15.01	Octadecanoic acid	Fatty acid	1.63	1.19	0.74	0.17	1.30	0.66	1.35	0.97
239.2	15.09	unsat. Hydrocarbon	Hydrocarbon	1.39	2.47	0.76	0.25	1.81	4.39	0.92	1.17
86.1	15.16	Unknown	?	2.11	2.47	n.d.	n.d.	2.10	4.39	n.d.	n.d.
170.1,358.2	15.29	Saccharide deriv.	Saccharide	1.01	0.85	0.78	1.07	1.05	1.00	0.83	0.75
204.1	15.32	Saccharide	Saccharide	n.d.	n.d.	0.68	0.62	n.d.	n.d.	0.72	1.13
204.1	15.41	Galactosylglycerol	Saccharide	1.06	0.75	0.86	0.61	0.94	1.56	0.99	1.61
140.1,180.1	15.47	unsat. Hydrocarbon	Hydrocarbon	1.13	0.68	0.70	0.34	1.25	1.50	1.30	1.08
211.2	15.57	Unknown	?	n.d.	1.16	n.d.	n.d.	n.d.	0.61	n.d.	n.d.
167	15.63	Unknown	?	1.24	0.92	0.14	1.45	1.09	1.57	3.55	0.82
204.1	15.71	Galactosylglycerol	Saccharide	n.d.	n.d.	0.79	0.37	n.d.	n.d.	1.58	1.47

Appendix Table 5 (continued)

Model-Ion	RT	Metabolite	Class	Fold change							
				Lytic				Non-lytic			
				4 hpi	24 hpi	32 hpi	48 hpi	4 hpi	24 hpi	32 hpi	48 hpi
343.3	15.85	Tetradecanoic acid deriv.	Fatty acid deriv.	n.d.	n.d.	4.92	10.99	n.d.	n.d.	1.53	0.79
285.2	15.87	Octadecanoic acid deriv. ?	Fatty acid deriv.	n.d.	1.25	n.d.	n.d.	n.d.	1.17	n.d.	n.d.
204	16.05	Fatty acid	Fatty acid	n.d.	0.81	0.61	0.26	n.d.	1.99	0.95	1.20
187.2,370	16.15	Unknown	?	n.d.	0.06	n.d.	0.25	n.d.	1.95	n.d.	1.18
105.1	16.25	Docosaehaenoic acid	Fatty acid	1.19	0.57	0.57	0.24	1.34	1.13	0.82	0.58
122.1,136.1	16.49	unsat. Hydrocarbon	Hydrocarbon	n.d.	1.01	1.94	0.43	n.d.	1.01	0.82	1.10
204.1	16.63	complex Saccharide	compl. Saccharide	1.18	0.84	0.80	0.12	1.29	1.58	0.98	1.34
371.3	16.89	Hexadecanoic acid deriv.	Fatty acid deriv.	0.00	0.00	2.58	2.22	2.51	1.45	1.87	0.69
283.3	16.95	Unknown	?	0.00	0.97	1.11	1.24	0.00	1.06	0.75	0.84
204.1	17.10	D-Xylobiose	compl. Saccharide	n.d.	n.d.	n.d.	0.51	n.d.	n.d.	n.d.	2.02
230.1	17.15	Adenosine ??	Other	n.d.	n.d.	n.d.	1.40	n.d.	n.d.	n.d.	1.55
217.1	17.17	complex Saccharide	compl. Saccharide	n.d.	n.d.	0.69	n.d.	n.d.	n.d.	0.55	n.d.
361.2	17.22	Sucrose*	compl. Saccharide	1.01	n.d.	n.d.	n.d.	0.78	n.c.	n.d.	n.d.
221.1	17.67	Maltose*	compl. Saccharide	n.d.	0.82	0.00	2.01	n.d.	0.90	0.00	2.61
221,361.20	17.75	Trehalose, alpha,alpha'-, D-*	compl. Saccharide	1.27	1.35	3.69	7.78	1.58	1.16	1.48	4.47
399.3	17.86	Octadecanoic acid deriv. ?	Fatty acid deriv.	n.d.	0.00	0.00	47.34	n.c.	0.34	5.99	0.00
311.3	17.93	Unknown	?	1.38	0.76	1.38	1.08	1.23	1.09	0.83	0.83
204.1	18.11	Disaccharide	compl. Saccharide	n.d.	n.d.	0.81	0.56	n.d.	n.d.	0.79	1.81
204.1	18.21	Disaccharide	compl. Saccharide	n.d.	n.d.	1.05	n.d.	n.d.	n.d.	0.95	n.d.
255.2	18.27	Ergostatriene isomer ?	Sterol	n.d.	0.60	0.92	0.31	n.d.	1.13	1.17	0.90
204.1	18.29	Disaccharide	compl. Saccharide	n.d.	n.d.	0.90	n.d.	n.d.	n.d.	0.81	n.d.
211.2	18.47	unsat. Hydrocarbon	Hydrocarbon	1.20	1.64	1.54	0.59	1.30	2.58	1.23	1.07
380.3	18.79	Ergostatriene isomer	Sterol	0.89	0.51	1.00	0.43	1.07	1.10	1.24	0.98
204.1	18.93	Melibiose	compl. Saccharide	1.05	0.78	0.57	0.34	1.33	1.49	1.23	1.34
380.3	19.02	Ergostatriene isomer	Sterol	0.93	0.50	0.99	0.39	1.08	0.95	1.15	0.74
253.2	19.20	Sterol	Sterol	0.99	0.89	0.64	0.50	1.03	0.96	1.12	1.12
204.1	19.40	Galactinol ??	Sugar alcohol	1.07	0.75	0.72	0.65	1.08	1.86	1.08	1.41
110.1	19.68	C31H60, 2DBE (Isomer RT 19.90)	Hydrocarbon	1.15	0.77	1.02	0.70	1.16	1.05	0.96	0.78

Appendix Table 5 (continued)

Model-Ion	RT	Metabolite	Class	Fold change							
				Lytic				Non-lytic			
				4 hpi	24 hpi	32 hpi	48 hpi	4 hpi	24 hpi	32 hpi	48 hpi
110.1	19.90	C ₃₁ H ₆₀ , 2 DBE (Isomer RT 19.68)	Hydrocarbon	1.07	0.71	1.06	0.59	1.13	0.98	0.87	0.66
204.1	19.99	Digalactosylglycerol	compl. Saccharide	1.04	1.16	0.94	0.40	0.96	2.26	1.22	1.42
204.1	20.11	Unknown	?	n.d.	n.d.	1.01	n.d.	n.d.	n.d.	1.12	n.d.
237.1	20.17	alpha-Tocopherol	Terpene	0.88	1.09	1.33	0.66	0.61	0.90	0.91	0.89
204.1	20.33	Disaccharide ?	compl. Saccharide	n.d.	n.d.	1.94	4.08	n.d.	n.d.	0.03	20.79
380.3	20.67	Epibrassicasterol	Sterol	1.24	0.74	0.68	0.53	1.20	1.08	0.80	0.66
204.1	20.75	Unknown	?	n.d.	n.d.	0.85	n.d.	n.d.	n.d.	0.79	n.d.
343.2	20.91	Sterol	Sterol	1.23	0.84	0.55	0.00	1.25	1.08	1.01	1.01
129.1	21.18	Sterol	Sterol	1.53	6.34	19.43	5.06	2.01	1.68	1.58	0.90
110.1	21.36	C ₃₃ H ₆₂ , 3DBE (Isomer RT 21.66)	Hydrocarbon	1.18	1.01	1.21	0.98	1.23	1.17	1.10	0.99
108.1,136	21.47	Fatty acid	Fatty acid	1.22	1.00	1.26	1.01	1.23	0.93	1.15	1.06
110.1	21.66	C ₃₃ H ₆₂ , 3DBE (Isomer RT 21.36)	Hydrocarbon	1.05	0.79	1.05	0.62	1.12	0.97	0.91	0.86
396.3	21.84	Ergostadienone ??	Sterol	n.d.	n.d.	0.30	0.19	n.d.	n.d.	1.76	1.66
204.1	21.93	Disaccharide	compl. Saccharide	0.65	0.87	0.66	0.71	0.62	0.84	0.91	1.19
204.1	22.40	complex Saccharide deriv.	compl. Saccharide	0.91	0.83	0.67	0.47	0.97	1.43	1.14	1.12
204.1	22.71	Disaccharide	compl. Saccharide	0.96	0.81	0.56	n.d.	1.17	0.74	0.63	n.d.
647.4	25.14	Unknown	?	n.d.	n.d.	0.51	1.06	n.d.	n.d.	0.38	0.69
204.1	27.02	Trisaccharide	compl. Saccharide	n.d.	n.d.	1.06	0.31	n.d.	n.d.	0.87	2.02

Metabolites with a reverse match between 800 and 700 are indicated by "?", or, if the reverse match lay between 700 and 600, by "??". "*" indicates metabolite identification confirmed by a standard or "+" an authentic, natural sample (compare 6.4.3). Abbreviations: compl., complex; DBE, double bond equivalent, deriv., derivative; hpi, hours post infection, n.c., not calculable; n.d., not detected; RT, retention time, unsat., unsaturated.

Curriculum Vitae

Personal Information

Name	Michaela Alexandra Mauß
Date of birth	23 rd October, 1982
Contact	michaela.mausz@gmail.com
Nationality	Austrian

Education

Since 01.02.2010	PhD-study in Chemistry, Friedrich Schiller University (FSU) Jena, Germany International Leibniz Research School (ILRS)
10.2004 – 16.12.2008	Diploma in Marine Ecology, University of Vienna, Austria
09.2005 – 01.2006	Term abroad, Ecology, Lund University, Sweden
10.2002 – 10.2004	Basic Study in Biology, University of Vienna, Austria
10.2001 – 06.2002	Study in Electrical Engineering, Technical University of Vienna, Austria
1997 - 2001	Matura, BORG Krems, Hainemann-Straße, Austria

Scientific Experience

01.10.2013 - 21.12.2013	Research stay, Dept. of Plant Sciences, Weizmann Institute of Science, Rehovot, Israel
06.07.2013 – 30.08.2013	Short term fellowship (8 weeks), Weizmann Institute of Science, Rehovot, Israel, granted by the Minerva Foundation Practical course supervision:
2010 – 2012	"Gel electrophoresis"
2012	"Determination of polyunsaturated aldehydes from diatoms"
12.2011 - 09.2012	Diploma student supervision
10. 2010 – 01.2011	Project student supervision
15.09.2009 - 31.01.2010	Research assistant, Dept. of Marine Biology, University of Vienna, Austria
16.04.2009 – 05.07.2009	Internship, Royal Netherlands Institute for Marine Research (NIOZ), Texel, The Netherlands

Field Experience

01. - 30.06.2012	Mesocosm, Norwegian National Mesocosm Centre, Espegrend, Norway
01.05. - 22.05.2010	Mesocosm, Umeå Marine Science Centre, Umeå, Sweden

Workshops

06.-12.01.2013	"Environmental Virology Workshop", Biosphere 2, Oracle, United States
29.08. - 02.09.2011	"Mesocosms in aquatic ecology: use, problems and potentials", IFM-GEOMAR, Kiel, Germany

Selbständigkeitserklärung

Ich erkläre, dass ich die vorliegende Arbeit selbständig und unter Verwendung der angegebenen Hilfsmittel, persönlichen Mitteilungen und Quellen angefertigt habe.

Jena,

Michaela A. Mauß